Analyse van scalaire menging bij hybride RANS-PDF-berekeningen van turbulente gas- en spray-vlammen

Analysis of Scalar Mixing in Hybrid RANS-PDF Calculations of Turbulent Gas and Spray Flames

Reni De Meester

Promotor: prof. dr. ir. B. Merci
Proefschrift ingediend tot het behalen van de graad van
Doctor in de Ingenieurswetenschappen: Werktuigkunde-Elektrotechniek

Vakgroep Mechanica van Stroming, Warmte en Verbranding
Voorzitter: prof. dr. ir. J. Vierendeels
Faculteit Ingenieurswetenschappen en Architectuur
Academiejaar 2011 - 2012

UNIVERSITEIT GENT

ISBN 978-90-8578-526-2
NUR 961
Wettelijk depot: D/2012/10.500/52

Promotor: prof. B. Merci

Vakgroep Mechanica van Stroming, Warmte en Verbranding
Sint-Pietersnieuwstraat 41
B-9000 Gent
België

Acknowledgements

First, I would like to thank my supervisor, Prof. Bart Merci, for giving me the opportunity to perform this PhD research in a stimulating but loose atmosphere. For giving me the opportunity to follow courses and go to conferences and for giving me the personal freedom to fill in this research as I saw fit, but also for reminding me every once and a while to work more towards results and not get lost in endless questions. Finally, for all the effort he has put into making my publications more clear.

I would especially like to acknowledge the help and support of Dr. Bertrand Naud, who has provided me with the computational framework for this PhD research. Without his help this PhD research would not have been possible. I would like to thank him for all the time he has invested in me. Whenever I had question I could ask him. It has been a pleasure to work together with him and he has truly become a friend.

Also without the help of Prof. Ulrich Maas this PhD research would not have been possible. I would like to thank him for providing me with the framework to construct REDIMs and for welcoming me into his research group. I have greatly enjoyed my stay in Karlsruhe. I would also like to thank Prof. Dirk Roekaerts for sharing his insight into PDF methods and for the many interesting discussions we have had over the years.

Thanks to all my colleagues for making it far more enjoyable to come to work. I have enjoyed the lunch breaks and beer evenings with all of you. Also a big thanks to Yves Maenhout, for his patience and for sharing his infinite wisdom of computers, his interesting sense of humour and his cookies. This work would be much harder without smoothly running computers, unexpected jokes and cookies. Also thanks to Elise and Joris for even more cookies.

It goes without saying that I would love to thank all my friends for all the great times during my PhD research. They know who they are and they know I am to lazy to name them all. They have given me a haven for clearing my mind, away from all

the worries regarding research. A special thanks goes out to my house mates, Jeroen and Wouter, for doing the dishes and tolerating my mess while I was in the final stages of writing this PhD thesis.

Finally, I wish to express my most sincere thanks to my parents, Marleen De Bock and Willy De Meester, and to Peter Vantournhout for always believing in me and being there for me. I think these last years have been more stressful for them than for me.

Summary

Due to global warming and environmental pollution there is growing need for reduction of greenhouse gases, i.e. CO_2, H_2O, CH_4 and pollutants, e.g. NO_x, SO_x, which are partly a result of combustion processes. This could be done by avoiding as many combustion processes as possible, but these combustion processes are essential in many industrial and domestic applications and their replacement is in many cases not economically feasible or simply not possible in the near future [1, 2]. Therefore it is important to make combustion processes as efficient as possible in order to minimize the exhaust of pollutants and greenhouse gases. In order to design these efficient combustion processes, one can refer to experiments or simulations. As large scale experiments are expensive and hard to study in detail, numerical simulations are needed in the first stages of design. Also to better understand the details of the important physical processes in an experiment, numerical simulations are the perfect tool.

In the efforts to reduce emissions, gas and spray flames are pushed to their limits resulting in more complex flames in which finite rate chemistry effects such as local extinction become more important. Therefore a modeling framework is needed which results in a good compromise between capturing enough of the complexity of the flame while still being numerically efficient. For statistically stationary gas flames the combination of the hybrid RANS-PDF framework and a tabulated combustion model, such as the Reaction Diffusion Manifold (REDIM), can be this compromise. In the hybrid RANS-PDF framework the gas phase is described simultaneously by the standard RANS equations and a PDF describing the statistics of the composition fields and/or the velocity fields in greater detail. The transport equation of the PDF is solved with a Monte Carlo method, using computational gas particles to statistically represent the gas.

In many practical applications, turbulent spray flames are encountered. Especially in transport applications most fuels are liquids because of the high energy density.

Numerical simulations thus need to be able to deal with the presence of the liquid phase, i.e. the droplets, in the gas. Therefore an extra modeling part needs to be added to the hybrid RANS-PDF framework which describes the gas phase. In this PhD research the liquid phase is described in a probabilistic manner, through a droplet PDF. Similar to what is done for the gas PDF, the transport equation of the droplet PDF is solved with a Monte Carlo Method calculating the evolution of computational droplet parcels which statistically represent a group of physical droplets with similar properties.

This thesis focuses on the numerical analysis of scalar mixing modeling in the framework of hybrid RANS-PDF and its influence on the predictions of turbulent gas and spray flames.

In the first part of this thesis, the governing equations of the RANS-PDF framework are introduced and the necessary sub-models are described. The advantage of the hybrid RANS-PDF framework is compared to standard RANS calculations with presumed PDF assumptions. Then the most commonly used combustion models are discussed and compared to the Reaction Diffusion Manifold (REDIM) model which is the primary combustion model used in this PhD research. Subsequently, the droplet PDF framework for the description of the droplets is introduced and the important sub-models are discussed.

After the description of the framework, experimental data of a gaseous swirling bluff-body flame are statistically analysed in order to test the influence of the assumptions often made in presumed PDF modeling. For this specific case it is shown that in the context of RANS, the mixing of intermediate combustion products with fresh air, which takes place in recirculation zone caused by the bluff body, is very hard to model with a presumed PDF, while a transported PDF method naturally accounts for this.

The hybrid RANS scalar-PDF framework is then first tested for the same swirling bluff body flame. For the combustion model, both a single laminar flamelet and a REDIM are tested. The advantage of the use of a progress variable in the REDIM is shown. The progress variable makes it possible to capture finite rate chemistry effect such as the mixing of intermediate combustion products with fresh air. The effect of the modeling of the scalar mixing, through the micro-mixing model, is then analyzed in more detail by tracing the computational particles which statistically represent the transported scalar PDF. The effect of the EMST and the CD mixing model on the

trajectories of the computational particles are discussed. This offers new insights into the behavior of these models. It is concluded that both mixing models are unable to capture the local extinction present in this flame, due to the use of a single mean mixing time scale.

The second part of this thesis focuses on the application of the hybrid RANS-PDF methodology for the description of the gas phase in the context of sprays. As discussed above, a droplet-PDF method is used to describe the spray.In this method the droplets are statistically represented by computational droplet parcels. Inherently, the droplets are assumed to be point particles. This means that the flow and composition field around the droplets, which strongly affects the dynamics and the evaporation rate of the droplets, are not resolved and therefore needs to modeled. As the gas phase is described by a velocity-scalar PDF, more information than in a standard RANS approach is available to model the flow and composition in the neighborhood of the droplet.

The inert swirling methanol spray of McDonell and Samuelsen is studied first to test the validity of the used boundary conditions. More importantly, also the influence of the scalar mixing modeling, i.e. the vapor distribution modeling, and the micro-mixing model on the evaporation rate is tested. Also the composition seen by the droplets needs to be modeled. In most calculations this is done by interpolating the cell mean composition at the position of the droplet parcel, but a new model is introduced which uses the properties of computational gas particles which are close to saturation. Calculations have been performed with different combinations of the models and the calculation results are compared qualitatively and quantitatively with the experimental measurements. The influence of the different models on the evaporation rate and thus also the mixture fraction fields is substantial.

With this knowledge in mind also the reactive case is simulated and compared to the experiments. As combustion model both a single flamelet and a REDIM are tested, and a strong influence on the resulting flame structure in physical and composition space is observed. Again the influence of the vapor distribution models and the seen composition models is tested and again it is shown to be substantial.

In conclusion, the potential and shortcomings of the hybrid RANS-PDF method in a gas and spray flames have been investigated. For the specifically studied gas flame, new insights on the interaction of the mixing and the combustion mode have been gained, through the analysis of the trajectories of the computational gas particles.

For the sprays, the modeling of the unresolved flow and composition field close to the droplet surface and the modeling of scalar mixing in the gas phase have been analysed and the influence on the evaporation rate, mixture fraction field and flame structure has been found to be important.

Hopefully, in time this PhD research will prove to be a step towards a greener future.

Samenvatting

Door problemen zoals opwarming van de aarde en milieuvervuiling is er een stijgende nood aan reductie van de uitstoot van broeikasgassen (CO_2, H_2O, CH_4) en milieuverontreinigende stoffen (NO_x, SO_x) die deels het resultaat zijn van verbrandingsprocessen. Dit zou men kunnen doen door zoveel mogelijk verbrandingsprocessen te vermijden, maar deze verbrandingsprocessen zijn essentieel in vele industriële en huishoudellijke toepassingen en hun vervanging is in vele gevallen niet economisch haalbaar of simpelweg onmogelijk [1, 2]. Daarom is het belangrijk om de noodzakelijke verbrandingsprocessen zo efficiënt mogelijk te maken, zodat de uitstoot van broeikasgassen en milieuverontreinigende stoffen tot een minimum beperkt wordt. Bij het ontwerp van deze efficiëntere verbrandingsprocessen kan er gebruik gemaakt worden van experimenten en numerieke simulaties. Aangezien grootschalige experimenten duur zijn en moeilijk om in detail te bestuderen, zijn simulaties het meest aangewezen voor de eerste stappen van het ontwerp. Ook om de belangrijkste fysische processen in experimenten te begrijpen, zijn simulaties het uitgelezen hulpmiddel.

In het streven naar een verminderde uitstoot, worden gas- en sprayvlammen tot het uiterste gedreven zodat in deze complexe vlammen reactiesnelheidsgerelateerde fenomenen, zoals lokale uitdoving belangrijker worden. Daarom is er een modelleringsstructuur nodig waarbij er een goed evenwicht gevonden wordt tussen het kunnen beschrijven van de complexe fenomenen en het beperken van de computationele kost. Voor statistisch stationaire vlammen, kan dit compromis gevonden worden in de combinatie van hybride RANS-PDF berekeningen en een getabelleerd verbrandingsmodel zoals de Reaction Diffusion Manifold (REDIM). Bij hybride RANS-PDF berekeningen wordt het gas tegelijkertijd beschreven door de Reynoldsgemiddele Navier Stokes (RANS) vergelijkingen en een PDF die de compositie- en/of snelheidsvelden gedetailleerder beschrijft. De transportvergelijking van de PDF wordt opgelost aan de hand van een Monte Carlo methode waarbij computationele gaspartikels het gas statistisch voorstellen.

In vele dagdagelijkse toepassingen worden turbulente spray-vlammen aangetroffen, vooral in transporttoepassingen waar de brandstof vaak een vloeistof is omwille van de energiedensiteit. Deze vloeistof wordt in spray-vlammen verneveld in kleine druppels om zo de verdamping van de vloeistof te stimuleren. Numerieke simulaties moeten dus in staat zijn om de aanwezigheid van vloeistof (druppels) in het gas te beschrijven. Daarom moeten extra modellen toegevoegd worden aan de hybride RANS-PDF beschrijving van het gas. In dit doctoraatsonderzoek wordt de vloeistof op een statistische manier beschreven aan de hand van een druppel-PDF. Gelijkaardig aan wat wordt gedaan bij de gas-PDF, wordt de transportvergelijking van de druppel-PDF opgelost met een Monte Carlo Methode die de evolutie berekent van computationele druppels, die een statistische voorstelling zijn van een verzameling van echte druppels met gelijkaardige eigenschappen.

Dit doctoraatsonderzoek focust op de analyse van de modellering van scalaire menging bij de hybride RANS-PDF methode en hoe die modellering de voorspelling van de turbulente gas- en spray-vlammen beïnvloedt.

In het eerste deel van deze thesis worden de vergelijkingen van de hybride RANS-PDF methode geïntroduceerd. Tevens worden de nodige submodellen beschreven. Het voordeel van de hybride RANS-PDF methode ten opzichte van de standaard RANS methode wordt in detail besproken. Vervolgens worden de meest voorkomende verbrandingsmodellen beschreven en vergeleken met het Reaction Diffusion Manifold (REDIM) model dat gebruikt wordt in dit doctoraatsonderzoek. Tenslotte worden de vergelijkingen voor de druppel-PDF methode en bijhorende submodellen beschreven.

Na de beschrijving van alle vergelijkingen en modellen, worden de meest voorkomende aannames bij standaard RANS berekeningen van verbranding getest aan de hand van een statistische analyse van de experimentele data van een gasvlam met swirl achter een breed lichaam. Voor dit specifiek geval wordt aangetoond dat, in de context van RANS berekeningen, het mengen van intermediaire verbrandingsproducten met verse lucht moeilijk te beschrijven is in de standaard RANS berekeningen, terwijl de hybride RANS-PDF methode dit op natuurlijke wijze beschrijft.

De hybride RANS-PDF methode wordt dan eerst getest door berekeningen te doen van de hierboven beschreven gasvlam. Als verbrandingsmodel, worden zowel een flamelet als een REDIM uitgetest en het voordeel van de REDIM wordt duidelijk aangetoond. De voortgangsvariable bij de REDIM maakt het immers mogelijk om reactiesnelheidsgerelateerde fenomen zolas het mengen van intermediaire verbran-

dingsproducten met verse lucht te beschrijven. De invloed van de modellen voor het beschrijven van scalaire menging via het micromengmodel, wordt dan gedetailleerder geanalyseerd door de trajecten van de computationele gaspartikels, die de gas-PDF statistisch voorstellen, te analyzeren. Op deze manier worden het EMST model en het CD model vergeleken en leidt dit tot nieuwe inzichten in verband met het gedrag van deze modellen. Hieruit volgt het besluit dat beide mengmodellen niet in staat zijn om de in deze testvlam aanwezige lokale uitdoving correct te voorspellen, omdat zij slechts gebruik maken van een enkele mengtijdschaal.

Het tweede deel van deze thesis focust op de toepassing van de hybride RANS-PDF methode voor het gas in de context van sprays. Zoals eerder vermeld wordt een druppel-PDF gebruikt voor de beschrijving van de spray. In deze methode worden druppels statistisch voorgesteld door computationele druppels. Stilzwijgend wordt hierbij aangenomen dat de druppels punten zijn. Dit betekent dat het snelheids- en compositieveld rond de druppels, die heel sterk de dynamica en de verdampingssnelheid van de druppels beïnvloeden, niet geresolveerd wordt en dus moet gemodelleerd worden. Doordat het gas beschreven wordt door een snelheid-scalair-PDF, is er meer informatie voor handen dan in de standaard RANS methode voor de modellering van het snelheids- en compositieveld in de buurt van de druppels.

De inerte methanol spray van McDonell en Samuelsen wordt eerst bestudeerd om de invloed van de modellering van scalaire menging, i.e. het dampdistributiemodel en het micromengmodel, op de verdampingssnelheid te testen. Ook de compositie gezien door de druppels moet gemodelleerd worden. In de meeste spray berekeningen wordt dit gedaan door het celgemiddelde van de compositie te interpoleren op de positie van de computationele druppel. In dit doctoraatsonderzoek wordt echter een nieuw model geïntroduceerd dat gebruik maakt van de eigenschappen van de computationele gas partikels die bijna gesatureerd zijn. Er worden berekeningen uitgevoerd met combinaties van de verschillende modellen en de resultaten worden op kwalitatieve en kwantitatieve wijze vergeleken met de experimentele metingen. Er is een substantiële invloed van de verschillende modellen op de verdampingssnelheid en het mengfractieveld.

Met deze kennis in het achterhoofd wordt ook de methanol spray vlam van McDonell en Samuelsen gesimuleerd en vergeleken met de experimenten. Opnieuw worden een flamelet en een REDIM getest als verbrandingsmodel, en er is een sterke invloed op de resulterende vlamstructuur in de fysische ruimte en compositieruimte. Ook de invloed van het dampdistributiemodel en het model voor de compositie gezien door

de druppels wordt opnieuw getest en opnieuw is de invloed groot.

Samenvattend, het potentieel en de tekortkomingen van de hybride RANS-PDF methode is bestudeerd in gas en spray vlammen. Voor de bestudeerde gasvlam heeft dit geleid tot nieuwe inzichten in verband met de interactie van het mengmodel en het verbrandingsmodel, via de analyse van de trajecten van computationele gaspartikels. Voor de inerte methanol spray en de methanol spray-vlam is de modellering van de niet-geresolveerde gasstroming en -compositie dicht tegen het druppeloppervlak en de modellering van scalaire menging in het gas bestudeerd. Hieruit is gebleken dat de invloed op de verdampingssnelheid, het mengfractieveld en de vlamstructuur heel groot is.

Hopelijk kan dit doctoraatsonderzoek een stap zijn naar een groenere toekomst.

Contents

List of Figures

List of Tables

Nomenclature

Acronyms

CD	Coalescence Dispersion
CFD	Computational Fluid Dynamics
DNS	Direct Numerical Simulation
DPM	Discrete Particle Method
EMST	Euclidean Minimum Spanning Tree
FGM	Flamelet Generated Manifold
FPI	Flamelet Prolongation of ILDM
FPV	Flamelet- Progress variable
GLM	Generalized Langevin Model
ILDM	Intrinsic Lower Dimensional Manifold
LES	Large Eddy Simulation
MDF	Mass Density Function
PCM	Presumed Conditional Moment
PDF	Probability density function
RANS	Reynolds-averaged Navier-Stokes
REDIM	Reaction Diffusion Manifold
RSM	Reynolds stress model
SLM	Simplified Langevin Model
UFPV	Unsteady Flamelet- Progress variable

Greek Symbols

α	Volume fraction
χ	Scalar dissipation rate, scalar unit/s
ϵ	Turbulence dissipation rate, m^2/s^3

Γ	Diffusivity, m^2/s
λ	Thermal conductivity, W/mK or Progress parameter
μ	Dynamic viscosity, $Pa.s$
ν	Kinematic viscosity, m^2/s
ω	Turbulence frequency, s^{-1}
ϕ	Scalar property
ρ	Density, kg/m^3
σ	Standard deviation
τ	Time scale, s
τ_{ij}	Shear stress tensor
$\boldsymbol{\phi}$	Composition vector

Roman Symbols

$\mathcal{F}$	Mass Density Function
A	Surface area, m^2
B_M	Mass transfer number
B_T	Heat transfer number
Bi	Biot number
c	Normalized progress variable
C_p	Specific heat capacity, J/kgK
C_ϕ	Mixing coefficient
D_p	Droplet diameter
Da	Damköhler number
F	Force, N
f	Probability Density Function
g	Gravitational acceleration, m/s^2
h	Convective heat transfer coefficient, W/m^2K
k	Turbulent kinetic energy, m^2/s^2
L	Integral length scale, m
Le	Lewis number
m	Mass, kg
$N_{max,cell}$	Maximum number of computational particles allowed in a cell
$N_{min,cell}$	Minimum number of computational particles allowed in a cell
$N_{p,cell}$	Actual number of computational particles in a cell
N_{TA}	Number of time steps for the iteration averages

Nu	Nusselt number
p	Pressure, Pa
q	Heat flux, W/m^2
Q_α	Conditional mean of scalar property
r	Radial coordinate
$rCO2$	Production rate of Y_{CO2}, Y_{CO2}/s
Re	Reynolds number
S_ϕ	Source term of ϕ
s_{ij}	Fluctuating rate of strain, s^{-1}
Sc	Schmidt number
Sh	Sherwood number
St	Stokes number
T	Temperature, K
U	Velocity, m/s
V	Volume, m^3, or Velocity, m/s
x	Axial coordinate
Y_c	Non-normalized progress variable
Y_F	Fuel mass fraction
Y_s	Vapor mass fraction seen by the droplet
$Y_{F,o}$	Fuel mass fraction in fuel stream
$Y_{O,o}$	Oxidizer mass fraction in oxidizer stream
Z	Mixture fraction

Subscripts and Superscripts

$''$	Favre fluctuation
$*$	Property of a computational particle
$[]^*$	Fluid property interpolated at the position of the computational particle
$\tilde{}$	Favre mean
b	Burnt
c	Chemical
$cntr$	Property at the droplet center
g	Gas
I	Interface
i, j, k	Coordinate index

M	Mass
m	gas film property with 1/3-rule
sat	Property at saturation
st	Stoichiometric
$surf$	Property at the droplet surface
T	Temperature
t	Turbulent
u	Unburnt
vap	Property of pure vapor
p	Property of the droplet
s	Property seen by the droplet

Chapter 1

Introduction

1.1 Motivation

Due to global warming and environmental pollution there is growing need for reduction of greenhouse gases, i.e. CO_2, H_2O, CH_4 and pollutants, e.g. NO_x, SO_x, which are partly a result of combustion processes. This could be done by avoiding as many combustion processes as possible, but these combustion processes are essential in many industrial and domestic applications and their replacement is in many cases not economically feasible or simply not possible in the near future [1, 2]. Therefore it is important to make combustion processes as efficient as possible in order to minimize the exhaust of pollutants and greenhouse gases. In order to design these efficient combustion processes, one can refer to experiments or simulations. As large scale experiments are expensive and hard to study in detail, numerical simulations are needed in the first stages of design. Also to better understand the details of the important physical processes in an experiment, numerical simulations are the perfect tool.

In the efforts to reduce emissions, gas and spray flames are pushed to their limits resulting in more complex flames in which finite rate chemistry effects such as local extinction become more important. Therefore a modeling framework is needed which results in a good compromise between capturing enough of the complexity of the flame while still being numerically efficient. For statistically stationary gas flames the combination of the hybrid RANS-PDF framework and a tabulated combustion model, such as the Reaction Diffusion Manifold (REDIM), can be this compromise. In the hybrid RANS-PDF framework the gas phase is described simultaneously by

the standard RANS equations and a PDF describing the statistics of the composition fields and/or the velocity fields in greater detail. The transport equation of the PDF is solved with a Monte Carlo method, using computational gas particles to statistically represent the gas.

In many practical applications, turbulent spray flames are encountered. Especially in transport applications most fuels are liquids because of the high energy density. Numerical simulations thus need to be able to deal with the presence of the liquid phase, i.e. the droplets, in the gas. Therefore an extra modeling part needs to be added to the hybrid RANS-PDF framework which describes the gas phase. In this PhD research the liquid phase is described in a probabilistic manner, through a droplet PDF. Similar to what is done for the gas PDF, the transport equation of the droplet PDF is solved with a Monte Carlo Method calculating the evolution of computational droplet parcels which statistically represent independent realizations of the dispersed phase.

This thesis focuses on the numerical analysis of scalar mixing modeling in the framework of hybrid RANS-PDF and its influence on the predictions of turbulent gas and spray flames.

1.2 Objectives

The objective of this PhD research is to better understand the behavior of the hybrid RANS-PDF modeling framework in combination with a reduced chemistry technique and its ability to capture finite rate chemistry effects, e.g. local extinction and mixing of incomplete combustion products with a fresh mixture, in complex gas and spray flames.

In gas flames, the focus is on better understanding the interaction between the mixing modeling and the reduced chemistry techniques, i.e. flamelet or REDIM, and how this effects the ability of the hybrid RANS-PDF framework to capture finite rate chemistry effects. A small detour is made, through an a priori study, to better understand the relationship between presumed and transported PDF techniques in calculations with pre-calculated chemistry tables.

In sprays, the hybrid RANS gas-PDF droplet-PDF framework first needs to be tested in the case of inert spray in order to assess its capabilities to correctly describe droplet dispersion, evaporation, vapor distribution and scalar mixing.

Only if the results of this test are satisfactory, it is useful to proceed to the case of a spray flame, where the focus is on testing the ability of the combination of the hybrid RANS gas-PDF droplet-PDF framework and a reduced chemistry technique, to capture the spray flame structure in physical and composition space.

1.3 Overview

In chapter 2, the framework for hybrid RANS-PDF calculations of reactive single phase flows is introduced first. Subsequently the framework for hybrid RANS gas-PDF droplet-PDF calculations of inert and reactive sprays is discussed. In chapter 3, the often made assumptions in presumed PDF modeling are discussed by analyzing the experimental data of a swirling bluff-body gas flame. In chapter 4, the hybrid RANS-PDF framework in combination with the REDIM combustion model is tested in the case of the swirling bluff-body flame, which was analyzed in chapter 3. The interaction of the mixing and the combustion model is investigated through the analysis of the trajectories of the computational gas particles, used to statistically represent the gas-PDF. In chapter 5, the hybrid RANS gas-PDF droplet-PDF framework is tested in the case of a swirling inert methanol spray. The influence of the vapor distribution modeling and the seen composition modeling is studied and found to be important. In chapter 6, the hybrid RANS gas-PDF droplet-PDF framework is used in combination with a flamelet or a REDIM to calculate a swirling reactive methanol spray. Finally in chapter 7, the conclusions of this PhD research are summarized and suggestions for future research are made.

Chapter 2

Framework

In the first part of this chapter the description of the gas phase is discussed, while in the second part the description of the spray is introduced.

2.1 Gas

In this section the framework for the modeling of turbulent reacting single phase flows is discussed. First the exact flow equations and the RANS equations are discussed and the basics of combustion are mentioned. Next, the turbulent models are described and the problem of the closure of the mean reaction term is highlighted. Subsequently, the different combustion models are discussed in relationship with REDIM. Finally, the PDF description of the gas phase is introduced and a consistent hybrid RANS-PDF framework is described.

2.1.1 Flow equations

Einstein summation convention

In this PhD thesis the Einstein summation convention, stating that repeated indices are implicitly summed over, is frequently used:

$$a_i b_i = \sum_{i=1}^{n} a_i b_i \tag{2.1}$$

$$a_{ij}b_{ik} = \sum_{i=1}^{n} a_{ij}b_{ik} \tag{2.2}$$

$$a_i \frac{\partial b_k}{\partial x_i} = \sum_{i=1}^{n} a_i \frac{\partial b_k}{\partial x_i} \tag{2.3}$$

The reader should keep this in mind while reading this PhD thesis.

Exact flow equations

The dynamics of a fluid flow are described by the following system of equations. The conservation of mass is described by the continuity equation [10]:

$$\frac{\partial \rho}{\partial t} + \frac{\partial \rho U_i}{\partial x_i} = 0 \tag{2.4}$$

Conservation of momentum is described by the Navier-Stokes equations:

$$\frac{\partial \rho U_j}{\partial t} + \frac{\partial \rho U_i U_j}{\partial x_i} = \frac{\partial \tau_{ij}}{\partial x_i} - \frac{\partial P}{\partial x_j} - \rho g_j \tag{2.5}$$

In this equation τ_{ij} is the viscous stress tensor

$$\tau_{ij} = 2\mu S^*_{ij} \tag{2.6}$$

with S^*_{ij} the pure strain without volume change

$$S^*_{ij} = S_{ij} - \frac{1}{3} S_{kk}\delta_{ij} \tag{2.7}$$

and S_{ij} the rate of strain tensor

$$S_{ij} = \frac{1}{2}\left(\frac{\partial U_i}{\partial x_j} + \frac{\partial U_j}{\partial x_i}\right) \tag{2.8}$$

For incompressible flows there is no volume change and $S^*_{ij} = S_{ij}$.

A very important term in the Navier-Stokes equation is the non-linear convection term $\frac{\partial \rho U_i U_j}{\partial x_i}$, which is responsible for the unstable nature of the equations when the

flow is turbulent. In turbulent flows it is responsible for the instability of the large vortices. These vortices keep breaking up until the viscous forces become important and the kinetic energy in the vortices is dissipated into heat. This phenomenon is better known as the energy cascade. The Reynolds number is a measure of this 'instability of the flow' and is defined as follows:

$$Re = \frac{U.L}{\nu} \tag{2.9}$$

with U a representative velocity and L a representative length scale. It is the ratio of inertial and viscous forces and is a measure used to know for whether or not a flow is turbulent.

The transport of a scalar property is described by the general scalar equation.

$$\frac{\partial \rho\phi}{\partial t} + \frac{\partial \rho U_i \phi}{\partial x_i} = \frac{\partial}{\partial x_i}\left(\rho\Gamma\frac{\partial \phi}{\partial x_i}\right) + S_\phi \tag{2.10}$$

with S_ϕ a source term. This scalar property can for example be temperature or enthalpy or a species mass fraction. For a conserved passive scalar such as mixture fraction the source term drops out:

$$\frac{\partial \rho\phi}{\partial t} + \frac{\partial \rho U_i \phi}{\partial x_i} = \frac{\partial}{\partial x_i}\left(\rho\Gamma\frac{\partial \phi}{\partial x_i}\right) \tag{2.11}$$

Scales In a turbulent flow there is usually a large range of scales: The integral scales are the larges scales encountered in the flow. They depend on the turbulent kinetic energy k:

$$k \equiv \frac{1}{2}\widetilde{u_i'' u_i''} \tag{2.12}$$

and the turbulence dissipation rate ϵ:

$$\epsilon \equiv 2\nu\widetilde{s_{ij} s_{ij}} \tag{2.13}$$

with s_{ij} the fluctuating rate of strain:

$$s_{ij} = \frac{1}{2}\left(\frac{\partial u_i''}{\partial x_j} + \frac{\partial u_j''}{\partial x_i}\right) \tag{2.14}$$

The integral length scale is then defined as:

$$L_u \equiv \frac{k^{3/2}}{\epsilon} \tag{2.15}$$

The integral time scale is:

$$\tau_u \equiv \frac{k}{\epsilon} = \omega^{-1} \tag{2.16}$$

The integral scalar scale is:

$$L_\phi \tag{2.17}$$

The Kolmogorov scales are the smallest scales in a turbulent flow and depend on and the turbulence dissipation rate ϵ and the molecular viscosity ν. The Kolmogorov length scale is:

$$\eta \equiv \left(\frac{\nu^3}{\epsilon}\right)^{1/4} \tag{2.18}$$

The Kolmogorov time scale is:

$$\tau_\eta \equiv \left(\frac{\nu}{\epsilon}\right)^{1/2} \tag{2.19}$$

The Batchelor scale represents the smallest scalar eddies. It is equivalent to the Kolmogorov scale but for the scalar field, so the relation to the Kolmogorov length scale is not surprising. The Schmidt number determines the size relative to the Kolmogorov length scale.

$$\lambda_B \equiv Sc^{-1/2}\eta = \frac{\eta}{\sqrt{Sc}} \tag{2.20}$$

with Sc the Schmidt number:

$$Sc = \frac{\nu}{\Gamma} \tag{2.21}$$

In gas-phase flows $Sc \approx 1$, so the smallest scalar eddies are comparable in size to the Kolmogorov eddies. In liquid-phase flows, where $Sc >> 1$, the smallest scalar eddies will be smaller than the Kolmogorov eddies.

Apart from the flow time scales, a chemical mechanism also contains a range of time scales connected to the partial differential equations describing the reactions. These time scales are the inverse of the eigenvalues of the Jacobian of the systems of equations describing the chemical mechanism. In turbulent reacting flows, the relative size of the chemical time scales compared to the flow time scales will affect the global flame structure. If chemical time scales have the same order of magnitude as the flow time scales, there will be interaction between both. This is often referred to as turbulence-chemistry interaction. The Damköhler number describes the ratio of a flow time scale and a chemical time scale and in turbulent reactive flows two different Damköhler numbers can be defined [4]. One based on the integral turbulent timescale τ_t:

$$Da = \frac{\tau_t}{\tau_c} \tag{2.22}$$

and one based on the local mixing timescale $\tau_{mix,st}$:

$$Da^* = \frac{\tau_{mix,st}}{\tau_c} = \frac{1}{\tau_c \widetilde{\chi}_{st}} \tag{2.23}$$

with $\widetilde{\chi}_{st}$ the conditional mean value for scalar dissipation rate at $Z = Z_{st}$:

$$\widetilde{\chi}_{st} \approx 2\Gamma \frac{\partial \phi''_{st}}{\partial x} \frac{\partial \phi''_{st}}{\partial x} \tag{2.24}$$

The latter determines the local balance of reaction and diffusion and therefore expresses the importance of finite chemistry effects. If $Da^* >> 1$,the chemical time scale is much faster than the flow time scale and chemistry can be assumed to be infinitely fast. If on the other hand, $Da^* \approx 1$, the chemical time scale and the mixing time scale have the same order of magnitude and the reactions will be affected by the flow. Finally if $Da^* << 1$, the chemical reaction is much slower than the mixing process and $\overline{S(\phi)} \approx S(\overline{\phi})$, as the reactions see a homogeneous mixture. In figure 2.1 the general order of magnitude of the different scales and the possible overlap of chemical and flow time scales is shown. This wide range of length and time scales makes it impossible to solve the exact flow and chemistry equations in practical turbulent flows, as it would take too long to solve. The solving of the exact equations is called the Direct Numerical Simulation (DNS). Therefore in most practical flows only the largest eddies, containing most of the turbulent kinetic energy are resolved and the effect of the unresolved scales on the resolved properties then has to be modeled.

This technique is better known as the Large Eddy Simulation (LES). In the RANS method, on the other hand, only the mean properties are calculated and the effect of the fluctuations on the mean properties has to be modeled. So in LES, still a range of flow scales (but not the full range) is resolved, while with RANS only the integral scales are resolved. In this PhD research, the RANS method is used and this will now be discussed in greater detail.

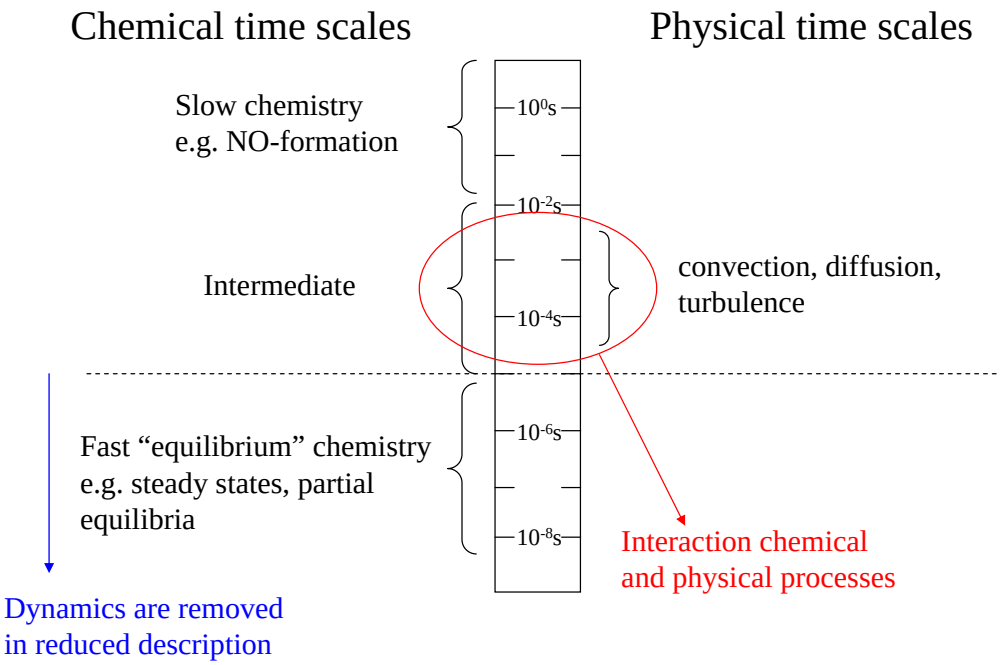

Figure 2.1: Range of physical and chemical timescales in a turbulent reactive flow (adapted from [3])

RANS

Favre averaging In RANS the Reynolds averaged Navier-Stokes equations are solved. However, in combustion processes large density fluctuations arise and with Reynolds averaging the fluctuations of density appear explicitly in the equations. This leads to a large number of extra unknowns. To implicitly take into account these fluctuations, density-weighted averages or Favre averages are used [3]:

$$\widetilde{q} = \frac{\overline{\rho q}}{\overline{\rho}} = \overline{q} + \frac{\overline{\rho' q'}}{\overline{\rho}} \tag{2.25}$$

A property q can then be split into its Favre-average $\widetilde{q}$ and fluctuation q'':

$$q = \widetilde{q} + q'' \tag{2.26}$$

This should be seen more as a mathematical trick than as a model based on the physics of the problem. It should be stressed that Reynolds average $\overline{q}$ and the Favre-average $\widetilde{q}$ are two different properties and this should be kept in mind when comparing results of experiments with calculations.

Equations The RANS equations are derived from the exact equations by Reynolds-averaging, or in this case Favre-averaging, The Favre-averaged continuity equation is:

$$\frac{\partial \overline{\rho}}{\partial t} + \frac{\partial \overline{\rho}\widetilde{U}_i}{\partial x_i} = 0 \tag{2.27}$$

The Favre-averaged momentum equation is:

$$\frac{\partial \overline{\rho}\widetilde{U}_i}{\partial t} + \frac{\partial \overline{\rho}\widetilde{U_i U_j}}{\partial x_i} = \frac{\partial \widetilde{\tau}_{ij}}{\partial x_i} - \frac{\partial \widetilde{P}}{\partial x_j} - \overline{\rho} g_j \tag{2.28}$$

$$\frac{\partial \overline{\rho}\widetilde{U}_i}{\partial t} + \frac{\partial \overline{\rho}\widetilde{U}_i\widetilde{U}_j}{\partial x_i} = \frac{\partial \widetilde{\tau}_{ij}}{\partial x_i} - \frac{\partial \widetilde{P}}{\partial x_j} - \overline{\rho} g_j - \frac{\partial \tau_{ij}^{turb}}{\partial x_j} \tag{2.29}$$

with the turbulent stresses τ_{ij}^{turb}

$$\tau_{ij}^{turb} = \overline{\rho}(\widetilde{U_i U_j} - \widetilde{U}_i\widetilde{U}_j) = \overline{\rho}\widetilde{u_i'' u_j''} \tag{2.30}$$

These turbulent stresses are then modeled with a turbulence model: a turbulent viscosity model or a Reynolds stress model. In this PhD research both $k-\epsilon$ and Reynolds stress models are used.

Turbulent viscosity model In the turbulent viscosity model, the Boussinesq assumption is used, which states that the anisotropy tensor a_{ij} is determined by the

mean velocity gradients:

$$a_{ij} = \widetilde{u_i'' u_j''} - \frac{2}{3}k\delta_{ij} = -2\nu_t \widetilde{S}^*_{ij} = -2\nu_t\left(\widetilde{S}_{ij} - \frac{1}{3}\widetilde{S}_{kk}\delta_{ij}\right) = -\nu_t\left(\frac{\partial \widetilde{U}_i}{\partial x_j} + \frac{\partial \widetilde{U}_j}{\partial x_i} - \frac{2}{3}\frac{\partial \widetilde{U}_k}{\partial x_k}\delta_{ij}\right) \tag{2.31}$$

with ν_t the turbulent viscosity. The turbulent stress τ_{ij}^{turb} then becomes:

$$\tau_{ij}^{turb} = -2\mu_t\left(\widetilde{S}_{ij} - \frac{1}{3}\widetilde{S}_{kk}\delta_{ij}\right) + \frac{2}{3}\overline{\rho}k\delta_{ij} \tag{2.32}$$

The mean momentum equation then becomes:

$$\frac{\partial \overline{\rho}\widetilde{U}_i}{\partial t} + \frac{\partial \overline{\rho}\widetilde{U}_i\widetilde{U}_j}{\partial x_i} = \frac{\partial}{\partial x_i}\left(2\mu\left(\widetilde{S}_{ij} - \frac{1}{3}\widetilde{S}_{kk}\delta_{ij}\right) - \frac{\partial \widetilde{P}}{\partial x_j} - \overline{\rho}g_j + \frac{\partial}{\partial x_i}\left(2\mu_t\left(\widetilde{S}_{ij} - \frac{1}{3}\widetilde{S}_{kk}\delta_{ij}\right) - \frac{2}{3}\overline{\rho}k\delta_{ij}\right)\right. \tag{2.33}$$

$$\frac{\partial \overline{\rho}\widetilde{U}_i}{\partial t} + \frac{\partial \overline{\rho}\widetilde{U}_i\widetilde{U}_j}{\partial x_i} = \frac{\partial}{\partial x_i}\left(2(\mu+\mu_t)\left(\widetilde{S}_{ij} - \frac{1}{3}\widetilde{S}_{kk}\delta_{ij}\right)\right) - \frac{\partial \widetilde{P}}{\partial x_j} - \overline{\rho}g_j - \frac{2}{3}\frac{\partial \overline{\rho}k}{\partial x_i}\delta_{ij} \tag{2.34}$$

For high Reynolds numbers, the turbulent viscosity is at least an order of magnitude larger than the molecular viscosity ν. Therefore the effect of molecular viscosity on the turbulence is often neglected. There are different turbulent viscosity models but only the $k-\epsilon$ models are discussed here, as such a model was used in this PhD. The $k-\epsilon$ model solves transport equations for k and ϵ in order to calculate the turbulent viscosity, μ_t:

$$\mu_t = \overline{\rho}C_\mu\frac{k^2}{\epsilon} \tag{2.35}$$

In the standard $k-\epsilon$ model, the transport equation for k is

$$\frac{\partial \overline{\rho}k}{\partial t} + \frac{\partial \overline{\rho}\widetilde{U}_i k}{\partial x_i} = \frac{\partial}{\partial x_i}\left((\mu + \frac{\mu_t}{Sc_{t,k}})\frac{\partial k}{\partial x_i}\right) + P_k - \overline{\rho}\epsilon \tag{2.36}$$

with $P_k \equiv -\overline{\rho}\widetilde{u_i''u_j''}\frac{\partial \widetilde{U}_i}{\partial x_j} = \overline{\rho}a_{ij}\widetilde{S}^*_{ij}$. The transport equation for ϵ is then:

$$\frac{\partial \overline{\rho}\epsilon}{\partial t} + \frac{\partial \overline{\rho}\widetilde{U}_i\epsilon}{\partial x_i} = \frac{\partial}{\partial x_i}\left((\mu + \frac{\mu_t}{Sc_{t,\epsilon}})\frac{\partial \epsilon}{\partial x_i}\right) + C_{\epsilon 1}\frac{\epsilon}{k}P_k - C_{\epsilon 1}\overline{\rho}\frac{\epsilon^2}{k+\sqrt{\nu\epsilon}} \tag{2.37}$$

In the realizable $k-\epsilon$ model a modified transport equation for ϵ is used:

$$\frac{\partial \overline{\rho}\epsilon}{\partial t} + \frac{\partial \overline{\rho}\widetilde{U}_i\epsilon}{\partial x_i} = \frac{\partial}{\partial x_i}\left((\mu + \frac{\mu_t}{Sc_{t,\epsilon}})\frac{\partial \epsilon}{\partial x_i}\right) + C_1\overline{\rho}\epsilon\sqrt{2S^*_{ij}S^*_{ij}} - C_2\overline{\rho}\frac{\epsilon^2}{k} \tag{2.38}$$

with $C_1 = max\left[0.43, \frac{\sqrt{2S^*_{ij}S^*_{ij}}}{\sqrt{2S^*_{ij}S^*_{ij}}+5}\right]$. C_μ is now calculated dynamically. In this PhD the cubic $k-\epsilon$ model of Merci et al. [11] is used, which takes into accounts curvature effects on the turbulence. This is important for the swirling flows that are studied. In this aspect the Merci $k-\epsilon$ model resembles the better known realizable $k-\epsilon$ model. In the Merci model a similar transport equation for ϵ is solved with some modifications for a low Reynolds approach:

$$\frac{\partial \overline{\rho}\epsilon}{\partial t} + \frac{\partial \overline{\rho}\widetilde{U}_i\epsilon}{\partial x_i} = \frac{\partial}{\partial x_i}\left((\mu + \frac{\mu_t}{Sc_{t,\epsilon}})\frac{\partial \epsilon}{\partial x_i}\right) + f_{R_y}C_1\overline{\rho}\epsilon\sqrt{2S^*_{ij}S^*_{ij}} - C_{\epsilon 2}f_2\overline{\rho}\frac{\epsilon}{\tau_t} + (1-f_{R_y})C_{\epsilon 1}\frac{P_k}{\tau_t} + E + Y_c \tag{2.39}$$

with f_{R_y} a blending function ranging from 0 at the wall to 1 and with

$$\tau_t = \frac{k}{\epsilon} + \sqrt{\frac{\mu}{\overline{\rho}\epsilon}}. \tag{2.40}$$

Also E and Y_c disappear away from the wall. So the equation at the wall resembles more the ϵ equation for the standard model, while away from the wall the ϵ equation resembles that of the realizable $k-\epsilon$ model:

$$\frac{\partial \overline{\rho}\epsilon}{\partial t} + \frac{\partial \overline{\rho}\widetilde{U}_i\epsilon}{\partial x_i} = \frac{\partial}{\partial x_i}\left((\mu + \frac{\mu_t}{Sc_{t,\epsilon}})\frac{\partial \epsilon}{\partial x_i}\right) + C_1\overline{\rho}\epsilon\sqrt{2S^*_{ij}S^*_{ij}} - C_{\epsilon 2}f_2\overline{\rho}\frac{\epsilon}{\tau_t} \tag{2.41}$$

The Merci model however does not use a single turbulent viscosity, but uses a cubic relation ship with several terms involving strain rate and vorticity terms for the

turbulent stresses:

$$\begin{aligned}\frac{\widetilde{u_i''u_j''}}{k} &= \frac{2}{3}\delta_{ij} - 2c_\mu f_\mu \tau_t S_{ij}^* + q_1\tau_t^2\left(S_{ik}^*S_{kj}^* - \frac{1}{3}\delta_{ij}S_{lm}^*S_{ml}^*\right) \\ &+ (q_2 + q_1/6)\tau_t^2\left(\Omega_{ik}S_{kj}^* - S_{ik}^*S_{kj}^*\right) + c_1\tau_t^3\left(S_{mn}^*S_{nm}^* + \Omega_{mn}\Omega_{nm}\right) \\ &+ c_2\tau_t^3\left(\Omega_{ik}S_{kl}^*S_{lj}^* - S_{ik}^*S_{kl}^*\Omega_{lj}\right)\end{aligned} \tag{2.42}$$

with Ω_{ij} the antisymmetric part of the deformation tensor:

$$\Omega_{ij} = \frac{1}{2}\left(\frac{\partial \widetilde{U}_i}{\partial x_j} - \frac{\partial \widetilde{U}_j}{\partial x_i}\right) \tag{2.43}$$

and coefficients c_μ, q_i and c_i depending on tensor invariants

$$S = \sqrt{2S_{ij}^*S_{ij}^*} \quad \text{and} \quad \Omega = \sqrt{2\Omega_{ij}\Omega_{ij}} \tag{2.44}$$

This is not discussed further as this is beyond the scope of this PhD research and the reader is referred to the original paper [11].

Reynolds stress model In the Reynolds stress model RSM), transport equations are solved for all the turbulent stresses [12]:

$$\begin{aligned}\frac{\partial \overline{\rho}\widetilde{u_i''u_j''}}{\partial t} + \frac{\partial \overline{\rho}\widetilde{U_k}\widetilde{u_i''u_j''}}{\partial x_k} = &\underbrace{-\frac{\partial}{\partial x_k}\left(\overline{\rho}\widetilde{u_i''u_j''u_k''} + (\widetilde{p''u_i''}\delta_{kj} + \widetilde{p''u_j''}\delta_{ik})\right)}_{D_{T,ij}=\text{Turbulent Diffusion}} + \underbrace{\frac{\partial}{\partial x_k}\left(\mu\frac{\partial \widetilde{u_i''u_j''}}{\partial x_k}\right)}_{D_{L,ij}=\text{Laminar Diffusion}} \\ &\underbrace{-\overline{\rho}\left(\widetilde{u_i''u_k''}\frac{\partial \widetilde{U}_i}{\partial x_k} + \widetilde{u_j''u_k''}\frac{\partial \widetilde{U}_j}{\partial x_k}\right)}_{P_{ij}=\text{Turbulence Production}} + \underbrace{p''\left(\widetilde{\frac{\partial u_i''}{\partial x_j}} + \frac{\partial u_j''}{\partial x_i}\right)}_{\phi_{ij}=\text{Pressure strain}} - \underbrace{2\mu\left(\widetilde{\frac{\partial u_i''}{\partial x_k}\frac{\partial u_j''}{\partial x_k}}\right)}_{\epsilon_{ij}=\text{Dissipation}}\end{aligned} \tag{2.45}$$

In high Reynolds flows, the laminar diffusion term $D_{L,ij}$ can often be neglected, while the turbulent diffusion term $D_{T,ij}$ is most often modeled with a gradient diffusion assumption:

$$D_{T,ij} = \frac{\partial}{\partial x_k}\left(\mu_T\frac{\partial \widetilde{u_i''u_j''}}{\partial x_k}\right) \tag{2.46}$$

The pressure strain term ϕ_{ij} is decomposed into a slow $\phi_{ij,s}$ and fast term $\phi_{ij,f}$. In this PhD research, the isotropisation of production model by Launder, Reece and Rodi (LRR-IPM) is used. In this LRR-IPM model, the linear return to isotropy model of Rotta is used for the slow term $\phi_{ij,s}$

$$\phi_{ij,s} = -C_1 \overline{\rho} \frac{\epsilon}{k} (\widetilde{u_i'' u_j''} - \frac{2}{3} k \delta_{ij}) \tag{2.47}$$

with $C_1 = 1.8$ and the fast term $\phi_{ij,f}$ is modeled as:

$$\phi_{ij,f} = -C_2 \left[P_{ij} - \frac{1}{3} P_{kk} \delta_{ij} \right] \tag{2.48}$$

with $C_2 = 0.6$. Compared to the turbulent viscosity models, the modeling effort is transferred towards the higher order terms. As in the $k-\epsilon$ model, still a transport equation for ϵ is solved. The dissipation term ϵ_{ij} is then modeled by assuming isotropy of the smallest eddies:

$$\epsilon_{ij} = \frac{2}{3} \epsilon \delta_{ij} \tag{2.49}$$

Scalar transport The mean transport equation for a general scalar is

$$\frac{\partial \overline{\rho} \widetilde{\phi}}{\partial t} + \frac{\partial \overline{\rho} \widetilde{U_i \phi}}{\partial x_i} = \frac{\partial}{\partial x_i} \left(\overline{\rho} \Gamma \frac{\partial \widetilde{\phi}}{\partial x_i} \right) + \widetilde{S}_\phi \tag{2.50}$$

$$\frac{\partial \overline{\rho} \widetilde{\phi}}{\partial t} + \frac{\partial \overline{\rho} \widetilde{\phi} \widetilde{U}_i}{\partial x_i} = \frac{\partial}{\partial x_i} \left(\overline{\rho} \Gamma \frac{\partial \widetilde{\phi}}{\partial x_i} \right) + \widetilde{S}_\phi - \frac{\partial J_i^{turb}}{\partial x_i} \tag{2.51}$$

with the turbulent scalar flux J_i^{turb}:

$$J_i^{turb} = \overline{\rho} (\widetilde{\phi U_i} - \widetilde{\phi} \widetilde{U}_i) = \overline{\rho} \widetilde{\phi'' u_i''} \tag{2.52}$$

which is often modeled with a gradient diffusion assumption:

$$\widetilde{\phi'' u_i''} = -\Gamma_t \frac{\partial \widetilde{\phi''}}{\partial x_i} \tag{2.53}$$

The mean scalar transport equation then becomes:

$$\frac{\partial \overline{\rho}\widetilde{\phi}}{\partial t}+\frac{\partial \overline{\rho}\widetilde{\phi}\widetilde{U}_i}{\partial x_i}=\frac{\partial}{\partial x_i}\left(\overline{\rho}\Gamma\frac{\partial \widetilde{\phi}}{\partial x_i}\right)+\frac{\partial}{\partial x_i}\left(\overline{\rho}\Gamma_t\frac{\partial \widetilde{\phi}}{\partial x_i}\right)+\widetilde{S}_\phi \tag{2.54}$$

$$\frac{\partial \overline{\rho}\widetilde{\phi}}{\partial t}+\frac{\partial \overline{\rho}\widetilde{\phi}\widetilde{U}_i}{\partial x_i}=\frac{\partial}{\partial x_i}\left(\overline{\rho}(\Gamma+\Gamma_t)\frac{\partial \widetilde{\phi}}{\partial x_i}\right)+\widetilde{S}_\phi \tag{2.55}$$

The transport equation for the mean scalar fluctuations is [13]:

$$\frac{\partial \overline{\rho}\widetilde{\phi''^2}}{\partial t}+\frac{\partial \overline{\rho}\widetilde{\phi''^2}\widetilde{U}_j}{\partial x_j}=-\underbrace{\frac{\partial \overline{\rho}\widetilde{\phi''^2u_j''}}{\partial x_j}}_{\text{Turbulent Diffusion}}\underbrace{-2\overline{\rho}\widetilde{\phi''u_j''}\frac{\partial \widetilde{\phi}}{\partial x_j}}_{\text{Production}}-\underbrace{\overline{\rho}\widetilde{\chi}}_{\text{Dissipation}}+2\overline{\rho}\widetilde{\phi''S_\phi''}+\underbrace{\frac{\partial}{\partial x_j}\left(\overline{\rho}\Gamma\frac{\partial \widetilde{\phi''^2}}{\partial x_j}\right)}_{\text{Molecular Diffusion}} \tag{2.56}$$

The scalar fluxes are again modeled with a gradient diffusion model:

$$\widetilde{\phi''^2u_j''}=-\Gamma_t\frac{\partial \widetilde{\phi''^2}}{\partial x_j}\text{ and }\widetilde{\phi''u_j''}=-\Gamma_t\frac{\partial \widetilde{\phi}}{\partial x_j} \tag{2.57}$$

This results in the following equation for the mean scalar fluctuation:

$$\frac{\partial \overline{\rho}\widetilde{\phi''^2}}{\partial t}+\frac{\partial \overline{\rho}\widetilde{\phi''^2}\widetilde{U}_j}{\partial x_j}=\frac{\partial}{\partial x_j}\left(\overline{\rho}(\Gamma+\Gamma_t)\frac{\partial \widetilde{\phi''^2}}{\partial x_j}\right)+2\overline{\rho}(\Gamma_t)\frac{\partial \widetilde{\phi}}{\partial x_j}\frac{\partial \widetilde{\phi}}{\partial x_j}-\overline{\rho}\widetilde{\chi} \tag{2.58}$$

The scalar dissipation rate is then modeled by the equilibrium model [14]

$$\widetilde{\chi}\equiv 2\Gamma\widetilde{\left(\frac{\partial \phi''}{\partial x_j}\right)^2}\approx C_\phi\frac{\widetilde{\epsilon}}{\widetilde{k}}\widetilde{\phi''^2} \tag{2.59}$$

LES

For completeness, also the Large Eddy Simulation (LES) [15, 16, 10] is mentioned. In LES, the dynamics of the largest scales in the turbulent flow are resolved, while the effect of the smaller unresolved eddies on the resolved eddies is modeled. Therefore in LES a range of turbulent scales is resolved while in RANS only the integral turbulent scale is resolved. As in LES only the effect of the smallest scales, which are often assumed to be isotropic, have to be modeled, the turbulence model is expected to

give better results than in RANS. However, LES is computationally more expensive than RANS and for large scale simulations LES might still be too costly. The best known turbulence model in LES is the Smagorinsky model [17], which is similar to the turbulent viscosity models in RANS, with the difference that for LES the turbulent viscosity depends on the filter width. The governing LES equations are very similar to the RANS equations presented above. It is, however, important to stress the conceptional difference between RANS and LES. In RANS the equations for the statistical means of the properties are solved. In LES, on the other hand, the equations for the filtered, i.e. volume-averaged, values of the properties are solved. For more details the reader is referred to literature [15, 16, 10].

2.1.2 Classification of Combustion

In general, flames can be divided in to different classes based on the degree of mixedness of the reactions or based on the physical mechanisms that stabilize the flame. In premixed flames, a premixed mixture reacts with a reaction front moving through the fresh mixture and leaving behind combustion products. The propagation of the reaction zone is caused by an imbalance of diffusion of heat and chemical reaction. [4] In the reaction zone, strong gradients of temperature, density and species mass fraction are observed. The strong temperature gradients lead to heat fluxes which preheat the fresh mixture. At a certain position in the flame, a progress variable c is often used to describe the progress of reaction at that point. The progress variable can be expressed in terms of temperature T or fuel mass fraction Y_F and varies from 0 for a fresh mixture to 1 for a completely burnt mixture:

$$c = \frac{T - T_u}{T_b - T_u} \tag{2.60}$$

$$c = \frac{Y_F - Y_{F,u}}{Y_{F,b} - Y_{F,u}} \tag{2.61}$$

These definitions, however, only truly represent reaction progress if temperature or fuel mass fraction monotonically increase with reaction progress. In non-premixed flames, also called diffusion flames, the fuel and the oxidizer are on opposite sides of the reaction front. The mixing of the reactants, due to molecular diffusion, determines the burning rate. Or, in other words, diffusion and reaction are balanced, as the diffusion

transports heat away from the reaction zone to heat up the reactants. The stronger the flow is strained, the stronger the mixing and the global reaction rate. However, the reaction rate cannot keep increasing, resulting in an imbalance of diffusion and reaction leading to local extinction. As a diffusion flame is mostly a mixing limited process, the mixture fraction Z, which describes the degree of mixedness between fuel and oxidizer, describes the position in the internal structure of the flame. For a non-premixed flame, the mixture fraction varies from 0 for pure oxidizer to 1 for pure fuel and is thus defined as follows [4]:

$$Z = \frac{\phi \frac{Y_F}{Y_{F,o}} - \frac{Y_O}{Y_{O,o}} + 1}{\phi + 1} \tag{2.62}$$

with $Y_{F,o}$ the fuel mass fraction in the fuel stream, $Y_{O,o}$ the oxidizer mass fraction in oxidizer stream and ϕ the chemical equivalence ratio:

$$\phi = \frac{sY_F, o}{Y_{O,o}} \tag{2.63}$$

with s the mass stoichiometric coefficient. One mixture fraction can only describe a two-stream problem. If more streams are involved extra mixture fractions need to be introduced. The rate of mixing is determined by the gradients of mixture fraction. The scalar dissipation of the mixture fraction which is defined as follows

$$\chi_Z = 2\Gamma \left(\frac{\partial Z}{\partial x_j} \frac{\partial Z}{\partial x_j} \right) \tag{2.64}$$

is therefore a measure of mixing. χ_Z is actually the inverse of the local mixing time scale. In modeling of non-premixed combustion it is one of the key parameters.

Partially premixed flames have features of both premixed and non-premixed flames and often occur as triple flames, which consist of a rich and a lean premixed flame with a diffusion flame further downstream [4]. Many practical non-premixed flames have a degree of premixing, making them actually partially premixed flames.

Finally there is also auto-ignition which is characterized by a build-up of a pool of radicals. In contrast to premixed, non-premixed and partially premixed combustion, there is a balance of reaction and convection in auto-igniting flames.

The focus of this PhD is on non-premixed combustion and therefore premixed combustion and auto-ignition are not further discussed.

Combustion regimes in non-premixed combustion In turbulent combustion modeling an often made assumption is that the local flame structure resembles a laminar flamelet. For premixed combustion, the validity of this assumption depends on the relative size of the reaction zone compared to the size of the Kolmogorov eddies, which is determined by the combination of the Reynolds number Re and the local Damköhler number Da^*. If the ensemble of reaction zone and preheat zone is smaller than the Kolmogorov eddies, then the laminar flamelet assumption is valid. The Kolmogorov eddies will then wrinkle the laminar flamelet structure, without affecting the inner structure.

In non-premixed combustion also Re and Da^* determine the combustion regime. In general there are two limits: the limit of the laminar flamelet assumption Da_{LFA} and the limit extinction limit Da_{ext} [4]. If $Da^* > Da_{LFA}$, the laminar flamelet assumption is valid. If $Da^* < Da_{ext}$, extinction occurs. If $Da_{LFA} > Da^* > Da_{ext}$, unsteady effects occur. This is also shown in figure 2.2

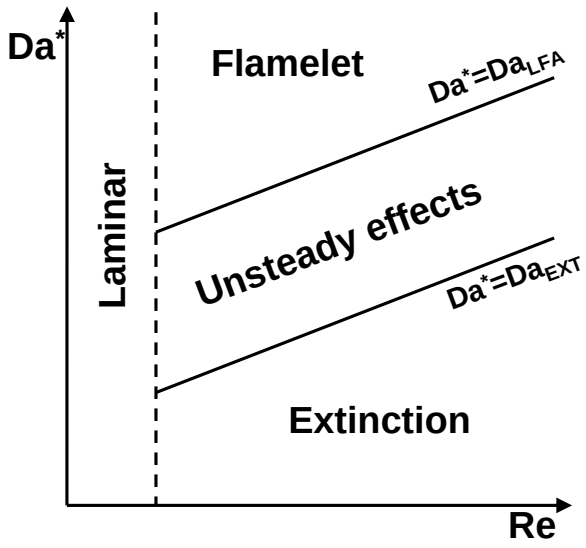

Figure 2.2: Combustion regimes for non-premixed combustion (reproduction from [4])

2.1.3 Non-premixed combustion modeling

In this section the focus is on combustion modeling for non-premixed combustion. All combustion models in RANS and LES respectively try to close the mean and filtered chemical source term. This is however not straightforward due to turbulence

chemistry interaction. The overlap of the range of scales in the chemical mechanism and the range of flow time scales is an important factor to determine whether a certain combustion model is adequate or not for a specific case. If all chemical time scales are larger than the mixing time scale, $\overline{S(\boldsymbol{\phi})} \approx S(\overline{\boldsymbol{\phi}})$, as the reactions 'see' a homogeneous mixture, represented by a Dirac distribution [18]. However, as soon as one chemical time scale is faster than the mixing time scale, the distribution of the composition 'seen' by the reactions differs from a Dirac and $\overline{S(\boldsymbol{\phi})} \neq S(\overline{\boldsymbol{\phi}})$, due to the strong non-linearity of the chemical source term. As the source term only depends on the local composition vector, a one-point composition PDF (probability density function) is sufficient to calculate the mean source term.

$$\overline{S(\boldsymbol{\phi})} = \int S(\boldsymbol{\phi}) f_{\boldsymbol{\phi}} d\boldsymbol{\phi} \tag{2.65}$$

$$\overline{\rho}\widetilde{S(\boldsymbol{\phi})} = \int S(\boldsymbol{\phi}) F_{\boldsymbol{\phi}} d\boldsymbol{\phi} \tag{2.66}$$

The PDF can be presumed or a transport equation for the PDF can be solved.

2.1.4 Reduced chemistry description

In a detailed chemical mechanism the chemical source terms are a function of the complete composition vector $\boldsymbol{\phi}$. As it is computationally too expensive to solve transport equations for all components of the composition vector, most combustion models try to describe the chemical source terms as a function of a reduced set of parameters. The amount of parameters needed depends on the amount of overlap between the range of chemical time scales and the range of mixing time scales. When $\tau_\chi >> \tau_c$, the mean reaction term depends only on mixture fraction Z:

$$\overline{S(Z)} = \int S(Z) f_Z dZ \tag{2.67}$$

In this case often a presumed β-PDF is used for the Z-PDF.

When there is overlap of the chemical and mixing time scales, the effect of diffusion on the chemistry needs to be taken into account and the mean reaction term will

depend on the mixture fraction Z and scalar dissipation rate χ_Z:

$$\overline{S(Z,\chi_Z)} = \int S(Z,\chi_Z) f_{Z,\chi_Z} dZ d\chi_Z = \int S(Z,\chi_Z) f_{\chi_Z|Z} f_Z dZ d\chi_Z = \int \overline{S(\chi_Z|Z)} f_Z dZ \tag{2.68}$$

Again the joint PDF is too hard to model with a presumed shape and therefore Z and χ_Z are assumed to be independent. The joint PDF can then be described by the product of the marginal PDFs $f_{Z,\chi_Z} \approx f_Z f_\chi$. The marginal Z-PDF is again modeled with a β-distribution. The marginal χ_Z-PDF is usually assumed to be a log-normal distribution.

When finite rate chemistry effects become important, a progress variable c is needed in the description and the mean reaction term will at the very least depend on mixture fraction Z and the progress variable c:

$$\overline{S(Z,c)} = \int S(Z,c) f_{Z,c} dZ dc = \int S(Z,c) f_{c|Z} f_Z dZ dc = \int \overline{S(c|Z)} f_Z dZ \tag{2.69}$$

In this case the joint $Z-c$-PDF could be modeled with a presumed PDF. This is, however, too difficult. Often, the progress variable is assumed to be independent of the mixture fraction making the conditional c-PDF independent of Z: $f_{c|Z} \approx f_c$. Then the joint $Z-c$-PDF is described by the product of the marginal PDFs. The assumption of independence is, however, not generally valid. This will be discussed in chapter 3. In this PhD research a modeled transport equation is solved for the joint $Z-c$-PDF, making the assumptions mentioned above unnecessary.

When finite rate chemistry effects like local extinction become more important, even more complex descriptions are needed. The mean source term will then depend on mixture fraction Z, a scalar dissipation rate χ_Z and a progress variable c:

$$\begin{aligned} \overline{S(Z,c,\chi_Z)} &= \int S(Z,c,\chi_Z).f_{Z,c,\chi_Z}.dZ.dc.d\chi_Z \\ &= \int S(Z,c,\chi_Z).f_{Z,c|\chi_Z}.f_{\chi_Z}.dZ.dc.d\chi_Z \\ &= \int \overline{S(Z,c|\chi_Z)} f_{\chi_Z}.d\chi_Z \end{aligned} \tag{2.70}$$

When the difference in mixing time for inert and reactive scalars is accounted for, this becomes even more complex and the mean source term will depend on mixture

fraction Z, two scalar dissipation rates χ_Z and χ_c, and the progress variable:

$$\begin{aligned}\overline{S(Z,c,\chi_Z,\chi_c)} &= \int S(Z,c,\chi_Z,\chi_c).f_{Z,c,\chi_Z,\chi_c}.dZ.dc.d\chi_Z.d\chi_c \\ &= \int S(Z,c,\chi_Z,\chi_c).f_{Z,c|\chi_Z,\chi_c}.f_{\chi_Z,\chi_c}.dc.d\chi_Z.d\chi_c \\ &= \int \overline{S(Z,c|\chi_Z,\chi_c)}.f_{\chi_Z,\chi_c}.d\chi_Z.d\chi_c\end{aligned} \tag{2.71}$$

It is important to stress the importance of the modeling of (micro-)mixing in non-premixed combustion. Physically, micro-mixing is the combination of molecular diffusion and the acceleration of the molecular diffusion by turbulent stretching of the iso-scalar surfaces [19, 20, 21, 22]. An extra effect is that vortex-stretching also causes engulfing of fluid from the environment. Micro-mixing is thus important in reactive flows as chemical reaction is a molecular-level process and micro-mixing brings together the reactants at a molecular level so that they can interact. Both in LES and RANS this micro-mixing is not resolved and has to be modeled. As the scalar dissipation rate χ determines the rate of scalar mixing, it is an important property that also needs to modeled. As local extinction is often attributed to fluctuations in scalar dissipation rate, it will therefore be essential to describe these fluctuations. This can be done statistically through the χ-PDF.

This PhD has been performed within the framework of hybrid RANS-PDF calculations using a single steady non-premixed flamelet or a REDIM table. In order to assess this modeling framework and put it into context, the most common turbulent combustion models for non-premixed combustion are discussed. This will highlight any advantages or disadvantages of the current modeling framework. In each combustion model the scalar dissipation rate or mixing time scale is needed and it is one of the key parameters in the modeling.

Turbulence-Chemistry interaction: Presumed vs Transported PDF

As described in the previous section, the chemical source terms can be described with a reduced number of parameters. For the simplest models the mean reaction source term only depends on the mixture fraction and only the knowledge of the mixture fraction PDF suffices to predict the mean chemical source term. The mixture fraction PDF is described well by a beta-PDF. Then only transport equations for the mean and the variance of the mixture fraction have to be solved.

In more complex combustion models, the chemical source term depends on mixture fraction and one or more progress variables. Then the joint mixture fraction progress variable PDF needs to be modeled. This can be done by splitting up the joint PDF into the product of the conditional progress variable PDF and the marginal mixture fraction PDF:

$$f(Z,c;\boldsymbol{x},t) = f(Z;\boldsymbol{x},t).f(c|Z;\boldsymbol{x},t). \tag{2.72}$$

Often independence of the mixture fraction and the progress variable is assumed, to describe the joint PDF as the product of the marginal PDFs.

$$f(Z,c;\boldsymbol{x},t) = f(Z;\boldsymbol{x},t).f(c;\boldsymbol{x},t). \tag{2.73}$$

The validity of this assumption depends on the definition of the progress variable and the physical processes involved. For one progress variable it is still possible to get reasonable results with a presumed joint mixture progress variable PDF, in particular for LES. For multiple progress variables, however, the prediction of the joint PDF is even harder and the assumption of independence of the progress variables is less valid and a transported PDF method is better suited. The validity of presumed PDF modeling of the joint $Z-c$ PDF will be discussed in more detail in chapter 3.

CMC

In the Conditional Moment Closure (CMC) model [23], transport equations are solved for the conditional means:

$$\frac{\partial Q_\alpha}{\partial t} + \widetilde{U_i|Z}\frac{\partial Q_\alpha}{\partial x_i} = \frac{1}{2}\widetilde{\chi|Z}\frac{\partial^2 Q_\alpha}{\partial^2 Z} + \frac{1}{\overline{\rho|Z}}\widetilde{S_\alpha|Z} + \frac{1}{\overline{\rho}\widetilde{P(Z)}}\frac{\partial[\overline{\rho}u_i''\widetilde{\phi_\alpha''|Z}\widetilde{P(Z)}]}{\partial x_i} \tag{2.74}$$

with $Q_\alpha = \widetilde{\phi_\alpha|Z}$ the conditional mean of the scalar property and $\widetilde{u_i''\phi_\alpha''|Z}$ the conditional turbulent scalar flux, which in RANS is usually modeled with the gradient diffusion assumption:

$$\widetilde{u_i''\phi_\alpha''|Z} \approx \Gamma_t \frac{\partial Q_\alpha}{\partial x_i} \tag{2.75}$$

This eventually results in the following equation:

$$\frac{\partial Q_\alpha}{\partial t} + \widetilde{U_i|Z}\frac{\partial Q_\alpha}{\partial x_i} = \frac{1}{2}\widetilde{\chi|Z}\frac{\partial^2 Q_\alpha}{\partial^2 Z} + \frac{1}{\overline{\rho}\widetilde{P(Z)}}[\widetilde{S_\alpha|ZP(Z)}] + \frac{\partial}{\partial x_i}\left(\Gamma_t \frac{\partial Q_\alpha}{\partial x_i}\right) \tag{2.76}$$

These equations are solved on a CMC-grid which is coarser than the CFD grid. Each CFD cell has its own presumed conditional scalar dissipation distribution which is connected to the assumed mixture fraction distribution in the cell. With this assumed distribution of the mixture fraction, the distribution of the unconditional scalar dissipation rate can be recovered. In first order CMC, the conditional fluctuations are neglected. Therefore the mean conditional source term can be modeled by evaluating the source term as a function of the conditional means of the scalars:

$$\widetilde{S_\alpha|Z} \approx S_\alpha(\widetilde{\phi_\alpha|Z}) \tag{2.77}$$

The unconditional mean is recovered from the conditional means through integration with the mixture fraction PDF which is assumed to be a β-PDF.

Transient flamelet model

In the transient flamelet model unsteady flamelet equations for mixture fraction and temperature are solved on the fly. The reaction is being thought of as taking place in thin reaction sheets, thinner than the Kolmogorov eddies. The flamelets thus have a one-dimensional structure with mixture fraction as parameter. The transport equation in physical space of a component of the composition vector is:

$$\frac{\partial \rho\phi}{\partial t} + \frac{\partial \rho U_i \phi}{\partial x_i} = \frac{\partial}{\partial x_i}\left(\rho\Gamma\frac{\partial \phi}{\partial x_i}\right) + S_\phi \tag{2.78}$$

By describing the direction perpendicular to the stoichiometric line in terms of mixture fraction, a flame attached coordinate system can be introduced. By conditioning on mixture fraction, i.e. $Z = \zeta$, and neglecting gradients of reactive scalars on iso-surfaces of mixture fraction, i.e. $\bigtriangledown_{Z//}(\phi_\alpha) = 0$, this results in the unsteady flamelet equation in composition space [18]:

$$\rho\frac{\partial \phi}{\partial \tau} = \rho\Gamma\left(\frac{\partial \zeta}{\partial x_i}\right)^2\left(\frac{\partial^2 \phi}{\partial \zeta^2}\right) + S_\phi \tag{2.79}$$

$$\rho\frac{\partial\phi}{\partial\tau}=\frac{1}{2}\rho\chi(\zeta,\tau)\left(\frac{\partial^2\phi}{\partial\zeta^2}\right)+S_\phi(\phi) \tag{2.80}$$

with $\chi(\zeta,\tau)$ the instantaneous conditional scalar dissipation rate:

$$\chi(\zeta,\tau)=2\left\langle\Gamma\left(\frac{\partial Z}{\partial x_i}\right)^2\middle|Z(\boldsymbol{x},t)=\zeta\right\rangle \tag{2.81}$$

The effect of diffusion in physical space on the reactions is thus accounted for through the scalar dissipation rate. However, the dependence of χ on Z must be known and this is usually derived from a one-dimensional counter-flow flame:

$$\chi=\frac{a_s}{\pi}exp\left(-2(erfc^{-1}(2Z))^2\right)=\frac{a_s}{\pi}F(Z) \tag{2.82}$$

with a_s the stagnation-point velocity gradient. This can be recalculated to

$$\chi=\chi_{st}\frac{F(Z)}{F(Z_{st})} \tag{2.83}$$

Fluctuations of the scalar dissipation rate are then accounted for through a distribution for χ_{st} which is usually assumed to be log-normal. Thus fluctuations of χ are accounted for, making it possible to capture local extinction, through the inclusion of non-burning flamelets in the integration of the mean reaction rate. This then leads to a lower reaction rate.[24] The unsteady flamelet technique, however, cannot capture re-ignition because transport along the mixture fraction iso-surface is neglected. Therefore the interaction between extinguished and burning regions, which causes re-ignition, is not captured. However, this problem can be solved by adding an extra transport term describing the transport along the mixture fraction iso-surface [25]. Note that transport along the mixture fraction iso-surface is naturally accounted for in the CMC equations, through the conditional convection and turbulent scalar flux term (eq. 2.76).

Chemical Look-up Tables

In this section chemical look-up tables, which can be constructed before the actual CFD calculation, are discussed. These look-up tables are predominantly used to speed up the CFD calculations as the chemical source terms do not have to be calculated

every time step. The use of these tables is justified by the observation that, after a short time which is smaller than the flow and mixing time scales in most practical flows, most of the observed compositions move in composition space according to a lower dimensional manifold [3]. So if one is not interested in the dynamics of the fastest reactions, this lower dimensional manifold could be used as a chemical look-up table.

When the flow and chemical time scales are fully separated, tables purely based on chemistry such as ILDM can be used. In this case mixing and reaction are fully decoupled. However, in most practical combustion problems, the diffusive time scales are of the same order as some of the chemical time scales. Then the effect of the diffusion on the chemical reactions has to be accounted for. This is done for example in flamelet based tables, e.g. FGM [26], FPI [27].

As discussed earlier there are two options to account for the turbulence-chemistry interaction: presumed or transported PDF. With a presumed PDF, the look-up table is usually pre-integrated with the presumed PDF. Therefore the integrated look-up table will be a function of the moments of the independent parameters of the non-integrated table. For example, when assuming a β-PDF for the mixture fraction, the mean and the variance of the mixture fraction will be parameters of the pre-integrated table. With a transported PDF, the non-integrated table can be used.

It is also possible to pre-integrate the chemical source term over a range fixed time steps and tabulating the value of the progress variable after these time steps. By doing this, the integration of the chemical source term is avoided during the CFD calculation. It is not completely clear how cost effective this technique is compared to integrating the chemical source term of the progress variable during the CFD calculation. Nonetheless this technique has been used in the calculations of this PhD.

The disadvantage of these tabulated chemistry techniques, is that usually the flame structure has to be known in advance in order to choose the correct assumptions regarding the flame structure when constructing the table. This can be somewhat circumvented by constructing both a table based on premixed combustion and one based on non-premixed combustion. A flame parameter, based on the relative orientation of the mixture fraction and progress variable gradients, is then used in the CFD calculations in order to decide which table should be used on a certain location in the CFD calculation. However, the gradients derived from the CFD flow field are gradients of the mean (RANS) or filtered (LES) field and as reaction is a sub-grid

phenomenon, the question remains to which extent these gradients represent the true gradient field.

Chemical equilibrium In the chemical equilibrium model, all chemical time scales are assumed to be faster than the mixing time scales. Local chemical equilibrium is thus determined only by the mixture fraction, with no other effects of the flow field. As a result the chemistry can be pre-calculated and stored in a chemical look-up table. In other words, the problem of closing the chemical source term has been transformed into a problem to determine the mixture fraction PDF. For this case a presumed PDF approach is justified as the mixture fraction PDF can be approximated very well by means of β-PDF. Therefore a table integrated with a β-PDF can be constructed. As a β-PDF can be determined by the mean and the variance, the integrated table will be parametrized by the mean and the variance of the mixture fraction. Of course, this technique will not be able to predict finite rate chemistry effects such as local extinction or mixing of mixtures of different reaction progress.

Flamesheet The flame sheet model by Burke-Schumann assumes infinitely fast reaction to take place at stoichiometry. For all other compositions, pure mixing between the equilibrium point at stoichiometry and the inlet oxidizer or fuel stream is taking place. In $Z - CO_2$-space this leads to two straight mixing lines connecting equilibrium with pure fuel and with pure oxidizer. This differs from the chemical equilibrium model, which does not behave linearly with mixture fraction.

Steady Laminar Diffusion Flamelet The steady laminar flamelet model is a derivation of the unsteady flamelet model. Instead of solving the unsteady flamelet equations on the fly, the steady flamelet equation is solved for different strain rates before the actual CFD calculation.

$$0 = \frac{1}{2}\rho\chi(Z)\left(\frac{\partial^2\phi}{\partial Z^2}\right) + S_\phi(\phi, Z) \tag{2.84}$$

The solutions of the steady flamelet equation can be represented in $T_{st} - \chi_{st}$-space by the well known S-curve. As the steady flamelet equation is solved, unsteady effects such as extinction and ignition cannot be represented. This is reflected in the fact that the laminar flamelets only burn for $\chi_{st} < \chi_q$. In $Z - T$-space the lowest flamelet is then the critical flamelet with a χ_{st} slightly smaller than χ_q. The low temperature

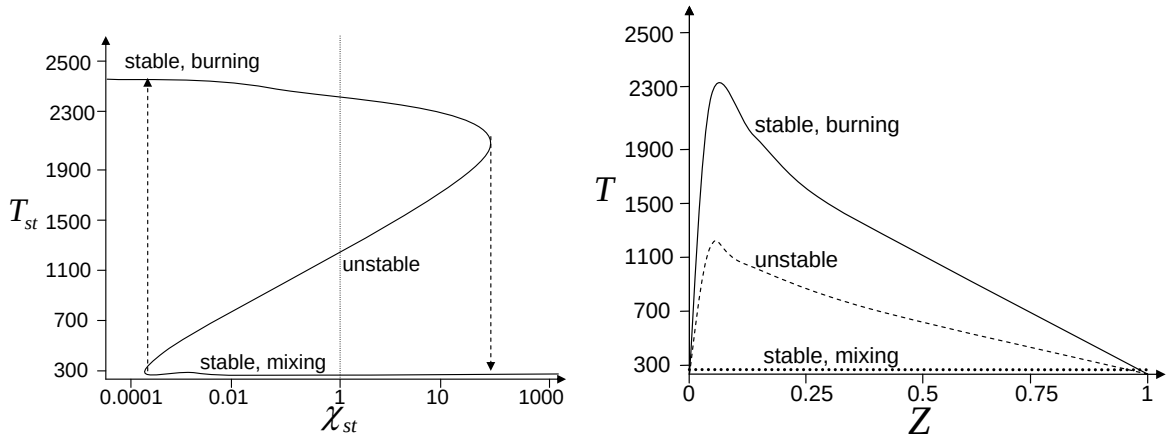

Figure 2.3: a/ S-Curve representing the complete solution of the flamelet equations. b/ Flamelet solutions corresponding to the 3 branches of the S-curve for $\chi = 1s^{-1}$. Adapted from [5].

region below this critical flamelet can therefore not be represented. This deficiency can be solved by parametrizing the data set of the flamelets with a progress variable instead of scalar dissipation as is done with FGM and FPI. This is discussed in more detail below.

From the data set of steady flamelets a look-up table with mixture fraction, Z, and the stoichiometric scalar dissipation rate, χ_{st}, as parameters can be constructed. Compared to the chemical equilibrium and the flame sheet model, the steady diffusion flamelet model has χ_{st} as extra parameter and results in a 2D table. Moreover, the effect of diffusion on the reactions is accounted for, which is not the case for the flame sheet and the chemical equilibrium model.

The turbulence chemistry interaction, in this case because the mixture fraction and scalar dissipation rate are random variables, has to be accounted for by integrating over the two parameters. As was discussed above, there are two options: presumed or transported PDF. With a transported PDF the table, obtained from projecting the flamelets onto a regular in $Z - \chi$-space, can be used directly. With a presumed PDF, the effect of the turbulence-chemistry interaction is brought into the table by integrating the table with the presumed PDF. Usually the table is integrated with a presumed PDF and mixture fraction and scalar dissipation are most often assumed to be statistically independent making it possible to write the joint PDF as a product of the marginal PDFs. The mixture fraction PDF is then assumed to be a β-function, while the scalar dissipation rate PDF is assumed to be a log-normal distribution. The

integrated table is then a function of the mean mixture fraction, the variance of the mixture fraction and the scalar dissipation rate. Sometimes fluctuations in the scalar dissipation rate are not accounted for and then only the mean of the scalar dissipation rate is needed.

As with most of the non-premixed combustion models discussed here, the main modeling issue is the modeling of the scalar dissipation rate or the mixing time scale. Usually the mean scalar dissipation rate is calculated with the equilibrium model, which assumes that the mean scalar mixing time scale is proportional to the mean turbulence time scale:

$$\widetilde{\chi} \equiv 2\Gamma \widetilde{\left(\frac{\partial \phi}{\partial x_j}\right)^2} = C_\phi \frac{\widetilde{\epsilon}}{\widetilde{k}} \widetilde{\phi''^2} = \frac{\widetilde{\phi''^2}}{\tau_{mix}} \tag{2.85}$$

In order to fully define the log-normal distribution also the variance of the scalar dissipation rate has to be known. For the standard deviation of the scalar dissipation rate, σ_χ, values between 2 and 4 are observed in experiments[18]. A constant value for σ_χ could thus be assumed, so that the mean turbulence time scale, τ_t, and the mixture fraction variance, suffice to describe the distribution of the scalar dissipation rate. In some of the calculations in this PhD research a single laminar flamelet, calculated for one specific scalar dissipation rate, is used. The scalar dissipation rate is then no longer a parameter.

ILDM As was explained in the introduction of the chemical look-up tables, the possible thermochemical states in a chemical mechanism move after a short time onto a lower dimensional manifold (ILDM) in state space. To calculate this ILDM a time scale analysis of the chemical mechanism through a local eigenvector analysis of the Jacobian is performed [28]. The eigenvalues correspond to the time scales and the eigenvectors represent the direction in state space. Large negative eigenvalues correspond to fast reactions, which then can be assumed to be in partial equilibrium compared to the slower reactions of the mechanisms [3]. In state space this partial equilibrium of the fast reactions is represented by the fact that all states are then situated on a Lower Dimensional Manifold. The dimension of this ILDM depends on how much of the dynamics of the reactions one wants to resolve. The chemical mechanism is described by the following equation:

$$\frac{\partial \boldsymbol{\phi}}{\partial t} = F(\boldsymbol{\phi}) \tag{2.86}$$

with $\boldsymbol{\phi}$ the composition vector The Jacobian $F_{\boldsymbol{\phi}}$ can then be decomposed into a slow and fast part:

$$F_{\boldsymbol{\phi}} = \begin{pmatrix} Z_s & Z_f \end{pmatrix} \begin{pmatrix} N_s & 0 \\ 0 & N_f \end{pmatrix} \begin{pmatrix} \hat{Z}_s \\ \hat{Z}_f \end{pmatrix} \tag{2.87}$$

with N_s and N_f, the matrices containing respectively the eigenvalues of the slow and fast subspace ,and Z_s and Z_f, the eigenvectors respectively spanning the slow and fast subspaces.

$$\begin{pmatrix} \hat{Z}_s \\ \hat{Z}_f \end{pmatrix} = \begin{pmatrix} Z_s & Z_f \end{pmatrix}^{-1} \tag{2.88}$$

The equation for the ILDM is then

$$\hat{Z}_f(\boldsymbol{\phi}) F(\boldsymbol{\phi}) = 0 \tag{2.89}$$

which expresses that the projection of the manifold onto the fast subspace is zero. However, this is an under-defined equation and a locally adapted parametrization needs to be defined. This is discussed in more detail in [29]. A disadvantage of the ILDM is that with a dimensionality used in CFD calculation, i.e 2 or 3, it does not exist in the low temperature region and a higher dimensional ILDM would be needed to capture this low temperature region. This problem can be partly solved by extending the ILDM into the low temperature region with a linear approximation based on the assumption of inert mixing. However, this linear extrapolation does not correctly predict the species mass fractions in that region. [27]

As the ILDM is purely based on the chemical mechanism, the effect of diffusion on the reactions is not accounted for. In laminar and turbulent flame calculations, diffusion will pull the states off the manifold due to the coupling with the chemistry. The fast decoupled reactions will then pull the states back to the manifold if the diffusion time scale is larger than the slowest decoupled time scale [3]. In this case, the diffusion will still result in a movement along the manifold, which has to be accounted for in the CFD calculations. Therefore in the CFD calculations the conservation equations projected onto the manifold have to be solved. This is due to the fact that mixing happens for the complete state in the complete state space and not just for the reduced variables on the manifold [30]. Therefore the mixing term has to be projected onto the manifold in order to describe the correct mixing for the reduced variables.

Different algorithms are discussed in [31].

To include the coupling of diffusion and reaction, the reaction diffusion manifold (REDIM) was developed. This will be discussed in more detail below.

FPV, FPI, FGM Now the flamelet-progress variable (FPV), Flamelet Prolongation of ILDM (FPI) and Flamelet generated manifolds techniques are discussed. All techniques were developed around the same time with the difference that FPI and FGM were developed for premixed combustion and FPV for non-premixed combustion. However, at this moment all three techniques can be seen as synonyms, as FPI and FGM were eventually extended to non-premixed combustion.

The FPV [32, 33] technique was originally developed as a reparametrization of a data set of steady non-premixed flamelets from $Z-\chi$ to $Z-Y_c$-space with Y_c a non-normalized progress variable. However, if only the steady burning flamelets are considered, only the top region of $Z-Y_c$-space is represented. As was discussed for the steady flamelet model, the steady flamelet equation has three solutions: the stable burning flamelets, the stable inert mixing and the unstable solution. This full solution of the steady flamelet equation is in $\chi_{st}-T_{st}$-space represented by the S-curve . The problem with the steady flamelet model parametrized by Z and χ is that only one of the three solutions corresponding to a certain value of χ_{st} can be represented. With Y_c, however, the full S-curve is unambiguously parametrized. The unstable solutions of the steady flamelet equation represent partially extinguished or ignited flamelets, that fill up the region in $Z-Y_c$-space between the steady burning flamelets and the inert mixing line. Therefore also these unstable solutions should be considered when constructing the FPV table.

The FPI [27] and FGM [26] techniques were originally developed for premixed combustion. It is basically a data set of premixed flamelet calculations with detailed transport over a range of equivalence ratios which is combined into a manifold, parametrized by a reduced number of variables. Outside the flammability limits linear interpolation to pure air and pure fuel is done. Generally, the manifold has two parameters: Z and Y_c. The big advantage of this technique over ILDM is that now the low temperature region is captured and compared to ILDM with a linear extension in the low temperature region the major species are now predicted correctly. Later on the FGM and FPI manifolds were also constructed from non-premixed flamelets, which is essentially the same as the FPV technique. For this manifold the effect of diffusion on the chemistry is accounted for as was the case for the steady diffusion flamelet

model. The part of $Z - Y_c$-space underneath the critical flamelet corresponding to the quenching scalar dissipation rate χ_q, is filled up with the unsteady solution of an extinguishing flamelet. An FGM based on non-premixed flamelets, can thus be seen as the same data set of non-premixed flamelets which was originally parametrized by Z and χ_{st} but now looked at from a different direction in composition space. Fiorina et al. [34] extended the technique to non-adiabatic partially premixed flames, by the introduction of enthalpy as a third parameter. The manifolds constructed from premixed flamelets have been tested for non-premixed combustion and mixed results were observed. In [35] an FPI based on premixed flamelets was not able to reproduce the temperature and the mass fractions of the main species for rich mixtures. Results were worse for more strained flames, as the interaction of diffusion and chemistry becomes more important. This resulted in the development of the PCM technique. In [36] better results for temperature were observed.

In order to be able to capture auto-ignition, Ihme et al. [37] extended the FPV method to the unsteady flamelet equations (UFPV), taking into account the transient evolution during ignition. However, the explicit dependence of the thermochemical state on the flamelet time is removed by using Y_c and $\chi_{Z,st}$ as parameters. The UFPV manifold is thus parametrized by three parameters: Z, Y_c and $\chi_{Z,st}$. By doing this, the structure of a flamelet is assumed to be independent of its history, which is not completely true for auto-ignition, but the assumption is often acceptable.

PCM, ADF-PCM, ADF-PCM$_\chi$ The PCM technique was developed from the previously discussed observation that FPI tables based on premixed flamelets did not correctly predict the temperature and mean species of a non-premixed flame. Therefore the reaction rate of Y_c was read from the FPI table, while the mass fraction was read from a data set of non-premixed flamelets at the corresponding $Z, \chi(Z, Y_c)$ point.

ADF-PCM tries to capture both auto-ignition and non-premixed combustion [38]. Finite rate chemistry and the effect of diffusion on the reactions are described with an FPI or FGM table. Turbulent effects are accounted for through the presumed conditional moment (PCM) technique. Contrary to the general method of using steady diffusion flamelets for the construction of the table, the solutions of auto-igniting perfectly stirred reactor calculations are tabulated in an FPI table with mixture fraction Z and progress variable Y_c as independent parameters. In particular the progress variable reaction rate $S_c^{AI}(Y_c, Z)$ is stored in the table. Afterwards the effect of diffusion

on the reaction is added by solving the unsteady flamelet equation in composition space:

$$\rho\frac{\partial Y_c}{\partial \tau} = \frac{1}{2}\rho\chi(Z,\tau)\left(\frac{\partial^2 Y_c}{\partial Z^2}\right) + S_{Y_c}^{AI}(Y_c, Z) \tag{2.90}$$

As with the flamelet model an empirical correlation based on laminar flamelets calculations is used to correlate χ and χ_{st}

$$\chi = \frac{a_s}{\pi} exp\left(-2(erfc^{-1}(2Z))^2\right) = a_s.F(Z) \tag{2.91}$$

The eventual reaction rate resulting from the combined effect of the chemistry and diffusion is then:

$$\begin{aligned} S_{Y_c}^{ADF-PCM}(Z,t,\chi_{st}) &= \rho\frac{\partial Y_c(Z,t,\chi_{st})}{\partial \tau} \\ &= \frac{1}{2}\rho\chi\left(\frac{\partial^2 Y_c}{\partial Z^2}\right) + S_{Y_c}^{AI}(Z, Y_c(Z,t,\chi_{st})) \\ &= \frac{1}{2}\rho\chi_{st}\frac{F(Z)}{F(Z_{st})}\left(\frac{\partial^2 Y_c}{\partial Z^2}\right) + S_{Y_c}^{AI}(Z, Y_c(Z,t,\chi_{st})) \end{aligned} \tag{2.92}$$

As this is only 1 equation that should be solved, this is computationally much more efficient than the unsteady flamelet technique, which has to solve the flamelet equations for all species in the mechanism.

The final ADF-PCM table is then generated by integrating with the joint distribution of Z and χ_{st}, $f(Z,\chi_{st})$. As with most presumed PDF methods Z and χ are assumed to be statistically independent so that $f(Z,\chi_{st}) = f(Z).f(\chi_{st})$. ADF-PCM assumes the distribution of χ_{st} to be a Dirac pulse at the mean value. ADF-PCM$_\chi$ is then an extension of the ADF-PCM model where a log-normal distribution is used for χ_{st}. As discussed before this will enable the technique to better account for the fluctuations of the scalar dissipation rate causing local extinction.

REDIM The Reaction Diffusion Manifold (REDIM) is the extension of the ILDM technique with the inclusion of the effect of diffusion, starting from the transport equation in physical space for the composition vector $\boldsymbol{\phi}$, which describes the full

thermodynamical state:

$$\frac{\partial \boldsymbol{\phi}}{\partial t} = F(\boldsymbol{\phi}) - \boldsymbol{U}.\nabla\boldsymbol{\phi} - \frac{1}{\rho}\nabla(D(\boldsymbol{\phi})\nabla\boldsymbol{\phi}) \tag{2.93}$$

With the REDIM, the aim is to describe the full thermodynamical state $\boldsymbol{\phi}$ by a reduced set of independent parameters represented by the reduced composition vector θ. The transport equation in composition space then becomes:

$$\frac{\partial \boldsymbol{\phi}}{\partial \tau} = F(\boldsymbol{\phi}) - \boldsymbol{U}.\nabla\boldsymbol{\theta}.\boldsymbol{\phi_\theta} - \frac{D}{\rho}\nabla\boldsymbol{\theta} \circ \boldsymbol{\phi_{\theta\theta}} \circ \nabla\boldsymbol{\theta} \tag{2.94}$$

with $(\nabla\boldsymbol{\theta})_{lm} = \frac{\partial\theta_l}{\partial x_m}$, $(\boldsymbol{\phi_\theta})_{kl} = \frac{\partial\phi_k}{\partial\theta_l}$ and $(\boldsymbol{\phi_{\theta\theta}})_{klm} = \frac{\partial\phi_k}{\partial\theta_l\partial\theta_m}$. The convection term drops out and the condition for the invariant REDIM manifold is then [39]:

$$0 = (I - \boldsymbol{\phi_\theta}\boldsymbol{\phi_\theta^+})\left[F(\boldsymbol{\phi}) - \frac{D}{\rho}\nabla\boldsymbol{\theta} \circ \boldsymbol{\phi_{\theta\theta}} \circ \nabla\boldsymbol{\theta}\right] \tag{2.95}$$

with $\boldsymbol{\phi_\theta^+}$ the Moore-Penrose pseudo inverse of $\boldsymbol{\phi_\theta}$ and $(I - \boldsymbol{\phi_\theta}\boldsymbol{\phi_\theta^+})$ the projection operator projecting onto the subspace orthogonal to the manifold. The invariant manifold condition thus expresses that the projection of the manifold on the subspace orthogonal to the manifold should be zero. The manifold is then found by solving the following relaxation equation:

$$\frac{\partial \boldsymbol{\phi}}{\partial \tau} = (I - \boldsymbol{\phi_\theta}\boldsymbol{\phi_\theta^+})\left[F(\boldsymbol{\phi}) - \frac{D}{\rho}\nabla\boldsymbol{\theta} \circ \boldsymbol{\phi_{\theta\theta}} \circ \nabla\boldsymbol{\theta}\right] \tag{2.96}$$

The solution is converged when the transient term disappears. The gradients of the reduced parameters in physical space are not known a priori and need to be presumed if the manifold is to be used as a pre-calculated table. The assumption of these gradients determines the eventual flame structure embedded in the manifold. One of the options is to use the gradients of laminar flamelet calculations in physical space resulting in a manifold which will not differ much from the FPV manifold or the FGM/FPI manifold based on non-premixed flamelets. Actually, in the construction of the REDIM manifold an FGM is used as the initial solution for solving the REDIM-equation. The biggest differences are found in strongly non-linear areas where the linear or cubic interpolation between the flamelets is less correct. Note however, even though the theoretical background of FGM and REDIM is different, this will still result in a similar outcome. In the framework of non-premixed combustion, FGM can

be seen as a re-parametrization of a data set of non-premixed flamelets. REDIM on the other hand, can be more seen as an extension of the ILDM technique to take into account the effect of diffusion. In general, the REDIM framework provides a higher flexibility as in theory any physical gradient can be used. However, physically correct gradients should be used in order to have a correct prediction of the flame structures. The possibilities of this flexibility are shown in the next paragraph.

MFM Tthe Multidimensional flamelet-generated manifolds are discussed as these show the possibilities of being able to freely choose the physical gradients determining the eventual flame structure embedded in the manifold. As discussed earlier this is also possible in the REDIM framework. Multidimensional flamelet-generated manifolds (MFMs) are the extension of FGM to partially premixed combustion [40]. The unsteady transport equations for all the species of the chemical mechanism are projected onto the reduced $Z - Y_c$ space.

$$\rho\frac{\partial Y_i}{\partial \tau} + \frac{\partial Y_i}{\partial Y_c}\dot{\omega_c} = \frac{\rho\chi_{Yc}}{Le_i}\frac{\partial^2 Y_i}{\partial Y_c^2} + \frac{\rho\chi_Z}{Le_i}\frac{\partial^2 Y_i}{\partial Z^2} + 2\frac{\rho\chi_{Z,Y_c}}{Le_i}\frac{\partial^2 Y_i}{\partial Z^2 \partial Y_c} + \dot{\omega}_i \tag{2.97}$$

Also a similar projected equation for temperature is solved. The three scalar dissipation rates are very important as they describe the transformation from physical space to the $Z - Y_c$ space. They also describe the mixing time scales. The scalar dissipation rate of Z, χ_Z, is assumed not to depend on the chemistry and is modeled as a function of Z with following standard equation:

$$\chi_Z(Z) = \frac{a}{2\pi} exp\left(-2(erfc^{-1}(2Z))^2\right) \tag{2.98}$$

The scalar dissipation rate of Y_c, χ_{Y_c}, on the other hand is affected by the chemistry, because the gradients of Y_c steepen within the reaction zone. It is modeled with the following equation which has a strong resemblance to the equation for χ_Z:

$$\chi_{Y_c}(Z, Y_c) = b(Z) exp\left(-2(erfc^{-1}(2Y_c/Y_c^{Eq}(Z)))^2\right) \tag{2.99}$$

with $b(Z)$ the maximum value of χ_{Y_c} for a value of Z. The model equation for $b(Z)$ is derived by fitting data of premixed flamelets:

$$b(Z) = b_{st} exp\left(-2(erfc^{-1}(Z/Z_{st}))^2\right) \tag{2.100}$$

with b_s the maximum value of $b(Z)$ at the stoichiometric mixture fraction Z_{st}. The cross scalar dissipation rate, χ_{Z,Y_c}, can be written as:

$$\chi_{Z,Y_c} = \boldsymbol{n_Z} \cdot \boldsymbol{n_{Y_c}} \sqrt{\chi_z \chi_{Y_c}} \tag{2.101}$$

with $\boldsymbol{n_Z} = \nabla Z/|\nabla Z|$ and $\boldsymbol{n_{Y_c}} = \nabla Y_c/|\nabla Y_c|$. So $\boldsymbol{n_Z} \cdot \boldsymbol{n_{Y_c}}$ has to be known to approximate χ_{Z,Y_c}, it depends strongly on the flame structure. However, the contribution of the term related to χ_{Z,Y_c} is mostly found to be negligible.[40]

The MFM has thus five parameters: Z, Y_c,χ_Z,χ_{Y_c} and χ_{Z,Y_c}. Depending on the ratio of χ_Z and χ_{Y_c}, the flame structure can be varied from diffusion to premixed flames, with all the partially premixed flame structures in between.

In the end, unsteady flamelet equations are solved in $Z - Y_c$ space resulting in $Z - Y_c$ flamelets. In [40], premixed and non-premixed flamelets are compared with these $Z - Y_c$-flamelets and it is shown that fluxes across the iso-Z and iso-Y_c surfaces have an important effect on the chemistry. This results in a different manifold than FPI or FGM manifolds based on premixed or non-premixed combustion.

A similar study could be done within the REDIM framework, as the gradients in physical space can also be freely chosen. As far as we know this MFM technique has not yet been applied to turbulent CFD calculations. A problem here would be the modeling of the scalar dissipation rates and its fluctuations.

ISAT

Finally, the In Situ Adaptive Tabulation (ISAT) technique [41] is discussed, in which a chemistry table is constructed on the fly. The calculation starts with an empty table and the reaction terms of all the species are directly integrated and stored in the ISAT table together with the full thermodynamical state. The following time steps, it is checked if the current thermodynamical state is close in composition space to any of the tabulated states. If this is the case, a linear interpolation is done from the tabulated state to the current thermodynamical state. There is also an error control algorithm included in order to ensure the accuracy of the linearly interpolated states retrieved from the ISAT table. This technique usually leads to large tables, but speed up factors of 5 to 10 are observed compared to direct integration of the full mechanism. It should be stressed that for RANS or LES calculations the ISAT technique can only be used within a transported PDF framework. In general, ISAT should be seen as a

more efficient way of calculating with the full chemical mechanism, than as an actual combustion model. So all the chemical time scales are still present.

Recently Contino et al. [42] have developed a combined technique of dynamic adaptive chemistry (DAC) reduction of a chemical mechanism together with the on the fly tabulation of ISAT, with speed-up factors of up to 300. It is, however, only cost effective for chemical mechanisms with hundreds of species and thousands of mechanisms. For smaller mechanisms with less then 150 species, ISAT by itself achieves similar speed-up factors (5 to 10) as the combined technique. However, it does find its application in combustion engine calculations, especially for HCCI where auto-ignition occurs and all the chemical time scales need to be retained.

In this area of speed-up techniques one could also mention the new developments of using GPUs to speed up the direct integration of chemical mechanisms.

Conclusion

Now that the context of the combustion models has been introduced, it is worthwhile to look at the advantages and disadvantage of the single steady flamelet and the REDIM technique compared to other models. This is summarized in table 2.1 The single steady flamelet model is used in this PhD research. It is one of the most basic pre-tabulated models, which is only parametrized by Z and therefore cannot capture local extinction or re-ignition. As the REDIM table has the progress variable Y_c as an extra parameter, it is expected to better capture local extinction and re-ignition. The REDIM tables which are used in this PhD research, are almost identical to an FGM or FPI, because in the REDIM calculations the physical gradients from flamelet calculations are used. So for practical use in a CFD code, the REDIM, FPI, FGM and FPV tables can be considered to be the same. All pre-tabulated techniques can be used in cooperation with presumed and transported PDFs.

2.1.5 Practical Construction of a REDIM table

Now the practical construction of a REDIM table is discussed, with the figures shown from the construction process of a CH_4-air REDIM. The framework for the construction of a REDIM table has been provided by Prof. U. Maas and consists of the INSFLA code, which is used for laminar flamelet calculations and the HOMREA code, which is used for the actual REDIM calculation. For a REDIM based on a

Table 2.1: Comparison of non-premixed combustion models

Properties	CMC	Unsteady Flamelet	Steady Flamelets	Single Steady Flamelet	REDIM, FPI, FGM, FPV	ADF-PCM
pre-tabulated	no	no	yes	yes	yes	partly
parameters	—	—	(Z, χ)	Z	(Z, Y_c)	(Z, Y_c, χ)
influence of χ from CFD	direct (CMC equation)	direct (flamelet equation)	direct (select flamelet)	indirect (transport equation Z or mixing model)	indirect (transport equation Z and Y_c or mixing model)	direct (ADF-PCM equation)
extinction	yes	yes	yes	no	yes	yes
re-ignition	yes	no	no	no	yes	yes

non-premixed flame structure the construction consists of the following steps:

1. Performing non-premixed laminar flamelet calculations in physical space with the INSFLA code for a range of strain rates, resulting in a data set of steady flamelets.

2. Performing a non-premixed laminar flamelet calculation in physical space with the INSFLA code for a strain rate higher than the extinction strain rate, resulting in a transient solution of an extinguishing flamelet.

3. Calculate the equilibrium composition at stoichiometry with a free flat flame calculation in INSFLA.

4. Perform two laminar flamelet calculations in INSFLA with the equilibrium as one inlet and pure oxidizer or pure fuel as the other inlet.

5. Combine the two previous flamelet calculations into one upper boundary for the flamelet data set.

6. Use the upper boundary as initial condition for calculation with low strain rate, to fill up the top region in $Z - Y_c$ space.

7. Combine the upper boundary, the solutions of the steady flamelets and the transient solution of the extinguishing flamelet into one data set as is shown in figure 2.4.

8. Project the data set of flamelets, which are all stored on different grids in composition space, onto one general grid in the reduced $Z - Y_c$ space.

9. Solve the REDIM equation in local coordinates with the HOMREA code, using the physical gradients from the flamelet equations.

10. Project the REDIM manifold expressed in local coordinates onto the global coordinate system of the reduced scalars, Z and Y_c.

Depending on the framework in which the REDIM will be used, some post-processing of the REDIM table needs to be done:

1. Pre-integrate the source term from a range of time steps and tabulate for each point in the table the value of $Y_c(t+\delta t)$.

2. Force the upper boundary of the flamelet data set onto the table.

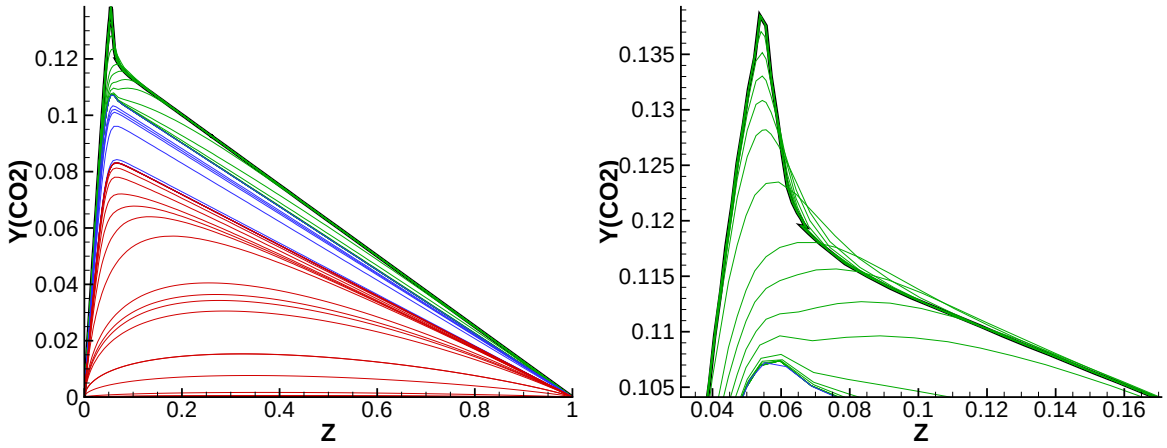

Figure 2.4: Flamelets used to construct the REDIM: a/transient solution of low strain rate calculation with upper boundary as initial solution (green), steady flamelets (blue) and transient solution of extinguishing flamelet (red) b/ zoom.

The choice of the progress variable Y_c affects the tabulation. The progress variable should rise monotonically with temperature and reaction progress in order to have a bijective relationship, so that each value of $Y_c(Z_{st})$ is unambiguously connected to one point on the flamelet S-curve. Y_{CO2} is therefore not the best choice for the progress variable, as for rich mixtures at high temperatures dissociation of CO_2 into CO occurs. This can be seen in figure 2.5, where negative rates of production of Y_{CO2} are shown to coincide with a positive rate of production of Y_{CO}. Therefore $Y_c = Y_{CO2} + Y_{CO}$ is

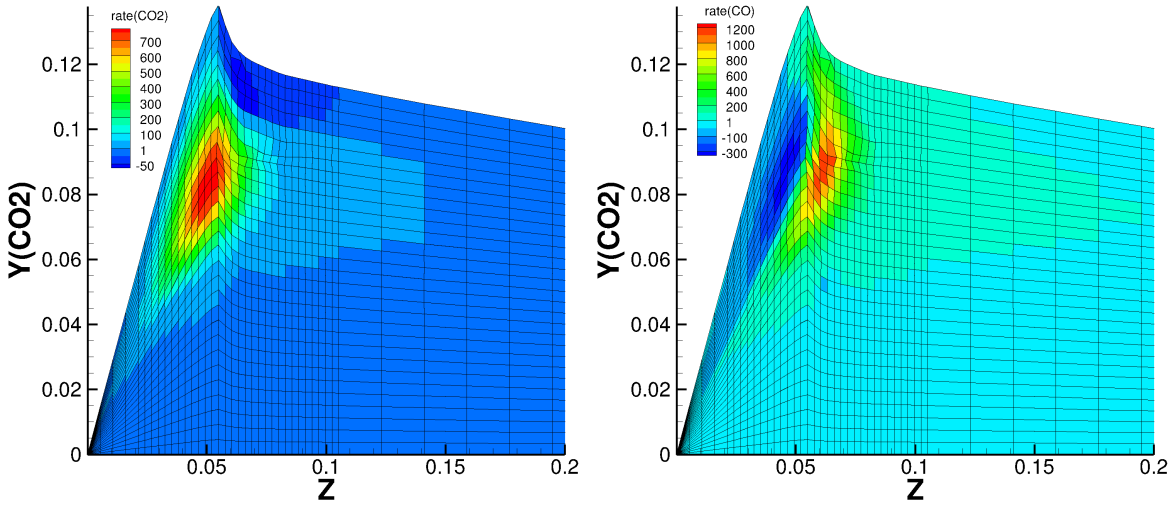

Figure 2.5: REDIM in $Z - Y_{CO_2}$-space: a/ production rate of Y_{CO_2}, b/ production rate of Y_{CO}.

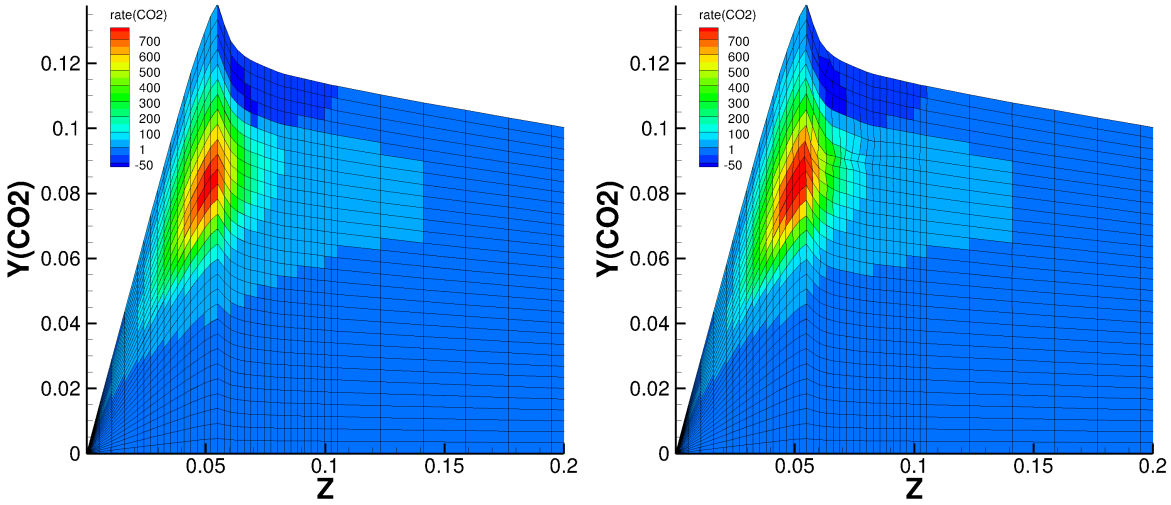

Figure 2.6: Comparison of projected flamelet data set (FGM) (left) and the REDIM (right).

often chosen as progress variable. Nonetheless, in this PhD research $Y_c = Y_{CO2}$ is used because of ease of implementation and because not a large influence is expected. The choice of $Y_c = Y_{CO2}$ is also reflected in the fact that the upper boundary constructed from combining the two flamelet calculations with equilibrium and pure air or oxidizer as inlets is not the upper boundary of the data set of flamelets, as can be seen in figure 2.4. For rich mixtures, flamelets with relatively low strain rates have higher Y_{CO2}-values than the constructed upper boundary.

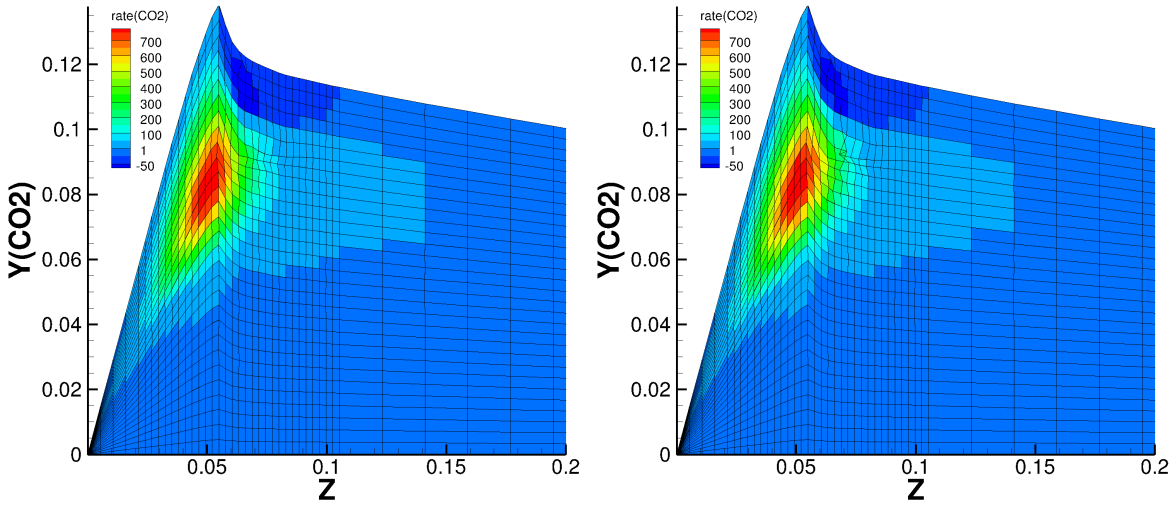

Figure 2.7: Influence number of timesteps REDIM: a/1000 time steps (left) b/2000 time steps (right).

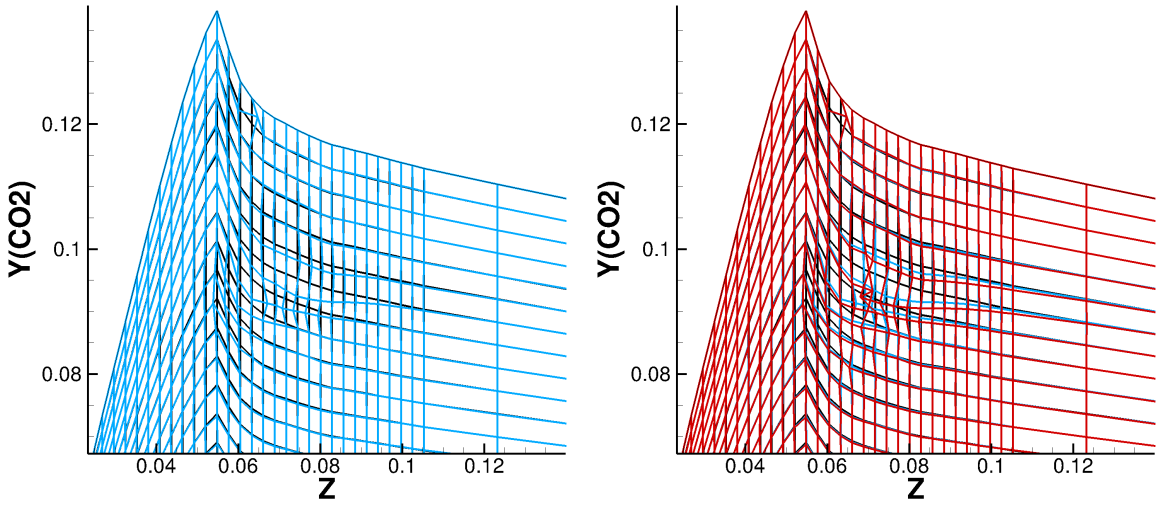

Figure 2.8: Change of grid during REDIM calculation: initial solution (black), REDIM (1000 time steps) (blue) and REDIM (2000 time steps) (red).

In the calculation of the REDIM, the upper boundary in $Z - Y_c$-space is fixed and it this therefore important that this upper boundary is not too low. The eventual upper boundary of the projected flamelets manifold is determined in the projection of the flamelets onto the $Z - Y_c$-grid and is the envelope of the constructed upper boundary and all the flamelets. It should be noted that the data set of projected flamelets is actually an FGM and it is used as the initial condition for the actual REDIM calculation.

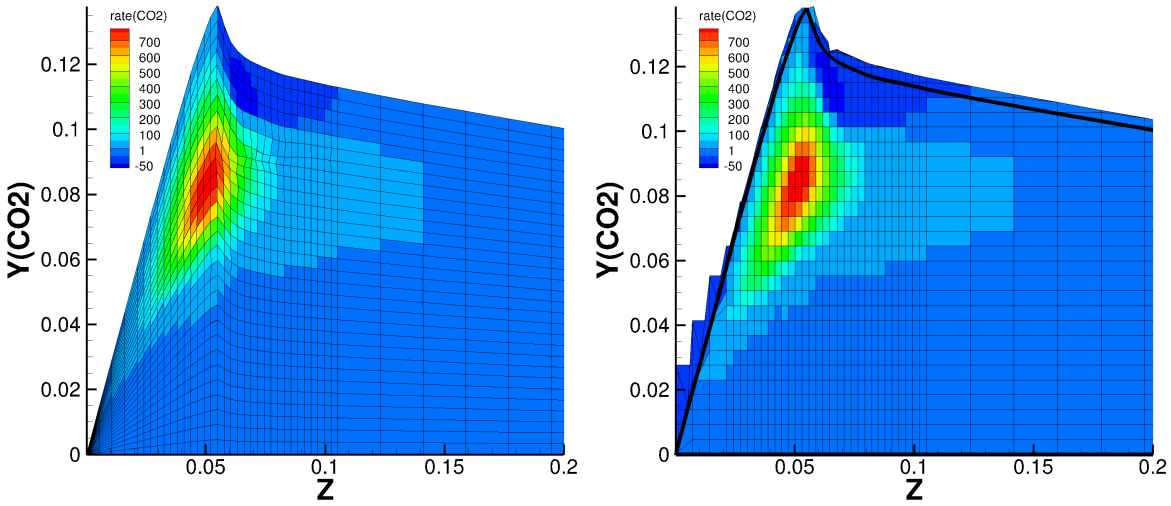

Figure 2.9: Comparison of the REDIM in local coordinates (left) and the REDIM in global coordinates projected onto a regular $Z - Y_{CO_2}$ grid (right).

In the REDIM calculation, each iteration consists of moving only one grid point on the manifold in state space [43]. This will eventually result in a REDIM manifold with a grid which is distorted when looked at in $Z - Y_{CO_2}$-space. This can be seen in figure 2.6, where the projected flamelet manifold is compared with the REDIM manifold. From this figure also the small difference between the projected flamelet manifold and the REDIM is observed. As explained earlier this was to be expected, due to the use of the physical gradients of the flamelet calculations, in the calculation of the REDIM.

It should also be noted that the REDIM calculation is done with the manifold expressed in local coordinates. In order to use the calculated manifold as a look-up table the manifold has to be transformed to a global coordinate system and projected onto a regular grid in $Z - Y_c$-space. In this process, the upper boundary of the REDIM is lost. This can be seen in figure 2.9, where the REDIM is shown before and after the projection process. In transported PDF calculations this loss of the upper boundary can lead to numerical fluctuations in composition space in the neighborhood of the boundary. This can be seen in figures 2.10 and 2.11, where scatter plots of a transported PDF calculation are shown with and without enforcing the upper boundary. Therefore the upper boundary needs to be re-enforced onto the table.

In the complete construction procedure the grid size has to be chosen twice. Once when the the data set of flamelets is projected onto a $Z - Y_c$ grid and once when

the REDIM expressed in local coordinates is projected on a $Z - Y_c$ grid. For both grids a piecewise uniform grid is chosen, which consists of three uniform grids for the lean, stoichiometric and rich regions of the table but each with a different grid size. The finest grid is chosen for the stoichiometric region as there the strongest gradients have to be captured. Too fine grids will lead to very small time steps in the REDIM calculation as an explicit solver is used. In this PhD research a time step of $10^{-8}s$ has been used. As there is no clear indicator for when the calculation is converged, the influence of the number of time steps has been compared. In figure 2.7 a REDIM after 1000 time steps is compared with a REDIM after 2000 time steps. The influence on the values of the production rate of Y_{CO_2} is rather small. However, the influence on the grid is larger as can be seen in figure 2.8. Still, 1000 time steps seem sufficient to consider the REDIM calculation as converged.

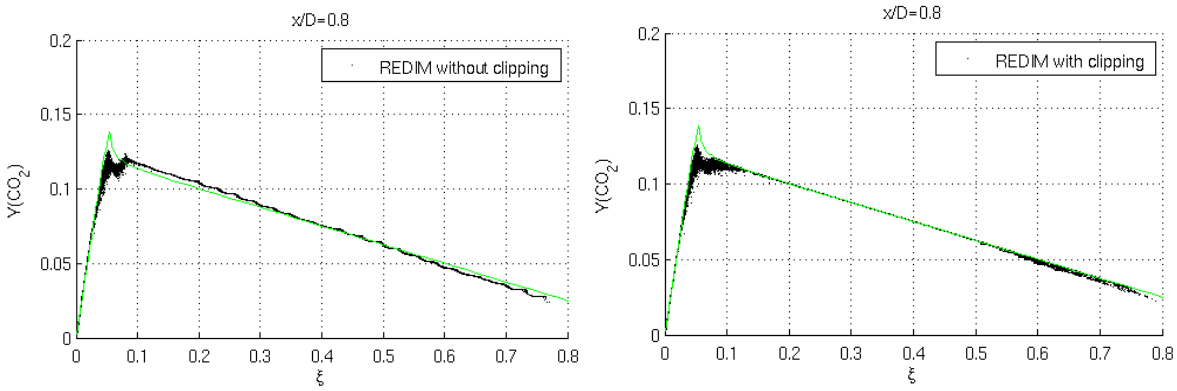

Figure 2.10: Influence of upper boundary in integrated table on scatter plots (black dots) of a swirling gas flame calculation: a/ without enforcing the upper boundary b/ with the upper boundary enforced. Upper boundary of the original REDIM manifold (green line).

2.1.6 Hybrid RANS-PDF

This PhD has been performed within the framework of hybrid RANS-PDF calculations, in which the standard RANS equations discussed in section 2.1.1 are solved in parallel with transported PDF equations. The RANS equations are solved with a Finite Volume (FV) method, but for the transported PDF equations this is not possible due to their high dimensionality. Therefore the transported PDF equations are solved indirectly through a Monte Carlo (MC) method, which consists of solving stochastic differential equations for computational particles which represent independent realiza-

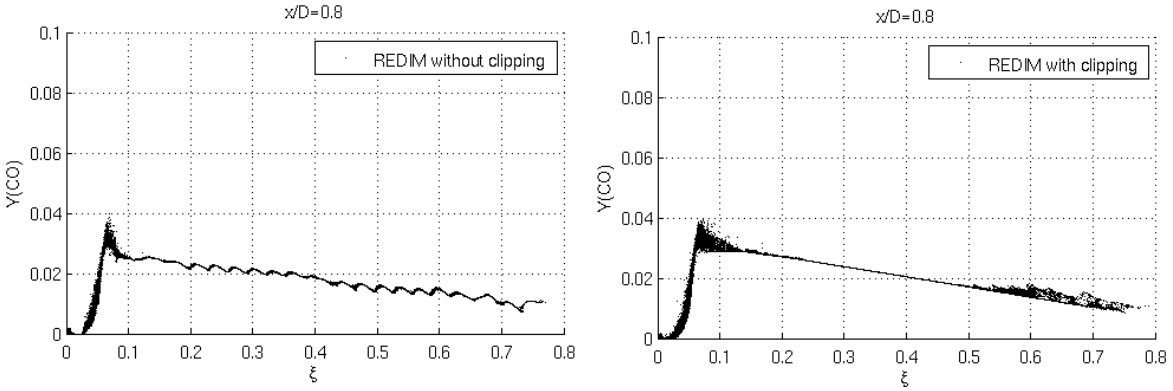

Figure 2.11: Influence of upper boundary in integrated table on scatter plots (black dots) of a swirling gas flame calculation: a/ without enforcing the upper boundary b/ with the upper boundary enforced.

tions of the turbulent reacting flow. Each particle 'carries' all the properties that the PDF represents and in one CFD cell the full PDF is then retrieved from the statistics of all the computational particles in that cell.

In the calculations described in this PhD thesis a composition or velocity-composition PDF is used. The biggest advantage of the inclusion of the composition vector in the PDF, is that the chemical source term and all other local source terms are closed on the level of the PDF transport equations. However, one should mention that the problem of the modeling is then moved to the modeling of the mixing of scalars due to diffusion, known as micro-mixing. This is explained by the fact that the PDF considered is a one-point PDF, describing the probability of certain events at one point. To describe processes that depend on physical gradients, such as the micro-mixing or the pressure gradient term, a two-point PDF would be needed. However, the description of the two-point PDF is far too complicated to benefit from it.

To better understand the hierarchical position of transported PDF methods we refer to standard work of Minier and Peirano [44]. There it is discussed that the PDF approach is somewhat in between the DNS approach which is described as a microscopic approach as all the scales are resolved and the RANS approach, which is called macroscopic as all the scales are averages and only the integral scales are retained. The PDF approach is then a mesoscopic approach which models the effect of the non-resolved scales through stochastic processes. Thus while in the standard RANS approach only the mean values and at the most the variances can be used to model the unclosed terms, in the PDF approach the modeling is done at the PDF

level where the full PDF is known and thus far more information is available for the modeling.

Transported PDF

To solve the transported PDF equations different methods have been developed. In this PhD research the Monte Carlo method is used, which consists of solving stochastic differential equations which describe the evolution of computational particles. The ensemble of all the stochastic particles in a cell represent the statistics of the flow in this cell. In other words, the full PDF and thus all the statistical moments can be retrieved from the ensemble of computational particles. However, it is also possible to solve the PDF transport equations in an Eulerian framework, by using stochastic fields or with a quadrature of moment method. The choice of the parameters of the PDF depends on the problem and on the turbulence model used in the RANS equations. In this PhD research both a scalar-PDF as a velocity-scalar PDF framework are used. The frameworks for these PDFs are now described.

Velocity-Composition PDF The transport equation for the velocity-scalar-PDF $f_{\boldsymbol{u},\boldsymbol{\phi}}$ is [45]:

$$\begin{aligned}&\frac{\partial \rho f_{\boldsymbol{u},\boldsymbol{\phi}}}{\partial t}+\frac{\partial \rho V_i f_{\boldsymbol{u},\boldsymbol{\phi}}}{\partial x_i}+\left(\rho g_i-\frac{\partial\langle p\rangle}{\partial x_i}+\frac{\partial\langle\tau_{ij}\rangle}{\partial x_j}\right)\frac{\partial f_{\boldsymbol{u},\boldsymbol{\phi}}}{\partial V_i}+\underbrace{\frac{\partial \rho S_\alpha f_{\boldsymbol{u},\boldsymbol{\phi}}}{\partial \psi_\alpha}}_{\text{reaction}}=\\&\frac{\partial}{\partial V_i}\left[\left\langle\left(-\frac{\partial \tau'_{ij}}{\partial x_j}+\frac{\partial p'}{\partial x_i}\right)|\boldsymbol{V},\boldsymbol{\psi}\right\rangle f_{\boldsymbol{u},\boldsymbol{\phi}}\right]+\underbrace{\frac{\partial}{\partial \psi_\alpha}\left[\left\langle\left(-\frac{\partial J_i^\alpha}{\partial x_i}\right)|\boldsymbol{V},\boldsymbol{\psi}\right\rangle f_{\boldsymbol{u},\boldsymbol{\phi}}\right]}_{\text{micro-mixing}}\end{aligned} \tag{2.102}$$

The buoyancy term, the mean pressure gradient term, the mean viscous stress term and the mean reaction source term on the left hand side are closed. The fact that the mean reaction source term is closed is the main advantage of the transported PDF method. The mean viscous stress term $\frac{\partial\langle\tau_{ij}\rangle}{\partial x_j}$ is negligible in high Reynolds number flows. The fluctuating viscous stress and pressure terms and the micro-mixing terms on the right hand side have to be modeled. For variable density flows it is more convenient to consider Mass Density Function (MDF)$\mathcal{F}_{\boldsymbol{u},\boldsymbol{\phi}}$ [46]:

$$\mathcal{F}_{\boldsymbol{u},\boldsymbol{\phi}}(\boldsymbol{V},\boldsymbol{\psi})=\rho(\boldsymbol{\psi})f_{\boldsymbol{u},\boldsymbol{\phi}}(\boldsymbol{V},\boldsymbol{\psi}) \tag{2.103}$$

The transport equation for the velocity-composition MDF $\mathcal{F}_{\boldsymbol{u},\boldsymbol{\phi}}$ is then:

$$\begin{aligned}&\frac{\partial \mathcal{F}_{\boldsymbol{u},\boldsymbol{\phi}}}{\partial t}+\frac{\partial V_i \mathcal{F}_{\boldsymbol{u},\boldsymbol{\phi}}}{\partial x_i}+\left(g_i-\frac{1}{\rho}\frac{\partial\langle p\rangle}{\partial x_i}+\frac{1}{\rho}\frac{\partial\langle\tau_{ij}\rangle}{\partial x_j}\right)\frac{\partial \mathcal{F}_{\boldsymbol{u},\boldsymbol{\phi}}}{\partial V_i}+\frac{\partial S_\alpha \mathcal{F}_{\boldsymbol{u},\boldsymbol{\phi}}}{\partial \psi_\alpha}= \\ &\frac{\partial}{\partial V_i}\left[\frac{1}{\rho}\left\langle\left(-\frac{\partial \tau'_{ij}}{\partial x_j}+\frac{\partial p'}{\partial x_i}\right)|\boldsymbol{V},\boldsymbol{\psi}\right\rangle\mathcal{F}_{\boldsymbol{u},\boldsymbol{\phi}}\right]+\frac{\partial}{\partial \psi_\alpha}\left[\frac{1}{\rho}\left\langle\left(-\frac{\partial J_i^\alpha}{\partial x_i}\right)|\boldsymbol{V},\boldsymbol{\psi}\right\rangle\mathcal{F}_{\boldsymbol{u},\boldsymbol{\phi}}\right]\end{aligned} \tag{2.104}$$

The MDF transport equation is solved with a Monte Carlo technique, in which computational fluid particles statistically represent the MDF. The equations for these computational particles are [45]:

$$dx_i^* = U_i^* dt \tag{2.105}$$

$$dU_i^* = A_i^* dt = \left(g_i-\frac{1}{\rho}\frac{\partial\langle p\rangle}{\partial x_i}\right)dt + a_{i,p'}^* dt + a_{i,\tau'}^* dt \tag{2.106}$$

$$d\phi_\alpha^* = S_\alpha(\boldsymbol{\phi^*})dt + \theta_{\alpha,mix}^* dt \tag{2.107}$$

with $\theta_{\alpha,mix}$ the micro-mixing model. We now look a bit deeper into the equation of the particle velocity. The acceleration terms $a_{i,p'}$ and $a_{i,\tau}$ have to be modeled. This is usually done with a drift term and a diffusion term. A more general framework for the modeling is the generalized Langevin model (GLM)

$$a_{i,p'}^* dt + a_{i,\tau'}^* dt = D_i dt + K dW_i = G_{ij}(U_j^* - \widetilde{U}_j)dt + \sqrt{C_0\epsilon}dW_i \tag{2.108}$$

with $C_0 = 2.1$ This results in the following equation for the particle velocity [46]

$$dU_i^* = \left(g_i-\frac{1}{\rho}\frac{\partial\langle p\rangle}{\partial x_i}\right)dt + G_{ij}(U_j^* - \widetilde{U}_j)dt + \sqrt{C_0\epsilon}dW_i \tag{2.109}$$

For the particle velocity fluctuation this becomes:

$$du_i^* = -\left(\frac{1}{\rho^*}-\left[\frac{1}{\overline{\rho}}\right]^*\right)\left[\frac{\partial\langle p\rangle}{\partial x_i}\right]^* dt - u_j^*\left[\frac{\partial \widetilde{U}_i}{\partial x_j}\right]^* + \left[\frac{1}{\overline{\rho}}\frac{\partial \overline{\rho}\widetilde{u_i'' u_l''}}{\partial x_j}\right]^* + [G_{ij}]^* u_j^* dt + \sqrt{C_0[\epsilon]^*}dW_i^* \tag{2.110}$$

G_{ij} determines the specific model that is used and each choice of G_{ij} corresponds to a certain Reynolds stress model. For the hybrid RANS-PDF framework to be consistent, G_{ij} has to be chosen so that it results in the same Reynolds stress model that is used in the RANS part of the calculation. In the calculations in this PhD, the isotropisation of production model by Launder, Reece and Rodi (LRR-IPM) has been used. Therefore in the particle equations the Lagrangian isotropisation of production (LIPM) is used, which has the following form for G_{ij} [46]:

$$G_{ij} = G_{ij}^{(1)} + G_{ij}^{(2)} \tag{2.111}$$

with

$$G_{ij}^{(1)} = \frac{\epsilon}{k}(\alpha_1 \delta_{ij} + \alpha_2 b_{ij} + \alpha_3 b_{ij}^2) \tag{2.112}$$

with $b_{ij} = \widetilde{u_i'' u_j''}/\widetilde{u_k'' u_k''}/ - 1/3\delta_{ij}$ the normalized anisotropy tensor

$$G_{ij}^{(2)} = -\frac{1}{5}\frac{\partial \widetilde{U_k}}{\partial x_k}\delta_{ij} + \frac{8}{5}\frac{\epsilon}{k}W_{ij} + C_2\frac{\partial \widetilde{U_j}}{\partial x_i} + 6\left(\frac{4}{5} - C_2\right)\frac{\epsilon}{k}b_{ik}W_{ik} \tag{2.113}$$

The values for are found from the following system of equations:

$$\begin{aligned} \frac{1}{2} + \frac{3}{4}C_0 + \alpha_1 + b_{kk}^2\left(\alpha_2 + \frac{1}{3}\alpha_3\right) + b_{kk}^2\alpha_3 + \left(-\frac{1}{5} + C_2\right)S_k k - \frac{1}{4}C_2\frac{P_{kk}}{\epsilon} &= 0 \\ 4\alpha_1 + \frac{4}{3}\alpha_2 + 2b_{kk}^2\alpha_3 - \frac{4}{5}S_{kk} &= -2C_1 \\ 4\alpha_2 + \frac{4}{3}\alpha_3 &= 0 \end{aligned} \tag{2.114}$$

with $C_1 = 1.8$ and $C_2 = 0.6$

Composition PDF The transport equation for the composition PDF $f_{\boldsymbol{\phi}}$ [45]

$$\frac{\partial \rho f_{\boldsymbol{\phi}}}{\partial t} + \frac{\partial \rho \widetilde{U}_i f_{\boldsymbol{\phi}}}{\partial x_i} + \frac{\partial \rho S_\alpha f_{\boldsymbol{\phi}}}{\partial \psi_\alpha} = -\frac{\partial}{\partial x_i}[\langle u_i'' | \psi \rangle \rho f_{\boldsymbol{\phi}}] + \frac{\partial}{\partial \psi_\alpha}\left[\left\langle -\frac{\partial J_i^\alpha}{\partial x_i} | \boldsymbol{\psi} \right\rangle f_{\boldsymbol{\phi}}\right] \tag{2.115}$$

The transport equation for the composition MDF is then:

$$\frac{\partial \mathcal{F}_{\boldsymbol{\phi}}}{\partial t} + \frac{\partial \widetilde{U}_i \mathcal{F}_{\boldsymbol{\phi}}}{\partial x_i} + \frac{\partial S_\alpha \mathcal{F}_{\boldsymbol{\phi}}}{\partial \psi_\alpha} = \underbrace{-\frac{\partial}{\partial x_i}[\langle u_i'' | \psi \rangle \mathcal{F}_{\boldsymbol{\phi}}]}_{\text{turbulent diffusion}} + \underbrace{\frac{\partial}{\partial \psi_\alpha}\left[\left\langle -\frac{1}{\rho}\frac{\partial J_i^\alpha}{\partial x_i} | \boldsymbol{\psi} \right\rangle \mathcal{F}_{\boldsymbol{\phi}}\right]}_{\text{micro-mixing}} \tag{2.116}$$

The terms on the left hand side are closed, so again the mean reaction source term is closed. The turbulent diffusion term and the micro-mixing term on the right hand side have to be modeled. The turbulent diffusion term is modeled with the gradient diffusion assumption:

$$-\frac{\partial}{\partial x_i}[\langle u_i''|\psi\rangle\mathcal{F}_{\boldsymbol{\phi}}] = \frac{\partial}{\partial x_i}\left[\Gamma_t\frac{\partial(\mathcal{F}_{\boldsymbol{\phi}}/\rho)}{\partial x_i}\right] \tag{2.117}$$

The equivalent equations for the evolution of the computational particles in physical space is [45]:

$$dx_i^* = \widetilde{U}_i^{\,*}dt + dx_{i,turb}^* + \left[U_i^c\right]^* dt \tag{2.118}$$

The turbulent diffusion term $dx_{i,turb}^*$ is modeled with a random walk model:

$$dx_{i,turb}^* = \left[\frac{1}{\overline{\rho}}\frac{\Gamma_t}{dx_i}\right]^* dt + \left[\sqrt{\frac{2\Gamma_t}{\overline{\rho}}}\right]^* dW_i \tag{2.119}$$

$$dx_i^* = \left[\widetilde{U}_i + \frac{1}{\overline{\rho}}\frac{\Gamma_t}{dx_i}\right]^* dt + \left[\sqrt{\frac{2\Gamma_t}{\overline{\rho}}}\right]^* dW_i + \left[U_i^c\right]^* dt \tag{2.120}$$

Transport in composition space is described by the following equation:

$$d\phi_\alpha^* = S_\alpha(\boldsymbol{\phi^*})dt + \theta_{\alpha,mix}^* dt \tag{2.121}$$

with $\theta_{\alpha,mix}$ the micro-mixing model.

Mixing models

Micro-mixing models have to describe the effect of molecular diffusion on the particle composition and more specifically how it changes the shape of the joint PDF. As discussed earlier, local scalar mixing is very important in non-premixed combustion as it is molecular diffusion which brings the reactants close to each other before they can react and can thus influence the global reaction rate. As can be seen from the PDF transport equation, the diffusion conditional on the composition vector needs to

be modeled. This is equivalent to modeling the conditional scalar dissipation rate.

$$\langle \Gamma_\alpha \bigtriangledown^2 \phi_\alpha | \Psi \rangle \tag{2.122}$$

Mixing time scale In the basic models the small-scale mixing time scale is assumed to be proportional to the turbulent timescale τ_t provided by the turbulence model. This is the equilibrium model which has been discussed above [14]. The characteristic mixing time scale is then:

$$\tau_{mix} = \frac{\tau_t}{C_\phi} = \frac{k}{C_\phi \epsilon} \tag{2.123}$$

where C_ϕ is the empirical mixing constant. The optimal value for C_ϕ differs from model to model and has been subject to extensive discussion. In [47] a $C_\phi > 3$ was needed to obtain a burning flame with CD. On the other hand in [48] obtains a burning flame with CD for $C_\phi = 2.3$ for the same test-case. For EMST, $C_\phi = 1.5$ or 2 is standard. The equilibrium model thus determines the mean scalar dissipation rate. More complex time scale models have been developed in the framework of partially premixed combustion. Kuan et al. [49] calculated the value of C_ϕ dynamically by introducing the effect of the Damköhler number through the ratio of the laminar flame speed and the Kolmogorov velocity. Even though C_ϕ is calculated dynamically, the model has parameters which need to be tuned. Mura et al. [50] developed a time scale model for the reactive scalar through blending of the classic time scale model in the thickened flame regime with a model derived from the Bray-Moss-Libby model in the flamelet regime. Stöllinger et al. [51] proposed a similar blending but for each regime a time scale model is derived from a modeled transport equation for the scalar dissipation rate of the reactive scalar. The advantage of the last two blending models is that no model parameters have to be tuned.

However, to truly capture finite rate chemistry effects such as local extinction, the full range of mixing scales has to be captured by the mixing model. This is equivalent to using a distribution of the scalar dissipation rate instead of Dirac distribution at the mean value. With a distribution for the scalar dissipation rate there is a possibility of having a smaller mixing time scale than the reaction time scale, which could eventually lead to local extinction due to local excessive diffusion of the progress variable, representing local excessive heat diffusion.

Another aspect is the different mixing time for inert and reactive scalars, due to

steepening of the gradients of the reactive scalars. This results in a smaller mixing time scale or larger C_ϕ for reactive scalars than for non-reactive scalars [52]. However, most mixing models, i.e. all the models used in this PhD, have only one C_ϕ for all the scalars. The different mixing time scale for inert and reactive scalars can however be accounted for with an extra model for the ratio of the timescales of a reactive and a non-reactive scalar [53]. The mixing time scale of the reactive scalar can then be calculated with the inert mixing time scale, obtained from a standard model.

IEM The most basic mixing model is IEM [54]. This is a deterministic model in which the particles linearly relax to the mean value of the cell. It is not used here, because the shape of the PDF does not change and therefore the PDF does not relax to the Gaussian shape in the case of a homogeneously mixed cell. It is not a good mixing model for reactive scalars, as for instance with a single flamelet model particles are pulled off the flamelet.

CD In the Coalescence Dispersion model [55], also known as the modified Curl model, particles mix in pairs in a stochastic manner. Every time step, pairs are randomly chosen and within a pair the particles interact in the following manner [46]:

$$\begin{aligned}
\phi_\alpha^{(p,t+\Delta t)} &= (1-a)\phi_\alpha^{(p,t)} + a\phi_{\alpha,mean}^{(p,q)} = (1-a)\phi_\alpha^{(p,t)} + a\frac{w_p\phi_\alpha^{(p,t)} + w_q\phi_\alpha^{(q,t)}}{w_p + w_q} \\
\phi_\alpha^{(q,t+\Delta t)} &= (1-a)\phi_\alpha^{(p,t)} + a\phi_{\alpha,mean}^{(p,q)} = (1-a)\phi_\alpha^{(q,t)} + a\frac{w_q\phi_\alpha^{(q,t)} + w_p\phi_\alpha^{(p,t)}}{w_p + w_q}
\end{aligned} \tag{2.124}$$

With p and q the 2 particles of the pair and a randomly chosen from a uniform distribution in $(0,1)$.

The CD model is a non-local mixing model as it allows interaction between particles which are not close to each other in composition space. Because of this, cold particles from the lean zone can interact with cold particles from the rich zone, resulting in cold particles in the reaction zone and in cold particles crossing the reaction zone without reacting. This often results in over-prediction of extinction. [47] This is often countered by using higher values of C_ϕ, meaning faster mixing and leading to a faster decay of the mixture fraction rms. This might, however, lead to under-prediction of the mixture fraction rms. Physically, the amount of mixing through extinguished flame regions is controlled by the local Damköhler number Da [48], but

this is not captured with CD, because there is no connection to the chemical time scale. The model described in [48] accounts for local Damköhler number effects through an algebraic model, including the ratio of the local laminar burning velocity and the local Kolmogorov velocity which increases monotonically with Da. Still only 1 single mixing frequency for reactive and non-reactive scalars is used. The influence of the micro-mixing models on flame calculations has been studied extensively in the past.

EMST In the EMST model [56], particles mix for stochastically chosen times. At each moment the total number of particles is divided into a subset of mixing particles and one of non-mixing particles. In the subset of mixing particles, which is chosen randomly, a Euclidean minimum spanning tree is constructed and particles interact along the branches of the EMST. The use of the Euclidean minimum spanning tree ensures that the mixing is local in composition space: particles can only interact with 'neighboring' particles in composition space. Due to the continuity of the scalar fields in physical space, this also implies localness in physical space. In [57] the mixing models are tested in joint velocity-scalar-frequency-PDF.

PSP With the PSP-model [58, 59, 60], each particle has a one-dimensional sinusoidal profile which is used to describe the scalar gradient in physical space, which determines the rate of micro-mixing:

$$Z(x',t) = \frac{Z^{*,+}(t-t_0) - Z^{*,-}(t-t_0)}{2} sin\left(\frac{x'\pi}{\lambda}\right) + \frac{Z^{*,+}(t-t_0) - Z^{*,-}(t-t_0)}{2} Z^{*,c} \tag{2.125}$$

with $Z^{*,+}$, $Z^{*,-}$, and $Z^{*,c} = (Z^{*,+} + Z^{*,-})/2$, the maximum, minimum and center value of the scalar profile. Each computational particle transports thus a scalar profile including information on the local scalar gradients. Therefore, more than the joint statistics of the scalars, the joint statistics of the profiles are obtained, providing more information on the mixing process. The joint composition - dissipation rate statistics are thus available. In other words the dissipation rate is now described by a full distribution. The PSP model can be interpreted as a local IEM model, as in the mixing process a particle moves towards the mean of a local ensemble of particles:

$$\frac{dZ^*}{dt} = -\frac{1}{2} C'_\phi \omega^* (Z^* - Z^{*,c}) \tag{2.126}$$

This equation resembles that of the the IEM model but here ω^* and $Z^{*,c}$ and thus also the mixing time scale are different for every computational particle, while with the IEM cell means were used. In other words, with the PSP model there is a distribution of mixing time scales in one computational cell. The corresponding scalar dissipation rate for a computational particle is then:

$$\chi_Z^*(Z) = C'_\phi \omega^* (Z^{*,+} - Z)(Z - Z^{*,-}) \tag{2.127}$$

The information of the local scalar gradient transported by the computational particle is thus used to calculate the 'local' scalar dissipation rate. Recently the PSP model was extended to reacting flows where the reactive scalar profiles are affected by the chemical reactions [61]. Other than in the previously discussed mixing models, the coupled reaction-diffusion problem is handled. A burning indicator is used to distinguish between burning and inert profiles. An ignition probability is then used to statistically model the ignition of inert profiles. In the reactive PSP model, inert profiles are still handled with the standard PSP model while burning profiles by a combination of the standard PSP model and the laminar flamelet concept. The PSP model has not been used in this PhD research, but it is mentioned nonetheless as it seems to have the potential to truly capture local extinction in PDF methods and it contains some interesting ideas regarding the modeling of mixing in reactive flows.

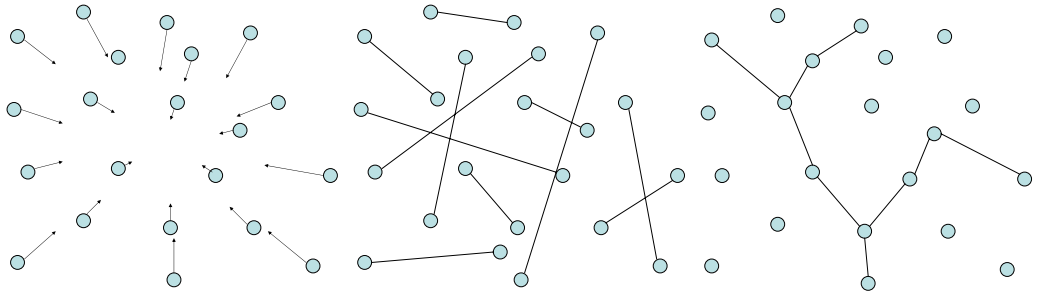

(a) IEM (b) CD (c) EMST

Figure 2.12: Particle interaction in composition space in mixing models: a/IEM, b/CD, c/EMST

Discussion The time scale model determines how fast the PDF changes and the mixing models determines how the PDF changes. [51] The equilibrium model for the time scale just determines the value of the mean mixing time scale. However, it does not force the distribution of the scalar dissipation rate to be a Dirac at the mean scalar dissipation rate. The mixing model describes specifically how the computa-

tional particles should behave during the mixing process. For the three basic models, i.e. IEM, CD and EMST, this is shown in figure 2.12, where the circles represent computational particles, which should be seen as realizations of the flow. Similarly the mixing process for each particle could be seen as realizations of the mixing process in the cell and a corresponding distribution for the scalar dissipation rate can be derived. For example, the non-local mixing of the CD model leads sometimes to strong mixing events, which could be seen as events of a high scalar dissipation rate.

Concluding, as with all combustion models previously discussed, the modeling of the scalar dissipation rate or the mixing time scale is the key issue. More specifically the (conditional) scalar dissipation rate of the mixture fraction, of the progress variable and their joint scalar dissipation rate needs to modeled correctly. The combination of the mixing time scale model and the actual mixing model determines the distribution of the scalar dissipation rate. In order to be able to capture extinction the fluctuations of the scalar dissipation rate need to be represented. Therefore a range of mixing time scales need to be modeled and therefore one mean mixing time scale as is used in this PhD does not suffice. In order to correctly describe mixing of reactive scalars the effect of the chemistry on the mixing, i.e. through steepening of the gradients of the reactive scalar field, needs to be accounted for. In this PhD research the EMST model is the primary mixing model as it is local in composition. However also the influence of the non-localness of the CD model is tested.

Numerical algorithms

Now that the theoretical foundation for transported PDF methods has been introduced, the numerical aspects specific for hybrid RANS-PDF calculations are discussed in this subsection.

Numerical errors The total numerical error in a hybrid RANS-PDF method is the sum of the different errors discussed below.

Statistical error The statistical error is a random error resulting from using a finite number of computational particles to represent the PDF and calculate mean properties in a computational cell. The statistical error scales with $N_{p,cell}^{-1/2}$ [62]. For statistical stationary flows the statistical error can be reduced by using iteration averages. The MDF is then approximated by the mean of the MDF approximations over

a range of subsequent time steps:

$$\mathcal{F}^{N_{TA}}_{\boldsymbol{u},\boldsymbol{\phi}}(\boldsymbol{x},\boldsymbol{V},\boldsymbol{\psi}) = \frac{1}{N_{TA}} \sum_{i=1}^{N_{TA}} c(\boldsymbol{x},\boldsymbol{V},\boldsymbol{\psi};t_i) \tag{2.128}$$

with $\mathcal{F}^{*}_{\boldsymbol{u},\boldsymbol{\phi}}$ In this PhD research iteration averages over 1000 time steps were used, but averages over less time steps are often also acceptable.

Bias error The bias error is a deterministic error resulting from using particle mean fields, calculated from a finite number of computational particles, to evolve particle properties. The bias error scales with $N^{-1}_{p,cell}$ and cannot be reduced with iteration averages [62].

Time discretisation error The time discretisation error results from handling the particle evolution with finite time steps instead of continuously. In [62] it has been shown, that this error is small compared to other numerical errors.

Spatial error In a hybrid RANS-PDF method, the total spatial discretisation error results both from the discretisation error in the RANS part and from the interpolation error connected to RANS properties being interpolated at the particle position.It is not completely clear how important this error is, but for a well chosen spatial discretisation the spatial discretisation error [46] should be small. Nonetheless, this needs further attention.

Particle number density control: splitting and clustering The initial particle distribution ensures that each cell has the desired amount of particles in a cell. However the particle evolution does not ensure this and over time the number of particles in different cells would diverge from the desired amount of particles. To ensure a fairly constant number of computational particles in each cell, i.e. $N_{min,cell} < N_{p,cell} < N_{max,cell}$, splitting and clustering algorithms are introduced [45]. Depending on the ratio of $N_{p,cell}$ with $N_{p,min}$ and $N_{p,max}$ a minimum and maximum allowed weight, $w_{min,cell}$ and $w_{max,cell}$, for the computational particles in a cell is calculated. Particles with a weight smaller than $w_{min,cell}$ are clustered to form a new particle with a weight larger than $w_{min,cell}$. The properties of the new particle are the properties of a randomly chosen particle from the ensemble of particles that formed

the cluster. Particles with a weight larger than $w_{max,cell}$ are split into a number of identical smaller droplets, with the same properties as the original particle.

Bilinear interpolation In this PhD research, bilinear basis functions are used to estimate mean properties at the grid nodes and interpolate mean properties from the grid nodes to the particle positions [63, 64]

Local time steps In the case of statistically stationary flows, local time stepping is used to speed up convergence to the statistically stationary solution [65]. In the local time step method a pseudo-time marching algorithm is used, which advances each particle with a time step which is different for each particle and depends on the physical location of the particle. The local time step is then [65]:

$$\Delta t_{i,j} = min[\Delta t_{lim}, \Delta t_{CFL_{i,j}} \Delta t_{\omega_{i,j}}] \tag{2.129}$$

with $\Delta t_{CFL_{i,j}}$ the minimum of the time steps imposed by the CFL-condition in all directions:

$$\Delta t_{CFL_{i,j}} = min[C_{CFL} \frac{(x_1^{i+1} - x_1^{i-1})/2}{U_1}, C_{CFL} \frac{(x_2^{j+1} - x_2^{j-1})/2}{U_2}], \tag{2.130}$$

$\Delta t_{\omega_{i,j}}$ the time step needed to reasonably resolve the integral turbulent time scale:

$$\Delta t_{\omega_{i,j}} = C_\omega \tau_t = C_\omega \frac{k}{\epsilon} \tag{2.131}$$

and Δt_{lim} an upper limit defined as:

$$\Delta t_{lim} = C_{\text{lim}} \Delta t_{min} \tag{2.132}$$

with Δt_{min} the minimum of $\Delta t_{CFL_{i,j}}$ and $\Delta t_{\omega_{i,j}}$ over the entire computational domain. Standard values for the constants are $C_{CFL} = 0.4$, $C_\omega = 0.2$ and $C_{\text{lim}} = 20$.

Method of fractional time steps The method of fractional time steps [66] is used to evolve the computational particles in physical and composition space. In this method, convection, micro-mixing and chemical reaction are handled subsequently instead of simultaneously. The validity of separating micro-mixing and chemical reaction is discussed in [67].

2.2 Spray

First the basics of multiphase flows are introduced. Then the transported PDF method for sprays is discussed, together with the modeling of droplet dynamics, evaporation, heat transfer and the unresolved gas field around the droplet. Finally, spray combustion is briefly discussed.

2.2.1 Classification of multiphase flows

In general, a multiphase flow is a flow which consists of at least two different phases, i.e. gas, liquid and/or solid. Multiphase flows can then be classified based on the distribution of the different phases: separated or dispersed. In a separated multiphase flow, there is only a small number of larger continuous zones of a certain phase. This is for example the case for the combined system of air and water in a channel flow. A dispersed multiphase flow on the other hand consists of a large amount of droplets, particles or bubbles dispersed in a continuous carrier phase. [68]

For dispersed multiphase flows a sub-division can made based on the volume fraction of the dispersed phase α_p:

$$\alpha_p = \frac{\sum_i N_i V_{p,i}}{V} \tag{2.133}$$

A dispersed flow is then considered dilute if $\alpha_p < 10^{-3}$. In a dilute dispersed flow inter-particle collisions can be neglected, while in dense dispersed flow inter-particle collisions need to be accounted for (4-way coupling). In dilute sprays, there is a sub-division based on the influence of the dispersed phase on the continuous phase. When $\alpha_p < 10^{-6}$, the influence of the dispersed phase on the continuous phase can be neglected and only the effect of the continuous phase on the dispersed phase has to be taken into account (1-way coupling). For $10^{-6} < \alpha_p < 10^{-3}$ also the influence of the momentum of the dispersed phase on the continuous phase has to be taken into account (2-way coupling) [68]. In sprays with evaporating droplets, there is always two-way coupling of the mass.

In this PhD research we study a specific case of the dispersed multiphase flows: the dilute liquid spray. This the combination of a continuous gas flow and a dilute dispersed liquid flow, i.e. liquid droplets. Sprays are used in many practical appli-

cations because of their large total interface surface, which enhances global heat and mass transfer.

As could be expected, the modeling of separated and dispersed flow is quite different. Liquid sprays can have a separated flow region in the neighborhood of the nozzle and a more dispersed flow further downstream. The continuous liquid zone then breaks up further downstream into smaller ligaments and eventually droplets. However in many applications, atomizers are used to break up the liquid into small droplets as fast as possible.

In the spray calculations investigated in this PhD, a pressure swirl atomizer is used and in the calculations we assume that the droplets do not break-up into smaller droplets. This might not be completely correct close to the atomizer, but we are more interested in the droplet behavior further downstream were this assumption is more valid.

2.2.2 Classification of dispersed multiphase flow calculations

In this discussion the focus is on the modeling of dispersed multiphase flows.

Resolution of flow around the droplet

A first classification can be done based on the resolution of the flow around the droplet. If the particle is much larger than the grid cells surrounding it, it is possible to resolve the flow around the particle to a certain extent. This does not necessarily mean that the grid size is small enough to fully resolve the flow. However, usually the Kolmogorov vortices in the continuous phase are resolved (DNS), so that these calculations provide important information for the modeling of the flow around the droplet.

If the particle is substantially smaller than the grid size, the particle can be considered to be a point particle. Obviously the flow around the droplet is then not resolved and all the effects of that flow on the interface phenomena, e.g. mass and heat transfer, must be modeled.

Both calculations have their own use and can be regarded as being complementary. The calculations resolving the flow around the droplets can be used to provide information for modeling of interfacial phenomena such as mass and heat transfer at

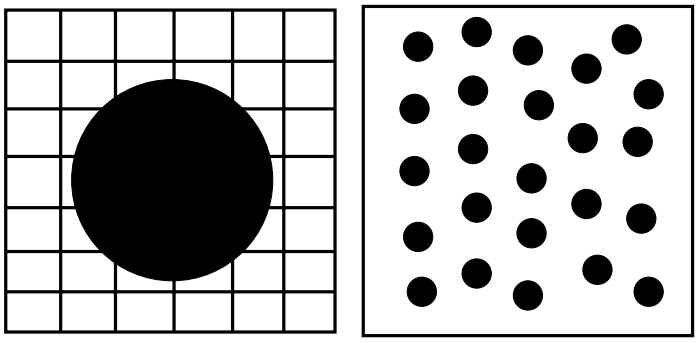

Figure 2.13: Grid resolution vs droplet size

the interface. The calculations not resolving the flow around the droplet on the other hand are better suited for practical problems where resolution of the flow around the droplets would require excessive computational resources. In this PhD research the droplets are substantially smaller than the grid size, so all the interfacial phenomena will have to be modeled.

Euler vs Lagrange

Another classification can be done based on the Eulerian or Lagrangian nature of the modeling.

In Eulerian approaches the dispersed phase is treated as if it was a continuum, and the equations are discretized on an Eulerian grid. In Lagrangian approaches, the dispersed phase is represented by computational particles whose evolution is computed in physical, diameter and temperature space. Eulerian approaches are inherently better suited for dense sprays, while Lagrangian approaches perform better in dilute sprays. In this PhD research a Lagrangian approach is used. To put this into context still both methods are discussed briefly.

Euler The most basic Eulerian method is the method of moments, which describes the dispersed phase by seeing it as a continuum and solving only equations for the first order moments. The Quadrature method of moments (QMOM) solves transport equations of the moments and recovers the PDF with a quadrature method. The Direct Quadrature method of moments (DQMOM), on the other hand, solves transport equations for the weights and the nodes of the quadrature approximation and reconstructs the moments [69]. The multi-fluid model divides the droplet diameter space into sections and for each section the transport equations for the moments are

solved. The largest disadvantage of this method is that in a certain section all droplets are assumed to have the same mean diameter and velocity. Therefore it is impossible to represent crossing trajectories of droplets from the same diameter bin. This can however be remedied by modeling the velocity PDF for example with the Mesoscopic Eulerian Formalism (MEF) [70, 71]. In the multi-fluid-multi-velocity model, the droplets in a certain section still all have the same mean diameter, but now have a distribution in velocity space which is solved with the DQMOM method [72]. This makes it possible to represent crossing trajectories of droplets from the same diameter bin. Finally, the Eulerian multi-size moment method (EMSM) uses higher order moments to describe the diameter distribution at a lower computational cost than the multifluid method. [73] However, with EMSM it is not possible to represent size conditioned velocities. Therefore the EMSM has been expanded with the Coupled Size-Velocity model (CSVM) to account for size conditioned velocities.

Lagrangian There are basically two Langrangian methods to describe the dispersed phase: the discrete particle method and the Monte Carlo transported PDF method. In the discrete particle method (DPM) each computational parcel represents one droplet. To simulate practical cases, this leads to excessive needs of computational power. Therefore a probabilistic method such as the transported PDF method is better suited to simulate practical cases. In the Monte Carlo transported PDF method, the computational parcels statistically represent independent realizations of the dispersed phase. Each parcel has a numerical weight, determining its importance on the statistics of the ensemble of parcels. In this PhD, the transported PDF method is used to represent the dispersed phase in a statistical manner.

2.2.3 Transported PDF method for sprays

Similar to what was done in the gas, a transport equation for the droplet-PDF is solved through a Monte Carlo method which solves stochastic differential equations for computational droplet parcels. Note that these computational parcels must not be interpreted as discrete droplets.

Droplet PDF transport equation

The first choice to make is which of the droplet properties will be included into the droplet PDF. Generally, the position $\boldsymbol{x}$, the velocity $\boldsymbol{V}_p$, the temperature T_p, diameter D_p of the droplet are included. However, also the velocity seen by the droplet $\boldsymbol{V}_s$ and the composition vector seen by the droplet $\boldsymbol{\psi}_s$ should be included. The latter consists usually of the temperature seen by the droplet T_s and the vapor mass fraction seen by the droplet Y_s. Depending on the modeling of the heat transfer inside the droplet, the temperature inside the droplets at different positions could also be added to $\boldsymbol{\psi}_s$. Then a vector $\boldsymbol{T}_p$ will be used. So the entire phase space is then $[\boldsymbol{x}, \boldsymbol{\Psi}] = [\boldsymbol{x}, \boldsymbol{V}_p, d_p, T_p, \boldsymbol{V}_s, \boldsymbol{\psi}_s]$. The droplet mass density function (MDF) $\mathcal{F}_p$ is defined as follows [46]:

$$\mathcal{F}_p(\boldsymbol{x}, \boldsymbol{\Psi}; t) = m_p(D_p) \left\langle \sum_{+\,\text{in cell}} \delta(\boldsymbol{X}_p^+(t) - \boldsymbol{x}).\delta(\boldsymbol{\Phi}_p^+(t) - \boldsymbol{\Psi}) \right\rangle \tag{2.134}$$

The transport equation for the droplet MDF is then [46]:

$$\begin{aligned} \frac{\partial \mathcal{F}_p}{\partial t} + V_{p,j} \frac{\partial \mathcal{F}_p}{\partial x_j} = &- \frac{\partial}{\partial V_{p,i}} \left[\left\langle A_{p,i}^+ | \boldsymbol{x}, \boldsymbol{\Psi}; t \right\rangle \mathcal{F}_p \right] - \frac{\partial}{\partial d_p} \left[\left\langle \dot{D}_{p,i}^+ | \boldsymbol{x}, \boldsymbol{\Psi}; t \right\rangle \mathcal{F}_p \right] \\ &- \frac{\partial}{\partial \theta_p} \left[\left\langle \dot{T}_{p,i}^+ | \boldsymbol{x}, \boldsymbol{\Psi}; t \right\rangle \mathcal{F}_p \right] - \frac{\partial}{\partial \psi_{s,\alpha}} \left[\left\langle \Theta_{s,\alpha}^+ | \boldsymbol{x}, \boldsymbol{\Psi}; t \right\rangle \mathcal{F}_p \right] \\ &- \frac{\partial}{\partial V_{s,i}} \left[\left\langle A_{s,i}^+ | \boldsymbol{x}, \boldsymbol{\Psi}; t \right\rangle \mathcal{F}_p \right] + \underbrace{\left\langle \frac{1}{m_p^+} \frac{dm_p^+}{dt} | \boldsymbol{x}, \boldsymbol{\Psi}; t \right\rangle \mathcal{F}_p}_{\text{evaporation}} \end{aligned} \tag{2.135}$$

As was the case for the gas PDF, also the transport equation of the droplet PDF is solved through a Monte Carlo Method. Now, computational droplet parcels represent the entire spray in a statistical way. The statistics of the spray in a certain CFD cell are then retrieved from the ensemble of droplet parcels in that cell.

The equations solved for each computational droplet parcel are then:

$$\begin{aligned} &\frac{d\boldsymbol{X}_p^+}{dt} = \boldsymbol{U}_p^+ \qquad \frac{d\boldsymbol{U}_p^+}{dt} = \boldsymbol{A}_p^+ \qquad \frac{d\boldsymbol{D}_p^+}{dt} = \dot{\boldsymbol{D}}_p^+ \qquad \frac{d\boldsymbol{T}_p^+}{dt} = \dot{\boldsymbol{T}}_p^+ \\ &\frac{d\boldsymbol{U}_s^+}{dt} = \boldsymbol{A}_s^+ \qquad \frac{d\boldsymbol{\phi}_s^+}{dt} = \boldsymbol{\Theta}_s^+ \end{aligned} \tag{2.136}$$

In the next sections the models for $\boldsymbol{A}_p^+$,$\dot{\boldsymbol{D}}_p^+$,$\dot{\boldsymbol{T}}_p^+$,$\boldsymbol{A}_s^+$ and $\boldsymbol{\Theta}_s^+$ are discussed.

2.2.4 Motion

The droplets are assumed to be spherical and rotation of the droplet is neglected. The equation of motion of a single droplet is then:

$$m_p \frac{dU_{p,i}}{dt} = \underbrace{m_p g_i}_{\text{gravity}} - \underbrace{\frac{m_p}{\rho_p}\left[\frac{\partial p}{\partial x_i}\right]_s}_{\text{undisturbed flow}} + \underbrace{F_{r,i}}_{\text{particle perturbation}} + \underbrace{[\overline{U}_{\sigma,i} - U_{p,i}]\frac{dm_p}{dt}}_{\text{jet propulsion effect}} \tag{2.137}$$

The mass transfer at the interface of the droplet is also assumed to be the same at every point of the surface, making it possible to neglect the jet propulsion effect. In the case of sprays $\rho_p >> \rho_g$, $\boldsymbol{F}_r = \boldsymbol{F}_{drag}$ and $\frac{\partial p}{\partial x_i} \approx \frac{\partial \langle p \rangle}{\partial x_i}$, reducing the equation of motion to:

$$m_p \frac{dU_{p,i}}{dt} = m_p g_i - \frac{m_p}{\rho_p}\left[\frac{\partial \langle p \rangle}{\partial x_i}\right]_s + F_{drag,i} \tag{2.138}$$

The drag force $\boldsymbol{F}_{drag}$ depends on the difference between the velocity seen by the droplet $\boldsymbol{U}_s$ and the droplet velocity $\boldsymbol{U}_p$:

$$\boldsymbol{F}_{drag} = m_p \frac{\boldsymbol{U}_s - \boldsymbol{U}_p}{\tau_p} = m_p \frac{3}{4}\frac{\rho_f}{\rho_p} C_D \frac{|\boldsymbol{U}_s - \boldsymbol{U}_p|}{D_p}(\boldsymbol{U}_s - \boldsymbol{U}_p) \tag{2.139}$$

with $\boldsymbol{U}_s$ the velocity of the fluid seen by the droplet. τ_p is the particle relaxation time:

$$\tau_p = \frac{4}{3}\frac{\rho_p}{\rho_f}\frac{D_p}{C_D|\boldsymbol{U}_s - \boldsymbol{U}_p|} \tag{2.140}$$

The Reynolds number which characterizes the flow around the droplet is the Particle Reynolds number:

$$Re_p = \frac{\rho_g |\boldsymbol{U}_s - \boldsymbol{U}_p| D_p}{\mu_g} \tag{2.141}$$

When $Re_p \to 0$, the fluid flow stays attached to the droplet and no separation is observed. This is better known as the Stokes regime. The particle relaxation time τ_p is then:

$$\tau_p^{St} = \frac{\rho_p D_p^2}{18\mu_g} \tag{2.142}$$

The force on the droplet is then linear with the slip velocity $\boldsymbol{U}_s - \boldsymbol{U}_p$. The drag coefficient C_D is usually given by semi-empirical correlations. In this PhD research the Schiller-Naumann correlation is used:

$$C_D = \begin{cases} \frac{24}{Re_p}(1+0.15Re_p^{0.687}) & \text{if } Re_p \leq 1000 \\ 0.44 & \text{if } Re_p > 1000 \end{cases} \tag{2.143}$$

2.2.5 Seen velocity

For the velocity seen by the droplet a modified simplified Langevin model (SLM) is used, which is based on the simplified Langevin model for a computational gas particle [46]:

$$dU_i = \underbrace{\left[-\frac{1}{\rho_g}\frac{\langle p\rangle}{\partial x_i} + \frac{1}{T_L^{(SLM)}}(U_i - \langle U_i\rangle)\right]}_{A_i} dt + \underbrace{\sqrt{C_0\epsilon}dW_i}_{B_{ij}dW_j} \tag{2.144}$$

with T_L the Lagrangian time scale. The modified SLM equation for the seen velocity increment is then:

$$dU_{s,i} = \underbrace{\left[-\frac{1}{\rho_g}\frac{\langle p\rangle}{\partial x_i} + \langle U_{r,j}\rangle\frac{\langle U_i\rangle}{\partial x_j} + G_{s,ij}(U_{s,j} - \langle U_j\rangle)\right]}_{A_{s,i}} dt + B_{s,ij}dW_j \tag{2.145}$$

with $\boldsymbol{U}_r = \boldsymbol{U}_p - \boldsymbol{U}_s$ the relative velocity of droplet. In this PhD research also the new modified GLM model, developed and implemented by B. Naud, is used [74]. Similarly to the modified SLM model being based on the SLM for the gas particles, this modified GLM model is based on the GLM model for the gas particles.

2.2.6 Modifications to gas phase equations

Due to interaction between the droplets and the gas phase, the gas phase may be affected by the droplets and in the gas phase equations this results in extra source terms. The droplets locally exert the drag force onto the gas phase, resulting in an exchange of momentum and seen as a source term in the momentum equations. The presence of the droplets can also affect the turbulence spectrum and the turbulent stresses. For the RANS-PDF framework this has been discussed in great detail in [75, 76], but this will not be accounted for in this PhD research. Evaporating droplets

also affect the continuity equation because mass is injected into the gas phase. Also the scalar transport equation is affected as the vapor mass fraction rises and the mass fraction of the other species should become smaller due to the extra vapor in the local gas mixture. Also the temperature and the enthalpy can be affected due to heat transfer with the droplets.

Mean equations

The modified mean transport equations are now discussed. The modified Favre-averaged continuity equation is:

$$\frac{\partial \overline{\rho}}{\partial t} + \frac{\partial \overline{\rho}\widetilde{U}_i}{\partial x_i} = \widetilde{S}_m^{(I)} \tag{2.146}$$

with $\widetilde{S_m^{(I)}}$ the mean mass source term due to evaporation. The modified Favre-averaged momentum equation is:

$$\frac{\partial \overline{\rho}\widetilde{U}_i}{\partial t} + \frac{\partial \overline{\rho}\widetilde{U}_i\widetilde{U}_j}{\partial x_i} = \frac{\partial \widetilde{\tau}_{ij}}{\partial x_i} - \frac{\partial \widetilde{P}}{\partial x_j} - \overline{\rho} g_j - \frac{\partial \tau_{ij}^{turb}}{\partial x_j} + \widetilde{S}_U^{(I)} \tag{2.147}$$

with the turbulent stresses τ_{ij}^{turb} and $\widetilde{S}_U^{(I)}$ the mean momentum source term due to the drag force of the droplets. The modified mean transport equation for a general scalar is then:

$$\frac{\partial \overline{\rho}\widetilde{\phi}}{\partial t} + \frac{\partial \overline{\rho}\widetilde{\phi}\widetilde{U}_j}{\partial x_i} = \frac{\partial}{\partial x_i}\left(\rho\Gamma\frac{\partial \widetilde{\phi}}{\partial x_i}\right) - \frac{\partial J_j^{turb}}{\partial x_j} + \widetilde{S}_\phi^{(chem)} + \widetilde{S}_\phi^{(I)} \tag{2.148}$$

with the turbulent scalar flux J_j^{turb}, $\widetilde{S}_\phi^{(chem)}$ the chemical source term and $\widetilde{S}_\phi^{(I)}$ the mean scalar source term due to the presence of the droplets. Depending on which property ϕ represents, the interpretation of $\widetilde{S}_\phi^{(I)}$ is different. For the mean vapor mass fraction this source term represents the rise in vapor mass fraction due to evaporation, while for the the mean mass fraction of the other species this term represents the decrease of the mass fraction due to dilution with vapor. For enthalpy and temperature this term takes into account the heat transfer between the droplets and the gas.

Gas PDF transport equations

In the spray calculations performed in this PhD research only the velocity-scalar PDF is used for the PDF description of the gas phase. Therefore only the modifications to the transport equations for the velocity-scalar PDF are discussed. The transport equation for the velocity-scalar PDF of the gas is then [46]:

$$\begin{aligned}
&\frac{\partial \mathcal{F}_g}{\partial t} + \frac{\partial V_i \mathcal{F}_g}{\partial x_i} + \left(g_i - \frac{1}{\rho}\frac{\partial \langle p \rangle}{\partial x_i} + \frac{\partial \langle \tau_{ij} \rangle}{\partial x_j} \right) \frac{\partial \mathcal{F}_g}{\partial V_i} + \frac{\partial S_\alpha \mathcal{F}_g}{\partial \psi_\alpha} = \\
&\frac{\partial}{\partial V_i}\left[\frac{1}{\rho} \left\langle \left(-\frac{\partial \tau'_{ij}}{\partial x_j} + \frac{\partial p'}{\partial x_i} \right) | \boldsymbol{V}, \boldsymbol{\psi} \right\rangle \mathcal{F}_g \right] + \frac{\partial}{\partial \psi_\alpha}\left[\frac{1}{\rho} \left\langle \left(-\frac{\partial J_i^\alpha}{\partial x_i} \right) | \boldsymbol{V}, \boldsymbol{\psi} \right\rangle \mathcal{F}_g \right] \\
&- \frac{\partial}{\partial V_i}\left[\frac{1}{\rho_g(\boldsymbol{\psi})} \left\langle S^I_{U_i} | \boldsymbol{V}, \boldsymbol{\psi} \right\rangle \mathcal{F}_g \right] - \frac{\partial}{\partial \psi_\alpha}\left[\frac{1}{\rho_g(\boldsymbol{\psi})} \left\langle S^I_{\phi_\alpha} | \boldsymbol{V}, \boldsymbol{\psi} \right\rangle \mathcal{F}_g \right] \\
&+ \frac{1}{\rho_g(\boldsymbol{\psi})} \left\langle S^I_m | \boldsymbol{V}, \boldsymbol{\psi} \right\rangle \mathcal{F}_g
\end{aligned} \tag{2.149}$$

The terms on the left hand side are closed, while the right hand side terms have to be modeled. The last three terms on the right hand side are due to the presence of the droplets with the same source terms as explained for the mean gas equations. Note that the gas MDF $\mathcal{F}_g$ used in spray calculations is different from the gas MDF $\mathcal{F}_{\boldsymbol{u},\boldsymbol{\phi}}$ used in the single phase calculations. For example the normalization condition is different [46]:

$$\int_{[\boldsymbol{V},\boldsymbol{\psi}]} [\rho(\boldsymbol{\psi})]^{-1} \mathcal{F}_{\boldsymbol{u},\boldsymbol{\phi}}(\boldsymbol{V},\boldsymbol{\psi};\boldsymbol{x},t).d\boldsymbol{V}.d\boldsymbol{\psi} = 1 \tag{2.150}$$

$$\int_{[\boldsymbol{V},\boldsymbol{\psi}]} [\rho(\boldsymbol{\psi})]^{-1} \mathcal{F}_{g}(\boldsymbol{V},\boldsymbol{\psi};\boldsymbol{x},t).d\boldsymbol{V}.d\boldsymbol{\psi} = \alpha_1(\boldsymbol{x},t) \tag{2.151}$$

with α_1 the volume fraction of the gas phase.

2.2.7 Heat transfer and Evaporation

In general, the heat and mass transfer at the interface are determined by the Spalding heat and mass transfer number B_T, B_M. The Spalding mass transfer number B_M

expresses the eagerness of the droplet to evaporate:

$$B_M = \frac{Y_{surf} - Y_s}{1 - Y_{surf}} \tag{2.152}$$

with Y_{surf} the vapor mass fraction at the droplet surface and Y_s the vapor mass fraction seen by the droplet. As it is common practice, in this PhD research Y_{surf} is assumed to be the saturation composition calculated with the Clausius-Clapeyron equation. However, for small droplets or strong evaporation rates non-equilibrium effects can cause Y_{surf} to be different from the saturation composition [77] and this can be modeled with a Langmuir-Knudsen model [78]. This is beyond the scope of this PhD research. From the definition of B_M it can be seen that it is mainly the difference between the surface and the seen vapor mass fraction $(Y_{surf} - Y_s)$ that determines the value of B_M. So B_M actually expresses more directly the eagerness of the evaporated vapor to diffuse to its surrounding, and it is this mass diffusion that in the end determines the evaporation rate. This can also be seen in the expression for the evaporation rate $\dot{m}_p$:

$$\dot{m}_p = -\pi D_p \rho_m \Gamma_m Sh_m ln(1 + B_M) \tag{2.153}$$

with Sh_m the Sherwood number based on properties evaluated with the 1/3-rule which is discussed below:

$$Sh_m = \frac{K.D_p}{\Gamma} \tag{2.154}$$

with K the mass transfer coefficient. The Sherwood number can thus be interpreted as the mass transfer equivalent of the Nusselt number. The Spalding heat transfer number, on the other hand expresses, the eagerness of heat transfer to the droplet:

$$B_T = \frac{C_{p,g}(T_s - T_{surf})}{L_v + \dot{q}_{drop}/m_p} \tag{2.155}$$

The numerator expresses the enthalpy difference of the gas seen by the droplet and the saturated gas at the surface of the droplet. This could be seen as being representative of the energy that is available in the surrounding gas. The denominator on the other hand expresses the amount of heat transfer due to convection that is needed for evaporation and to heat up the droplet. The expression of the evaporation rate based

on the B_T is then:

$$\dot{m}_p = -\pi \frac{\lambda_m}{C_{p,g}} Nu_m ln(1+B_T) = -\pi \rho_m \alpha_m Nu_m ln(1+B_T) \tag{2.156}$$

This description of mass and heat transfer based on transfer numbers is a more macroscopic view. The heat transfer on the hand can also be described in more detail by a balance equation describing the heat transfer at the droplet interface:

$$\dot{m} L_p = A_p \left(\lambda_g \frac{\partial T_g}{\partial r}\bigg|_s - \lambda_p \frac{\partial T_p}{\partial r}\bigg|_s \right) \tag{2.157}$$

with the droplet surface $A_p = 4\pi R_p^2 = \pi D_p^2$. Dividing by the droplet mass m_p:

$$\frac{\rho D_p}{6} \frac{\dot{m} L_p}{m_p} = \left(\lambda_g \frac{\partial T_g}{\partial r}\bigg|_s - \lambda_p \frac{\partial T_p}{\partial r}\bigg|_s \right) \tag{2.158}$$

In the case of evaporation, the term containing the evaporation rate acts as a heat sink and the heat flux comes from the surrounding gas and/or from the droplet. As heat flux coming from the surrounding gas is determined by convection from further away, this equation can also be written as:

$$\frac{\rho D_p}{6} \frac{\dot{m} L_p}{m_p} = \left(h_m (T_s - T_{surf}) - \lambda_p \frac{\partial T_p}{\partial r}\bigg|_s \right) \tag{2.159}$$

So there is a balance between heat transfer due to convection between the surface and the gas surrounding, heat transfer due to conduction between the inside of the droplet and the surface, consumption of heat due to evaporation. Based on this equation different scenarios can be thought of, depending on the temperature and composition of the surrounding gas.

For example if the temperature of the surrounding gas is much higher than the surface temperature of the droplet there will be a strong heat flux from the surrounding gas to the droplet. Depending on the evaporation rate, this heat flux will be consumed by evaporation or will heat up the droplet, or both. The evaporation rate is then mainly determined by the difference $(Y_{surf} - Y_s)$ and if this difference is large, there will be a large evaporation rate and a large part of the heat flux coming from the surroundings will be consumed by the evaporation, so that less heat will go into heating up of the droplet. This has been studied by Kurose et al [79] with a DNS study resolving both the flow inside and around the droplet, showing that the seen properties

strongly influence the evaporation rate and the heat balance at the droplet surface. However, with the point particle assumption used in this PhD research this interaction has to be modeled as the droplet and its immediate surrounding are not resolved. This is the reason why the macroscopic description with the Spalding transfer numbers is used.

2.2.8 Models for heat transfer inside the droplet

Several assumptions can be made concerning the temperature profile in the droplets. The validity of this assumption is determined by the Biot number:

$$Bi = \frac{hD_p}{\lambda_p} \tag{2.160}$$

If $Bi << 1$, the heat transfer between the droplet surface and the surrounding gas due to convection is substantially slower than the heat transfer from the droplet surface to the center of the droplet. This results in a quasi uniform temperature profile inside the droplet, as changes of the surface temperature due to heat transfer with the surrounding of the droplet are almost instantly compensated by heat transfer from the interior of the droplet to the droplet surface, eventually resulting in a uniform temperature distribution inside the droplet. In this case the temperature inside the droplet can be assumed to be uniform which is equivalent to assuming an infinitely large conductivity of the droplet. If $Bi >> 1$, the heat transfer between the droplet surface and the surrounding gas due to convection is substantially faster than the heat transfer from the droplet surface to the center of the droplet. Then the droplet has a non-uniform temperature profile and this should be taken into account in the calculations.

This can also be seen from the heat transfer balance at the surface of a non-evaporating droplet:

$$\lambda_{p,surf} \frac{\partial T_p}{\partial r}\bigg|_{surf} = \lambda_{g,surf} \frac{\partial T_g}{\partial r}\bigg|_{surf} = h(T_s - T_p) \tag{2.161}$$

$$Bi \sim \frac{h}{\lambda_{p,surf}} = \frac{\frac{\partial T_p(R_p)}{\partial r}}{T_s - T_p} \tag{2.162}$$

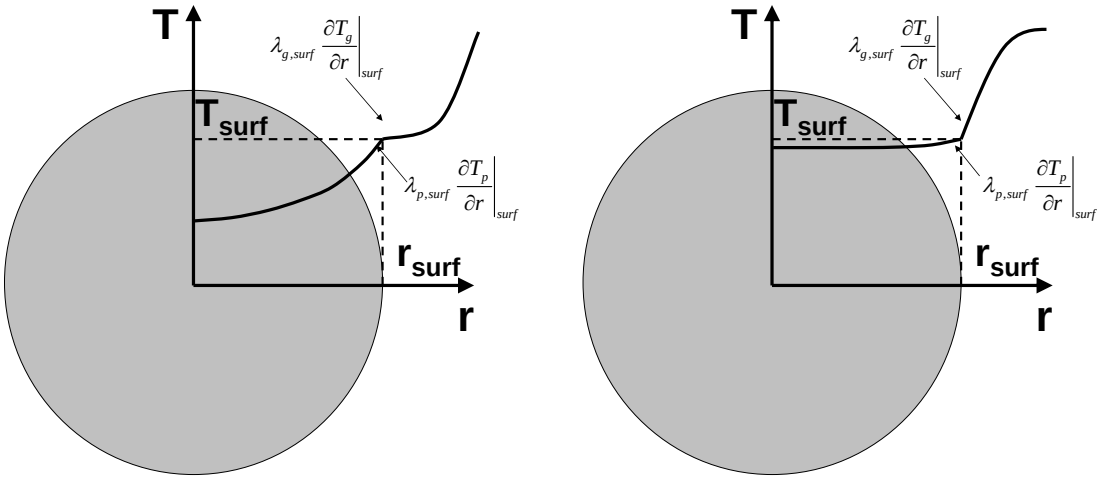

(a) $Bi >> 1$ (b) $Bi << 1$

Figure 2.14: Influence of Biot number on temperature inside a droplet

Infinite droplet conductivity

For the assumption of infinite conductivity inside the droplet, the basic equation for the evolution of the temperature with evaporation, but neglecting radiation is :

$$m_p C_{pp} \frac{dT_p}{dt} = h\pi D_p^2 (T_s - T_p) + \dot{m}_p L_v(T_p) \tag{2.163}$$

$$\frac{dT_p}{dt} = 6h \frac{(T_s - T_p)}{\rho_p C_{pp} D_p} + \frac{\dot{m}_p}{m_p C_{pp}} L_v(T_p) = \frac{T_s - T_p}{\tau_{p,T}} + \frac{\dot{m}_p}{m_p C_{pp}} L_v(T_p) \tag{2.164}$$

with the particle thermal relaxation time $\tau_{p,T}$

$$\tau_{p,T} = \frac{\rho_p C_{pp} D_p}{6h} = \frac{\rho_p C_{pp} D_p^2}{6 N u_s \lambda_s} \tag{2.165}$$

with Nu_s the particle Nusselt number

$$Nu_s = \frac{h D_p}{\lambda_s} \tag{2.166}$$

The equation for the droplet temperature then becomes:

$$\frac{dT_p}{dt} = 6 N u \lambda_m \frac{(T_s - T_p)}{\rho_p C_{pp} D_p^2} + \frac{\dot{m}_p}{m_p C_{pp}} L_v(T_p) \tag{2.167}$$

Finite droplet conductivity

When the Biot number is not much smaller than 1, the temperature profile inside the droplet has to be taken into account. Traditionally this would demand solving the temperature transport equation. However, a cheaper way to take this into account is to assume a parabolic profile which is determined by the temperature at two locations in the droplet, e.g. at the surface and in the center, or by the mean temperature and the temperature at one location. An equation for the mean temperature can then be solved. The heat flux going into the droplet $\dot{q}_{drop}$:

$$\dot{q}_{drop} = \dot{q}_{conv} - |\dot{q}_{evap}| = \pi D_p Nu \lambda_m (T_s - T_{surf}) - \dot{m}_p L_v(T_{surf}) \tag{2.168}$$

The parabolic temperature profile is defined as follows:

$$T_p(r,t) = T_{cntr}(t) + [T_{surf}(t) - T_{cntr}(t)] \left(\frac{r}{R_p} \right)^2 \tag{2.169}$$

The boundary condition at the droplet surface is:

$$\lambda_p \frac{\partial T_p}{\partial r}\bigg|_{surf} = \frac{\dot{q}_{drop}}{A_p} = \frac{Nu\lambda_m}{D_p}(T_s - T_{surf}) - \frac{\dot{m}_p}{\pi D_p^2} L_v(T_{surf}) \tag{2.170}$$

The volume averaged droplet temperature is then:

$$\overline{T}_p(t) = \frac{\int_0^{R_p} T_p(r,t) 4\pi r^2 dr}{4/3\pi R_p^3} = \frac{2T_{cntr}(t) + 3T_{surf}(t)}{5} \tag{2.171}$$

The conduction problem inside the droplet written in spherical coordinates reads:

$$\rho_p C_{p,p} \frac{\partial T_p}{\partial t} = \frac{\lambda_p}{r^2} \frac{\partial}{\partial r} \left(r^2 \frac{\partial T_p}{\partial r} \right) \tag{2.172}$$

Integrating between $r = 0$ and $r = R_p$ and using the boundary condition, it is shown that $\overline{T}_p$ satisfies the same equation as the uniform droplet temperature in the infinite conductivity model.

$$\frac{d\overline{T}_p}{dt} = \frac{6Nu\lambda_m}{\rho_p C_{pp} D_p^2}(T_s - T_{surf}) + \frac{\dot{m}_p}{m_p C_{pp}} L_v(T_{surf}) = \frac{6Nu\lambda_m}{\rho_p C_{pp} D_p^2}(T_s - T_{surf}) + \frac{dT}{dt}\bigg|_{evap} \tag{2.173}$$

This eventually results in the following partial differential equation for $\overline{T}_p$:

$$\frac{d\overline{T}_p}{dt} = \frac{1}{1+0.2\zeta}\left[\frac{6Nu\lambda_m}{\rho_p C_{pp} D_p^2}(T_s - \overline{T}_p) + \left.\frac{dT}{dt}\right|_{evap}\right] \tag{2.174}$$

with

$$\zeta = \frac{Nu}{2}\frac{\lambda_m}{\lambda_p} \tag{2.175}$$

which becomes 0 for the infinite conductivity model.

This equation looks like the equation for the droplet temperature in the infinite conductivity model, but multiplied with a factor which is smaller than 1. The volume averaged temperature $\overline{T}_p$ in the parabolic model, will thus change more slowly than the uniform droplet temperature in the infinite conductivity model. Note that this model is actually the conduction limit model but with the assumption of a parabolic temperature profile.

Effective droplet conductivity

A third possible model is the effective conductivity model [80], which takes into account the effect of the internal circulation in the droplet on the heat transfer without calculating the flow inside the droplet. In terms of predicted evaporation rate, the effective conductivity model lies somewhere in between the finite and infinite conductivity model. To test the influence of the temperature profiles inside the droplet the more extreme models, i.e. the finite and infinite conductivity model, are used and therefore the effective conductivity model was not used in this PhD research.

2.2.9 Models for heat and mass transfer in the gas phase

The evaporation of a droplet in a non-saturated gaseous environment is a problem where mass and heat transfer are coupled. This is different from boiling of a liquid in a pure component environment. The vapor composition Y_{surf} and temperature T_{surf} at the droplet surface are thus determined by the coupling of the heat and the mass transfer. In the calculations, this means that the expression for evaporation rate based on the heat transfer should be equal to the expression based on the mass transfer. The vapor composition at the droplet surface Y_{surf} is assumed to be equal to the

saturated vapor mass fraction which can be calculated with the Clausius-Clapeyron equation:

$$X_{sat} = \frac{p_{sat}}{p_{atm}} = exp\left[\frac{L_v(T_{sat})}{R/W_{vap}}\left(\frac{1}{T_{boil}} - \frac{1}{T_{sat}}\right)\right] \tag{2.176}$$

The saturated vapor mass fraction Y_{sat} is then:

$$Y_{sat} = Y_{vap}^{sat} = X_{vap}^{sat}\frac{W_{vap}}{\overline{W}} \text{ with } \overline{W} = \sum_{\alpha} X_{\alpha}^{sat} W_{\alpha} \tag{2.177}$$

In a non-reacting case, there is only air and vapor so the mean molar weight at the surface is:

$$\overline{W} = X_{vap}^{sat} W_{vap} + X_{air}^{sat} W_{air} = X_{vap}^{sat} W_{vap} + (1 - X_{vap}^{sat}) W_{air} \tag{2.178}$$

In the reacting case however, combustion products might intrude the film close to the surface. Therefore, at a surface a mixture with non-vapor species in the same proportion as in the seen composition is proposed [63]:

$$\overline{W} = X_{vap}^{sat} W_{vap} + (1 - X_{vap}^{sat}) \sum_{\alpha \neq vap} X_{\alpha}^{*} W_{\alpha} \text{ with } X_{\alpha}^{*} = \frac{X_{\alpha}^{seen}}{1 - X_{vap}^{seen}} \tag{2.179}$$

The combination of the Clausius-Clapeyron equation and the fact that the expressions for the evaporation rate based on heat and mass transfer should be equal, determines Y_{surf} and T_{surf}. The effect of the boiling temperature T_{boil} comes in through the Clausius-Clapeyron relation. If $T_{surf} = T_{sat}$ comes close to the boiling temperature, $Y_{surf} = Y_{sat}$ will come close to 1 and the Spalding mass transfer number B_M will go towards infinity. The evaporation rate will then be determined by the heat transfer to the droplet and the corresponding Spalding heat transfer number. B_T.

D^2 law

The simplest evaporation model is the D^2 law, which assumes a uniform droplet temperature and does not take into account effect of evaporation on the heat transfer and diffusion close to the droplet.

$$\dot{m}_p = \pi D_p \rho_m \Gamma_m Sh_0 ln(1 + B_M) \tag{2.180}$$

or in its better known form:

$$\dot{m}_p = \frac{\pi}{4} D_p \rho_p \frac{d(D_p^2)}{dt} \tag{2.181}$$

Abramzon and Sirignano model

The Abramzon and Sirignano model assumes there is a gas film around the droplet which affects the heat and mass transfer. Gas phase heat and mass transfer are assumed to be quasi steady. The film theory is used to take into account the effect of the movement of the droplet (relative to the gas) on the heat and mass transfer. This is done by assuming that there is a film with a constant thickness around the droplet. However this film becomes thicker due to the flow of evaporated vapor coming out of the droplet, i.e. the Stefan flow, and this will be accounted for through a correction factor F. The evaporation rate based on the mass diffusion of the vapor expressed by the mass transfer number is:

$$\dot{m}_p = \pi D_p \rho_m \Gamma_m Sh B_M = \pi D_p \rho_m \Gamma_m Sh^* ln(1 + B_M) \tag{2.182}$$

with Sh the actual Sherwood number

$$Sh = Sh^* \frac{ln(1 + B_M)}{B_M} \tag{2.183}$$

and Sh^* the modified Sherwood number

$$Sh^* = 2 + \frac{Sh_0 - 2}{F_M} \tag{2.184}$$

with the Ranz-Marshall correlation for Sh_0:

$$Sh_0 = 2 + 0.552 Re^{1/2} Sc^{1/3} \tag{2.185}$$

The correction factor F_M is used in order to take into the effect of the Stefan flow on the mass transfer of the droplet:

$$F_M = (1 + B_M)^{0.7} \frac{ln(1 + B_M)}{B_M} \tag{2.186}$$

On the other hand the evaporation rate based on the heat transfer reads:

$$\dot{m}_p = \pi D_p \frac{\lambda_g}{C_{p,m}} Nu B_T = \pi D_p \rho_m \frac{\lambda_g}{C_{p,m}} Nu^* ln(1+B_T) \tag{2.187}$$

with Nu the actual Nusselt number

$$Nu = Nu^* \frac{ln(1+B_T)}{B_T} \tag{2.188}$$

and Nu^* the modified Nusselt number

$$Nu^* = 2 + \frac{Nu_0 - 2}{F_T} \tag{2.189}$$

with the Ranz-Marshall correlation for Nu_0:

$$Nu_0 = 2 + 0.552 Re^{1/2} Pr^{1/3} \tag{2.190}$$

The correction factor F_T is used in order to take into the effect of the Stefan flow on the heat transfer around the droplet

$$F_T = (1+B_T)^{0.7} \frac{ln(1+B_T)}{B_T} \tag{2.191}$$

B_T, Nu^* and F_T are then obtained iteratively from:

$$B_T = (1+B_M)^{\phi} - 1 \tag{2.192}$$

with

$$\phi = \left(\frac{C_{pp}}{C_{pg}}\right)\left(\frac{Sh^*}{Nu^*}\right)\frac{1}{Le} = \frac{\rho_m \Gamma_m Sh^*}{(\lambda_m / C_{p,m} Nu^*)} = \frac{ln(1+B_M)}{ln(1+B_T)} \tag{2.193}$$

The resulting algorithm then goes as follows [80]:

1. It is assumed that T_{surf}, T_s, Y_s and U_s are known.
2. Y_{surf} is calculated with Clausius-Clapeyron as a function of T_{surf}.
3. all the average gas film properties are calculated based on the 1/3-rule.
4. Re, Pr and Sc are calculated.
5. Nu_0 and Sh_0 are calculated.

6. B_M, F_M and Sh^* are calculated.
7. $\dot{m}_p$ is calculated with the expression based on the mass transfer number.
8. assume $B_T = B_M$.
9. F_T is calculated .
10. Nu^* is calculated.
11. ϕ is calculated.
12. Corrected value of B_T is calculated with ϕ.
13. return to step 9 to recalculate F_T based on new value of B_T.
14. iterate until new value of B_T is close to the value from the previous iteration.
15. With this final value of B_T, the final value of F_T can be calculated.
16. Finally Nu^* can be calculated from Nu_0 and F_T.

With Nu^* the heat transfer to the droplet due to convection $\dot{q}_{conv}$ can be calculated. As the heat consumed by the evaporation $\dot{q}_{evap} = \dot{m}_p L_v$ is also known, the heat penetrating into the droplet $\dot{q}_{drop}$ can also be calculated.

Concluding, the main difference between the D^2-law and the Abramzon-Sirignano model is that the latter takes into account the effect of the Stefan flow on Nu and Sh.

Evaluation of properties inside the gas film

As discussed before, the flow around the droplets is not resolved in the hybrid RANS-PDF calculations, resulting in the need to model drag, heat transfer and mass transfer in the neighborhood of the droplet. In these models, the gas properties have to be evaluated.

The gas properties are evaluated according to the 1/3-rule [81], i.e the properties are evaluated at:

$$T_m = T_p + \frac{1}{3}(T_s - T_p) \text{ and } Y_m = Y_{surf} + \frac{1}{3}(Y_s - Y_{surf}) \tag{2.194}$$

In [82] it is recommended to use the 1/3-rule to evaluate μ_g, λ_g and C_{pg}. However to calculate Re_p, ρ_g should be evaluated at the seen properties (Y_s,T_s)

It should be noted that this choice for evaluating the properties has a strong influence on the results and is somewhat arbitrary. This rule has been investigated in [83] with a DNS study and the best results were obtained when the evaluated properties were close to the properties of the saturated gas at the droplet surface. It is therefore suggested to use the properties from inside the thin gas film around the droplet.

Also the choice of the seen properties in the model is not that straightforward. The seen properties are representative for the environment of the droplet. However, there is no clear definition f this 'environment'. The evaporation model is based on the idealised situation of quasi steady evaporation of single droplet in a homogeneous environment with a certain T_s and Y_s. The seen properties are then described as the properties at infinity. However it is not straightforward to translate this situation to a turbulent flow with multiple droplets. We will discuss the different options for the modeling of the seen properties in the next section.

2.2.10 Influence of gas phase modeling

In this PhD a hybrid RANS-PDF approach is used to describe the gas phase. This approach has a strong advantage over the standard RANS approach as the statistics of the flow are better known and therefore more information is available to model the unresolved flow and composition fields around the droplet.

Validity of the β-PDF assumption in sprays

As has been shown in [84, 85, 86, 87, 88], the β-PDF assumption for the mixture fraction PDF P_Z is not valid anymore in the case of evaporating droplets. In [84] a modified β-PDF is proposed but a transported PDF approach for the gas phase naturally takes into account the effect of evaporation on the mixture fraction PDF.

Modeling of seen composition vector

Now modeling of the seen composition vector is discussed. This seen composition vector consists of the temperature and the vapor mass fraction seen by the droplets.

The big advantage of using a PDF method to describe the gas phase is that there are more options for the modeling of the seen properties. In general, the full PDF of the scalars is known, and therefore more information is available for the modeling. Specifically for the Monte Carlo method, properties of computational gas particles can be used to model the seen properties.

In this PhD research three models have been used for the seen composition:

1. use of the interpolated mean cell value,
2. use of the properties of a randomly chosen gas particle in the same cell,
3. use of the properties of the gas particle which is in enthalpy space closest to saturation.

Model 3 is now discussed in more detail. This model has been recently developed and implemented into the PDFD code by B. Naud [63]. The idea behind this model is that the gas particles which are close to saturation in enthalpy space, should in physical space be close to the droplet surface. So these gas particles can then be thought of as being situated just outside the gas film around the droplet. This is somewhat similar to what was suggested in [83] as taking the seen properties from inside the "shell" around the droplet. This model would then also seem to be consistent with the vapor distribution model distributing the vapor to the most saturated gas particles. Another advantage of this model is that it makes the assumption of the 1/3-rule less important, as the difference between the properties at the surface of the droplet and the seen properties is reduced in this model.

Distribution of evaporated fuel

Evaporated vapor from all the computational droplets in a cell is combined into one average mass source term for the cell which is then distributed over the computational gas particles. The vapor distribution model then distributes this source term over the computational gas particles. The vapor distribution models used in this PhD research are:

1. the 'uniform distribution' model: the vapor is homogeneously distributed over the entire cell or over all the computational gas particles in that cell,

2. the 'feed the saturation peak' model: the computational gas particles are fed with vapor based on their level of saturation, with the most saturated gas particles first.

The 'uniform distribution' model is the equivalent of what is done in a standard RANS equation where there is just a transport equation for the mean and the variance of the vapor mass fraction and the evaporation results in source terms in both equations, without the change of the presumed PDF.

The 'feed the saturation peak' model is based on the observation that evaporation results in the appearance of a peak at saturated conditions in the gas phase composition PDF [89, 90]. The 'feed the saturation peak' model distributes the vapor evaporated from the droplets of a given size class among the 'most saturated' gas phase particles, where the saturated condition is evaluated given the mean surface temperature of the given droplet size class $\overline{T}_{surf,class}$ The algorithm connected to this model has been implemented by B. Naud and is described in detail in [46]. However, unlike in [46] the model is now implemented in an iteration average sense [63]:

1. Given a sample of the dispersed phase PDF, and given the mean surface temperature of its size class, $\overline{T}_{surf,class}$, it is tried to give the evaporated mass $\omega_{vap,class}.dt$ to each of the 'surrounding' gas-phase particles:
   (a) Each gas-phase particle has a new possible enthalpy h^* and a new vapor mass fraction Y^* (after it receives the mass $\omega_{vap,class}.dt$).
   (b) The saturated vapor mass fraction Y_{sat} and enthalpy h_{sat} are evaluated at $\overline{T}_{surf,class}$ for an inert mixture of vapor and air (the enthalpy of pure vapor h_{vap} is also evaluated at $\overline{T}_{surf,class}$).
   (c) If $h^* > h_{sat}$ and $Y^* < Y_{sat}$, then the gas-phase particle is not super-saturated and is a candidate for receiving the amount of vapor $\omega_{vap,class}.dt$.
2. All possible candidates for receiving the vapor are sorted from the 'least saturated' to the 'most saturated', based on $\delta = (h^* - h_{sat})(h^* - h_{vap})$, such that the lowest value of δ corresponds to the 'most saturated' surrounding gas-phase particle.
3. The evaporated mass $\omega_{vap,class}.dt$ is given to the 'most saturated' surrounding gas-phase particle. When all the computational gas particles in the cell are saturated the rest of the vapor that needs to be distributed in that time step is then distribute uniformly over all the computational gas particles in that cell.

Note that in the reacting case Y_{sat} and h_{sat} are calculated for the inert mixture. It should also be noted that, while this has not been proven theoretically, it seems logical to do the modeling of the seen properties consistent with the modeling of the distribution of the vapor, as the seen properties are used as representatives of the environment of the droplet in the modeling of the heat and mass transfer. Therefore the modeling seems to be more consistent when the evaporated fuel is then also distributed to the computational gas particles whose properties were used as seen properties for the modeling. So in this reasoning the combination of the feed the peak distribution model and the seen gas particles closest to saturation seems to be the most consistent.

Mixing in spray calculations

The mixing in evaporating sprays needs to be divided into two parts: the mixing from the droplet surface to the nearby environment of the droplet and the micro-mixing outside the immediate neighborhood of the droplet. The latter is obviously handled by the micro-mixing model as was the case for single phase flows.

Mixing close to the droplet surface The mixing from the droplet surface to the environment of the droplet is not explicitly modeled in this PhD research. For example when the evaporated fuel is distributed uniformly over the gas particles, this mixing in the immediate neighborhood of the droplet is not modeled as a lot of gas particles which are far away from saturation (and in physical thus far away from the droplet surface) instantly receive evaporated fuel. The mixing in the nearby environment of the droplet is thus somewhat skipped. With the vapor distribution model, distributing vapor to the most saturated gas particles, on the other hand, particles which are expected to be close the droplet surface receive most of the vapor. The subsequent mixing with the less saturated gas particles is then handled by the micro-mixing model. It is thus expected that the latter distribution model will perform better in the calculations, as a larger part of the diffusion is modeled. However, the diffusion from the droplet surface to these most saturated particles, receiving the vapor from the vapor distribution model is not modeled. It is not completely clear how important this part of the mixing is, as it is not clear how close the most saturated gas particles are to the completely saturated state at the droplet surface. Durand et al. [89] accounted for this mixing close to the droplet (from the droplet surface to one Kolmogorov scale away from the droplet) explicitly with a quasi laminar model, which

results in a distribution which is inversely proportional with the vapor mass fraction. This distribution is then used to assign properties to newly injected computational gas particles which together represent the total evaporation mass source term in the cell. For a more detailed discussion the reader is referred to literature [91, 92]

Micro-mixing In most spray calculations, the micro-mixing models which were developed for single phase flow are used. However, the presence of the droplets can modify the turbulence of the gas phase leading to a different mixing time scale. This can be accounted for in the model for the mixing time scale without the necessity to adjust the original single phase micro-mixing model. However, this has not been done within the this PhD research. Mixing models are expected to have an influence on the global evaporation rate as they determine the evolution of the shape of the composition PDF. This will affect the properties seen by the droplets and therefore also the evaporation rate of the droplet.

LES vs RANS

In this PhD research, only RANS calculations have been performed, so it is important to highlight the influence of this choice on the modeling. With RANS we only capture the mean flow features and large scale unsteadiness is not captured. With LES calculations, the large scale coherent structures are resolved and the effect of eddies on the droplet dynamics is better captured. More specifically, phenomena which depend on the dynamics of eddies, such as preferential segregation of droplets [87], cannot be captured with a RANS technique. This will affect the prediction of the droplet dispersion. This is a rather serious disadvantage of RANS as the droplet dispersion has a strong impact on the local evaporation rate of the droplets and therefore also on the global fuel vapor field. On top of this, RANS does not provide detailed information about the scalar dissipation rate and its fluctuations. This will be mainly important in the predictions of the spray flames, where finite chemistry effects might occur due to locally high scalar dissipation rates. This was already discussed for the single phase flames.

2.2.11 Turbulent spray combustion regimes

In spray flames different flame structures than the ones for gas flames are observed in physical space. In [93] a group combustion model is discussed where flame structures vary from single droplet combustion to an external flame around the spray depending on the concentration of the droplets. In [94] a more detailed study is done based on 2D DNS and new complex flame structures are observed. However, some of the features seem to be strongly dependent on the dynamics of the large scale eddies so we should not expect to capture these features as we do not capture the dynamics of the large scale eddies. In general, flame structures in spray flames seem to be a combination of all the flame structures observed in gas flames: non-premixed, premixed and partially premixed combustion. In [95], combustion modeling of spray flames with a flamelet based manifold is discussed and the best results were obtained with mixture fraction and enthalpy as independent parameters.

2.3 Conclusions

In the first part of this chapter the framework for hybrid RANS-PDF calculations of reactive gas flows has been discussed extensively. First the exact flow equations and the RANS equations have been discussed and the basics of combustion have been mentioned. Next, the turbulent models have been described and the problem of the closure of the mean reaction term has been highlighted. Subsequently, the different combustion models have been discussed in relationship with REDIM. Finally, the PDF description of the gas phase has been introduced and a consistent hybrid RANS-PDF framework has been described

In the second part of this chapter the framework for hybrid RANS gas-PDF droplet-PDF calculations of spray flames has been discussed. First the basics of multi-phase flows have been introduced. Then the transported PDF method for sprays has been discussed, together with the modeling of droplet dynamics, evaporation, heat transfer and the unresolved gas field around the droplet. Finally, spray combustion has been briefly discussed.

Chapter 3

A priori investigation of PDF-modeling assumptions

3.1 Introduction

In turbulent non-premixed combustion modeling, turbulence-chemistry interaction is a key issue. The introduction of the PDF (probability density function) of mixture fraction Z is useful to model the effect of turbulence on chemistry. In order to account for finite rate chemistry effects using a reduced description (FGM [26], FPI [27], REDIM [39] and ADF-PCM$_\chi$ [96]), a second scalar representing the progress of the reaction is typically introduced: a 'progress variable' c [97, 33] or a 'reaction progress parameter' λ [98]. Unless a transported PDF approach [66] is adopted, assumptions must be made on the shape of the PDF and on statistical (in)dependence of Z and c or Z and λ. Many similar studies on commonly used assumptions in presumed PDF modeling in a RANS context have been performed in the past [99, 98, 38]. Here, we study some of these assumptions for the joint Z-c and Z-λ PDF in the specific case of the swirling non-premixed methane/air bluff-body flame 'SM1' [100, 101, 102, 103, 104], by directly analyzing the experimental scatter data, made freely available on the internet [105]. The observations are in general also valid for e.g. flame 'SM2', for which more scatter (due to local extinction) has been observed experimentally [100, 101, 102, 103, 104].

This study sheds new light onto some of the previously made conclusions on presumed PDF modeling. It is mainly focused on a RANS modeling framework, but some implications for LES modeling are also discussed. The main difference com-

pared to previous studies is the presence of recirculation of combustion products (see the sketch of the swirling flame in Figure 3.1). The resulting mixing line in (Z, c) or (Z, λ) space is different from typical non-premixed flame structures, and is similar to a case of multiple stream mixing [106]. We show below that this mixing line renders some of the often made assumptions invalid. More specifically, Z and c or Z and λ are not independent for this case, and $\overline{c|Z} \neq \overline{c}$ or $\overline{\lambda|Z} \neq \overline{\lambda}$.

Moreover, we recall that in presumed PDF modeling, it is necessary to solve the transport equation for the mean value of the progress variable or parameter, $\overline{c}$ or $\overline{\lambda}$, (and possibly the variance) which is usually avoided, due to the extra modeling complications compared to standard reacting scalars.

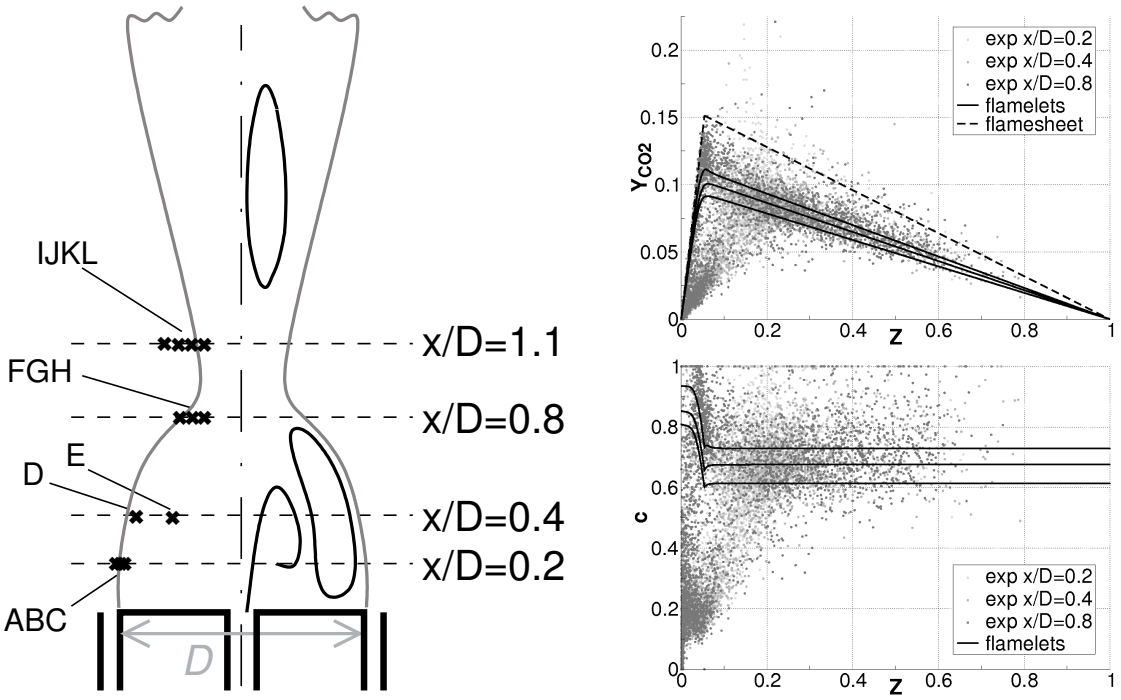

Figure 3.1: Sketch of the Sydney swirling flame SM1, and locations where experimental data is analyzed (crosses with labels 'A'-'L'). Right: experimental scatters plots (dots), non-premixed flamelets (solid lines) and the flamesheet used for normalization (dashed line). $D = 50mm$ is the bluff-body diameter and x the distance from the burner.

3.2 Progress variable definitions

The progress variable is defined in many different ways and possible definitions may be in terms of a reduced temperature [98] or a linear combination of species mass fractions [97, 33, 99, 5, 107]. In this study, we will refer to the latter with the symbol Y_c and we choose $Y_c = Y_{CO_2}$. The definition $Y_c = Y_{CO_2} + Y_{CO}$ is often used [34, 99], because it leads to a better monotonicity of temperature and species in regions where CO_2 decomposes into CO. For the study at hand, the choice $Y_c = Y_{CO_2}$ leads to very similar observations and conclusions as $Y_c = Y_{CO_2} + Y_{CO}$. Such a definition for the progress variable generally implies two problems in the context of presumed PDF modeling, since both commonly made (and detailed in the next section) assumptions cannot be satisfied: (i) statistical independence between Y_c and Z, and (ii) approximation of the marginal PDF of Y_c using a β-function. In order to use (ii), the progress variable needs to have the same possible minimum and maximum values everywhere. This is the case for a normalized progress variable taking its values between 0 and 1 [108]. Normalization of Y_c can also help to better satisfy (i) [99, 38].

Following this idea, a second definition of progress variable c is Y_c normalized with a value depending on Z. In this study, we normalize with the corresponding flame sheet (Burke-Schumann model) value $Y^{(\mathrm{fs})}_{CO_2}(Z)$ with $Y^{(\mathrm{fs})}_{CO_2}(Z_{\mathrm{st}}) = 0.1513$ at $Z_{\mathrm{st}} = 0.054$:

$$c(Z, Y_c) \equiv Y_c / Y_c^{(\mathrm{fs})}(Z) = Y_{CO_2} / Y^{(\mathrm{fs})}_{CO_2}(Z). \tag{3.1}$$

This is similar to the definitions used in [108, 99, 38] where equilibrium values are involved in the normalizations. In Figure 3.1 we see that the normalization leads to essentially constant c-values for non-premixed flamelets[1] (since the corresponding Y_{CO_2} profiles have shapes similar to the flame sheet), except around stoichiometry where c and Z have a non-linear relationship. Note that some measured Y_{CO_2} values are higher than the flame sheet. In the normalization procedure, the value of c for these points is clipped to 1. Compared to these first two traditional definitions of the progress variable, there are other methods to describe reaction progress. For example, in [98], the 'reaction progress parameter' λ is introduced. Each point in (Z, Y_c) or (Z, c) space belongs to a (stable or unstable) steady non-premixed flamelet. The reaction

[1] The steady non-premixed flamelets represented in Figure 3.1 were calculated in the axisymmetric opposed-flow configuration, with Warnatz mechanism [3], assuming unity Lewis number, for different strain rates ($a = 100, 320, 392 s^{-1}$).

progress parameter λ is then the value of the (traditional) progress variable Y_c at stoichiometry on that steady non-premixed flamelet:

$$\lambda(Z,Y_c) \equiv \left\{Y_c^{(\text{stoich})}\right\}_{\text{flamelet 'F'}} \quad \text{such that} \quad (Z,Y_c) \text{ is on flamelet 'F'.} \tag{3.2}$$

This parameter is constant along that flamelet and is thus statistically independent of Z as long as the flame structure corresponds to a steady non-premixed flamelet. In [109], another progress variable is defined based on the enthalpy of formation integrated over Z-space, making it statistically independent of Z.

Both definitions of the progress variable c and of the reaction progress parameter λ will be useful in order to satisfy (i) for presumed PDF modeling of flame SM1 if the composition in (Z,Y_{CO_2}) space mainly corresponds to steady turbulent non-premixed flamelets. We show in Section 3.5 that introducing such progress variables in a priori studies of the experimental data can help to identify steady non-pemixed flamelet structures.

3.3 Presumed PDF modeling assumptions

The probability density function (PDF) of Z at point $\boldsymbol{x}$ and time t, $P(Z;\boldsymbol{x},t)$, is often approximated by a β-distribution based on the mean mixture fraction $\widetilde{Z}(\boldsymbol{x},t)$ and mixture fraction variance $\widetilde{Z''^2}(\boldsymbol{x},t)$ [13] (assumption (ii) mentioned above). For the progress variable PDF, $P(c;\boldsymbol{x},t)$, and progress parameter PDF, $P(\lambda;\boldsymbol{x},t)$, different shapes have been used. Although recently the 'statistically most probable distribution' was introduced [5, 107], only δ- and β-functions, which are still most commonly applied, are tested here. Considering the joint PDF, statistical independence of the variables is usually assumed such that $P(Z,c) = P(Z).P(c)$ or $P(Z,\lambda) = P(Z).P(\lambda)$, assumption (i). When the variables are not statistically independent, the general definition of the joint PDF involves a conditional PDF instead of one of the marginal PDFs:

$$P(Z,c;\boldsymbol{x},t) = P(Z;\boldsymbol{x},t).P(c|Z;\boldsymbol{x},t). \tag{3.3}$$

Comparison of conditional PDFs for different values of Z thus indicates to what extent the assumption (i) of statistical independence is correct. In [98], based on a study of DNS data it is concluded that $P(\lambda|Z) \neq P(\lambda)$ for $Z < 0.2$ and $Z > 0.8$, due to unsteady

transport phenomena during extinction and re-ignition. In [99], the experimental data of a piloted jet flame (SANDIA D) [110, 111, 112] is studied and based on the results it is assumed that $P(c|Z) = P(c)$. However in [38], Michel *et al.* conclude based on a study of the experimental data of a lifted flame (Cabra) [113, 114] that $P(c|Z) \neq P(c)$, suggesting that the validity of the assumption of independence varies for different types of flames.

The dependence on the position in physical space is explicitly included in Eq. (3.3). In a turbulent flame, experimental scatter data and the corresponding PDFs strongly depend on the position, as will be shown below. They also may depend on the resolution of the measurement: the larger the measurement volume, the larger the spreading in mixture fraction and/or progress variable. For flame SM1, the spatial resolution of the composition measurements is 0.75mm [102]. Note that for LES modeling of this flame the mesh size could be smaller at some locations, such that statistics should be collected in time on several cells in order to compare to experimental data. On the other hand, and more importantly, we should keep in mind that 'instantaneous LES solutions' imply in principle less fluctuations to be modeled on the sub-grid level, since by definition part of the large scale fluctuations is resolved. Therefore, the sub-grid PDFs of an LES solution are expected to be more narrow than the PDF of a RANS solution.

Added modeling issues with c and λ As mentioned above, definitions of normalized progress variables or reaction progress parameters are useful in order to satisfy (i) and (ii) in the context of presumed PDF modeling. In this case, at some point the modeling of the mean or filtered value, and possibly the variance, of c or λ will be required. However, the transport equations for the mean or filtered progress variable/reaction progress parameter and the variance contain non-negligible terms which are harder to model than the corresponding terms in the standard transport equations for Y_c [115, 107].

In [99, 38], in the context of RANS, an assumption is formulated for the mean progress variable (i.e. the first moment of the PDF): $\overline{c|Z} = \overline{c}$, which is less stringent than the assumption of complete statistical independence, $P(c|Z) = P(c)$. Solving the transport equation for the mean progress variable $\overline{c}$ is avoided. Instead, the transport equation for the mean non-normalized progress variable $\widetilde{Y}_c$ is solved and the mean normalized progress variable is evaluated afterwards as $\overline{c} = \widetilde{Y}_c / \widetilde{Y_c^{eq}}$, with $Y_c = Y_{CO_2} + Y_{CO}$ and $\widetilde{Y_c^{eq}}$ obtained from $Y_c^{eq}(Z)$ and $P(Z)$. In [109], on the other

hand, the transport equation for the mean normalized progress variable (based on enthalpy) is solved, but the terms related to χ_{cc} and χ_{cZ} are neglected. However, for most definitions of progress variable these terms are of the same order as the reaction term so they cannot be neglected [115]. In [107], in the context of LES, Ihme *et al.* avoid solving the transport equation for λ by assuming a 'statistically most likely distribution' for $P(\lambda)$.

3.4 Comparison of experimental and modeled marginal PDFs

Figures 3.2 and 3.3 show the marginal PDFs of Z, c and λ as retrieved from the experimental data, at two axial locations, $x/D = 0.2$ (points A, B, C in Figure 3.1) and $x/D = 1.1$ (points I, J, K, L in Figure 3.1), at radial locations in the shear zone, where mixing is the strongest and the largest differences are expected (r is the distance from the symmetry axis and $R = D/2$). In order to have a sufficient amount of samples in each bin, the experimental data has been divided for each scalar (Z, c or λ) into 25 equally sized bins. Dependence of the results on the bin size has been checked by comparing with results where bins have only half the size and the same general trends have been observed. Note that the experimental PDFs of c and λ include non-zero values respectively at $c = 1$ and $\lambda = 1$, corresponding to the clipping of experimental measurements above the flame sheet in (Z, Y_c) space. In Figure 3.2 ($x/D = 0.2$), we study the shear zone where recirculated combustion products of a first recirculation zone behind the bluff body mix with air from the swirling annulus. In Figure 3.3 ($x/D = 1.1$), we study the shear zone behind this recirculation zone where a rich mixture coming from the fuel jet mixes with lean combustion products coming from the swirling annulus. The corresponding β-PDFs, with the same values for mean and variance, are also shown. To simplify the comparison, λ is normalized with $\lambda_{max} = Y_{CO_2}^{max}(Z_{stoich}) = 0.1513$. The vertical line at the mean value represents the δ-PDF.

In general, the δ-PDF assumption is clearly insufficient to model the marginal Z, c and λ PDFs, corresponding to the resolution of the measurements representative of a RANS context. The β-PDF, on the other hand, is a good approximation for Z. It should be noted, though, that in the context of LES, the β-PDF assumption for Z seems less valid, as is discussed by Floyd et al.[106]. For c and λ, however, strong

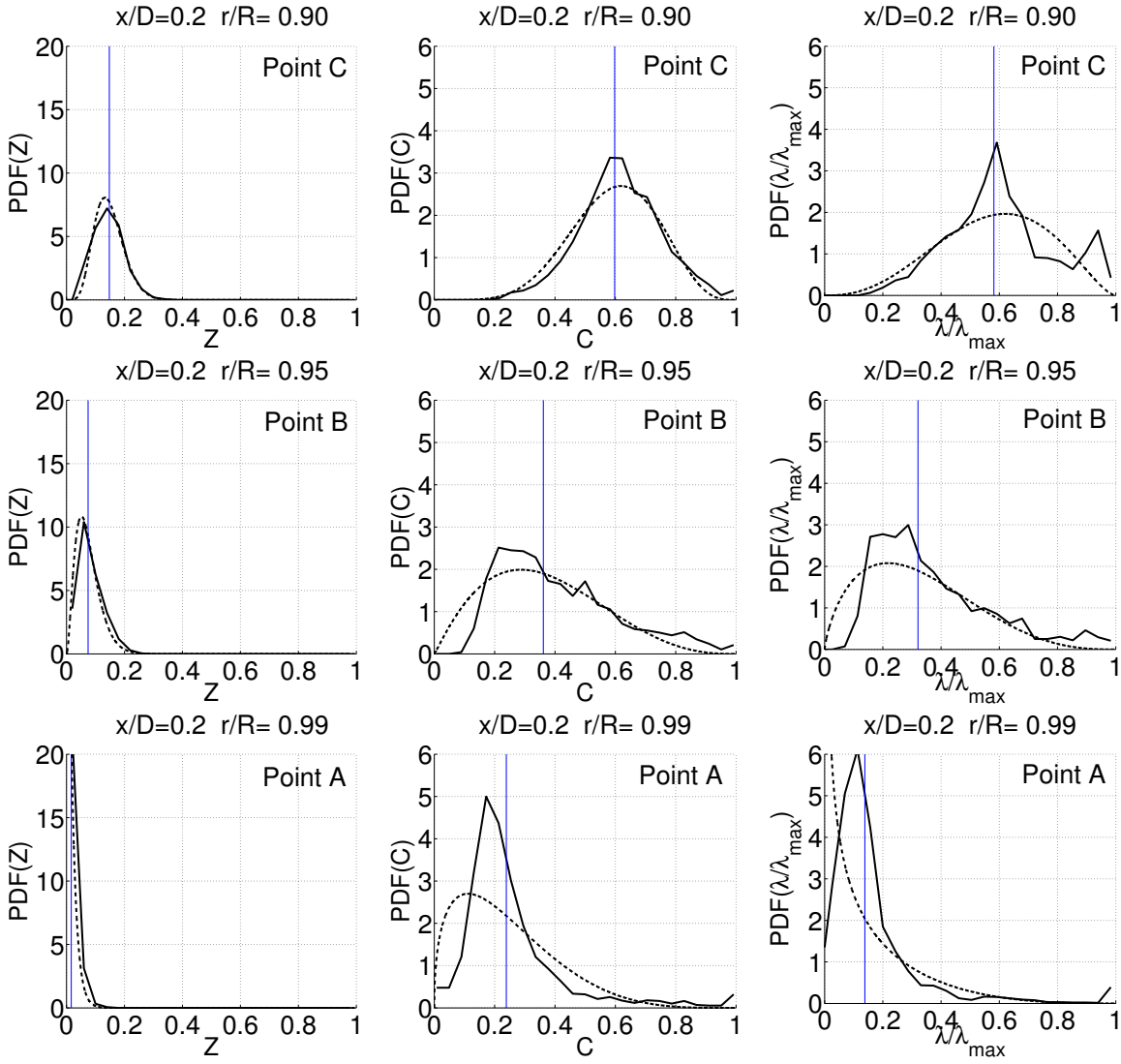

Figure 3.2: Experimental PDF (full line) and corresponding β-PDF (dashed line) at $x/D = 0.2$ [points C ($r/R = 0.90$), B ($r/R = 0.95$) and A ($r/R = 0.99$)] for Z (left), c (middle) and λ (right). The vertical line indicates the mean value (δ-PDF).

deviations are observed at some locations, suggesting that the β-PDF assumption is not generally applicable for these variables. This is in line with [5]: higher order statistical information is needed to represent complex PDFs (highly skewed or bimodal PDFs).

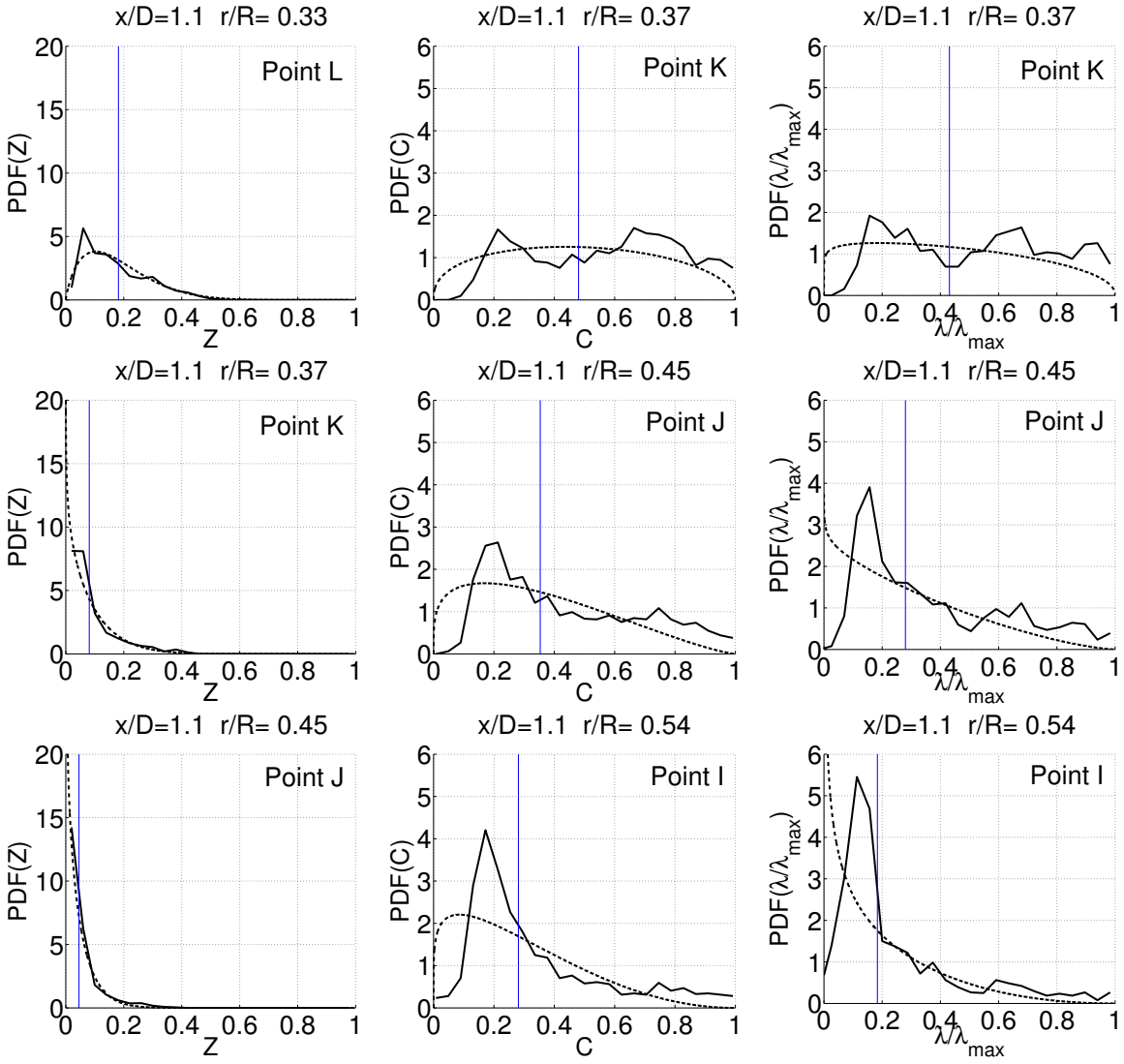

Figure 3.3: Experimental PDF (full line) and corresponding β-PDF (dashed line) at $x/D = 1.1$ [points L ($r/R = 0.33$), K ($r/R = 0.37$), J ($r/R = 0.45$) and I ($r/R = 0.54$)] for Z (left), c (middle) and λ (right). The vertical line indicates the mean value (δ-PDF).

3.5 Statistical (in)dependence and flame structures

Comparison of conditional PDFs At a given location, if Z and c (or Z and λ) are independent, the conditional PDF $P(c|Z)$ (or $P(\lambda|Z)$) becomes identical to the marginal PDF $P(c)$ (or $P(\lambda)$), for all Z-values. Figure 3.4 shows the conditional PDFs $P(Y_{CO_2}|Z)$, $P(c|Z)$ and $P(\lambda|Z)$ at two points in the first recirculation zone ($x/D = 0.4$) — in the shear zone where recirculated combustion products mix with air from the swirling annulus (point D) and in the inner recirculation zone (point E)

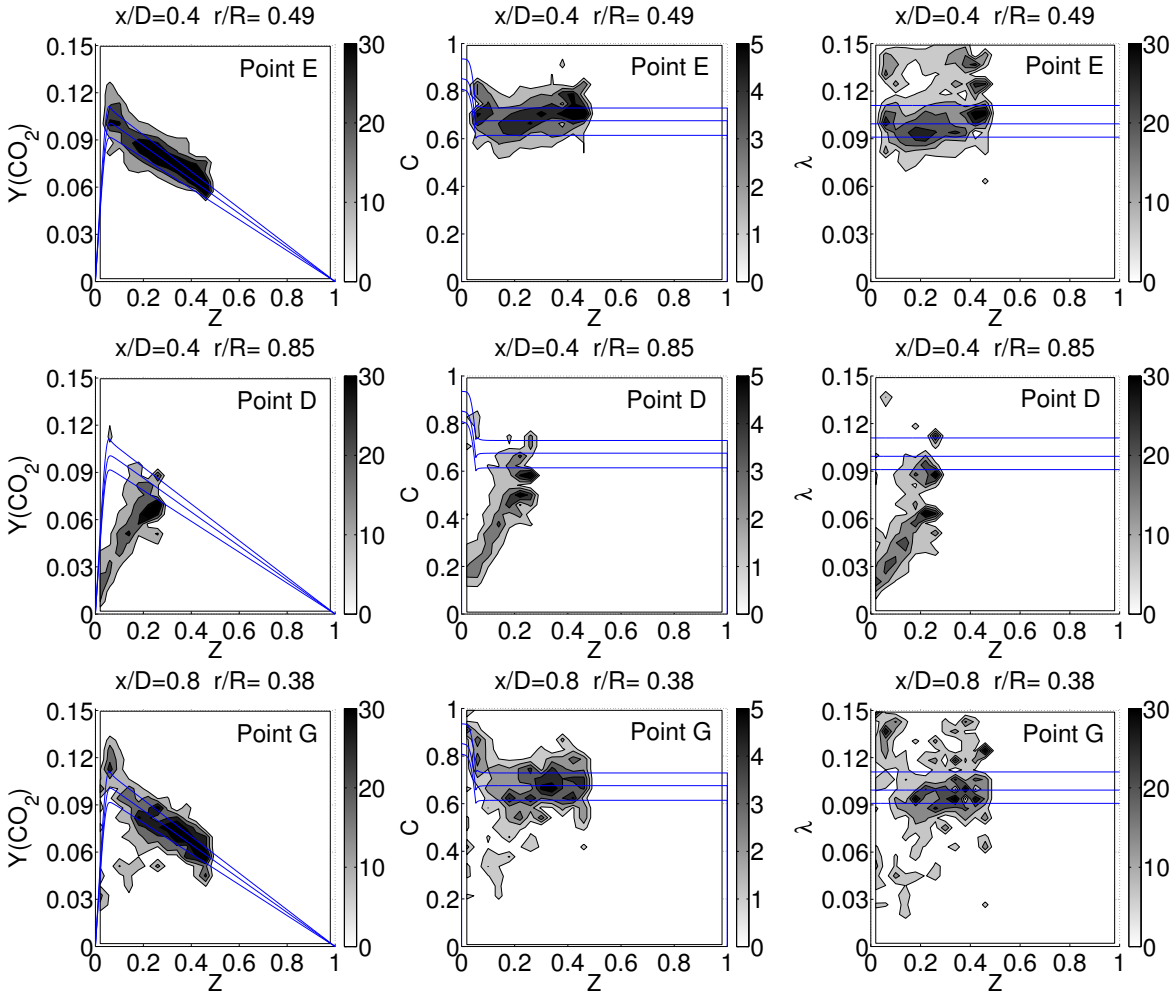

Figure 3.4: Conditional Y_{CO_2}-, c- and λ-PDF at $x/D = 0.4$ [points E ($r/R = 0.49$) and D ($r/R = 0.85$)] and $x/D = 0.8$ [point G ($r/R = 0.38$)]. Probability indicated with gray scale ranging from white (zero probability) to black (highest probability) solid lines correspond to steady non-premixed flamelets.

— and at point G at the tip of the first recirculation zone ($x/D = 0.8$). Different structures in composition space are observed which can also help to decide a priori on which laminar flamelet structure (premixed or non-premixed) the reduced, pre-tabulated chemistry should be based for better modeling of a given turbulent flame. At $x/D = 0.4$, a rich flamelet branch predominantly characterized by the mixing between combustion products at stoichiometry and pure fuel is observed at point E ($r/R = 0.49$), while a mixing line representing mixing of fresh air with rich combustion products [116], caused by the recirculation of combustion products, is observed at point D ($r/R = 0.85$). At point G ($x/D = 0.8$), a rich flamelet branch with local

extinction is observed.

At point E (rich flamelet branch), we observe a large difference between the conditional PDFs of Y_{CO_2} and those of c or λ. The latter stay fairly constant as a function of Z, indicating that Z and c or Z and λ are more or less statistically independent, while this is clearly not the case for Z and Y_{CO_2}. At point D (mixing line), the three conditional PDFs are similar, all indicating a linear dependence between Z and the progress variable (Y_{CO_2}, c or λ). In this case, $\overline{c|Z} \neq \overline{c}$ and $\overline{\lambda|Z} \neq \overline{\lambda}$ as this mixing line differs too strongly from any steady non-premixed flamelet structure (horizontal line) or premixed flamelet structure (vertical line). Therefore none of the proposed definitions can ensure independence of Z with the progress variable. Note that in this case, Y_{CO_2}, c and λ do not really indicate the progress of reaction as it would in a reacting homogeneous mixture, but rather the mixing between fresh air and recirculated combustion products without any significant reaction (see also [116]). At point G, on the other hand, local extinction is observed in the experiments, reflected in the conditional PDFs in Figure 3.4 as areas of higher probability for lower values of the progress variable. For all the definitions of the progress variable these areas of local extinction only have a minor influence on the statistical independence with Z, as there is only a limited amount of local extinction at this location.

It is important to stress that the mechanism for the deviation from the flamelet structure is different for the mixing line at point D and local extinction at point G. The mixing line is caused by a general flow feature, i.e. the recirculation zone at the bluff body. This recirculation zone 'creates' a third stream [106] of rich combustion products, resulting in a mixing of air with rich combustion products. This leads to deviation from the flamelet structure, in a confined, line shaped structure in composition space, resulting in $\overline{c|Z} \neq \overline{c}$ and $\overline{\lambda|Z} \neq \overline{\lambda}$. Concerning local extinction, however, the combination of finite rate chemistry and high local scalar dissipation causes the deviation from the flamelet structure. 'Extinguished fluid' at lower reaction progress can mix with extinguished fluid or with burning fluid from the lean and rich branches of the flamelet structure. In other words, local extinction 'creates' new boundary conditions for the local mixing problem [112], resulting in more spreading in composition space with a less severe impact on the assumptions $\overline{c|Z} = \overline{c}$ and $\overline{\lambda|Z} = \overline{\lambda}$. This was also seen for the SANDIA D flame [99], which only has a small amount of local extinction. Concluding, the different mechanisms causing the mixing line and local extinction lead to a different validity of the assumptions $\overline{c|Z} = \overline{c}$ and $\overline{\lambda|Z} = \overline{\lambda}$ and therefore also differently influence the validity of the assumption of statistical independence. Note

that in LES, the mixing is mostly captured on the grid level by the transport equation for the filtered scalars (the sub-grid PDF covers a smaller area in composition PDF) and the assumption of independence should then be less critical.

Comparison of joint PDFs and mean reaction rate The above observations on the assumption of statistical independence are confirmed in Figures 3.5, 3.6 and 3.7 where the experimental joint PDFs are compared to the products of the experimental marginal PDFs at $x/D = 0.2$ and 0.8 (points B, F and H). In order to have a more quantitative comparison, the mean production rate of Y_{CO_2}, $\langle rCO_2 \rangle$, has also been calculated from a REDIM table [39] and the joint PDFs, with and without the assumption of independence. The REDIM table is a pre-calculated table describing rCO_2 as a function of Z and Y_{CO_2}. The $\langle rCO_2 \rangle$ values have been added in Figs. 3.5-3.7. Clearly, substantial differences are observed: the values are much higher when statistical independence is assumed. [Note that, for the different definitions of the progress variable, $\langle rCO_2 \rangle$ as calculated without the assumption of independence, (i.e. the numbers in the top rows in Figs. 3.5-3.7) should be the same. The small differences observed are due to discretisation errors.]

In Figure 3.5 (at point B), the mixing line structure is clearly visible for the experimental joint PDFs with the different progress variable definitions and it is not reproduced when statistical independence is assumed. This is also reflected in $\langle rCO_2 \rangle$, which is a factor $1.7 - 1.9$ larger with the assumption of independence, since the PDFs $P(Z).P(Y_{CO_2})$, $P(Z).P(c)$ and $P(Z).P(\lambda)$ cover larger area of high rCO_2 values. In Figure 3.6 (at point H), the experimental joint Z-Y_{CO_2} PDF differs substantially from the Z-c and Z-λ PDFs. As observed before, the rich flamelet branch structure appears as a rather horizontal line in the experimental Z-c and Z-λ PDFs. The assumption of statistical independence of Z and c or Z and λ is clearly more justified than for Z and Y_{CO_2}, and the PDFs $P(Z).P(c)$ and $P(Z).P(\lambda)$ indeed resemble the experimental joint Z-c and Z-λ PDFs. However, $\langle rCO_2 \rangle$ calculated with assumption of independence is a factor 3.5 larger with c as progress variable, the same as with Y_{CO_2}. For λ the results are slightly 'better' with only a factor 3 difference. The difference can be explained by the larger area covered in composition space by the joint PDFs with the assumption of independence, resulting in higher values of the PDF in the region where rCO_2 is large (around stoichiometry and at intermediate values of the progress variable), eventually leading to a higher mean $\langle rCO_2 \rangle$. In Figure 3.7 (at point F), a bimodal PDF is observed for all definitions of the progress variable. This

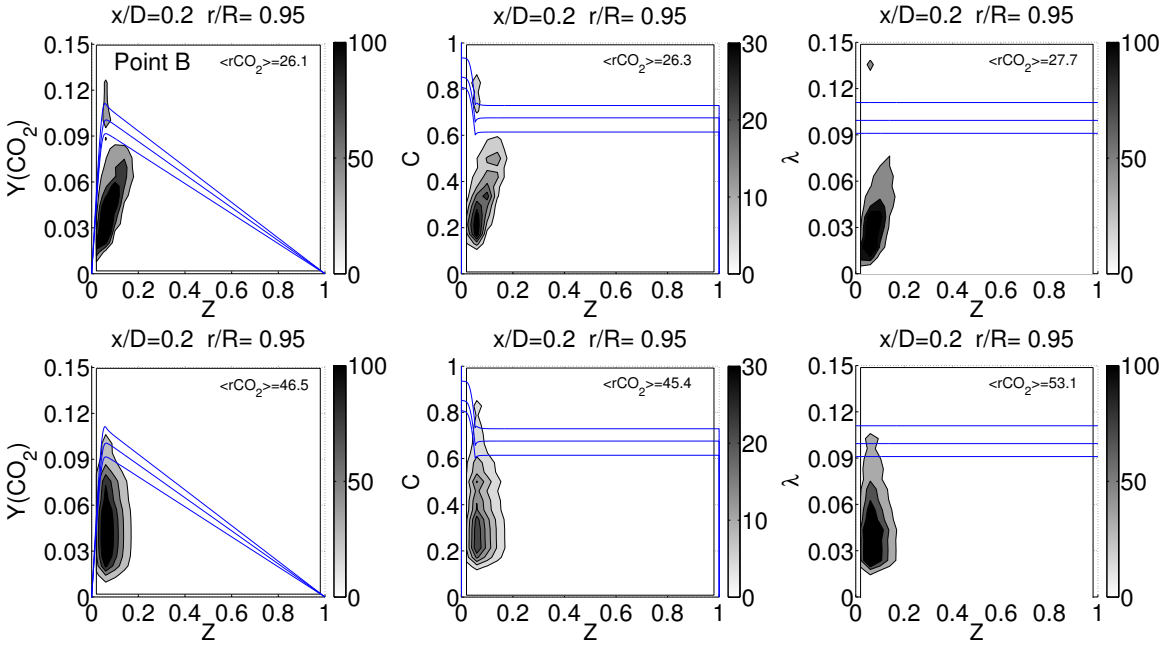

Figure 3.5: Joint PDFs at point B ($x/D = 0.2$ and $r/R = 0.95$) Top: experimental Z-Y_{CO_2}, Z-c and Z-λ joint PDFs. Bottom: products of the experimental marginal PDFs, $P(Z).P(Y_{CO_2})$, $P(Z).P(c)$ and $P(Z).P(\lambda)$. Probability indicated with gray scale ranging from white (zero probability) to black (highest probability.) $\langle rCO_2 \rangle$: corresponding mean production rate of Y_{CO_2}, calculated with REDIM table .

corresponds to a combination of mixing, reaction and local extinction. Apart from $P(Z).P(c)$ and $P(Z).P(\lambda)$ PDFs, now also the $P(Z).P(Y_{CO_2})$ is in good agreement with the experimental joint PDF, due to the narrow Z-PDF. This observations is very relevant for LES simulations: the potential error when assuming Z and c or Z and λ to be statistically independent becomes small when the filter size is such that the sub-grid fluctuations of mixture fraction are limited to a narrow range (see e.g. [117], where scatter plots of the resolved mixture fraction and Y_{CO_2} are similar to the experimental ones). At point F, the mean $\langle rCO_2 \rangle$ values calculated with the assumption of independence are a factor $1.4 - 1.8$ larger. This is again due to the joint PDFs with the assumption of independence being more spread out in the region where rCO_2 is large, but now the difference between the joint PDFs with and without the assumption of independence is smaller than at point H. Concluding, the influence of the assumption of independence on the mean properties is the strongest in the regions in compositions space where the properties have high values. Therefore, even when the assumption of independence seems valid based on the figures of the conditional

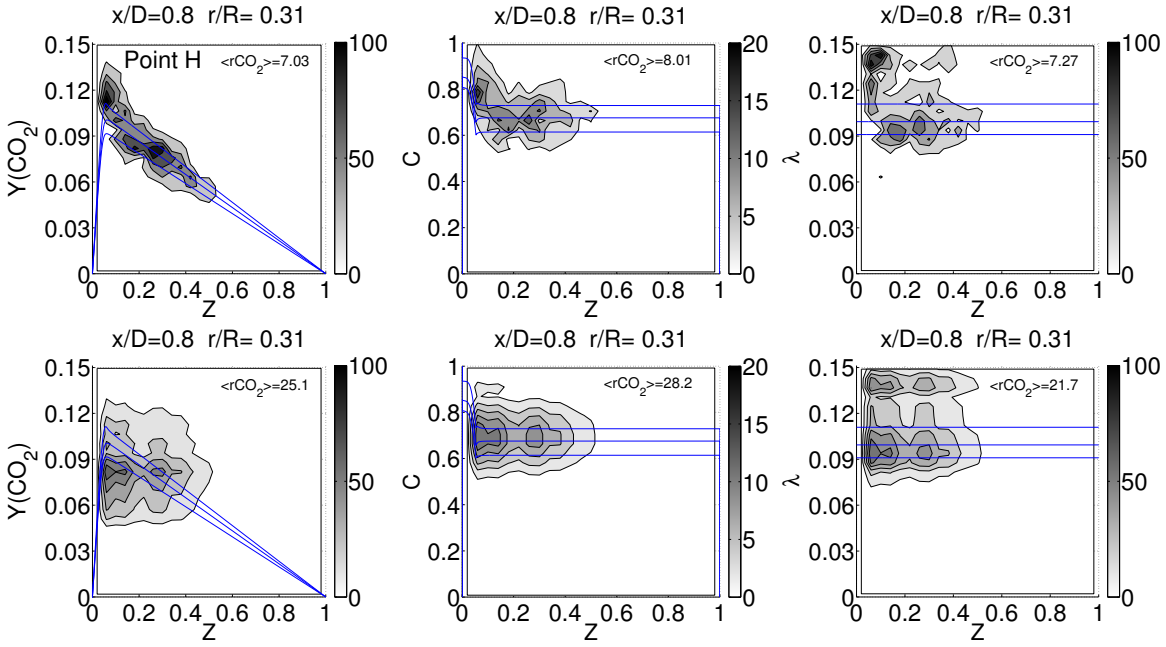

Figure 3.6: Joint PDFs at point H ($x/D = 0.8$ and $r/R = 0.31$). (legend: see Fig. 3.5)

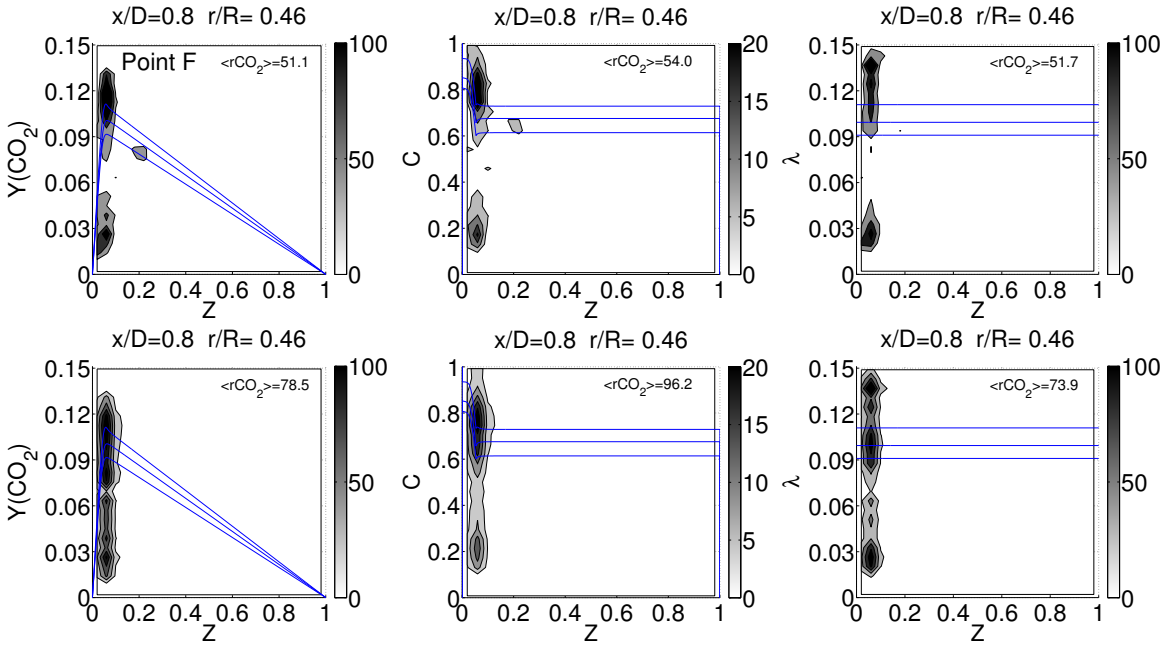

Figure 3.7: Joint PDFs at point F ($x/D = 0.8$ and $r/R = 0.46$) (legend: see Fig. 3.5).

and joint PDFs, substantial errors in the mean properties can still occur.

3.6 Conclusions and recommendations

In the context of a reduced scalar approach (FGM [26], FPI [27], REDIM [39] and ADF-PCM$_\chi$ [96]), an a priori study of the experimental data as presented in this chapter is useful in order to identify underlying flame structures (e.g. flamelets).

Considering presumed PDF modeling based on mixture fraction Z and a progress variable c or λ, this a priori study permits to test assumptions on the joint Z-c or Z-λ PDF shape. In a turbulent flame, with complex flow pattern, such as the Sydney swirling flame SM1, different limitations can be observed. First of all, although the shape of the marginal PDF of Z is quite well modeled by a β-function, this is not generally the case for the marginal PDF of c or λ. Also, statistical independence is only observed with the proposed definition of c or λ in zones where steady flamelet structures appear in composition space. More precisely, there is strong statistical dependence in case of a mixing line representing mixing of pure air and rich combustion products, which differs from any steady flamelet structure. In this case, it is not correct to circumvent solving the transport equation for c by assuming $\overline{c|Z} = \overline{c}$ and solving the transport equation for Y_c instead. In the case of local extinction, the assumption of statistical independence seems more valid, although the normalizations used for c and λ, based on a flamelet or equilibrium, do not necessarily ensure complete statistical independence with Z. The influence of the statistical independence assumption has been quantified through the mean production rate of Y_{CO_2}, showing substantial differences.

These limitations of presumed Z-c-PDF modeling are naturally superseded in transported PDF modeling where no assumptions on PDF shapes and statistical independence are required and Y_c (here Y_{CO_2}) can directly be considered. Transported PDF approaches are therefore recommended for RANS calculations of reacting flows with complex flow patterns. In well-resolved LES, the limitations of presumed Z-c- or Z-λ-PDF modeling are less severe, as the sub-grid fluctuations of mixture fraction are limited to a narrow range in composition space.

Chapter 4

Calculations of a swirling bluff body flame

4.1 Introduction

Swirl-stabilized turbulent flames are important for many industrial applications, because the swirling motion creates recirculation zones which enhance mixing and stabilize the flame. This leads to better combustion efficiency and less pollutant formation. However, swirl flames are not yet fully understood. One of the complex phenomena concerns vortex breakdown leading to flow instability, i.e. a precessing vortex core and periodically expanding/shrinking recirculation zone. Several modeling approaches have been used to simulate these complex flows. The unsteady 3D effects are in principle better handled by LES than RANS, but LES calculations have a higher computational cost. Therefore, we consider it still useful to study hybrid RANS/PDF (probability density function) calculations, in particular for cases where there is no strong influence from a precessing vortex core.

Besides flow field complexity, local extinction is also important, as it leads to e.g. incomplete combustion and therefore more pollutants. Physically, extinction in laminar non-premixed flames occurs due to local high gradients, resulting in excessive local heat (and mass) transfer, which cannot be sustained by local heat production from chemical reactions [4]. It is characterized by the local Damköhler number, defined as the inverse of the product of the chemical time scale and the scalar dissipation rate. In [118] Kolmogorov scale eddies are stated to be important in the extinction of turbulent non-premixed flames with a similar physical mechanism as for laminar

flames. In [119], on the other hand, extinction is said to be caused by large-scale eddies through total flame stretching, and not through small-scale flame wrinkling. There are also other mechanisms for local extinction, e.g. radical pools being swept away by a vortex [120]. Apart from experiments, also DNS studies have been done to investigate local extinction of non-premixed flames. In [121], following Lagrangian particles in the flow, it is shown that local extinction is purely due to fluctuations of the scalar dissipation rate. In [122], where DNS with one-step global reaction is performed in order to study the influence of turbulent mixing on re-ignition, local extinction is again shown to be due to fluctuations of the scalar dissipation rate, causing excessive heat loss.

In transported PDF modeling, traditional mixing models use the mean integral turbulent time scale in order to determine the mixing time scale. Moreover, in a RANS framework, the flow and mixing fields in physical space are steady and not all fluctuations in scalar dissipation rate can be expected to be captured. The PSP model [58, 60, 59, 61], which uses one-dimensional parametrized scalar profiles (PSPs) to model the unresolved scalar length-scales characterizing the scalar micro-mixing, can capture the fluctuations in scalar dissipation rate better, as it provides joint statistics of scalars and their scalar dissipation rate. In LES, resolved fluctuations in instantaneous flow and mixing fields result in resolved fluctuations of the scalar dissipation rate. In [123], where LES calculations with presumed PDF modeling and a flamelet generated manifold [26] are discussed, coherent structures of high scalar dissipation are seen to lead to flame stretching and local extinction.

In the present study, we investigate the swirling bluff body flame SM1 [124, 101, 102, 103, 104], which has been studied numerically in the past by several authors. Masri et al. [125] performed a joint velocity-scalar-frequency PDF calculation for a reacting case. James et al. [126] performed an LES/PDF calculation of two reacting cases (SM1 and SMA1) with satisfactory results. Unfortunately no detailed study of turbulence-chemistry interaction is reported. LES results of non-reacting and reacting cases have been presented with flamelet chemistry in [127, 128, 129, 130] and with FGM chemistry in [117]. A comparable quality of flow and mixing field results is obtained here with axisymmetric steady RANS calculations with a non-linear k-ϵ model [11]. The obvious advantage of this approach is that transported (scalar) PDF simulations can be performed within reasonable computing time, in order to study turbulence-chemistry interaction.

For chemical reaction, a pre-calculated chemistry table is used. We adopt the

Reaction Diffusion Manifold (REDIM) [39] approach, as it has already been used for calculations of non-swirling bluff-body flames [131, 132]. In the latter, the combination of REDIM with EMST mixing model [56] led to reasonable results, but scatter in Y_{CO_2} space was clearly under-estimated. This was not attributed to the use of REDIM as reduced chemistry, but to the localness property of EMST leading to too little local extinction. In the present study, we discuss results with similar model settings, but for a swirling flame. Moreover the trajectories in physical and composition space of computational particles are studied in detail. This proves to be useful in order to correlate positions in composition space and in physical space. It also permits to focus on the distinction between mixing and extinction, and to discuss the limitations of the modeling in a more precise manner — for instance to better formulate the limitation of EMST instead of generally referring to its 'localness in composition space'.

4.2 Test case description and modeling framework

4.2.1 Sydney swirling flame SM1

Figure 4.1 depicts the burner. The bluff body (50mm diameter) contains the central fuel jet (3.6mm diameter). Swirling air is provided through a 5mm wide annulus surrounding the bluff-body. The swirl component is created by three tangential ports. The burner is placed inside a wind tunnel with square cross section. A wide range of testing conditions has been examined experimentally [124, 101, 102, 103, 104]. All cases are characterized by: the bulk axial velocity of the central jet (U_j), the bulk axial and tangential velocities of the swirling air annulus (U_s and W_s) and the bulk axial velocity of the co-flow of the wind tunnel (U_e).

We consider flame SM1 only, because for this flame the precessing vortex core is the weakest. This is important since we consider here a steady RANS modeling framework. In the experiments [104], velocity measurements were performed with CNG, while CH_4 was used for the composition measurements. No physical changes in the flow field are reported. We use CH_4 as fuel in the simulations. The stoichiometric mixture fraction is $Z_{\mathrm{st}} = 0.054$. The flow parameters are summarized in Table 4.1 with the swirl number geometrically defined as $S_g = W_s/U_s$. The flow field of SM1 contains two recirculation zones: one close to (and caused by) the bluff body and one further downstream near the central axis (caused by vortex breakdown). The simulation results (Figure 4.1, right) reproduce the qualitative experimental finding

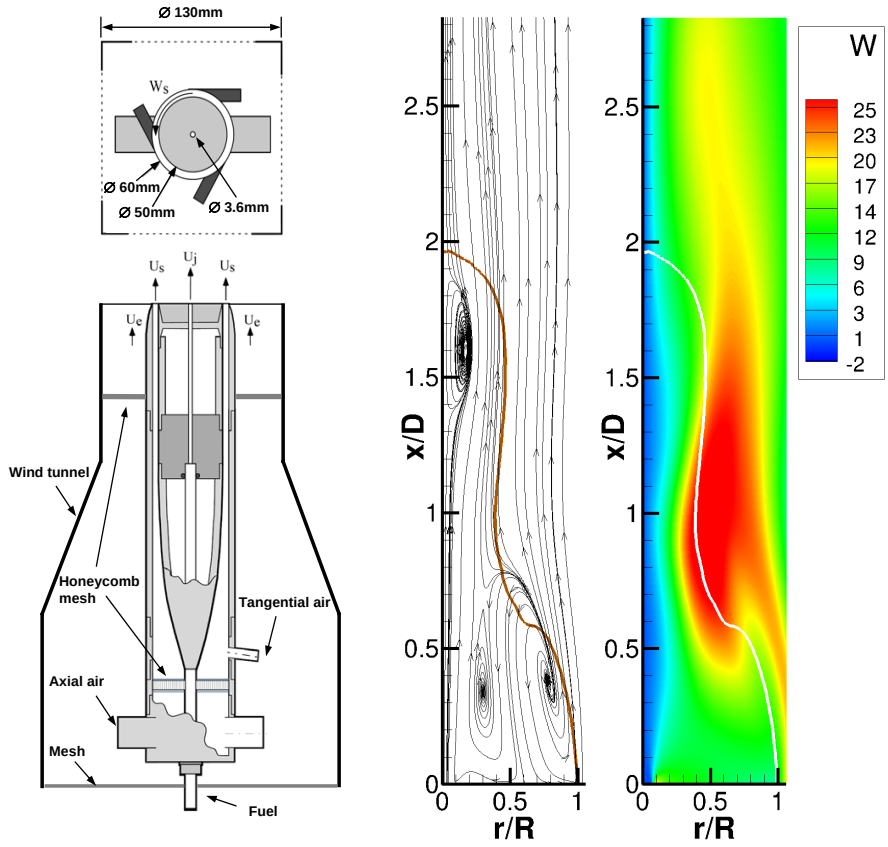

Figure 4.1: Sydney Swirl Burner (adapted from [6]) and stream lines and contours of tangential velocity in an axisymmetric slice of a transported PDF calculation with EMST and REDIM. Brown and white lines: stoichiometric mixture fraction isocontour.

that the recirculation zones are separated by a region of high shear stress which coincides with a highly rotating collar. In [104], local extinction is believed to occur in this region of high shear stress between the two recirculation zones, while the hot, re-circulated combustion products from the second recirculation zone are believed to cause re-ignition.

Table 4.1: Flow parameters of SM1

Case	Fuel	U_e (m/s)	U_j (m/s)	U_s (m/s)	W_s (m/s)	S_g (-)
SM1	CNG/CH_4	20	32.7	38.2	19.1	0.5

4.2.2 Turbulence-chemistry interaction in RANS modeling framework

The non-linear k-ϵ turbulence model of [11] is used, as it takes into account the effect of streamline curvature and rotation on turbulence.

In order to deal with turbulence-chemistry interaction, a transported scalar PDF approach is used. In the transported scalar PDF approach, the transport equation is modeled and solved for the mass density function $\mathcal{F}_\phi(\boldsymbol{\psi}) = \rho(\boldsymbol{\psi})\, f_\phi(\boldsymbol{\psi})$, with f_ϕ the joint scalar PDF [66], and with $\boldsymbol{\phi}$ the composition vector of independent scalars, (in this work) consisting of mixture fraction, Z, and CO_2 mass fraction, Y_{CO_2}:

$$\begin{aligned} \frac{\partial \mathcal{F}_\phi}{\partial t} \; + \; & \frac{\partial \widetilde{U}_j \mathcal{F}_\phi}{\partial x_j} + \frac{\partial}{\partial \psi_\alpha}\left[S_\alpha(\boldsymbol{\psi})\, \mathcal{F}_\phi\right] \\ = \; & \underbrace{-\frac{\partial}{\partial x_j}\left[\left\langle u_j'' \middle| \boldsymbol{\psi} \right\rangle \mathcal{F}_\phi\right]}_{\text{gradient diffusion}} \underbrace{-\frac{\partial}{\partial \psi_\alpha}\left[\frac{1}{\rho(\boldsymbol{\psi})}\left\langle -\frac{\partial J_j^\alpha}{\partial x_j} \middle| \boldsymbol{\psi} \right\rangle \mathcal{F}_\phi\right]}_{\text{mixing model}} . \end{aligned} \tag{4.1}$$

In this general equation, S_α is the reaction source term for scalar α and $\boldsymbol{J}^\alpha$ the molecular scalar flux.

A Lagrangian particle method is used to model and solve (4.1) [66]. The two terms on the right hand side need to be modeled. For the first term, the effect of conditional velocity fluctuations is modeled as a turbulent diffusion flux, by using a gradient diffusion model:

$$\frac{\partial}{\partial x_j}\left[\left\langle u_j'' \middle| \boldsymbol{\psi} \right\rangle \mathcal{F}_\phi\right] = -\frac{\partial}{\partial x_j}\left[\Gamma_T \frac{\partial\left(\mathcal{F}_\phi/\langle\rho\rangle\right)}{\partial x_j}\right], \tag{4.2}$$

where Γ_T is the turbulent diffusivity, modeled as $\Gamma_T = \mu_T / Sc_T$, with μ_T the dynamic turbulent viscosity (from the model of [11]), and with the turbulent Schmidt number Sc_T chosen to be variable depending on $\widetilde{u}\widetilde{v}$ (see appendix A). For the second term on the right hand side of Eq. (4.1), which represents the effect of molecular diffusion in the turbulent flow, we use the EMST mixing model [56] with $C_\phi = 2$.

4.2.3 Hybrid RANS/PDF approach

All calculations are steady axisymmetric and are performed with the same code PDFD [133], which has already successfully been applied to non-swirling Sydney bluff-body burner cases [131, 132]. In transported PDF calculations, the equations are solved using a consistent hybrid finite-volume/particle method [133]. Mean velocity $\widetilde{U}$, turbulent kinetic energy k and turbulent dissipation rate ϵ are obtained by a standard finite-volume (FV) method based on a pressure correction algorithm. The transport equations for turbulent kinetic energy (k) and turbulent dissipation rate (ϵ) solved in the FV method provide the turbulent timescale, required in the mixing model. The mean density $\langle\rho\rangle$ in the FV method is obtained from the iteration averaged mean density in the particle method (averaged over 1000 particle time steps).

For the evolution of the particles the fractional step method is used [66]. In every particle time step, the particles first mix and subsequently react. The mixing causes particle motion in 2D composition space of the independent scalars to a new position (Z^*, $Y^*_{CO_2}$). At this new position the particles react with the reaction rate for CO_2 as obtained from the REDIM table (Figure 4.2). As mixture fraction is conserved during the reactions, the particles move in the 1D Y_{CO_2}-space to the final position in the 2D composition space of the independent scalars (Z^*, $Y^{**}_{CO_2}$). At this final position all the dependent scalars, e.g. temperature, density and species, are retrieved from the REDIM table. A local time-stepping algorithm, developed in the framework of statistically stationary problems [65], is applied. The number of particles per cell is 100.

An outer iteration consists of a number of FV iterations and particle time steps. We use a fixed number of particle time steps (typically 5), while the FV method is iterated until the residuals of all equations are decreasing and the global mean pressure correction is below a specified threshold (with a maximum of 1000 FV iterations per outer iteration).

4.2.4 Computational domain and boundary conditions

The 0.3m long computational domain starts at the burner exit. In radial direction, it is 0.15m wide. A non-uniform rectangular grid of 160×128 cells is used. Grid independence has been verified, but will not be discussed in detail. Inlet mean velocity boundary conditions are generated from separate calculations inside the burner, using

the LRR-IP turbulence model [12]. The turbulent kinetic energy (k) levels obtained from the calculations inside the burner are much lower than the experimental values measured close to the burner ($x = 1.89D_{\text{jet}}$). Therefore, we decided to upscale the k profiles from the separate calculations by multiplying with a constant factor to match the experimentally measured peak value at $x/D = 0.2$. The profiles from the separate calculations for the turbulent frequency $\omega = \epsilon/k$ were then used to deduce the ϵ profiles. In the fuel jet, $Z = 1$, whereas the air flows correspond to $Z = 0$. The mixture fraction variance is zero at the inlet.

As already observed for the non-swirling bluff-body burner [134], we verified in presumed-PDF calculations (not shown here) that the results are insensitive to the applied boundary condition at the bluff-body face (either no-slip boundary condition, with standard wall functions or free slip boundary condition). The bluff body is treated here as a free slip wall and the gradients normal to the bluff body are assumed to be zero. Symmetry conditions are applied at the symmetry axis. A convective outlet condition is used. The outer boundary of the computational domain is modeled as a free-slip wall (symmetry boundary condition), which forces the fluxes to be zero.

4.2.5 Particle tracking technique

A similar technique as in [135] is used to track computational particles. Tracers are randomly selected among the particles introduced into the computational domain at the inlet. Not all particles are injected simultaneously, but since the solution is statistically stationary, the time of injection is not essential. Special measures are taken in order to cope with the particle number control algorithm ('splitting and clustering' of computational particles). When a tracer particle is split, only one of the resulting particles continues to be a tracer particle. In case of clustering where one or more tracers are involved, the particle after clustering plays the role of the tracer. Consequently, if more than one tracer is involved in the clustering, the number of tracers is reduced. In [135] clustering was disabled to avoid this.

From a statistical point of view, each computational particle is representative of one realization of the flow [66]. In one computational cell the computational particles determine together the PDF. However, one individual computational particle does not behave exactly as a fluid element. Therefore the trajectories investigated below must not be interpreted as flow paths of fluid elements. They must be interpreted in a statistical sense. The tracers also do not represent the instantaneous flame

structure [135]. Nevertheless, the trajectories in physical space and composition space provide insight in a Lagrangian manner.

In [135] the evolution of the tracers was studied using axial position as surrogate for time. This is not possible for the bluff-body case, as there are several recirculation zones, resulting in a non-monotonous evolution of the axial coordinate with time. We therefore need to use 'time' or 'particle age' to describe the progress in the evolution of the tracer, when studying multiple tracers simultaneously. The 'particle age' is set to zero at the time of injection of the particle into the domain.

4.3 Reduced Chemistry Modeling

The Reaction Diffusion Manifold (REDIM) [39] is used in this study as tabulated chemistry model. Obviously, there are other options to reduce the calculation time for the chemistry, such as in situ adaptive tabulation (ISAT) [41] in which a chemistry table is stored on the fly. This technique has recently been applied in parallel computations [136]. Yet, pre-calculated tables based on reduced mechanisms are still more economical in global computing time. There are also other ways than REDIM to construct manifolds, e.g. FGM [26] or FPI [27], using a progress variable. It is not intended here to compare different manifold techniques. An overview of existing techniques can be found e.g. in [137].

4.3.1 Reaction-Diffusion Manifold (REDIM)

In a Reaction Diffusion Manifold [39], progress variables (in this work only one, namely Y_{CO_2}) are introduced as extra parameters in addition to mixture fraction, in order to consider finite-rate chemistry effects, such as low temperature chemistry and mixing of burnt and unburnt gases. REDIM can be seen as an extension of the ILDM concept [28] to incorporate the effect of coupling of reaction and diffusion processes. Contrary to ILDM, the REDIM manifold also exists in regions where the temperature is low and thus the chemistry rate is slow. Starting from a detailed reaction mechanism with a certain number of species and reactions, the REDIM concept reduces the system to a lower dimensional invariant reaction/diffusion manifold, which approximates the full system dynamics in the state space but with fewer degrees of freedom. In the construction of the REDIM, the scalar gradients in physical space $\nabla\phi_\alpha$ need to be specified [39]. For each (Z, Y_{CO_2}) value, the final REDIM therefore includes

'underlying' scalar dissipation rates $\chi_\alpha^\star$, where $\chi_\alpha^\star = 2D_\alpha \nabla\phi_\alpha.\nabla\phi_\alpha$ depends on the specified scalar gradients $\nabla\phi_\alpha$ and on the diffusion coefficient D_α (which depends on the REDIM composition). In the REDIM concept the choice of the scalar gradients $\nabla\phi_\alpha$ determining the underlying flame structure is free. In this study the gradients form laminar diffusion flamelet calculations are used, resulting in a manifold similar to FGM [26], if the generated manifolds are based on diffusion flamelets. Note, however, that the REDIM concept allows to cover the domain, where due to strain no flamelets exist (see below).

We apply the REDIM concept to reduce the Warnatz mechanism [3] for CH_4 to a 2-dimensional manifold with mass fractions Y_{N_2} and Y_{CO_2} as independent parameters. The mixture fraction is directly related to Y_{N_2} through the following relationship:

$$Z = 1 - \frac{Y_{N_2}}{Y_{N_2,0}}, \tag{4.3}$$

with $Y_{N_2,0}$ the N_2 mass fraction value in the co-flowing air. This definition of mixture fraction does not account for differential diffusion. Equal diffusivities for all species and unity Lewis number are assumed.

The REDIM is stored as a pre-calculated table. Figure 4.2 shows contours of the CO_2 reaction rate as function of mixture fraction and Y_{CO_2}.

4.3.2 Parametrization

Since mixture fraction is a conserved scalar, there is no chemical source term ($S_Z(Z, Y_{CO_2}) = 0$) and evolution in composition space in the Z-direction is only caused by mixing. The REDIM uses the progress variable approach with (in this work) Z and Y_{CO_2} as independent parameters. The latter can be seen as a non-normalized progress variable and evolution in composition space in the Y_{CO_2}-direction is caused by both mixing and reaction.

The information contained in the REDIM does not necessarily differ strongly from the information contained in a multiple flamelet, consisting of steady flamelets for a range of scalar dissipation rates. However, the essential difference is the choice of the parametrization of the data set: mixture fraction and Y_{CO_2} instead of mixture fraction and its scalar dissipation rate, $\chi = 2D\nabla Z.\nabla Z$. The influence of the parametrization can be observed when solving the flamelet equation and plotting the flamelet temperature at stoichiometry as function of χ_{st} (the scalar dissipation rate at stoichiometry).

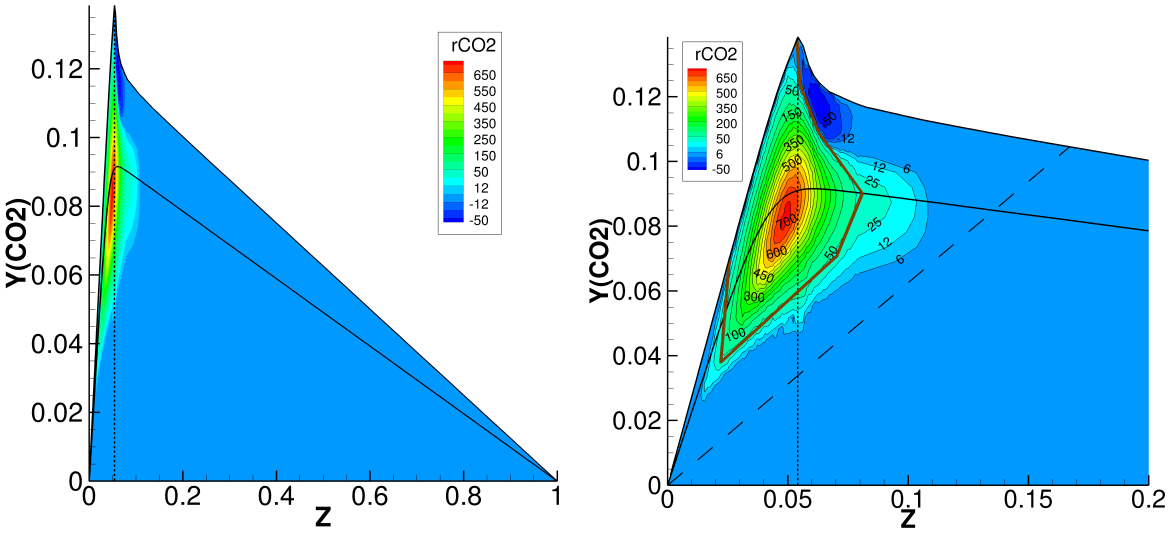

Figure 4.2: REDIM CO_2 reaction rate ($rCO2$). Vertical dotted line: stoichiometry ($Z_{\mathrm{st}} = 0.054$). Reference lines: 1/ steady non-premixed flamelet close to extinction, 'critical flamelet', calculated in the opposed-flow configuration with Warnatz mechanism [7, 3] (black line). 2/ reference mixing line (dashed line). 3/ approximation of iso-contour $rCO2 = 50s^{-1}$, separating zones of low and high reactivity (brown line).

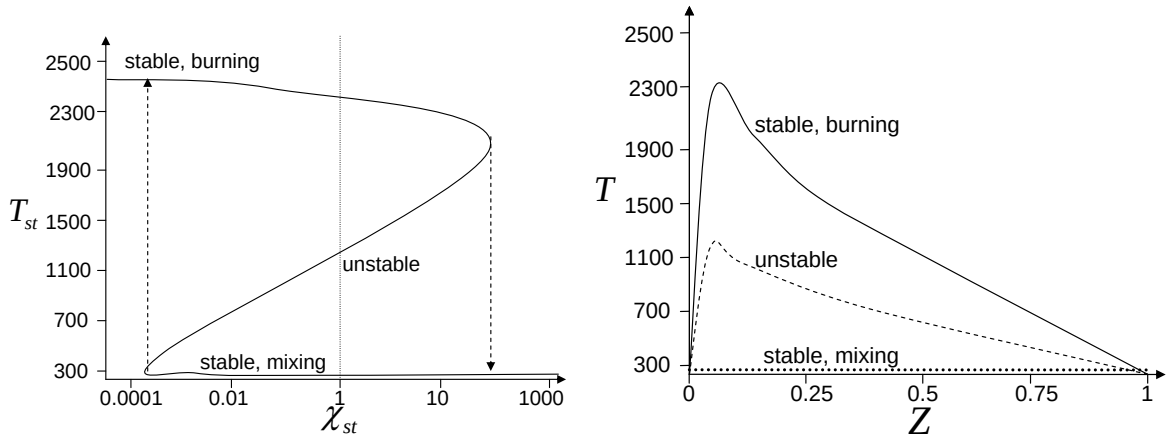

Figure 4.3: a/ S-Curve representing the complete solution of the flamelet equations. b/ Flamelet solutions corresponding to the 3 branches of the S-curve for $\chi = 1s^{-1}$. Adapted from [8].

The well known S-curve is then obtained (Figure 4.3) [8], consisting of an upper stable burning branch, a lower stable inert mixing branch and an intermediate unstable branch representing the unstable solution of the flamelet equation. With χ as second parameter, the S-curve is projected onto the χ-axis and therefore only one branch can

be represented at a time. With a progress variable, however, the S-curve is projected onto the vertical axis and the complete S-curve, including the unstable branch can be reached [8] as it evolves monotonically with the progress variable. This is discussed in several papers on the use of the flamelet/progress variable approach in LES [33, 115, 8] and most of the conclusions in those references remain valid for RANS.

With the use of a progress variable in the REDIM, also the low temperature region, which cannot be represented by steady diffusion flamelets, is parametrized. In the temperature-mixture fraction diagram, this zone is situated underneath the 'critical' flamelet, corresponding to the critical scalar dissipation rate at which extinction occurs. As mentioned before, the REDIM includes an 'underlying' scalar dissipation rate χ'. In our case, in the zone above the critical flamelet, the scalar gradients that need to be specified in order to build the REDIM are obtained from steady laminar diffusion flamelets. In the low temperature region, the scalar gradients $\nabla\phi_\alpha^{(c)}$ from the 'critical flamelet' are specified, such that $\chi' = 2D\nabla Z^{(c)}.\nabla Z^{(c)}$, where D depends on (Z, Y_{CO_2}).

In the PhD thesis of C.D. Pierce [32] it is discussed how in a chemistry table parametrized by Z and Y_c the fictitious scalar dissipation rate $\chi'(Z, Y_c)$, corresponding to a certain point in the table and therefore also corresponding to a certain flamelet, is usually different from the actual scalar dissipation rate in the flow χ. The steady flamelet equation used to build up the FPV table is [32]:

$$\rho\chi'\frac{d^2Y_i}{dZ^2} = -\dot{\omega}_i \tag{4.4}$$

By adding $\chi\frac{d^2Y_i}{dZ^2}$ to both sides of the previous equation we get:

$$\rho(\chi-\chi')\frac{d^2Y_i}{dZ^2} = \rho\chi\frac{d^2Y_i}{dZ^2} + \dot{\omega}_i \tag{4.5}$$

Which resembles the unsteady flamelet equation:

$$\rho\frac{\partial Y_i}{\partial t} = \rho\chi\frac{d^2Y_i}{dZ^2} + \dot{\omega}_i \tag{4.6}$$

The difference between χ and χ' therefore seems to result in a relaxation towards the steady flamelet solution corresponding to χ, as for a certain Z, χ' will change with Y_c. This is applicable to any manifold based on non-premixed flamelets and parametrized by Z and Y_c and thus also on the REDIM.

4.3.3 A Priori test of the REDIM

Before discussing the transported PDF calculations, the intrinsic potential of the 2D REDIM to reproduce experimentally measured values is tested in compositional space. For a given Y_{CO_2} value (or Z value), scatter plots of the experimental measurements from all the axial positions are compared with the REDIM. A slice is taken from the REDIM at the specified Y_{CO_2} value (resp. Z value) and all the experimental measurements for $Y_{CO_2} \pm 0.02 Y_{CO_2}$ (resp. $Z \pm 0.02Z$) are plotted. This 2% relative margin is somewhat arbitrary and accounts for experimental uncertainty.

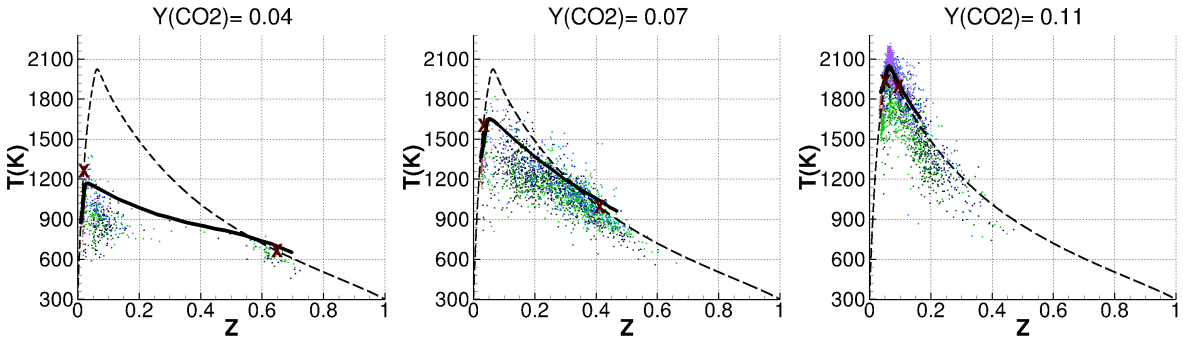

Figure 4.4: A Priori test: Temperature for constant values of Y_{CO_2}. Experimental measurements (dots), REDIM (full line) and reference steady non-premixed flamelet (dashed line and crosses).

In Figure 4.4 the temperature for constant values of Y_{CO_2} is plotted. The REDIM is able to follow the experimental measurements along with the reaction progress, albeit that the temperature is too high, especially for low Y_{CO_2}-values. This is in line with [138] where it was reported that temperatures tend to be over-predicted by the Warnatz mechanism due to early onset of combustion. For comparison, a reference steady non-premixed flamelet is plotted in Figure 4.4 as a dotted line. The two points on the flamelet corresponding to the given constant Y_{CO_2} value are marked as 'X'. This steady flamelet was calculated in the opposed-flow configuration with strain rate 100s^{-1} using the Warnatz mechanism [3] (intermediate between the upper REDIM boundary and the critical flamelet shown in Figure 4.2).

In Figure 4.5 the temperature for constant values of Z is plotted. The reference steady flamelet is also represented as a dotted line in this Y_{CO_2}-temperature space (and the flamelet value corresponding to the considered Z value is marked as 'X'). For all mixture fractions, the REDIM provides higher temperatures than what is experimentally measured. This is particularly true for low values of Y_{CO_2}, as already

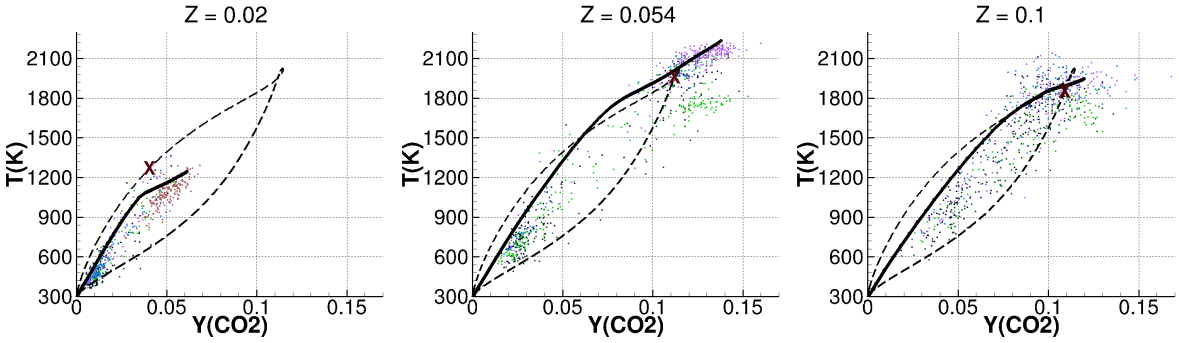

Figure 4.5: A Priori test: Temperature for constant values of Z. Experimental measurements (dots), REDIM (full line) and reference steady non-premixed flamelet for strain rate $100s^{-1}$ (dashed line and cross).

mentioned. Differences to the experimentally measured mean temperature are typically around 10%, but in specific regions they go up to 25%. This will result in over-prediction of the mean temperature in the simulations discussed below.

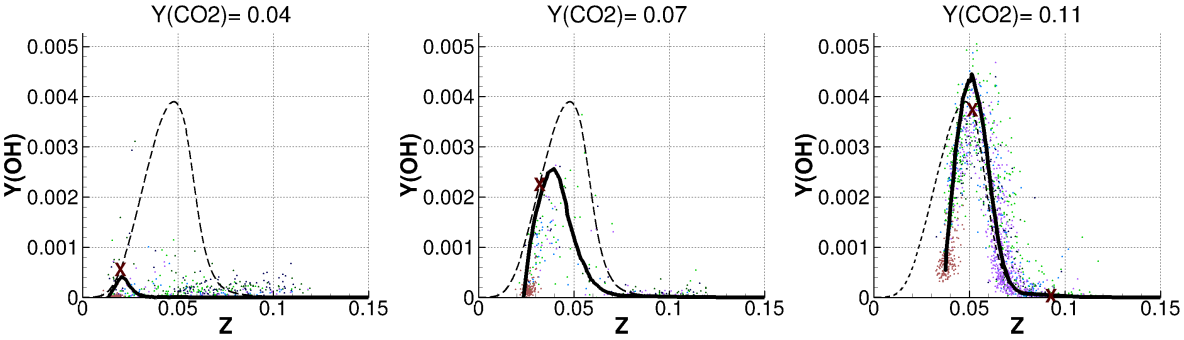

Figure 4.6: A Priori test: Y_{OH} for constant values of Y_{CO_2}. Experimental measurements (dots), REDIM (full line) and reference steady non-premixed flamelet (dashed line and crosses).

In Figure 4.6 the mass fraction of OH, $Y(OH)$, for constant values of Y_{CO_2} is plotted. The REDIM correctly predicts the lowest reactive mixture fraction for the different levels of reaction progress. Also the correlation between Z and $Y(OH)$ is captured quite well. In Figure 4.7 $Y(OH)$ is plotted for constant values of Z. Around stoichiometry, the REDIM captures quite well the correlation between Y_{CO_2} and $Y(OH)$. For lean and rich mixtures, on the other hand, there is more experimental scatter which cannot be predicted by the REDIM.

In general, the substantial amount of scatter around the REDIM seems to suggest that with a 3D REDIM more of the compositional space would be accessed, as in

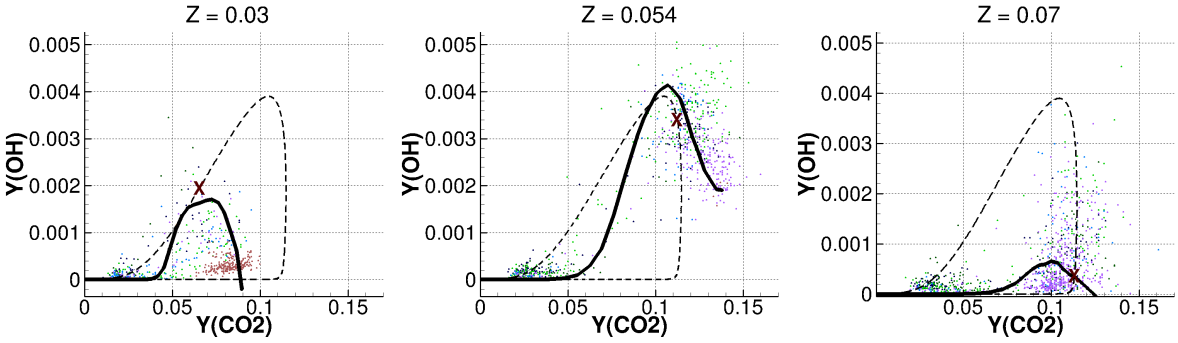

Figure 4.7: A Priori test: Y_{OH} for constant values of Z. Experimental measurements (dots), REDIM (full line) and reference steady non-premixed flamelet for strain rate $100s^{-1}$ (dashed line and cross).

the experimental measurements. However, this scatter is certainly partly due to the experimental uncertainty [102]. In [139] the required dimension of the REDIM for a good representation of the kinetics is investigated, and there it is concluded that a 2D or 3D REDIM is optimal for CFD calculations. This is confirmed by the a priori study: the overall quality of the REDIM is deemed satisfactory for the modeling of the specific swirling flame considered.

4.4 Results

4.4.1 Flow and mixing fields (physical space)

We discuss here the mean velocity and scalar profiles obtained in physical space corresponding to the transported scalar PDF calculation using REDIM and EMST ('REDIM-EMST') with the ad hoc adjustment of the turbulent Schmidt number Sc_T described in appendix A. The latter is necessary in order to capture the mean mixture fraction plateau in the region above the bluff body, and in order to correctly model the mixing of pure air with burnt products in the recirculation zone when using REDIM (the 'mixing line' in composition space discussed in the next section). In addition to the REDIM-EMST calculation, two calculations with a fast chemistry model are also considered: a presumed-PDF calculation ('Fastchem-β-PDF') and a transported scalar PDF with the same settings as the REDIM calculation ('Fastchem-EMST'). These calculations are included in order to show the impact of the 'mixing line' on the results in physical space (since with the adjusted Sc_T, this 'mixing line' is indeed captured with REDIM and not with the fast chemistry that always leads to a burning

solution). As 'fast chemistry' model, the single steady laminar flamelet with strain rate of 100s^{-1} is used (the dashed line represented in Figure 4.4).

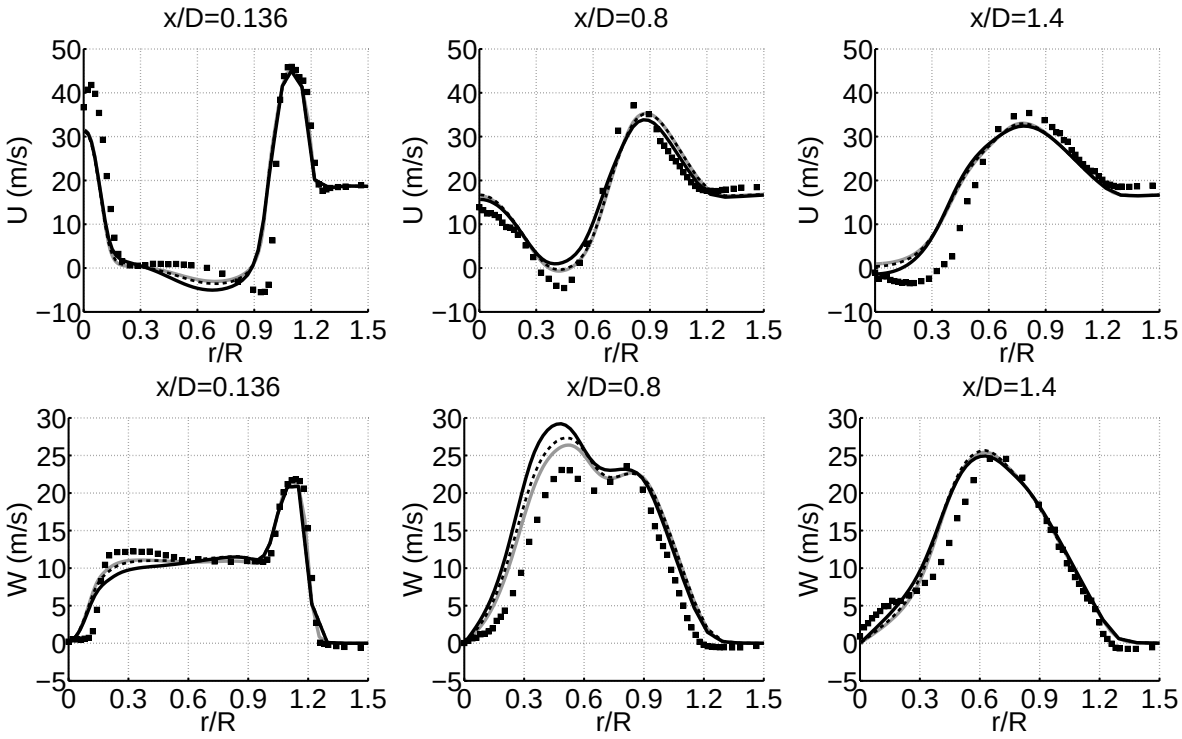

Figure 4.8: Mean axial and tangential velocity profiles. Grey line: Fastchem-β-PDF, Dashed black line: Fastchem-EMST, Full black line: REDIM-EMST, Symbols: experimental data.

Figure 4.8 reports the mean axial velocity $\widetilde{U}$. At $x/D = 0.136$, $\widetilde{U}$ is under-predicted by all calculations on the center line. The radial position of the first recirculation zone is not correctly predicted, but in the REDIM calculation the absolute value of the negative velocity is correct. At $x/D = 0.8$, the axial velocity in the center region is slightly over-predicted by all the calculations. The results show (almost) no small negative axial velocities. In the experiments, however, an area of negative velocities is still observed, indicating that the length of the first recirculation zone is under-predicted by all calculations. For all calculations, the width of the recirculation zone is smaller than in the experiments, but the axial position of the beginning of the second recirculation zone is reasonably predicted. The predictions of the mean tangential velocity $\widetilde{W}$ are also satisfactory. At $x/D = 0.136$, the sharp gradient around $r/R = 0.15$ could not be captured by any of the calculations. The difference between Fastchem-EMST and REDIM-EMST results is the largest at $x/D = 0.8$, with all calculations over-predicting the experimental mean tangential velocity. Further downstream all the calculations

correctly predict the tangential velocity. In general, agreement with experimental data is quite good, comparable to what was obtained with LES in [127]. As already observed in similar simulations of the non-swirling Sydney bluff-body flames [131, 132], the differences in mean density between the three different calculations do not strongly affect the mean flow field.

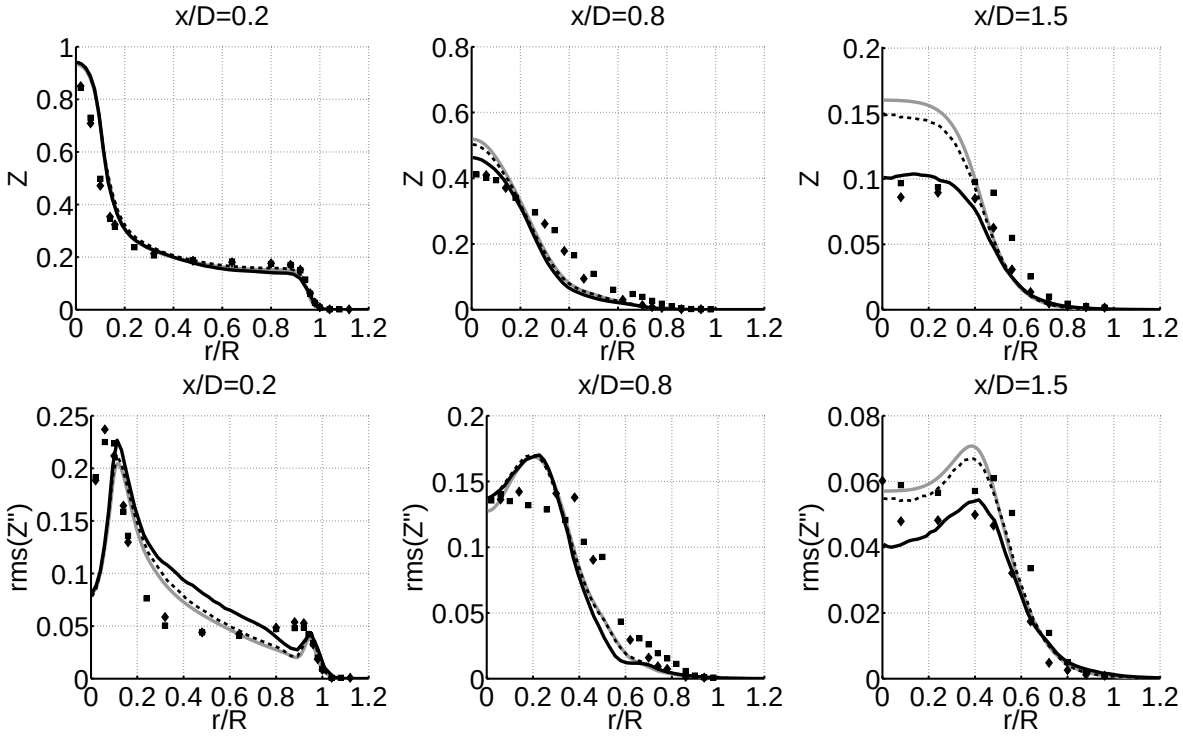

Figure 4.9: Mean mixture fraction and mixture fraction rms profiles. Grey line: Fastchem-β-PDF, Dashed black line: Fastchem-EMST, Full black line: REDIM-EMST, Symbols: experimental data.

In Figure 4.9 the mean mixture fraction and mixture fraction rms profiles are shown. At $x/D = 0.2$, the plateau in the bluff-body region and the steep gradient in the annulus region ($0.9 < r/R < 1.1$) have to be well predicted, as these regions are close to stoichiometry and therefore will strongly affect the flame. This is the reason for the choice of the variable Sc_T depending on $\widetilde{u}\widetilde{v}$ (see appendix A). The motivation for this ad hoc adjustment is that good results for the mean mixture fraction field, particularly in the reaction region around $Z = 0.054$, are indispensable to discuss the influence of the tabulated chemistry on the results.

As can be observed in Figure 4.9, the REDIM-EMST calculation leads to overall good results. It is quite remarkable that, whereas the mean velocity results are similar for the three calculations, the mean mixture fraction results differ quite strongly,

especially at $x/D = 1.5$. Such differences are not observed when using the standard value $Sc_T = 0.7$ (not shown), and neither were they observed in the non-swirling bluff-body flame calculations [131, 132] where a standard constant value for Sc_T was used. In these cases, the REDIM calculations do not correctly reproduce the mixing between pure air and hot products in the recirculation zone (no 'mixing line') and mainly lead to a burning solution similar to a single diffusion flamelet. The possible differences in mean density are then not strong enough to affect the mean mixture fraction field. In the present case, however, the difference in mean density is larger, and moreover, the decrease of the relative importance of turbulent diffusion on mean mixture fraction compared to convective terms (through the increase of Sc_T) makes the evolution of mean mixture fraction more sensitive to differences in mean density. These differences in mean density between REDIM and Fastchem calculations are strongly related to the use of the progress variable Y_{CO_2} in REDIM, as will be discussed in the next section, and can be indirectly observed in Figure 4.10 showing the profiles of mean CO_2 mass fraction $\widetilde{Y}_{CO_2}$ (since the mean density mainly depends on the mean temperature, which is in this case strongly correlated to $\widetilde{Y}_{CO_2}$).

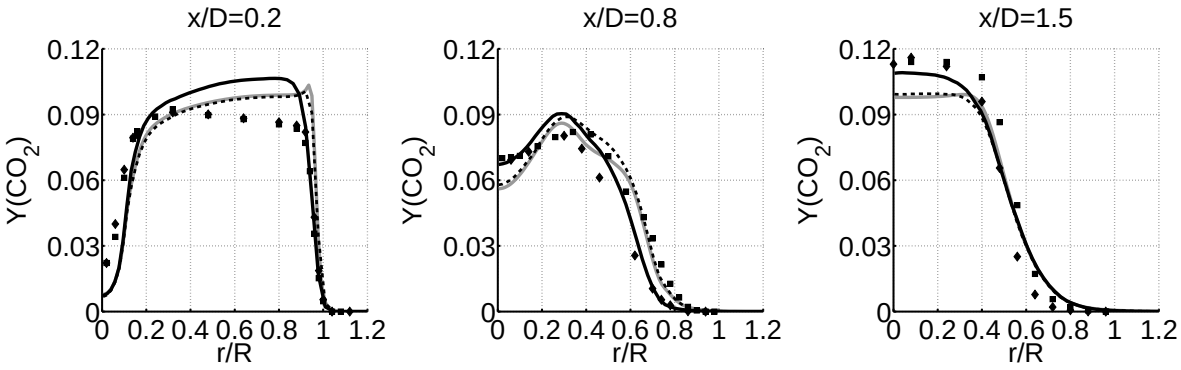

Figure 4.10: Mean Y_{CO_2} profiles. Grey line: Fastchem-β-PDF, Dashed black line: Fastchem-EMST, Full black line: REDIM-EMST, Symbols: experimental data.

4.4.2 Joint scalar PDF (composition space)

Figure 4.11 shows the scatter plots of Y_{CO_2}, experimentally observed and numerically simulated. More quantitative information is given in Figure 4.12 showing the corresponding profiles for the conditional mean of Y_{CO_2}. Obviously, using the reference steady laminar flamelet (as 'fast chemistry model'), all points would lie on this single laminar flamelet, as can be observed in Figure 4.12. With REDIM, a deviation

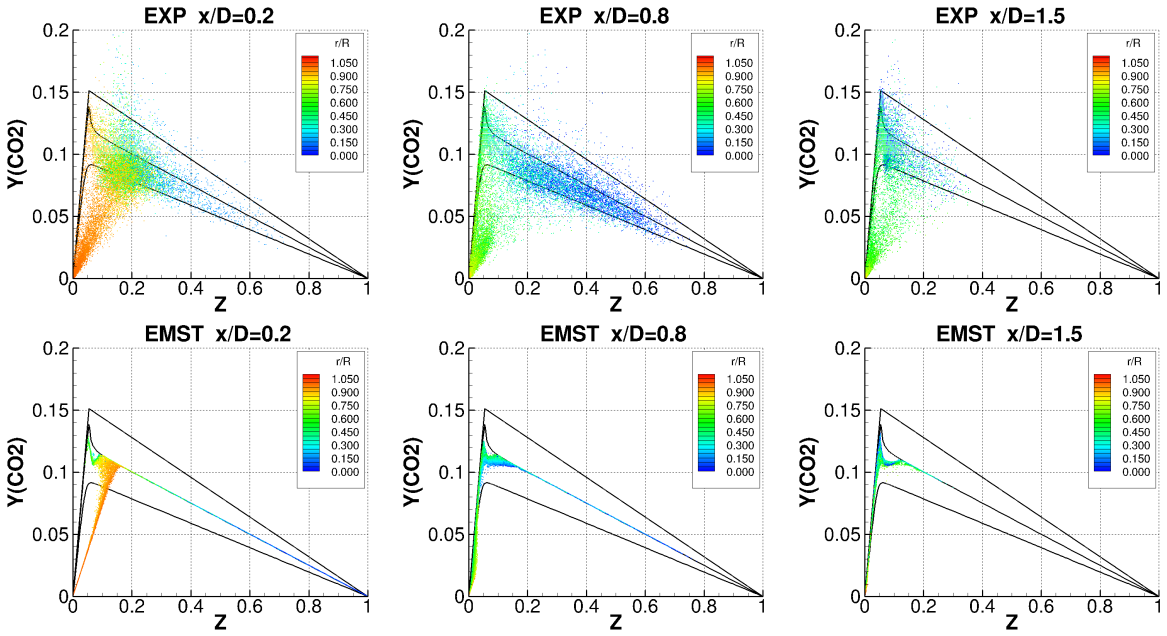

Figure 4.11: Scatter plots of Y_{CO_2} for experiments and REDIM-EMST calculation colored with r/R. The Burke-Schumann flame sheet (upper black line), upper boundary of the REDIM (middle black line) and the critical flamelet (lower black line) are also shown.

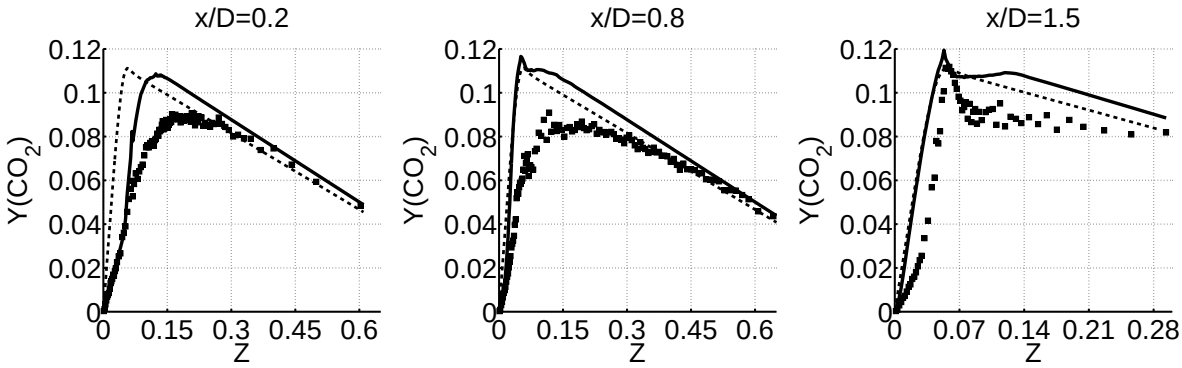

Figure 4.12: Conditional mean of Y_{CO_2}: Dashed black line: Fastchem-EMST, Full black line: REDIM-EMST, Symbols: experimental data.

from the single laminar flamelet is observed because Y_{CO_2} is a second independent parameter that enables to represent mixing of unburnt and burnt gases, different from the mixing in the laminar steady non-premixed flamelet. However, hardly any scatter is observed, as expected in our RANS-EMST framework. On the one hand, the use of RANS may not permit to capture some large scale intermittency. On the

other hand, and more importantly, the EMST mixing model which uses a mixing time scale proportional to the integral turbulent time scale, has limitations to model high scalar dissipation rate events [58, 60] as will be discussed below when introducing Equation (4.7).

In [124], local extinction and a mixing asymptote in the experimental results in compositional space are reported. In Figure 4.11 the latter can be recognized in the experimental scatter plot at $x/D = 0.2$ as the clustering of points around a line starting in the left bottom corner. This line, which is most likely due to mixing of burnt and unburnt gases in the shear layer between the annulus air flow and the recirculation zone close to the bluff body, is reproduced in the REDIM calculation with EMST as mixing model (and in [140], also with the modified Curl's mixing model [55]). This mixing line was also observed in [141], for the bluff-body flame HM1, which also has a recirculation zone caused by the bluff body. As shown in Figure 4.12, we can then correctly predict the conditional mean of Y_{CO_2} for lean mixtures at $x/D = 0.2$, although the cluster of experimental data around the laminar flamelet line observed in Figure 4.11 is missed. However, for rich mixtures between stoichiometry and $Z \approx 0.3$, the conditional mean is overestimated, due to the lack of scatter in the results.

At $x/D = 0.2$, for richer mixtures ($Z > 0.3$), we observe no scatter and all computational particles get their composition from the REDIM upper boundary. This could simply reflect the general limitations of our RANS-EMST modeling framework discussed above. It could also be explained by heat loss to the burner which is not taken into account, as discussed by Ihme et al. [142] for another swirling flame (SMH1). In Figure 4.11, the scatter plots are colored by the radial position in order to represent some correlation between composition and physical space. In the next section, the correlation between the scatter plots in composition space and the positions in physical space will help to better visualize how this rich branch in the modeled flame corresponds to a region located above the bluff body, consistent with the hypothesis of neglected heat loss of [142].

Note that in the experimental data the scatter, which is missed in our modeling approach, is observed both above and below the REDIM upper boundary, so that we still have good agreement for the conditional means.

At $x/D = 0.8$ and 1.5, the REDIM-EMST scatter plots resemble a single diffusion flamelet, while the experimental scatter plots show a large amount of scatter below the 'critical flamelet', which is reflected in an over-prediction of the conditional mean

of Y_{CO_2} in the simulations (Figure 4.12). This suggests that at these locations the REDIM-EMST calculation cannot capture the local extinction observed in the experiments and this will be discussed further in the next section, based on trajectories of computational particles.

4.5 Tracer trajectories

4.5.1 Characteristic regions in composition space

Following representative trajectories of particles is useful in order to discuss the correlation between the trajectories in physical space and the scatter plots in (Z, Y_{CO_2}) space. In order to correlate the trajectories in physical and composition space, we divided our (Z, Y_{CO_2}) space in different regions as shown in Figure 4.13a. These regions are delimited by the reference lines shown in Figure 4.2. Above the critical flamelet, we distinguish four zones: a lean region (dark blue), a stoichiometric region (yellow), a moderately rich region (green) and a rich region (brown). Below the critical flamelet, we make a distinction between a 'mixing line' region (light blue on the lean side, and dark purple on the rich side) and an intermediate region (red).

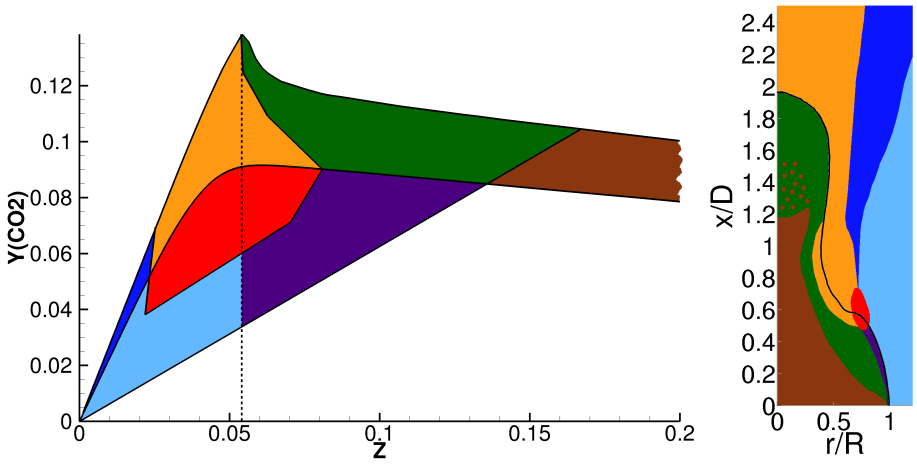

Figure 4.13: a/ Characteristic regions in composition space (left). b/ Map of the corresponding regions of the modeled flame in physical space (right).

The critical flamelet is used in the DNS study of [121] in order to distinguish between a continuously burning region and a region where extinction and re-ignition

occurs. In [121], not all points below the critical flamelet are interpreted as local extinction. Only particles coming from the flame zone and moving below the critical temperature profile are marked as extinguished. The history of the particle is clearly important. From Figure 4.2, we see that in the REDIM the critical flamelet goes through the region of highest CO_2 reaction rates. We can clearly see that the intermediate red region below the critical flamelet corresponds to a region of high CO_2 reaction rate such that this region will be modeled as a reaction zone (causing an upward motion in (Z, Y_{CO_2})-space). In order to possibly model extinction in this region of composition space, the mixing model should 'drive particles downwards' faster than the 'upwards motion' due to reaction. We would need a short mixing time compared to the reaction time (inverse of reaction rate) along the Y_{CO_2} direction in composition space. This mixing time can be written $1/\chi^*_{CO_2}$, where we can expect the modeled scalar dissipation rate for Y_{CO_2} to be of the IEM-type when using the EMST mixing model:

$$\chi^*_{CO_2} = C_\phi \omega^* \left(Y^*_{CO_2} - \widetilde{Y_{CO_2}} \right)^2 \quad \text{with} \quad \omega^* = \frac{\epsilon}{k}. \tag{4.7}$$

This scalar dissipation rate will be large if both the particle turbulence frequency ω^* and the particle Y_{CO_2}-fluctuation squared are large. However, the use of a mean turbulence frequency ϵ/k in the EMST mixing model implies a strong limitation in order to model high $\chi^*_{CO_2}$ events. A mixing model based on a scalar dissipation rate of the form of Equation (4.7) including a modeled fluctuating turbulence frequency ω^* like the PSP mixing model [58, 60, 59, 61] could provide a better framework in order to model local extinction.

We can therefore expect that it will be difficult to model local extinction below the critical flamelet with our modeling approach. Following particle trajectories will be useful in order to distinguish between local extinction and mixing, and to better understand the capacities and limitations of our modeling approach.

4.5.2 Map of characteristic regions of the modeled flame in physical space

Figure 4.13b shows a general map of the different characteristic zones of the modeled flame in physical space. It provides a general qualitative correlation between the different regions of composition space represented in Figure 4.13a and the positions in

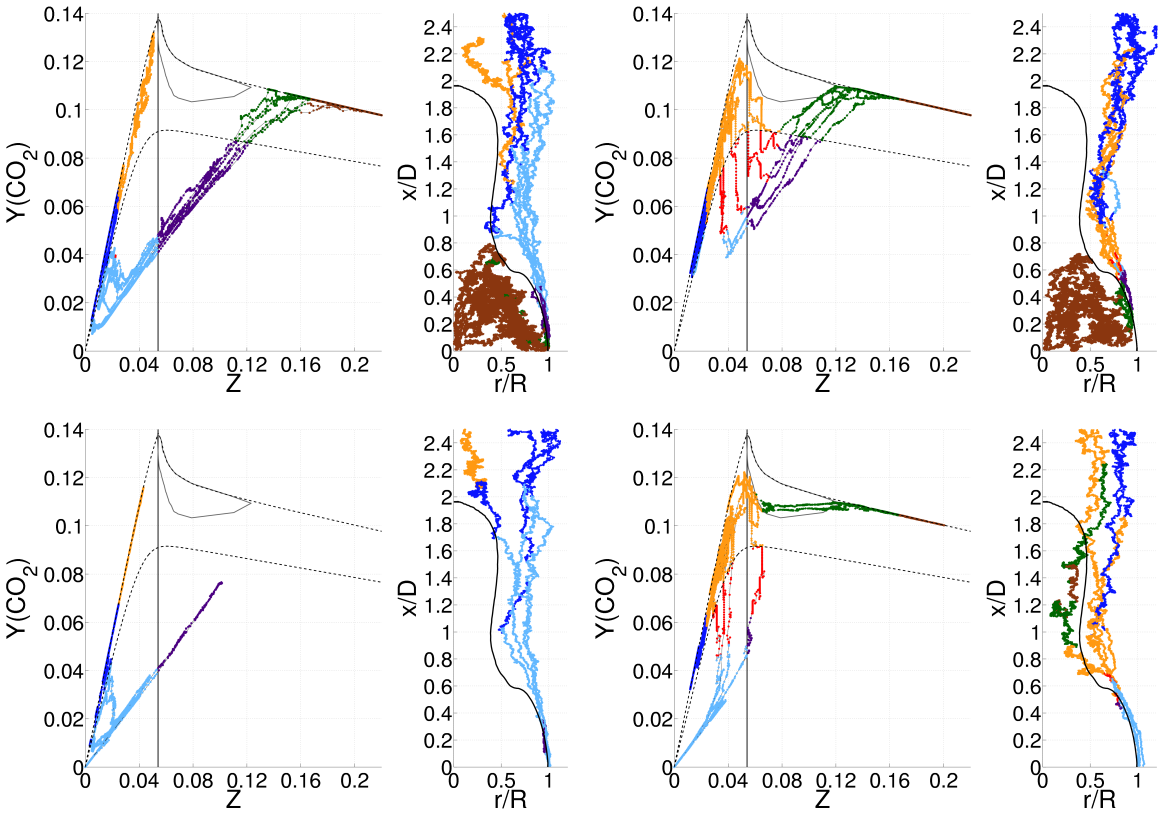

Figure 4.14: Trajectories of tracers interacting with the first recirculation zone. Tracers injected in the fuel jet: a/ without reaction and b/ reacting at the tip of the first recirculation zone. Tracers injected in the air coflow: c/ without reaction and d/ reacting at the tip of the first recirculation zone. Colour legend: see Figure 4.13

physical space. This map was drawn by looking at a large number of tracer trajectories as shown in Figures 4.14 and 4.15. Note that from the scatter plots shown in Figure 4.11, we could already identify that the mixing line observed in the scatter plots corresponds to the mixing of burnt and unburnt gases in the shear layer at the edge of the outer recirculation zone (light blue and dark purple regions), or that the rich flamelet branch corresponds to the inner recirculation zone (brown region). On the other hand, the tracer trajectories help to show that ignition occurs at the tip of the outer recirculation zone (red region). A more detailed discussion of representative tracer trajectories will now permit to show that our modeling approach cannot capture local extinction in the highly rotating collar region, and we will see that the second recirculation zone (where re-ignition is observed experimentally) is modeled as a rich hot zone.

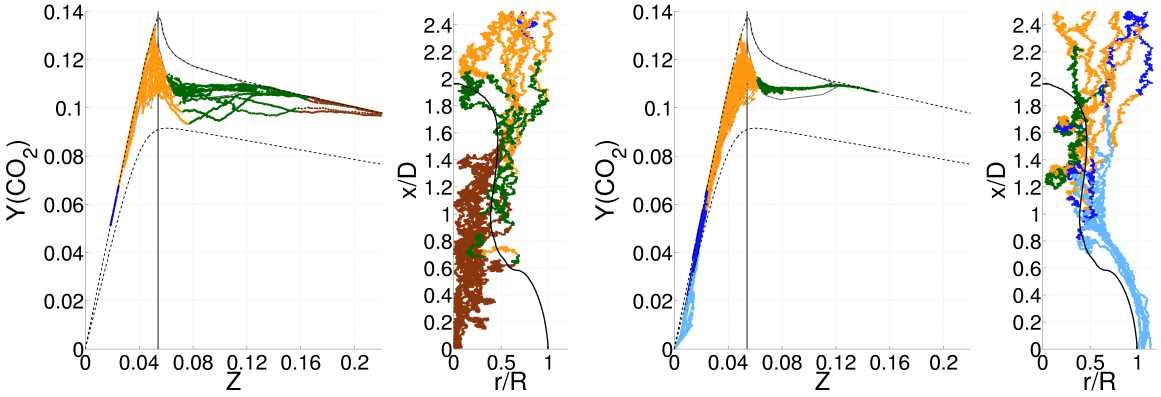

Figure 4.15: Trajectories of tracers passing around the first recirculation zone: a/ tracers injected in the fuel jet and b/ tracers injected in the air coflow. Color legend: see Figure 4.13

4.5.3 Trajectories in the outer edge of the first recirculation (mixing line)

Fuel and air tracers may have trajectories in the outer edge of the first recirculation zone as shown in Figure 4.14, where the fuel tracers have to cross the first recirculation zone, while the air tracers are directly injected at the outer edge. While crossing the first recirculation zone, the fuel tracers mix in the outer vortex with recirculated combustion products, resulting in an evolution towards stoichiometry along the rich flamelet branch. Eventually this hot (high Y_{CO_2}) rich mixture, mixes with air in the outer edge of the first recirculation zone. This mechanism of heating up the rich mixture before it mixes with fresh air stabilizes the flame and it is a direct result of the recirculation zone caused by the bluff-body. Depending on the trajectory in physical space, the particles fully mix in (Z, Y_{CO_2}) space towards the origin (as in Figure 4.14a) or deviate from the mixing line due to reaction (as in Figure 4.14b), and similar observations can be made for tracers injected in the air coflow.

Such representative trajectories of single tracers are shown in Figures 4.16 and 4.17 and will now be discussed in more detail. Note that after interaction in the shear layer between the outer vortex and the annulus air flow, a part of the particles recirculate in the outer vortex. These more complex recirculating trajectories can easily be interpreted as combinations of simpler trajectories. Therefore, in order to make the discussion easier, we choose to focus on simple trajectories that provide the essential information.

Mixing line: no reaction at the tip of the recirculation zone

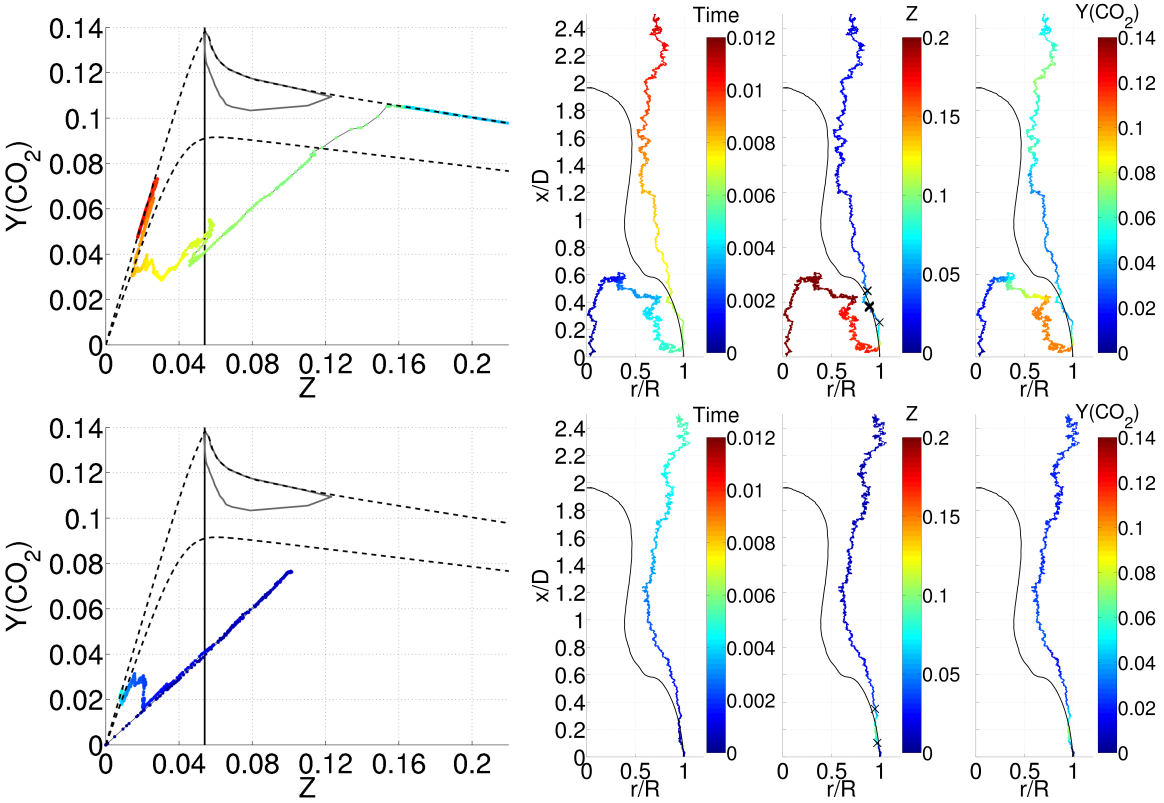

Figure 4.16: Representative trajectories of tracers interacting with the outer edge of the first recirculation zone without reaction (top: injected in the fuel jet / bottom: injected in the air coflow). Left: evolution in (Z, Y_{CO_2}) space colored by time. Right: evolution in physical space colored by time, Z (color-scale clipped at $Z = 0.2$, crosses: Z_{st}) and Y_{CO_2}. Black line: mean stoichiometric mixture fraction line.

Figure 4.16 reveals that the representative fuel tracer is first picked up by the inner vortex and passed on to the outer vortex in the first recirculation zone. During this period in time, the particle evolves in composition space along the rich flamelet branch. Once the annulus region is reached, the particle starts to mix with fresh air, represented in composition space by a mixing line almost straight from the point where the particle leaves the rich flamelet branch towards the origin $(0, 0)$. Evolution along this mixing line brings the particle below the 'critical flamelet' but this is no local extinction as the particle was not burning during or prior to its evolution along the mixing line. For this specific tracer there is a deviation from this mixing line, around stoichiometry: the tracer evolves to higher Y_{CO_2} and Z values, due to mixing with

rich combustion products. Eventually the particle moves horizontally in composition space to the lean flamelet branch, along which it evolves upwards, due to mixing with combustion products. Finally, it evolves downward, along the lean flamelet branch due to mixing with leaner gases.

Similar observations can be made for the air tracer. We mainly observe mixing between fresh air and hot products, and Y_{CO_2} remains low enough such that those tracers do not enter the region of high reactivity (i.e. it does not enter the red region in composition space in Figure 4.13).

Mixing line: reaction at the tip of the recirculation zone

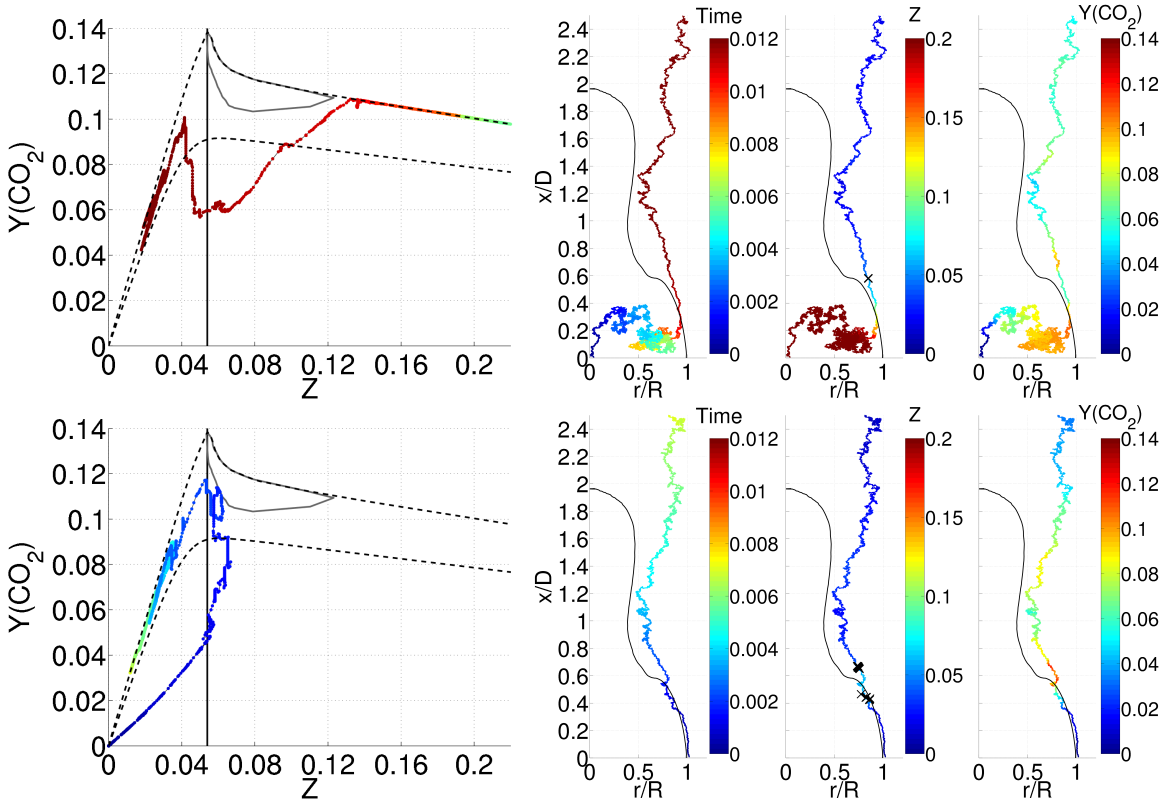

Figure 4.17: Representative trajectories of tracers interacting with the outer edge of the first recirculation zone and reacting at the tip of the recirculation zone (top: injected in the fuel jet / bottom: injected in the air coflow). Legend: see Figure 4.16.

Figure 4.17 shows tracer trajectories with an upward motion in Y_{CO_2}-space, also observed as a steep increase of Y_{CO_2} in physical space at the tip of the first recirculation zone, where the tracer enters the red zone of high reactivity in composition space

(Figure 4.13).

The representative fuel tracer first moves away horizontally from the mixing line, before reacting. The tracer evolves in a stepwise sense to the lean flamelet branch, intermittently switching between reaction (vertical) and mixing (sideward). Downstream interaction with air corresponds to an evolution along the lean flamelet branch. Similar trajectories were shown in Figure 4.14b. Along these trajectories there are small downward movements in the red and yellow zone in (Z, Y_{CO_2}) space, indicating that mixing may compete with reaction in the region of high reactivity, which corresponds to the highly rotating collar zone in physical space. These are relatively rare events causing only a small downward movement in (Z, Y_{CO_2}) space compared to the upward movements due to reaction. In general, no local extinction is observed for these tracers.

4.5.4 Trajectories passing around the first recirculation

Fuel particles crossing the neck zone

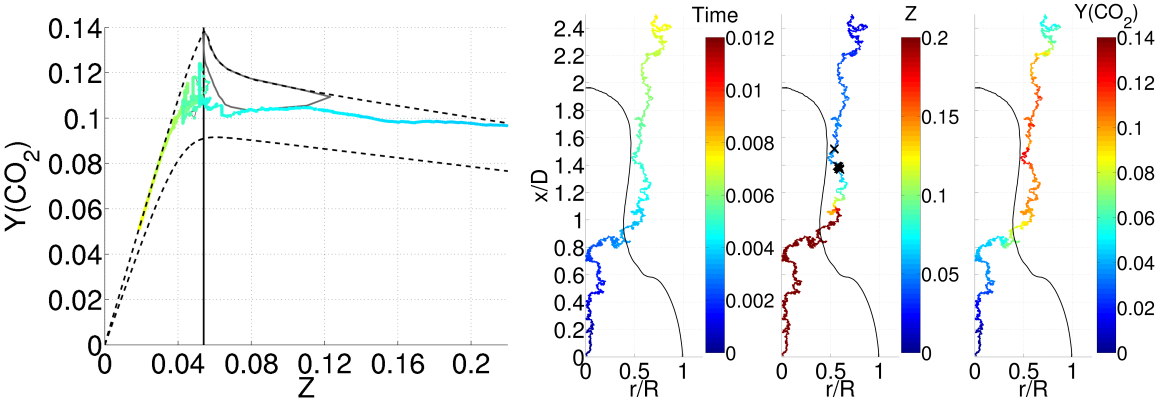

Figure 4.18: Representative trajectory of a fuel tracer not crossing through the first recirculation zone. Legend: see Figure 4.16.

Figure 4.18 shows a tracer trajectory that resembles a non-premixed flamelet in composition space and a jet-like trajectory in physical space. The particle flows past the first recirculation zone, meanwhile interacting with the inner vortex. In composition space this corresponds to an evolution along the rich flamelet branch. Downstream of the first recirculation zone the particle becomes stoichiometric towards the outer side of the second recirculation zone. There, around stoichiometry, there is much alternating vertically upward (reaction), downward and sideward (mixing) evolution

in composition space. Note that this corresponds to the end of the highly rotating collar region. As observed in the previous section, in the upstream part of the highly rotating collar region, we may say that mixing competes with reaction, but not enough in order to model local extinction. Further downstream the particle interacts with air, in composition space corresponding to an evolution along the lean flamelet branch.

Air particles interacting with the second recirculation zone

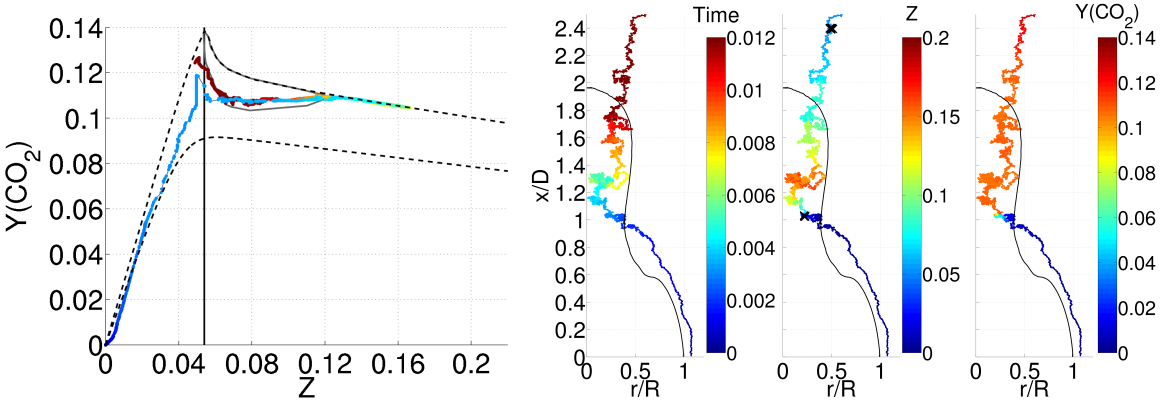

Figure 4.19: Representative trajectory of an air tracer interacting with the second recirculation zone. Legend: see Figure 4.16.

The representative tracer shown in Figure 4.19 first follows very briefly a mixing line, but very quickly evolves upward in composition space along a lean flamelet branch. Interaction with reacting particles thus appears in composition space as a flamelet-like evolution. Crossing stoichiometry, reaction takes place. In the rich region, which corresponds to the second recirculation zone in physical space, mixing with rich hot products takes place, seen as horizontal paths in composition space. This is in agreement with the experimental observation that the re-circulated hot products from the second recirculation zone would cause re-ignition.

4.6 Influence of the micro mixing model and the mixing constant C_ϕ

4.6.1 Flow and mixing fields

Now the influence of the micro-mixing model is discussed using REDIM. As was discussed above, with the EMST model a steady solution is obtained for $C_\phi = 2$. With CD, on the other hand the flame extinguishes for $C_\phi = 2$ and $C_\phi = 3$ is needed to obtain a burning solution. Similar observations were reported in [143] for the non-swirling bluff body flame HM3.

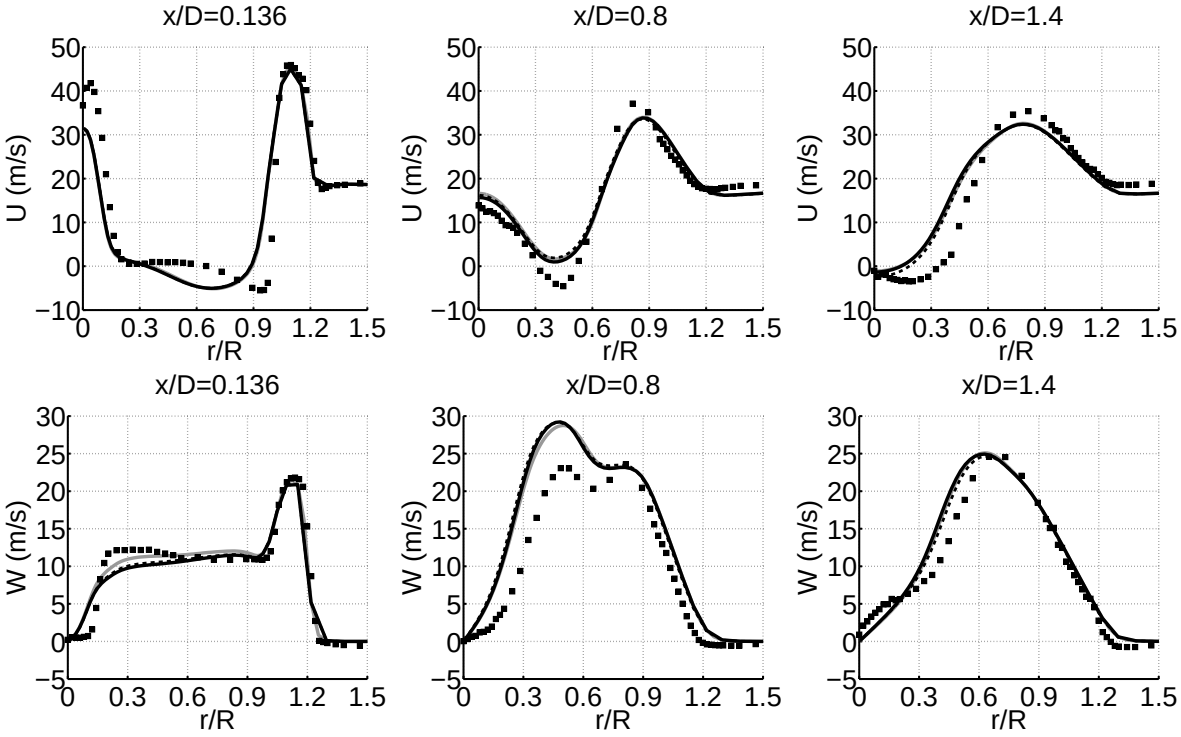

Figure 4.20: Mean axial and tangential velocity profiles. Full black line: REDIM-EMST $C_\phi = 2$, Grey line: REDIM-EMST $C_\phi = 1.5$, Dashed black line: REDIM-CD $C_\phi = 3$, Symbols: experimental data.

First we discuss the flow field shown in Figure 4.20. All calculations have almost identical profiles, suggesting that the micro-mixing model and the mixing constant C_ϕ do not have a substantial influence on the flow field. The largest difference is observed for the tangential velocity profiles at $x/D = 0.136$, where the EMST calculation with $C_\phi = 1.5$, has slightly higher values in the bluff body region.

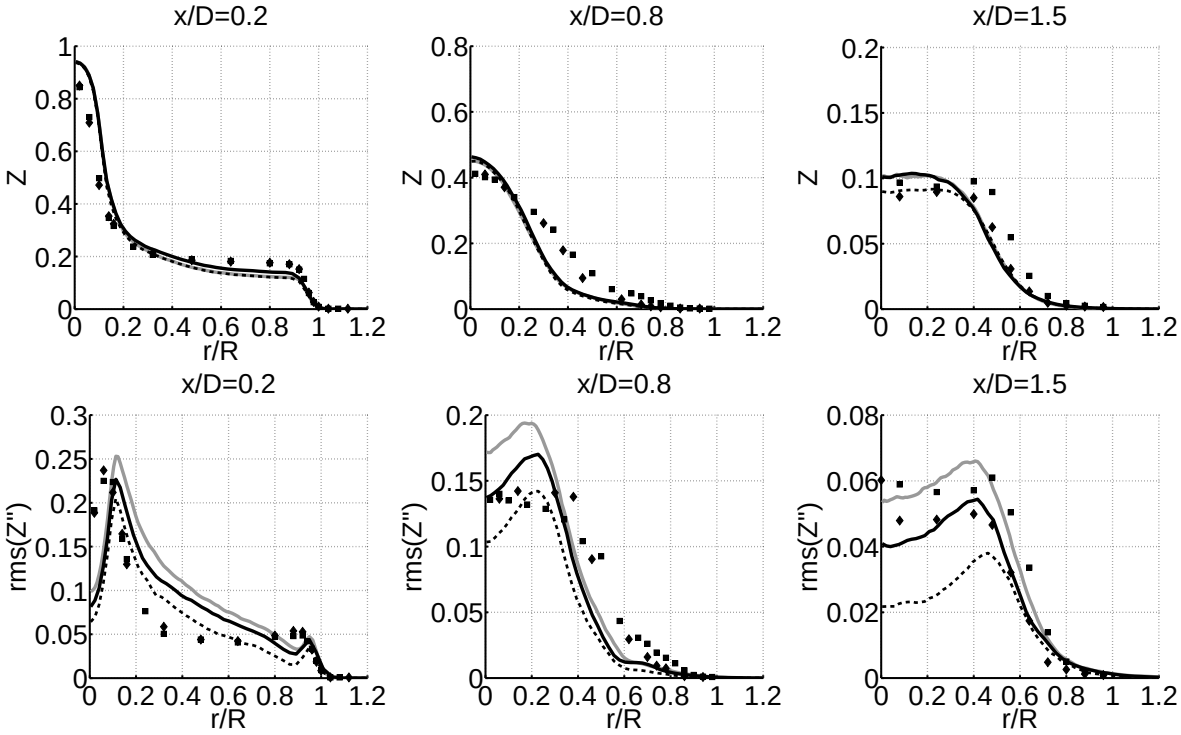

Figure 4.21: Mean mixture fraction and mixture fraction rms profiles. Full black line: REDIM-EMST $C_\phi = 2$, Grey line: REDIM-EMST $C_\phi = 1.5$, Dashed black line: REDIM-CD $C_\phi = 3$, Symbols: experimental data.

Next we discuss the mixing fields, i.e. the mean mixture fraction and mixture fraction rms profiles shown in figure 4.20. At $x/D = 0.2$, all calculations have almost identical profiles, but the EMST calculation with $C_\phi = 1.5$ and the CD calculation have a slightly lower mean mixture fraction in the bluff body region. All calculations under-predict the mixture fraction rms in the center region and over predict it in the bluff body region. Contrary to the mean mixture fraction the mixture fraction rms profiles of the different calculations differ substantially, with higher rms values for lower C_ϕ values. This is as expected, as lower C_ϕ values correspond to a slower decay of the scalar fluctuations. It should be noted that the influence of the mixing model on the rms values, cannot be determined from these profiles. At $x/D = 0.8$, the mean mixture fraction profiles are even more identical for all calculations and they are steeper compared to the experimental profile suggesting the calculations under-predict turbulent mixing of mass. The mixture fraction rms profiles, differ now the most in the center region, again with higher rms values corresponding with lower C_ϕ values. At $x/D = 1.5$, the CD calculation correctly predicts the mean mixture fraction in the

center region while the EMST calculations slightly over-predict it. The CD calculation however under-predicts the mixture fraction rms due to the high C_ϕ value, while the lower C_ϕ values of the EMST calculations lead to better results for the rms values. In general, the influence of the micro-mixing model on the mean mixture fraction only becomes important at a substantial distance from the burner. The mixing constant C_ϕ on the other hand mainly influences the mixture fraction rms.

4.6.2 Progress variable

Means

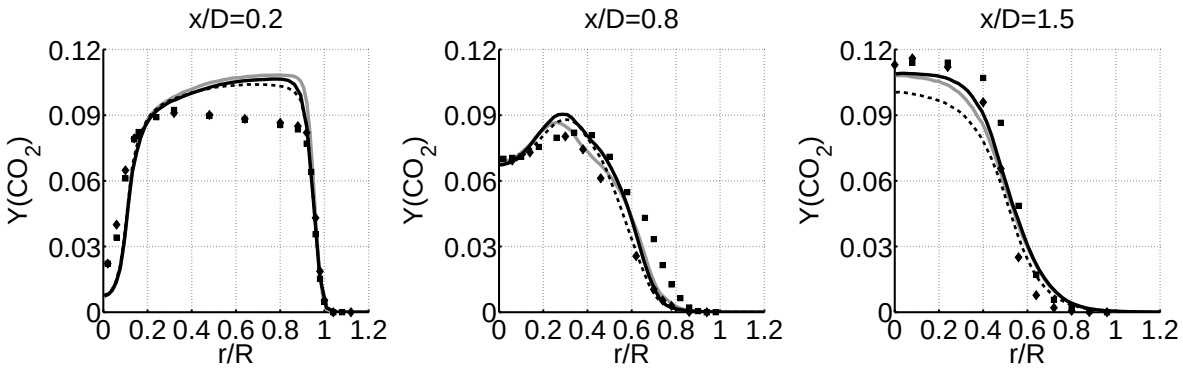

Figure 4.22: Mean Y_{CO_2} profiles. Full black line: REDIM-EMST $C_\phi = 2$, Grey line: REDIM-EMST $C_\phi = 1.5$, Dashed black line: REDIM-CD $C_\phi = 3$, Symbols: experimental data.

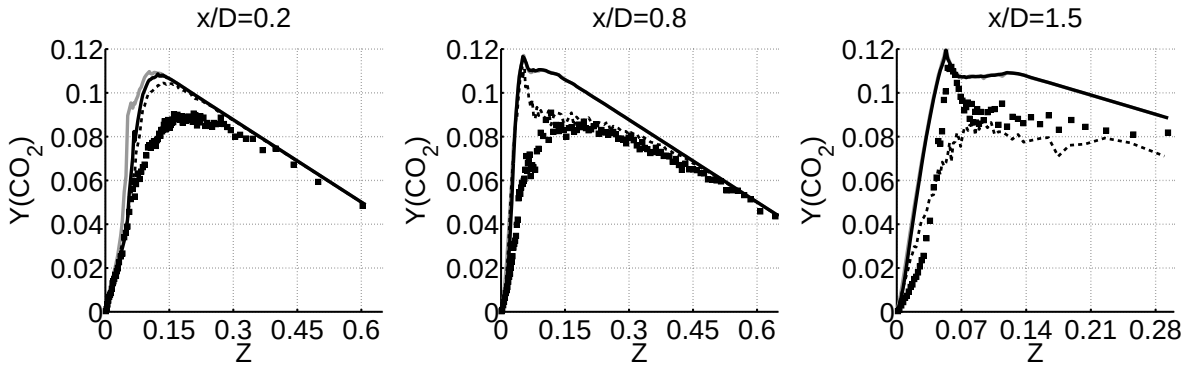

Figure 4.23: Mean conditional Y_{CO_2} profiles. Full black line: REDIM-EMST $C_\phi = 2$, Grey line: REDIM-EMST $C_\phi = 1.5$, Dashed black line: REDIM-CD $C_\phi = 3$, Symbols: experimental data.

The mean profiles of Y_{CO_2}, the second independent parameter of the REDIM table, are shown in figure 4.22. At $x/D = 0.2$, all the calculations over-predict Y_{CO_2} in the

bluff body region due to the under-prediction of the mean mixture fraction in that region and due to the over-prediction of the conditional mean Y_{CO_2} for $Z = 0.06 - 0.4$. In the center region, on the other hand, all calculations under-predict the mean Y_{CO_2} only due to the over-prediction of Z. The profiles of the calculations slightly differ among each other mainly due to differences in mean mixture fraction and conditional mean Y_{CO_2}. At $x/D = 0.8$, all calculations give very good predictions of the mean Y_{CO_2}, even though the mean mixture fraction was not predicted well at this axial position. The EMST calculations over-predict the conditional mean of Y_{CO_2} for $Z < 0.5$, while the CD calculation only over-predicts the conditional mean of Y_{CO_2} for $Z < 0.15$. Nonetheless, the mean Y_{CO_2} profiles of the EMST calculation with $C_\phi = 2$ and the CD calculation do not differ that much (Fig. 4.22). At $x/D = 1.5$, the EMST calculations slightly under-predict the mean Y_{CO_2} in the center region while the CD calculations predict even lower values, due to the lower conditional mean of Y_{CO_2} counteracting the lower mean mixture fraction for the CD calculations in that region. This higher conditional mean of Y_{CO_2} for CD indicates there is more scatter in Y_{CO_2}-space compared to the EMST calculations even though there is less scatter in Z-space (Figure 4.21). This is confirmed by the scatter plots shown in figure 4.24. In general the influence of the mixing model on the mean and conditional mean of Y_{CO_2} becomes more important further downstream. The mixing constant C_ϕ , on the other hand, only influences the conditional mean Y_{CO_2} close to the bluff body. The mean Y_{CO_2} is there mainly affected by differences of the conditional mean of Y_{CO_2} and Z. Further downstream, the mean Y_{CO_2} predictions are influenced indirectly by C_ϕ , through the changed mixture fraction rms.

Scatter plots

Now we analyse more closely the scatter plots of Y_{CO_2} shown in Figure 4.24. The green line is the upper boundary of the REDIM and the blue line is a steady diffusion flamelet close to extinction. Note that as these lines are plotted over the points, they might obscure some points. At $x/D = 0.2$, the scatter plots of the calculations are very similar, with slightly more scatter for the CD calculations. The line like structure, connecting the origin with the rich flamelet branch, is a mixing line representing mixing of combustion products with unburnt gasses as discussed in section 4.5. Also the points in the experimental scatter plots are clustered around a mixing line indicating a large part of the scatters in this region are due to mixing, although the scatters deviating from the mixing line might be due to extinction. At $x/D = 0.8$,

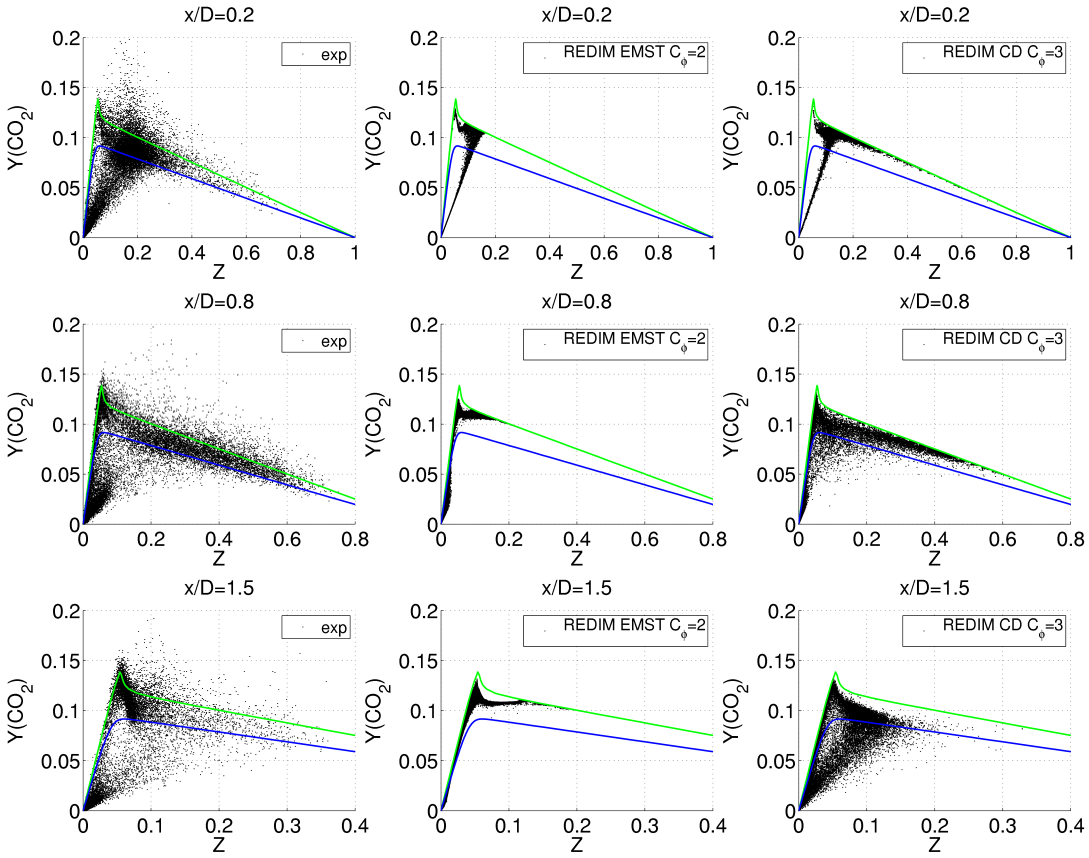

Figure 4.24: Scatter plot of Y_{CO_2} for $x/D = 0.2$, 0.8 and 1.5: upper boundary of REDIM(green line), steady diffusion flamelet close to extinction (blue line)

the scatter plots of the calculations differ substantially. The computational particles of the EMST calculation only access a confined space similar to a flamelet structure. The CD calculation, on the other hand, shows more scatter and accesses a larger area in composition space. Still, the level of scatter as observed in the experiments is not obtained. At this axial location, the majority of the scatter observed in the experiments are likely due to local extinction and subsequently mixing of extinguished mixtures with mixtures situated on the flamelet structure. At $x/D = 1.5$, the scatter plot of the EMST calculation still resembles a flamelet. The CD scatter plot, contains a substantial amount of scatter, but the distribution of the points in composition space is different from that in the experimental scatter plot as is also reflected in the conditional mean. Again a mixing line structure is observed in the scatter plot of the CD calculation, but now with more scatter around this mixing line. This is due to mixing of unburnt gases with combustion products from the second recirculation zone. This mixing line structure can not be easily observed in the experimental

scatter plots, where again local extinction and subsequent mixing is most likely the cause for the observed scatter. In Figure 4.25, three scatter plots between $x/D = 0.2$

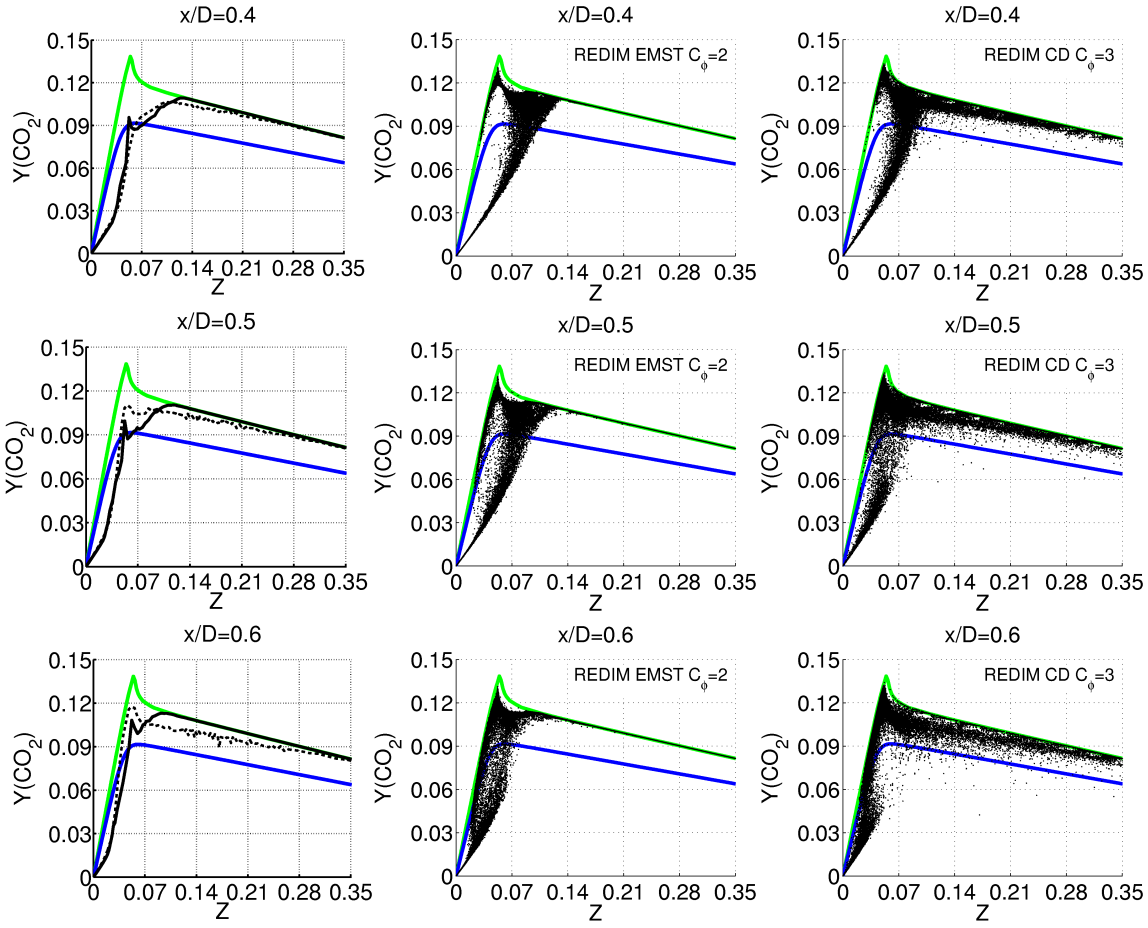

Figure 4.25: a/ Conditional mean of Y_{CO_2} for $x/D = 0.4$, 0.5 and 0.6 b/ Scatter plot of Y_{CO_2} for $x/D = 0.4$, 0.5 and 0.6 upper boundary of REDIM (green line), steady diffusion flamelet close to extinction (blue line)

and $x/D = 0.8$ are shown, in order to further investigate the evolution of the flame structure for both mixing models. At $x/D = 0.4$, the flame structure for both mixing models is still reasonably similar, but for CD more points deviate from the upper boundary of the REDIM, while for EMST all points for $Z > 0.15$ are on the upper boundary. This is confirmed by the almost identical conditional means. At $x/D = 0.5$, on the other hand, the flame structures are quite different for both mixing models. For the EMST calculation, most of the particles still follow the mixing line and a minority deviates from this mixing line due to reaction. For CD, the majority of the particles start deviating from the mixing line around stoichiometry due to reaction.

The higher conditional mean around stoichiometry confirms this higher reactivity for the CD calculation. The reason for this not completely clear, but the higher C_ϕ value for the CD calculation is a possible cause. A second probable explanation is the non-localness of CD making it easier for particles on the mixing line to be 'pulled off' that mixing line due to mixing with reacting particles. Finally, at $x/D = 0.6$, the particles in the EMST calculation are now also deviating from the mixing line due to reaction, while in the CD calculation the flame structure has already evolved to a more flamelet like structure. Further downstream, the flame structure in the EMST calculation also evolves towards a flamelet like structure.

In general, the amount of scatter for CD is substantially higher than for EMST and the difference is larger further downstream, due to the difference in localness. With CD, all particles can interact with each other (non-localness), while with EMST only particles which are close in composition space will interact (localness). We analyse the behaviour of the mixing models more profoundly in the next subsection by following the computational particles as they move through composition space.

Tracers

First, the temporal evolution of a group of representative tracers is discussed for both mixing models. Keep in mind that in order to keep the pictures clear, we only look at the less complex trajectories, without multiple recirculations. Nonetheless, this does not affect the global validity of our conclusions.

In Figure 4.26 the evolution of some representative tracers from the EMST-calculation with $C_\phi = 2$ are shown. The particles injected at the annulus either move along the lean flamelet branch or the flatter mixing line, as seen in the Eulerian scatter plots at $x/D = 0.2$. The particles injected at the fuel jet first follow the rich flamelet branch before reacting or mixing with leaner, less reactive gases, resulting in a mixing line structure, which connects with the mixing line of the annulus injected particles. The tracers of the CD calculations shown in Figure 4.27 are harder to follow as they jump in composition space due to the non-localness of CD. This also leads to the higher amount of scatter observed in the Eulerian scatter plots. The tracers injected at the fuel inlet can jump off the rich flamelet branch at a richer mixture fraction than is the case with the EMST model, leading to flatter mixing lines which are different from the mixing line structure at $x/D = 0.2$. Therefore lower Y_{CO_2} values are reached for $Z = Z_{stoich} - 0.4$ as seen in the scatter plots of CD at $x/D = 0.8$ and 1.5. This is

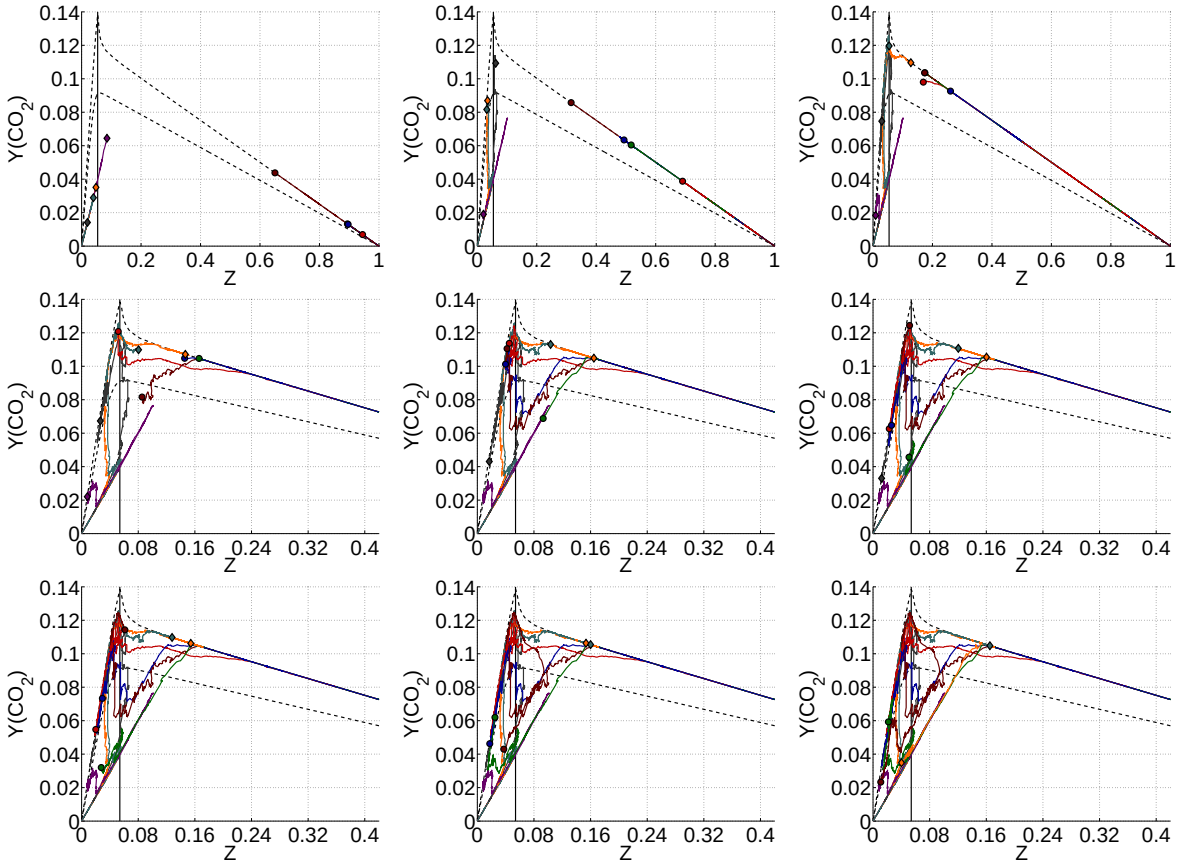

Figure 4.26: Evolution of representative computational particles for EMST calculation with $C_\phi = 2$: particles injected at the fuel inlet (diamonds), particles inject at annulus air inlet (circle) upper boundary of the REDIM (upper dashed line), steady diffusion flamelet close to extinction (lower dashed line), stoichiometric mixture fraction (vertical black line)

discussed in more detail below.

Now we look at the tracers as we have done in section 4.5. As was shown in Figure 4.27, a new area in composition space is accessed in the CD calculations. Therefore, we have added the gray area to the map in composition space in Figure 4.28. In physical space this gray area starts around $x/D = 0.8$ and is mainly situated in the shear zone between the second recirculation vortex and the annulus air flow. In Figure 4.29, the tracers interacting with the first recirculation zone are shown. In composition space, these trajectories do not differ much from the trajectories of the EMST calculation.(Figure 4.14). The same mixing line structure is seen and a similar area in composition space is accessed. This explains the similar scatter plots at $x/D = 0.2$ for the EMST and CD calculations.(Figure 4.24) Of course, some jumps

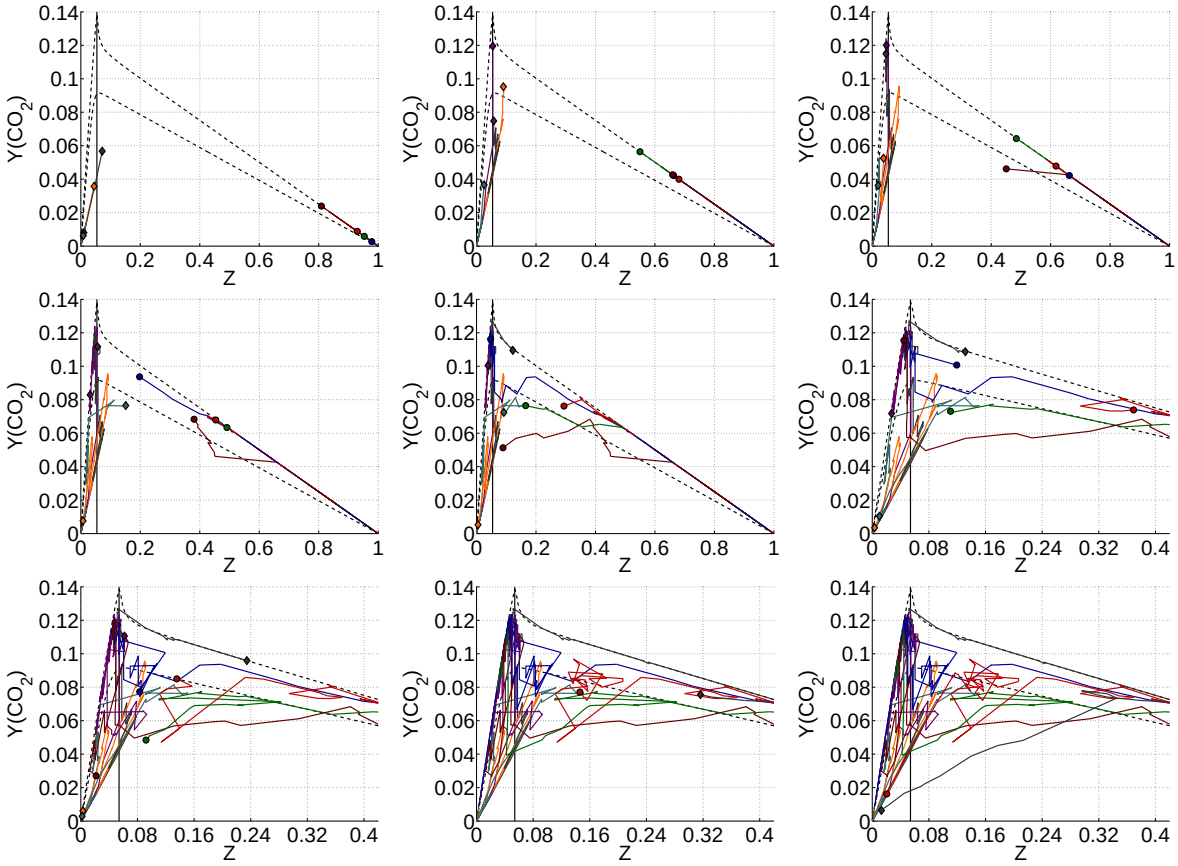

Figure 4.27: Evolution of representative computational particles for CD calculation with $C_\phi = 2$: particles injected at the fuel inlet (diamonds), particles inject at annulus air inlet (circle) upper boundary of the REDIM (upper dashed line), steady diffusion flamelet close to extinction (lower dashed line), stoichiometric mixture fraction (vertical black line)

in composition space due to the non-localness of CD can be seen, but they do not strongly affect the flame structure in the neighborhood of the first recirculation zone.

Also the CD trajectories shown in Figure 4.30 are fairly similar to the EMST trajectories shown in Figure 4.15. These trajectories mainly follow a flamelet structure in composition space, although some trajectories shortly pass below the critical flamelet coinciding with a movement in physical space through the shear layer between the second recirculation zone and the more radially outward air flow. In this shear layer the corresponding tracers mix with computational particles situated below the critical flamelet, resulting in the passages below this critical flamelet. This was not observed for the EMST calculations and is therefore specific for the CD calculations. More specifically, as was observed in the scatter plots of Figure 4.24, the EMST cal-

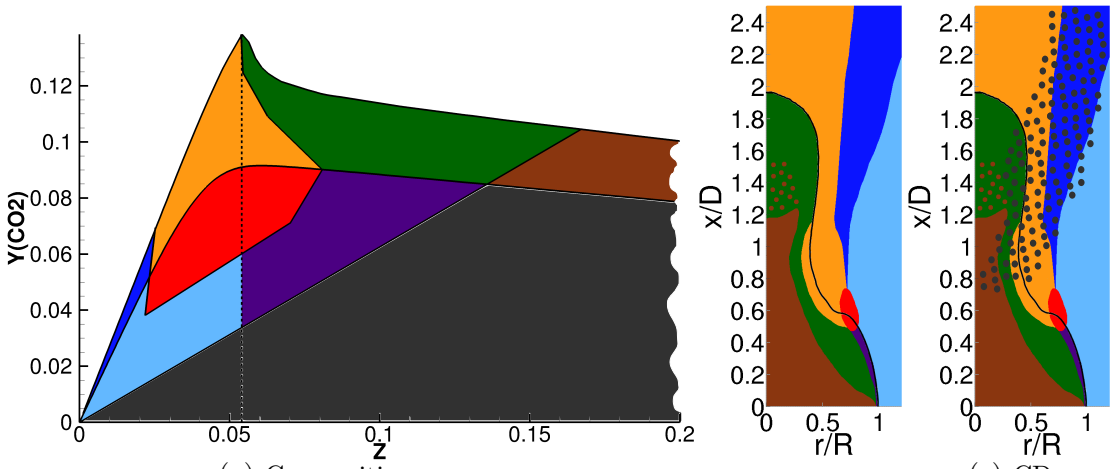

(a) Composition space (b) EMST (c) CD

Figure 4.28: a/ Characteristic regions in composition space (left). b/ Map of the corresponding regions of the modeled flame in physical space with EMST (middle). c/ Map of the corresponding regions of the modeled flame in physical space with CD (right).

culations have a flamelet structure in composition space for $x/D \geqslant 0.8$. In the CD calculations, on the other hand, there is still scatter below the critical flamelet at $x/D = 0.8$ due to the non-localness of the mixing. Further downstream the amount of scatter below the critical flamelet even increases due to the combined effect of the non-localness of the mixing model and the presence of scatter below the critical flamelet. In Figure 4.31 we show the trajectories responsible for this scatter below the critical flamelet observed in the CD scatter plots for $x/D \geqslant 0.8$. A first important observation is that the trajectories situated in composition space below the critical flamelet, move in physical space through the shear layer between the second recirculation zone and the radially more outward air flow. For the tracers injected at the fuel inlet two scenarios can be observed. For both scenarios the tracers leave the rich flamelet branch due to mixing with particles from the gray zone. However, depending on the slope of the mixing line, the tracers either mix towards the origin (pure air) or react around stoichiometry. This is similar to the trajectories which interacted with the first recirculation zone (Figure 4.29 a and b), but now the mixing lines are less steep and they are spread over a wider area in composition space. These trajectories explain the mixing line structure observed in the scatter plot of the CD calculation at $x/D = 1.5$. For the tracers injected at the air inlet only one scenario is observed: mixing followed by reaction around stoichiometry. In composition space the trajectories are almost identical to the trajectories in Figure 4.29d. The only difference is the

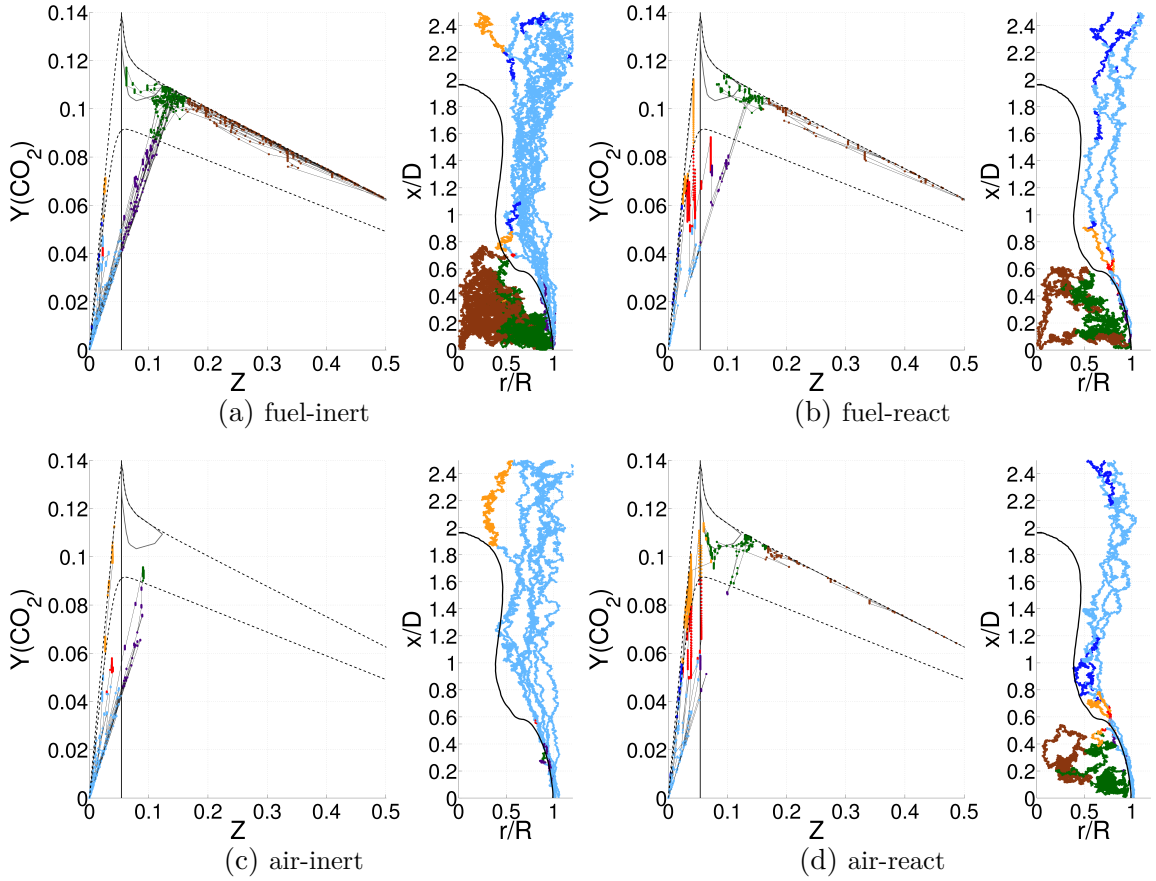

(a) fuel-inert (b) fuel-react

(c) air-inert (d) air-react

Figure 4.29: Trajectories of tracers interacting with the first recirculation zone. Tracers injected in the fuel jet: a/ without reaction and b/ reacting at the tip of the first recirculation zone. Tracers injected in the air coflow: c/ without reaction and d/ reacting at the tip of the first recirculation zone. Colour legend: see Figure 4.28

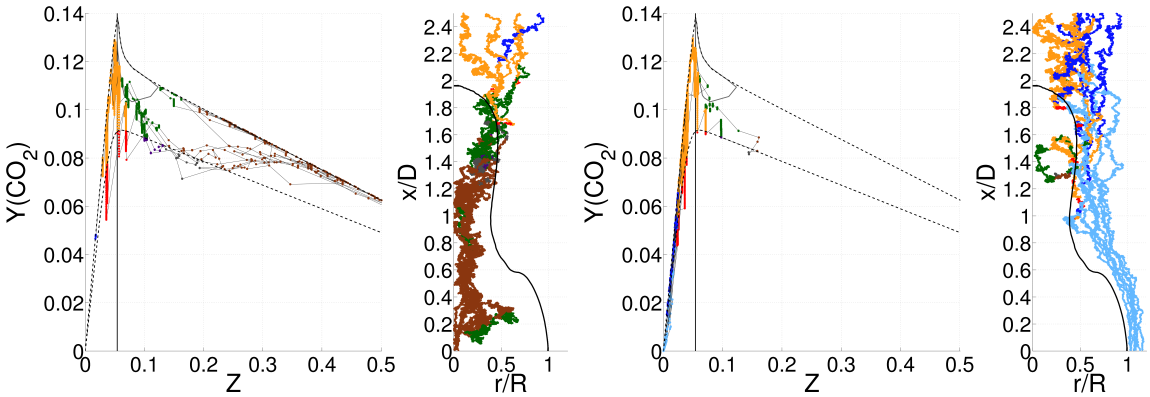

(a) fuel-flamelet (b) air-flamelet

Figure 4.30: Trajectories of tracers following a flamelet structure in composition space: a/ tracers injected in the fuel jet and b/ tracers injected in the air coflow. Color legend: see Figure 4.28

place of interaction in physical space: either the first or the second recirculation zone. No trajectories were found, which cross from the origin to the rich flamelet branch through the gray area in composition space. As 10000 tracers, injected over more than 200 time steps, were analysed, it seems reasonable to conclude that these trajectories are very unlikely in these calculations. A reason for this could be the short residence time of the air stream tracers, restricting the time to mix with richer particles.

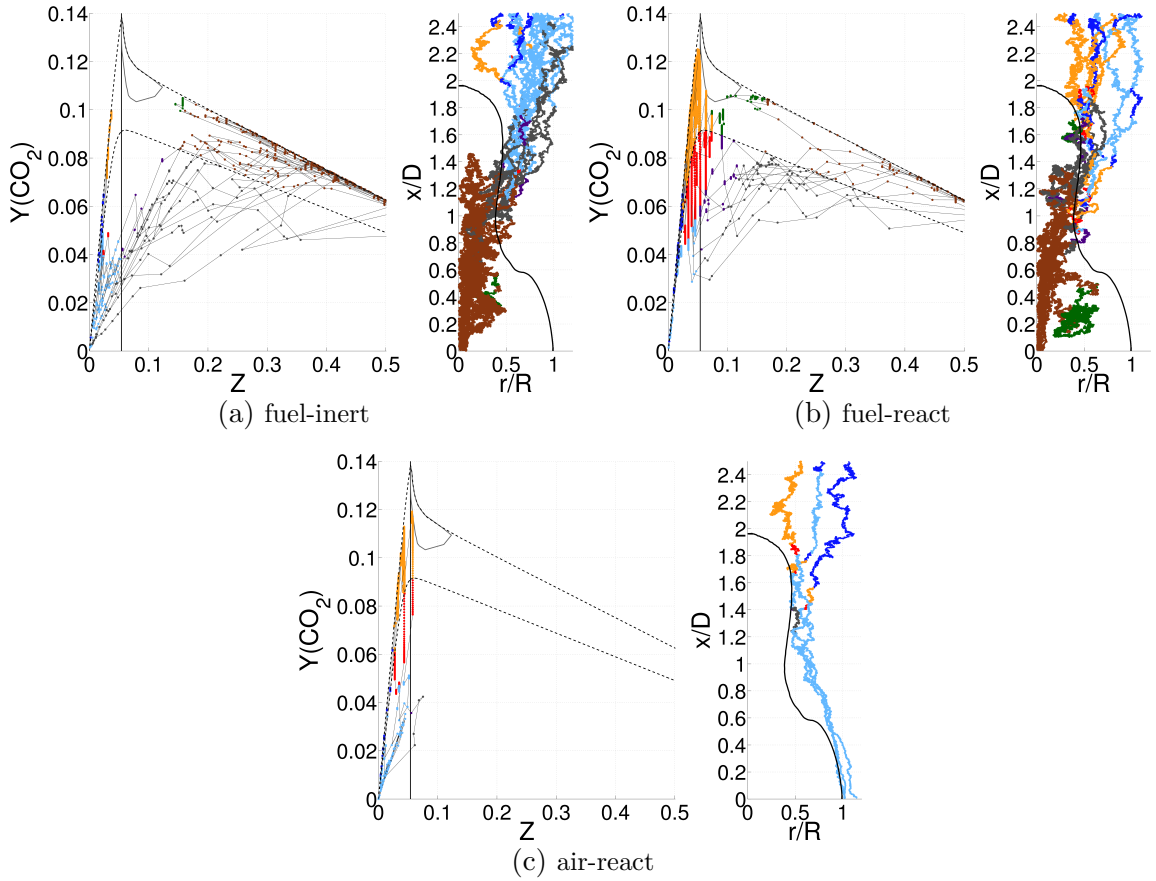

(a) fuel-inert (b) fuel-react

(c) air-react

Figure 4.31: Trajectories of tracers interacting with the second recirculation zone. Tracers injected in the fuel jet: a/ without reaction and b/ with reaction. Tracers injected in the air coflow: c/ with reaction. Color legend: see Figure 4.28

Local extinction Now we briefly discuss the modelling of local extinction for the two mixing models. As has been discussed in section 4.5.1 the EMST model is limited in its ability to predict local extinction due to the mean mixing time scale. As the mean mixing time scale prevents the occurrence of high scalar dissipation rates and the mixing with the EMST model is local in composition space, strong mixing events will be very rare. Also the CD model uses this mean mixing time scale, but due to the non-local mixing of CD strong mixing events are possible for specific particles. However, this does not mean that the CD model correctly predicts local extinction, as local extinction is a function of the local Damkohler number and this is not accounted for in the CD model. This often lead to an over-prediction of "local extinction". In [144], the Damkohler effect is accounted for through a dynamically calculated C_ϕ, which results in a modified mixing time scale [49]. In [144] this leads to a better overal prediction for the CD calculation of the HM2 flame. We now look at some tracers from the CD calculation, to show this specific behaviour of the CD mixing model. In Figure 4.32, trajectories of tracers injected in the fuel jet are shown. On both trajectories pure reaction, recognized by a purely vertical movement in $Z - Y_{CO_2}$ space, is interrupted by a downward movement due to mixing. This could be interpreted as local extinction, as physically local extinction can be caused by excessive mixing of a reacting mixture with a colder mixture. The downward movement is done by a relatively large jump in composition space, suggesting that the non-localness of CD is responsible for this jump as in the EMST trajectories smaller jumps were observed. In Figure 4.32a, the jumps representing local extinction are still relatively small and they take place above and under the critical flamelet, but never cross the critical flamelet. In Figure 4.32b, on the other hand, a big jump, crossing the critical flamelet and stoichiometry, is observed. This is definitely due to the non-local mixing of the CD model. In Figure 4.33, trajectories of tracers injected in the air annulus with local extinction at the first recirculation zone are shown. For the trajectory shown in Figure 4.33a, the tracer first mixes with combustion products along a mixing line as seen for EMST and CD calculations. The tracer then returns towards the origin along a similar mixing line until it deviates from this mixing line due to mixing with a more reactive mixture. The tracer eventually starts to react, as seen by the red vertical part of the trajectory, but is then extinguished due to mixing with a less reactive mixture and finally mixes further with air towards the origin. In other words, the mixing of the tracer with a less reactive mixture has prevented the tracer from completely reacting to the flamelet region. The tracer shown in Figure 4.33b, also has some local extinction close to stoichiometry, but this tracer still completely reacts to the flamelet

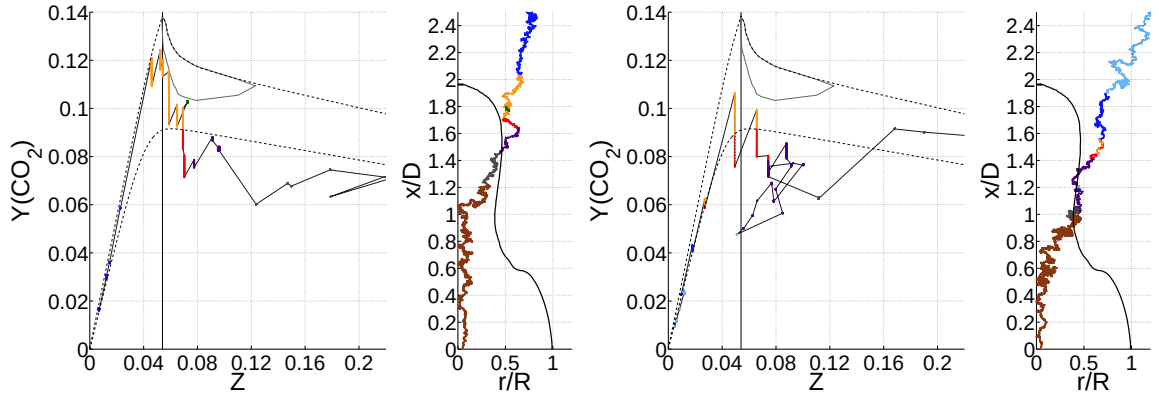

(a) extinction below critical flamelet (b) extinction crossing critical flamelet

Figure 4.32: Representative trajectory of a tracer injected in the fuel jet with local extinction: a/ below critical flamelet and b/ crossing critical flamelet. Color legend: see Figure 4.28

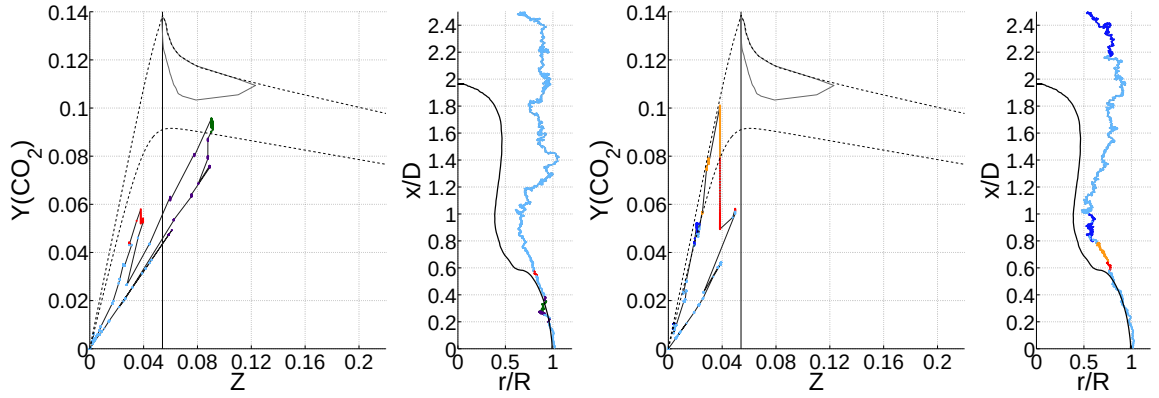

(a) extinction - no reaction afterwards (b) extinction - reaction afterwards

Figure 4.33: Representative trajectory of a tracer injected in the air annulus with local extinction in the first recirculation zone: a/ no reaction afterwards and b/ reaction afterwards. Color legend: see Figure 4.28

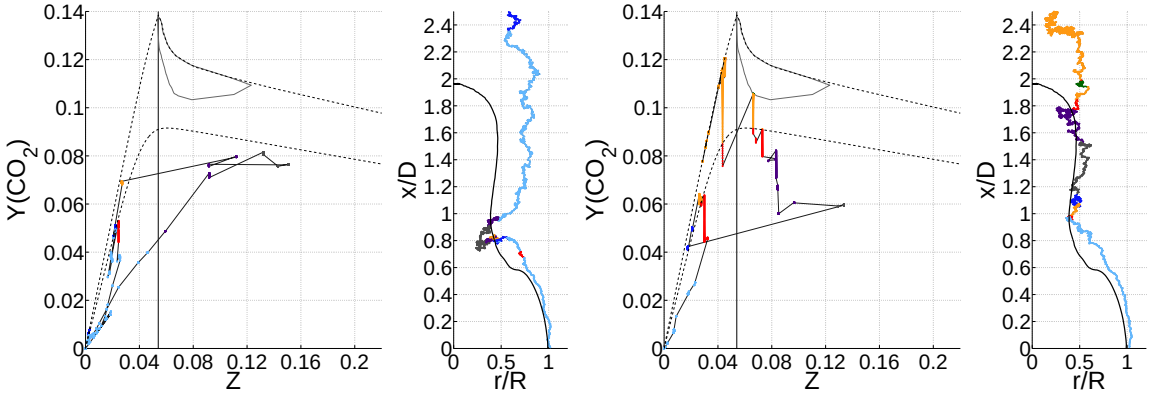

(a) skip reaction zone - no reaction afterwards

(b) skipreaction zone - reaction afterwards

Figure 4.34: Representative trajectory of a tracer injected in the air annulus crossing stoichiometry without reacting: a/ no reaction afterwards and b/ reaction afterwards. Color legend: see Figure 4.28

region afterwards, as the mixing is not strong enough to completely extinguish the tracer. Finally in Figure 4.34, tracers are shown which jump over the reaction zone without reacting. These jumps take place in the shear layer of the fuel and air stream after the first recirculation zone ($x/D = 0.8 - 1.2$). It is these kind of jumps which are often pinpointed as the reason for the over-prediction of local extinction with the CD model. In the very least, the competition between mixing and reaction is not represented correctly during these jumps. The tracer in Figure 4.34a, jumps over the reaction zone, mixes further into the gray area and finally mixes back to the origin. The tracer in Figure 4.34a, on the other hand, mixes back towards stoichiometry to finally react to the flamelet region. For this tracer also a jump over the critical flamelet, which could be interpreted as local extinction, is observed, similar as for the fuel tracer in Figure 4.32b.

Concluding, in the framework of hybrid RANS-PDF calculations none of the mixing models are able to correctly model local extinction. EMST under-predicts the amount of scatter. CD on the other hand predicts a reasonable amount of scatter, which might be interpreted as local extinction in the scatter plots, but this is rather a consequence of the non-localness. This non-local mixing allows the particles situated on the flamelet structure to mix with particles which do not lay on this flamelet, hence pulling the former from the flamelet. This has been shown clearly by the means of Lagrangian tracers. For the CD calculation also some trajectories seemed to predict local extinction events, but this was again a consequence of the non-local

mixing of CD and does not correctly describe the competition between mixing and reaction described by the local Damkohler number. To truly model local extinction the fluctuations of the scalar dissipation rate need to be represented and this is not the case for this modeling framework, as a mean mixing time scale is used within one cell. Although the mixing model is definitely an important factor in the prediction of local extinction, other limitations in the current modelling framework might also have strong impact on the results as discussed above: limitations of REDIM in order to model local extinction or even limitations of the RANS approach for this flame where unsteady effects in physical space may have a strong impact on the results in composition space. A profound study of the different time scales involved could help to better highlight the true influence of the mixing model but this is beyond the scope of this PhD research.

4.6.3 Dependent properties: T and Y_{OH}

Finally, we discuss the mean results for T and Y_{OH}. In the framework of this study these are dependent properties as for each computational particle they are read from the REDIM table based on Z^* and $Y^*_{CO_2}$. Although both Y_{CO_2} and temperature are

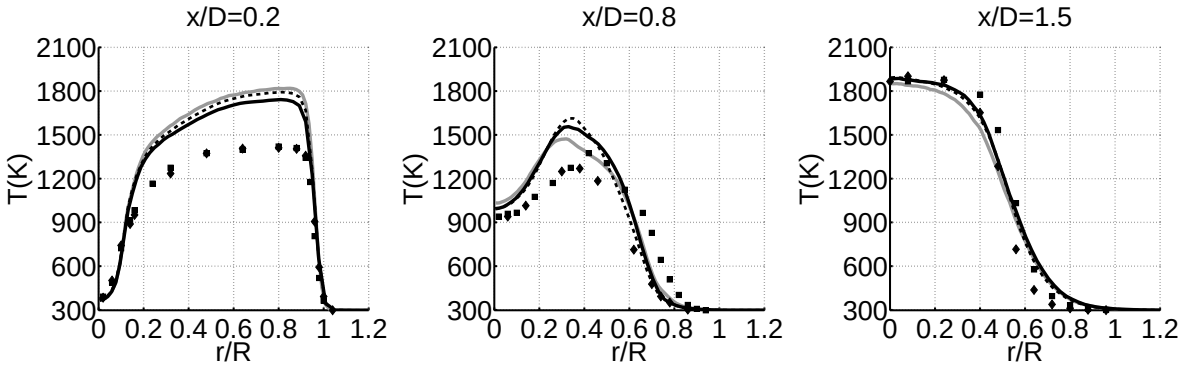

Figure 4.35: Mean temperature profiles. Full black line: REDIM-EMST $C_\phi = 2$, Grey line: REDIM-EMST $C_\phi = 1.5$, Dashed black line: REDIM-CD $C_\phi = 3$, Symbols: experimental data.

measures of reaction progress, the mean profiles differ. For example at $x/D = 0.2$, while the CD calculations predict lower values of Y_{CO_2} compared to the EMST calculation with $C_\phi = 2$, the temperature in the CD calculation is higher than that of the EMST calculation with $C_\phi = 2$. This is due to the smaller difference in the conditional mean of temperature (Figure 4.36) for both calculations, compared to the conditional mean of Y_{CO_2}. Therefore the lower mean mixture fraction value of the CD calculation

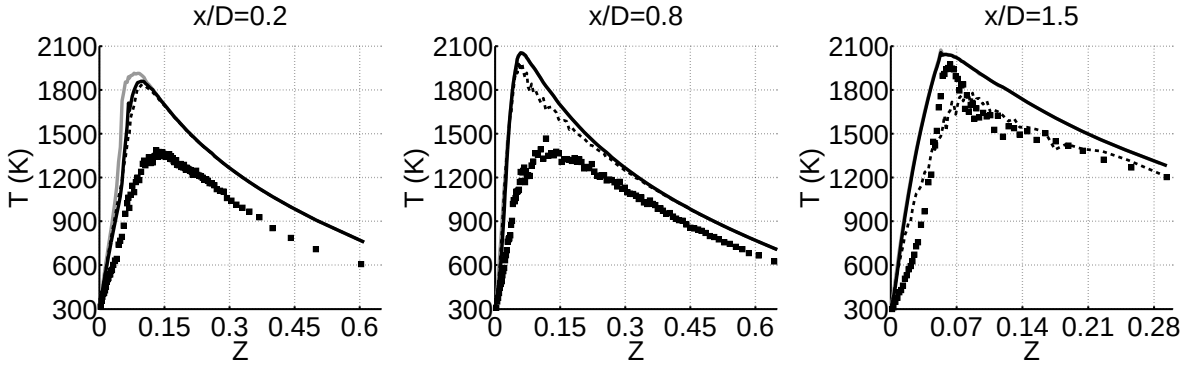

Figure 4.36: Mean conditional temperature profiles. Full black line: REDIM-EMST $C_\phi = 2$, Grey line: REDIM-EMST $C_\phi = 1.5$, Dashed black line: REDIM-CD $C_\phi = 3$, Symbols: experimental data.

is now not counteracted by the lower conditional mean of temperature. With the exception of the CD calculation at $x/D = 1.5$ the conditional mean of temperature is in general over-predicted more strongly than the conditional mean of Y_{CO_2}. This is in line with the results of the a priori study (section 4.3.3). At $x/D = 0.2$ and $x/D = 0.8$ this leads to a stronger over-prediction of the mean temperature. At $x/D = 1.5$, on the other hand, this results in a correct prediction of the mean temperature for all calculations.

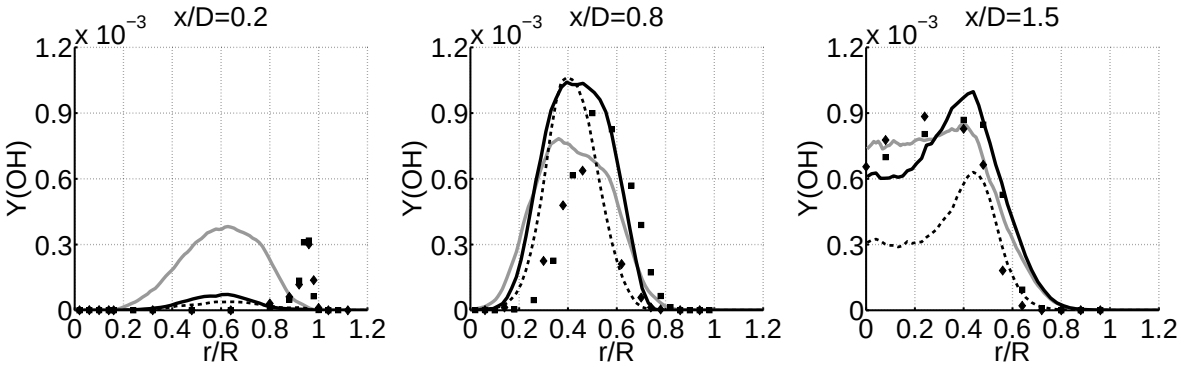

Figure 4.37: Mean Y_{OH} profiles. Full black line: REDIM-EMST $C_\phi = 2$, Grey line: REDIM-EMST $C_\phi = 1.5$, Dashed black line: REDIM-CD $C_\phi = 3$, Symbols: experimental data.

Finally, we discuss the mean and conditional mean of Y_{OH}.(Figures 4.37 and 4.38) In general, the mean Y_{OH}-profiles for the different calculations differ strongly due to the different prediction of the mean mixture fraction close to stoichiometry and the different conditional means of Y_{OH}. As for temperature, the conditional means of

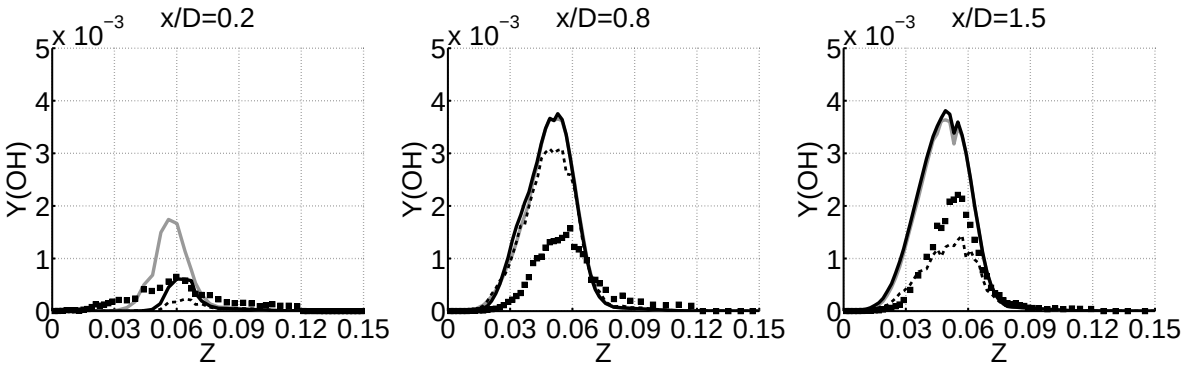

Figure 4.38: Mean conditional Y_{OH} profiles. Full black line: REDIM-EMST $C_\phi = 2$, Grey line: REDIM-EMST $C_\phi = 1.5$, Dashed black line: REDIM-CD $C_\phi = 3$, Symbols: experimental data.

Y_{OH} in the EMST calculations are only influenced by the different values of C_ϕ close to the bluff body, where the calculation with $C_\phi = 2$ gives the best prediction.. Further downstream, the EMST calculation systematically over-predicts the conditional mean of Y_{OH} due to the under-prediction of the amount of scatter in Y_{OH}-space, resulting from an under-prediction of the amount of scatter in Y_{CO_2}-space. The CD calculation on the other hand has more scatter in Y_{CO_2} and Y_{OH}-space, resulting in lower conditional means of Y_{OH}.

4.7 Conclusions

Steady axisymmetric transported scalar PDF modeling of a swirling flame stabilized behind a bluff-body burner (swirling flame 'SM1') with a 2D Reaction Diffusion Manifold (REDIM) has been discussed. With an ad hoc adjustment of the turbulent Schmidt number, the results in physical space for flow and mixing fields, obtained in a non-linear k-ϵ RANS modeling framework, are in reasonable agreement with experimental data and comparable to LES results from the literature.

In REDIM, the concept of progress variable is used — in the present case the CO_2 mass fraction Y_{CO_2} — and the entire (Z, Y_{CO_2}) space is covered. An a priori study has been performed, indicating that the REDIM can capture the main features of the experimental measurements in (Z, Y_{CO_2}) space. Compared to a modeling based on a single steady laminar flamelet (which can be seen as a fast chemistry model in the 1D Z-space), results obtained with REDIM for the turbulent flow, temperature and composition fields are in general in better agreement with experimental data

in physical space. This is related to the modeling in composition space, where the REDIM benefits from the use of a progress variable, allowing access to the low Y_{CO_2}-region. As a result, the mixing between fresh air and hot products in the recirculation zone above the bluff-body burner can be modeled.

This important qualitative agreement is observed in the (Z, Y_{CO_2}) scatter plots, as a mixing line in composition space. This mixing line, also observed in the non-swirling bluff-body flames, is indeed due to mixing between fresh air and hot products and not due to local extinction. On the other hand, the calculation results represent too little scatter compared to the experimental data, especially downstream. This indicates that the local extinction which is assumed to occur experimentally in the highly rotating collar region is not captured in the present modeling framework. The fact that heat loss at the bluff-body surface is neglected, as discussed by Ihme et al. [142] for another swirling flame, also appears to be a plausible explanation for the underestimation of scatter on the rich side.

The trajectories of computational particles in composition space and physical space have been studied as these allow to distinguish mixing from local extinction, which is not possible by means of local scatter plots alone. Through analysis of the trajectories, we can also better understand the correlation between the scatter plots in composition space and the positions in physical space. After defining some characteristic zones in composition space, we could sketch a corresponding map in physical space, by looking at a large number of tracer trajectories.

The trajectories confirm the hypothesis of the mixing of particles with different reaction progress in the annulus region close to the bluff body, resulting in a mixing line in composition space. This illustrates how mixing of fresh air with hot products in the first recirculation zone — the main mechanism that stabilizes the bluff-body flames (swirling and non-swirling) — is modeled in this transported scalar PDF modeling approach. The trajectories also show how the second recirculation zone is modeled as a hot region of rich combustion products, in agreement with experimental observations.

The influence of the mixing model and the mixing constant C_ϕ has been investigated. With the CD model a value of $C_\phi = 3$ was needed to obtain a burning solution. The turbulent flow and composition field predictions are in good agreement with experimental data. The influence of the micro-mixing model on the results in physical space is small, but becomes more important further downstream. The influence of the micro-mixing model is observed more clearly, where the larger fluctuations in Y_{CO_2}-

space for the CD model lead to lower conditional means. This effect is again stronger further downstream. The mixing constant C_ϕ influences the results in physical space, through the mixture fraction variance. Its influence in composition space on the other hand is only visible close to the bluff body. Using EMST, the local extinction seen in the experiments cannot be predicted. The steady CD solution leads to a higher amount of scatter than with EMST, resulting in lower values for temperature and Y_{CO_2}. However, this is a consequence of the non-localness of the CD mixing model and does not mean that local extinction is correctly predicted. This is explained by looking at the trajectories of the CD calculation which can differ from the trajectories of the EMST calculations. In the shear layer behind the first recirculation zone ($x/D = 0.8 - 2.0$), mixing lines different from the mixing lines at the first recirculation zone are observed. This way the computational particles access a larger area in composition space.

Local extinction, in the sense of initially burning particles moving in composition space into a region below the critical flamelet, has not been observed in the EMST simulations. However, in (Z, Y_{CO_2}) space some small downward movements have been observed in the zones of high reactivity, corresponding to the highly rotating collar region in physical space. This indicates that we are able to capture the competition between mixing and reaction in this region of physical space, but not enough in order to model local extinction. This can be attributed to the limitation of modeling high Y_{CO_2} scalar dissipation rate events when using the EMST mixing model based on the mean integral turbulent time scale.

The trajectories of the CD calculation contain 2 specific phenomena connected to the prediction of local extinction. First, reaction, seen in composition space as a purely vertical movement, is interrupted by downward jumps, larger than the ones observed for EMST trajectories. Second, large mainly horizontal jumps in composition space crossing the entire reaction zone, resulting in more particles below the critical flamelet. The latter are often named as the cause of over-prediction of local extinction with the CD model, as the Damkohler effect, i.e. the competition of mixing and reaction influencing local extinction, is not captured during these jumps crossing the reaction zone.

To truly model local extinction the fluctuations of the scalar dissipation rate need to be represented and this is not the case for this modeling framework, as a mean mixing time scale is used within one cell. Although the mixing model is definitely an important factor in the prediction of local extinction, other limitations in the current

modelling framework might also have strong impact on the results as discussed above: limitations of REDIM in order to model local extinction, limitations of the velocity-scalar correlation modelling (i.e. the use of joint scalar PDF modelling instead of joint velocity-scalar PDF), or even limitations of the RANS approach for this flame where unsteady effects in physical space may have a strong impact on the results in composition space. A profound study of the different time scales involved could help to better highlight the true influence of the mixing model but this is beyond the scope of this PhD research.

Chapter 5

Calculations of a swirling inert methanol spray

5.1 Introduction

Before the REDIM is tested in a reacting spray, the models and the boundary conditions are tested in the case of an inert methanol spray, namely the swirling methanol spray of McDonell and Samuelsen [9]. The large advantage of this series of experiments is that the same inlet conditions are used for the inert and the reacting case. This makes it possible to test the models and the boundary conditions in the inert spray case without the added complexity of combustion and use the same boundary conditions for the calculation of the reacting case. This series of experiments is also one of the few where the fuel vapor concentration is measured. In the inert case, the mixture fraction can be calculated from the measured mole fraction of methanol and therefore the modeling of the mixing and evaporation can be assessed. The non-swirling inert and reacting case of the McDonell and Samuelsen spray have been studied by Ge et al. [84, 85] within the framework of a hybrid RANS gas PDF and a droplet PDF. This is similar to the modeling framework used in this PhD research. In [84, 85] the important influence of the boundary conditions on the results is mentioned. Also the validity of the β-PDF assumption for the mixture fraction PDF is tested and a modified β-PDF model is suggested to better cope with the smaller mixture fraction range present in sprays. The validity of the β-PDF assumption is also briefly discussed in this chapter.

5.2 Test case description and modeling framework

5.2.1 Inert swirling methanol spray

In this chapter the inert swirling methanol spray of of McDonell and Samuelsen [9] is simulated. The general setup of the experiment is shown in figure 5.1a. The atomizer is mounted, oriented downward, in a $495mm$ x $495mm$ duct. The air flow in the duct has a velocity of $0.8m/s$. At about $180mm$ of the centerline the zero gradient assumption is valid, making it possible to use a symmetry boundary condition for the outer boundary. A simplex atomizer is used, which is in this case assisted with swirling atomizing air. However, the cases studied in this PhD research are part of a larger series of inert and reacting spray experiments, with non-swirling atomization air or without atomization air. The geometry of the atomizer is shown in figure 5.2. The diameter of the atomizer opening is $4.90mm$ and the burner has a total width of $50.8mm$. The methanol is injected at a mass flow rate of $1.26g/s$. The mass flow rate of the atomizing air is $1.32g/s$. Methanol and air are injected at $18-22°C$.

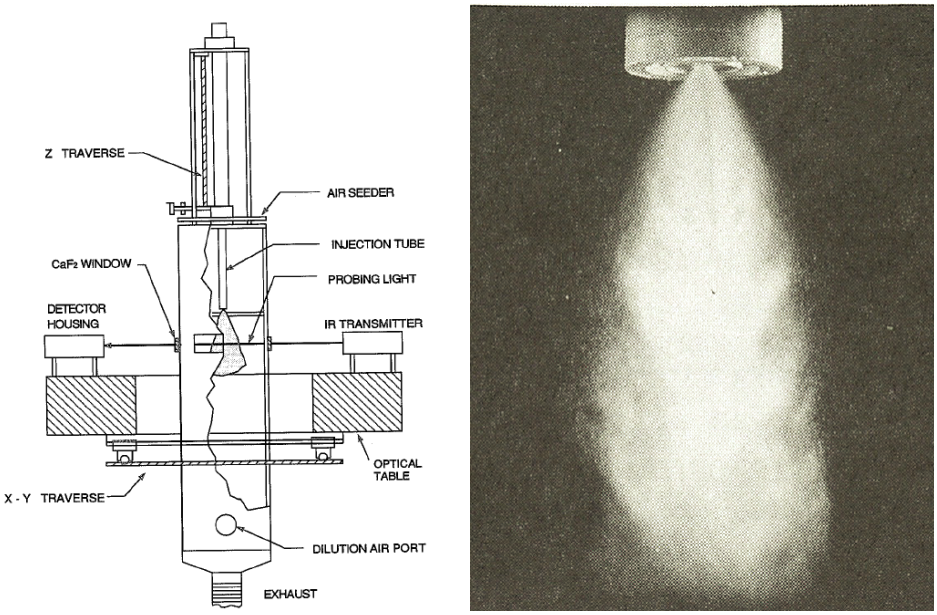

Figure 5.1: a/Setup of the McDonell and Samuelsen spray experiments (adapted from [9]) b/Photo of the inert swirling spray experiment.

Phase Doppler-Interferometry (PDI) is used to measure the gas and droplet velocities and velocity fluctuations, the droplet diameter and the droplet rate. The error on a single droplet size and velocity measurement is respectively 3 percent and 1 percent.

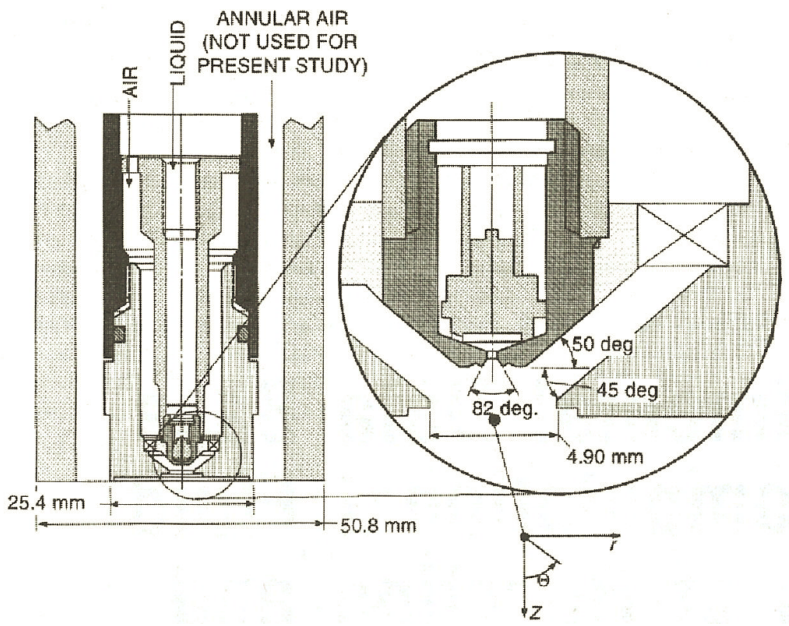

Figure 5.2: Atomizer geometry of the McDonell and Samuelsen spray experiments (from [9]).

However, the size of the measurement volume depends on the droplet size in the volume. Also only one droplet can be inside the measurement volume. If, on the other hand, two or more droplets are in the measurement volume at least one of the droplets will not be measured which will affect the droplet rate and mass flux measurements. While this has all been accounted for in the reporting of the measurements, it still raises attention to be cautious of the correctness of the measurements. In [9] a test has been done in which the total measured droplet mass flux and vapor mass flux are summed to check how much of the initial methanol mass flux is measured. It seems that close to the burner inlet only half of the mass is measured due to many multi-droplet occurrences. Also close to the inlet there might still be ligaments which break up into smaller droplets, corrupting the measurements. It is expected that this affects the measurement of the droplet concentration and of the volume flux. However, the effect on the distribution averages is expected to be much smaller. The first PDI measurement is done at $7.5mm$ from the burner inlet, making it hard to guess the inlet conditions for the droplets. The methanol vapor volume fraction is measured with the IRES technique. [145] Note that this technique is very different from the mixture fraction measurements in the swirling bluff-body flame and cannot be expected to have the same precision. The error on the vapor measurements is reported to be 7 percent in the case of the inert spray. [9] The stoichiometric mixture fraction for this

case is $Z_{\mathrm{st}} = 0.1346$.

5.2.2 Modeling of the gas phase

The gas phase is described with the same hybrid RANS-PDF technique as was used in the calculation of the swirling bluff-body flame (chapter 4). However, now, instead of a a scalar PDF, a velocity-scalar PDF is used. The composition vector, described by PDF, consists of mixture fraction and enthalpy. Again a Monte Carlo method is used to solve the transport equation of the PDF. The gas properties are read from an inert mixing flamelet table.

Turbulence modeling

The LRR-IPM turbulence model of [12] is used. In order to deal with turbulence-chemistry interaction, a transported velocity-scalar PDF approach is used and the general Langevin model is consistent with the LRR-IPM model.

Micro-mixing

The EMST mixing model [56] with $C_\phi = 2$ is used. However, also the CD mixing is tested, in order to see the influence of the mixing model on the results. As the mixing model affects the shape of the mixture fraction PDF which is seen by the droplets, it is expected that it will affect the local evaporation rate. As the CD mixing model is non-local, it is expected that peaks in the mixture fraction PDF will be flattened faster.

Heat transfer

The effect on the gas phase of heat transfer with the droplets is accounted for through the calculation of the enthalpy change of the gas. From the gas enthalpy, the gas temperature is calculated.

5.2.3 Modeling of the droplets

The spray is represented statistically by a droplet PDF. Similar to what is done for the gas PDF, the transport equation of the droplet is solved with a Monte Carlo

method. For the evaporation model the Abramzon-Sirignano model is used. [80] The evaporation temperature of methanol at atmospheric pressure is 337.55K, but this temperature will not be reached by the droplets.

Droplet temperature

Both the infinite conductivity and the parabolic temperature profile have been tested and no effect on the results was seen. This can be explained by the the Biot number. For droplets with a diameter of $10\mu m$ the Biot number is always smaller than 0.1. This means that for the smallest droplets, $D_p < 10\mu m$, the temperature profile inside the droplets can be assumed to be uniform. As the smallest droplets have by far the largest contribution to the global evaporation rate, the effect of the model for the temperature profile inside the droplet will not affect the global evaporation rate. The largest Biot number, observed for the largest droplets, is approximately 0.4. However, the contribution of these droplets to the global evaporation rate is marginal. Nonetheless, in the calculations discussed in this chapter the parabolic temperature profile has been used.

Vapour distribution

As discussed in in Chapter 2, two different models will be used to distribute the evaporated methanol vapor over the computational gas particles: the uniform distribution model and the 'feed the saturation peak' model. The former is the most basic model and 'uniformly' distributes the vapor over all gas particles. This means that the vapor is distributed non-conditional on the mixture fraction of the gas particles. The latter model is more advanced and physically more correct and gives the vapor to the computational particles which are in composition space closest to the saturated vapor conditions at the droplet surface. This results, as the name suggests, in a peak at the saturated properties. For further details we refer to Chapter 2.

Velocity seen by the droplets

In the calculations discussed in this chapter a new model for the seen velocity is used. This model is a modified GLM model and is thus based on the GLM model for computational gas particles. This results in a more consistent modeling as the turbulence model, the GLM model and the modified GLM model are now all based

on the LRR-IPM model. For more details the reader is referred to [74].

Composition vector seen by the droplets

The composition vector seen by the droplets is a property of the computational droplet parcels and mainly the seen vapor mass fraction and the seen temperature are important. As discussed in Chapter 2, the description of the gas phase through a transported PDF approach provides more information for the evaporation modeling as the full PDF of the composition vector is known. In this chapter three models for the seen composition vector will be tested:

1. the interpolated mean cell value ('seen mean properties model')(M) is used,
2. the properties of a randomly chosen gas particle in the same cell are used ('seen random properties model')(R),
3. the properties of the gas particle which is in enthalpy space closest to saturation are used ('closest to saturation seen properties model')(S).

The first model is the most basic model and is often used in standard RANS and LES calculations. The second model is more an ad hoc model. The last model is expected to work best with the 'feed the saturation peak' model as both models give priority to the gas particles which are closest to saturation. This should lead to a more consistent modeling framework as the seen properties which are used in the calculation of the evaporation rate are sampled from the gas particles that receive most of the vapor. This is represented schematically in figure 5.3, where the interaction in composition space between the vapor distribution, seen composition and mixing model is shown. The 'closest to saturation' seen properties model is also expected to be the least influenced by the 1/3-rule assumption, as the seen properties are closer to the saturation properties. Therefore the combination of the 'feed the saturation peak' (P) model and the 'closest to saturation seen properties' (S) model is considered to be the standard framework to which all the other models will be compared.

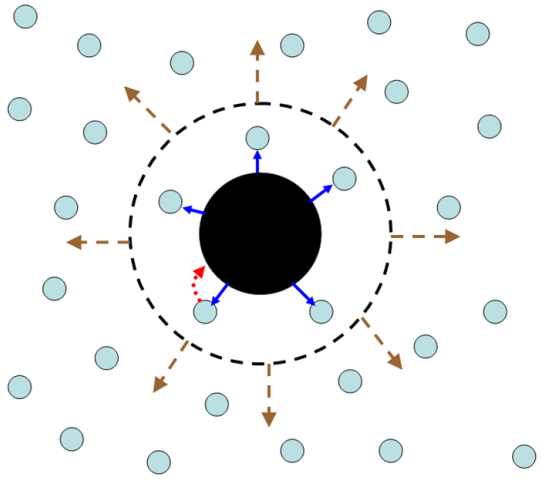

Figure 5.3: Representation of the interaction in composition space between the 'feed the saturation peak' vapor distribution model (full blue arrow), the 'closest to saturation' seen composition model (dotted red arrow) and a mixing model (dashed brown arrow). Large black dot: computational droplet, smaller grey dots: computational gas particles

5.2.4 Hybrid RANS gas-PDF droplet-PDF approach

All calculations are steady axisymmetric and are performed with the same code PDFD [133], which has already been used for spray calculations [46, 75]. In transported PDF calculations, the gas phase equations are solved using a consistent hybrid finite-volume/particle method [133]. Mean velocity $\widetilde{U}$, the mean pressure gradient $\partial\langle p\rangle/\partial x_i$, the mean velocity gradient $\partial\langle U_i\rangle/\partial x_j$ and turbulent dissipation rate ϵ are obtained by a standard finite-volume (FV) method based on a pressure correction algorithm. The transport equation of turbulent dissipation rate (ϵ) solved in the FV method is needed to obtain the turbulent timescale, required in the mixing model. The mean density $\langle\rho\rangle$ in the FV method is obtained from the iteration averaged mean density in the particle method (averaged over 1000 particle time steps). For the evolution of the particles the fractional step method is used [66]. A local time-stepping algorithm, developed in the framework of statistically stationary problems [65], is applied. The number of particles per cell is 50. An outer iteration consists of a number of FV iterations and particle time steps. The FV method is iterated until the residuals of all equations are decreasing and the global mean pressure correction is below a specified threshold (with a maximum of 1000 FV iterations per outer iteration). Subsequently 10 coupled gas-PDF droplet-PDF iterations are performed. The general

structure of the calculation framework is shown in figure 6.3.

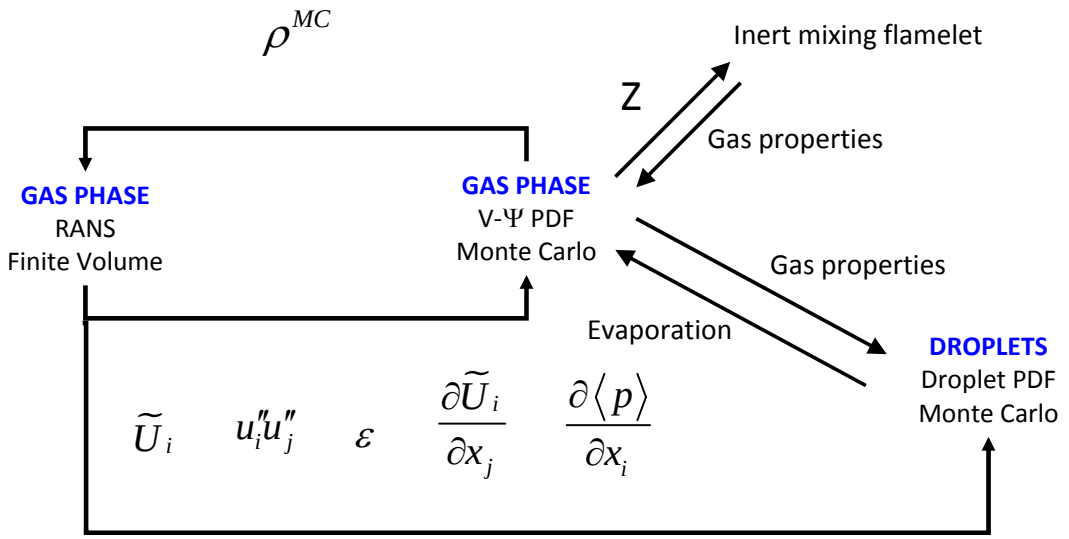

Figure 5.4: General structure of the calculation framework for inert spray calculations.

5.2.5 Computational domain and boundary conditions

The 0.15m long computational domain starts at the burner exit. In radial direction, it is 0.15m wide (figure 5.5). A non-uniform rectangular grid of 96×128 cells is used. Grid independence has been verified, but will not be discussed in detail. Inlet conditions for the gas and droplets have been found by trial and error, based on the the experimental measurements closest to the inlet. Uniform velocity profiles were chosen. The mean mixture fraction and mixture fraction variance at the inlet are

Table 5.1: Gas boundary conditions of inert spray calculation

Inlet	U (m/s)	V (m/s)	W (m/s)	u_iu_i	u_iu_j	ϵ	T(K)
Jet	58.77	0	-58.77	256	0	10^7	295.15
Coflow	0.8	0	0	0.64	0	40	295.15

zero. There is still a large uncertainty about the inlet conditions of the droplets, so the study discussed in this chapter will focus mainly on the relative influence of the different models, rather than looking for the best models which can capture the profiles the best.

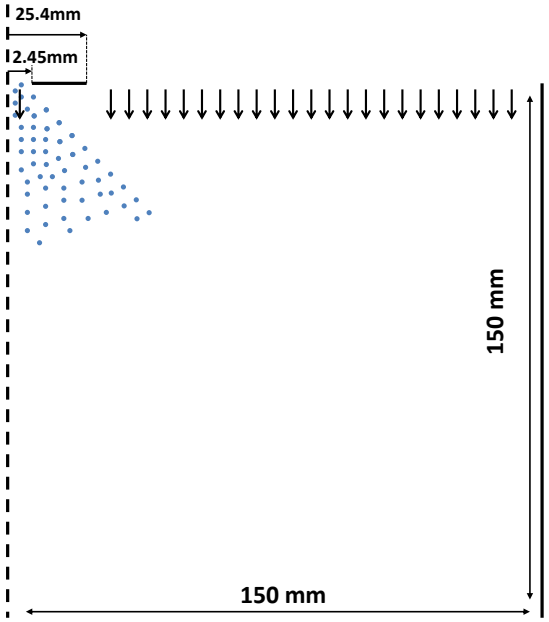

Figure 5.5: Schematic representation of computational domain for the spray calculations.

5.3 Results

In this chapter different combinations of the vapor distribution model and the seen composition model are tested. All combinations are summarized in table 5.2 and will be referred to by their acronym.

Table 5.2: Combination of models tested.

Case	Vapor distribution model	Seen composition model
PS	feed saturation peak (P)	closest to saturation (S)
PM	feed saturation peak (P)	cell mean (M)
PR	feed saturation peak (P)	random gas particle (R)
US	uniform (U)	closest to saturation (S)
UM	uniform (U)	cell mean (M)

5.3.1 Flow Fields

The PS calculation with the feed the saturation peak (P) model and the seen properties close to saturation (S) is considered to be the reference calculation, as it represents

the most physically consistent framework.

Gas

First the flow fields of the gas phase are compared with the experiments. In order to assess the influence of the vapor distribution model and the seen composition properties model on the flow fields, results are shown for three combinations of models: PS, US and UM. It is expected that these models do not influence the flow fields of the gas as a difference in evaporation due to the models affects the gas density only marginally. This is confirmed in the following discussion.

In figure 5.6, the profiles of the mean axial gas velocity U are shown. In general, the calculations correctly predict the mean axial gas velocity with the exception of a slight over-prediction of the peak value and an under-prediction of the spreading. In the experiments, close to the bluff body a small recirculation zone is observed in the center region. This recirculation zone is also captured by the calculations, but the length of the recirculation zone is somewhat over-predicted.

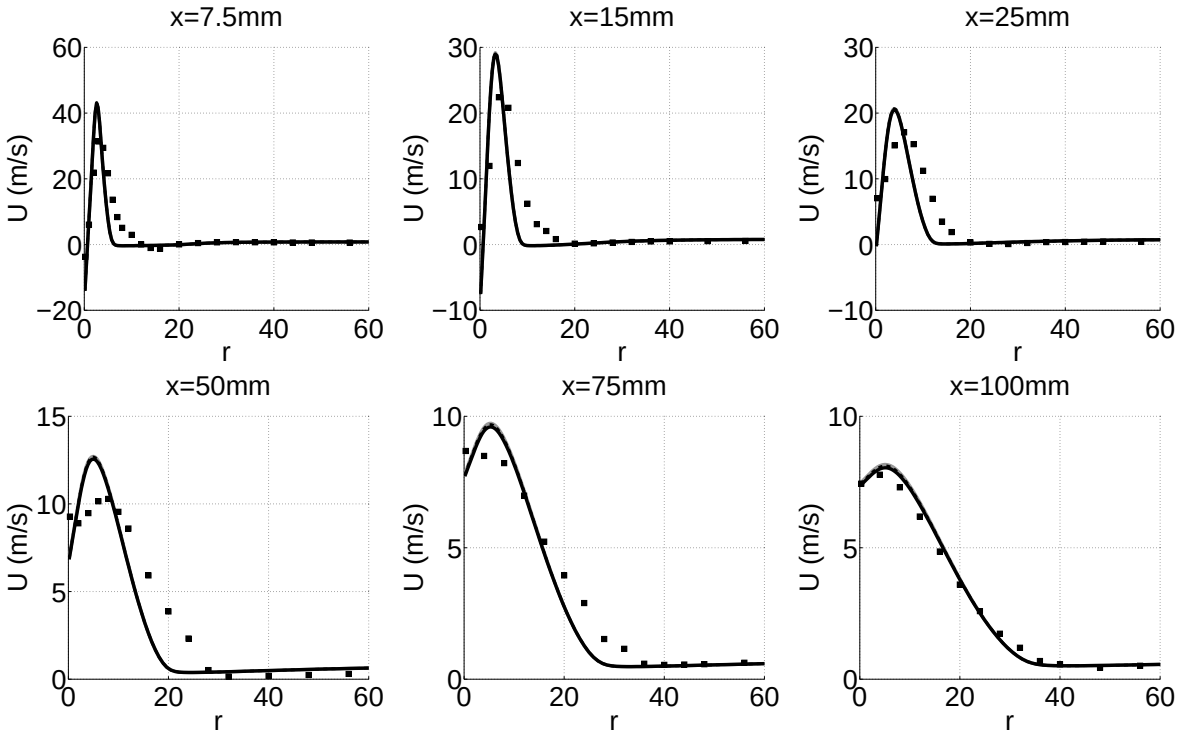

Figure 5.6: Mean axial gas velocity profiles. Grey line: UM, Dashed black line: US, Full black line: PS, Symbols: experimental data.

In figure 5.7, the profiles of the mean tangential gas velocity W are shown. Close

to the inlet the general shape of the experimental W-profile is well captured with the exception of an over-prediction of the peak value. However, further downstream the experimental tangential velocities decrease faster than the predicted velocities and the shapes strongly differ. The mean radial gas velocity, shown in figure 5.8 is not

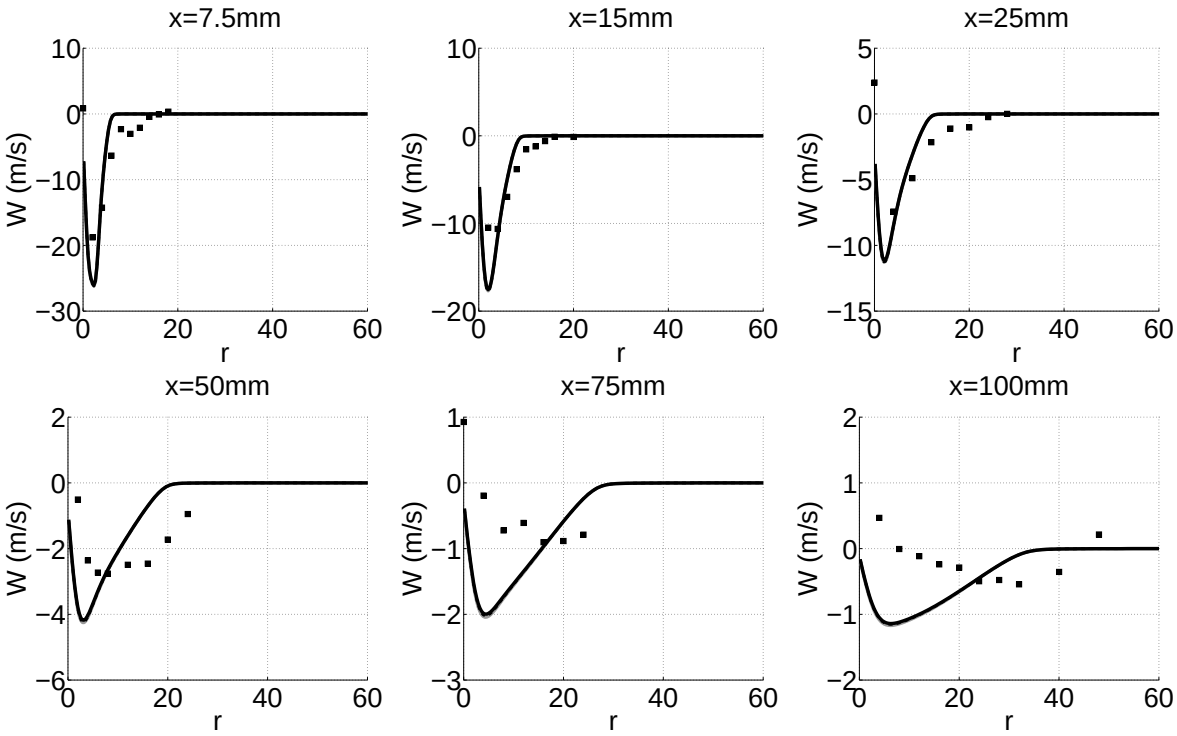

Figure 5.7: Mean tangential gas velocity profiles. Grey line: UM, Dashed black line: US, Full black line: PS, Symbols: experimental data.

predicted well. Close to the inlet, i.e. $x = 7.5mm$, the peak value is correctly predicted, but the profile is too narrow compared to the experimental profiles. Further downstream the profile of the calculation widens but the overall amount of radial momentum is largely under-predicted. This is most likely due to limitations of the RANS framework and its inability to model the gas flow of a swirling atomizer. However, it should also be noted that there are centerline values of V different from zero. This either means that the experiment is not completely axisymmetric or that there are errors in the measurements due to non-uniform seeding. In figures 5.9, 5.10 and 5.11 the normal Reynolds stresses are shown. All the stresses are severely over-predicted in the center region. This might be due to the large normal Reynolds stresses at the inlet. However, the inlet conditions for the gas phase were chosen in order to have the best overall results for the mean velocities. This over-prediction of the normal stresses coincides with a large over-prediction of the shear stresses uv. The latter can

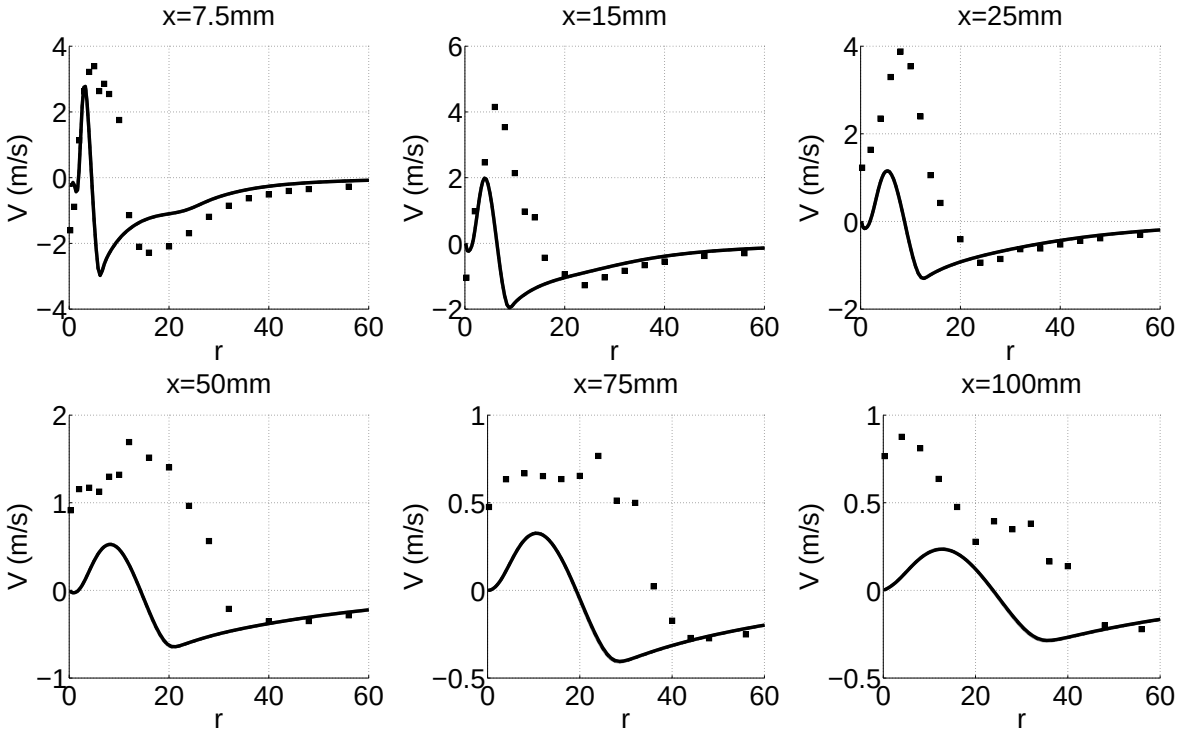

Figure 5.8: Mean radial gas velocity profiles. Grey line: UM, Dashed black line: US, Full black line: PS, Symbols: experimental data.

also be a reason for the over-prediction of the normal stress as the interaction of shear stresses with mean velocity gradients results in production of turbulent stresses. This is even enhanced by the over-prediction of $\frac{\partial \widetilde{U}}{\partial y}\ \frac{\partial \widetilde{V}}{\partial x}$. Concluding, the gas phase flow field is predicted reasonably, but the less than satisfactory prediction of the radial velocity might affect the spreading of the smaller droplets.

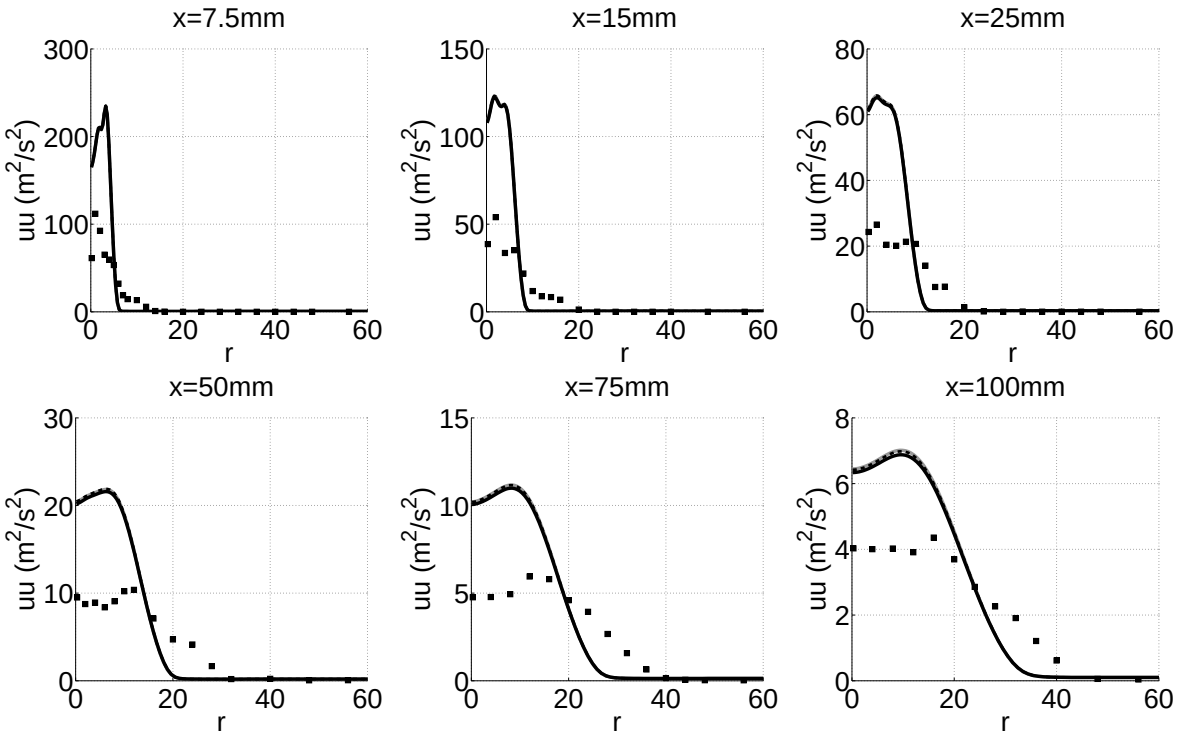

Figure 5.9: Mean axial gas velocity fluctuations profiles. Grey line: UM, Dashed black line: US, Full black line: PS, Symbols: experimental data.

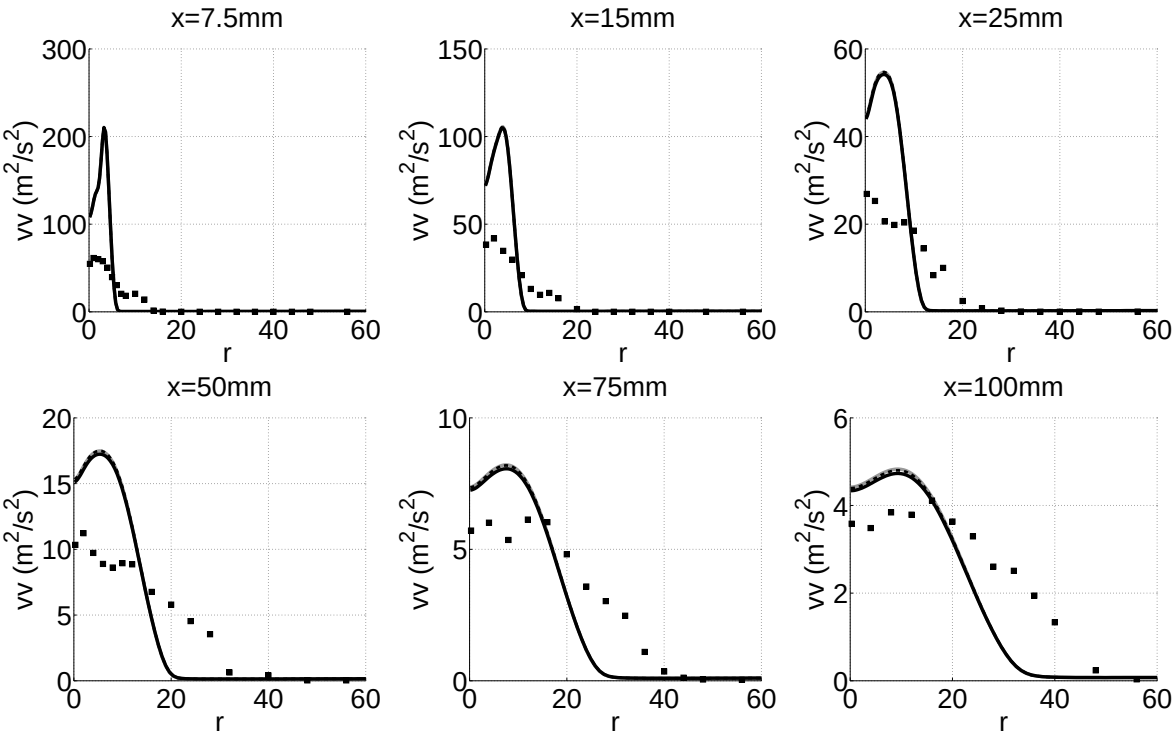

Figure 5.10: Mean radial gas velocity fluctuations profiles. Grey line: UM, Dashed black line: US, Full black line: PS, Symbols: experimental data.

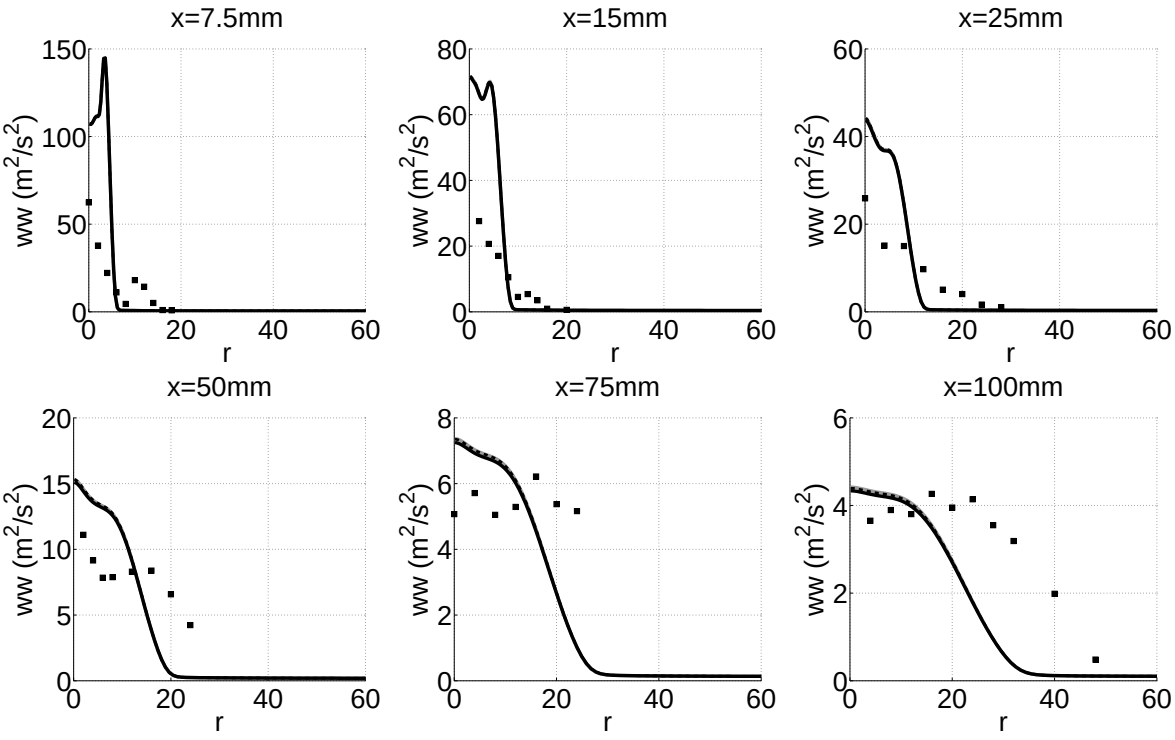

Figure 5.11: Mean tangential gas velocity fluctuations profiles. Grey line: UM, Dashed black line: US, Full black line: PS, Symbols: experimental data.

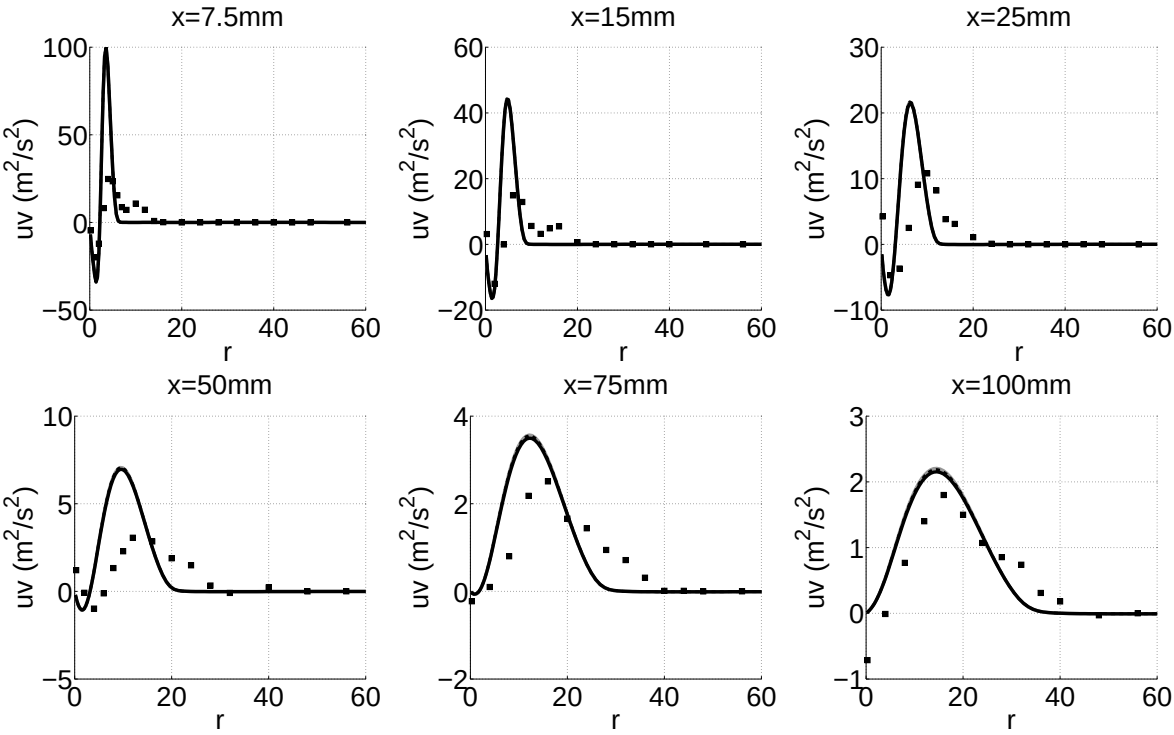

Figure 5.12: Mean u"v" fluctuation profiles. Grey line: UM, Dashed black line: US, Full black line: PS, Symbols: experimental data.

Droplets

Now the flow fields of the droplets are discussed only for the reference calculation (PS) as the droplet flow fields will not be affected by the vapor distribution or seen composition models. In all figures the calculations are compared with the experiments for 3 different droplet size classes: $0-10\mu m$, $20-30\mu m$ and $40-50\mu m$. Based on the different Stokes number of the particles, the different classes are expected to have a different dynamic behavior. The response of the droplets to the gas flow field is determined by the Stokes number. In literature two different Stokes numbers are used.

The Stokes number based on the integral turbulence time scale τ_L:

$$St_L = \frac{\tau_p}{\tau_L} = \frac{\rho_p D_p^2/18\mu_g}{k/\epsilon} \tag{5.1}$$

with τ_p the particle relaxation time. This Stokes number quantifies how the droplets respond to the largest eddies in the flow.

The other Stokes number is the one based on the Kolmogorov time scale:

$$St_k = \frac{\tau_p}{\tau_\eta} = \frac{\rho_p D_p^2/18\mu_g}{\sqrt{\nu/\epsilon}} \tag{5.2}$$

with τ_η the Kolmogorov time scale. This Stokes number quantifies how the droplets respond to the smallest eddies in the flow.

In RANS calculations St_L is the most relevant Stokes number, as only the integral turbulence scales are resolved. Therefore St_L will be a measure of how the droplets in the calculations are affected by the calculated mean gas flow.

In the DNS study of [87] it is discussed how St_k determines the preferential segregation of the droplets. The droplets with $St_k \approx 1$ tend to concentrate in the regions of low vorticity in between vortices. This is because these droplet are ejected out of the vortices due to their inertia, but on the other hand they have insufficient inertia to move through the vortices without being affected. Droplets with $St_k << 1$ or $St_k >> 1$ are more uniformly distributed as they respectively follow the gas flow closely or move largely independent of the flow field. As none of the eddies, ranging from the Kolmogorov scale up to the integral length scale, are resolved in RANS calculations, it will not be possible to capture this effect of preferential segregation

within the hybrid RANS-PDF framework. Therefore, it is important to also keep St_k in mind, when analyzing the simulated droplet dynamics, as differences from the experimental measurements might be due to not capturing this preferential segregation effect.

Before analyzing the droplet flow field first the Stokes numbers, St_L and St_η, for different droplet sizes are shown in figure 5.13. These Stokes numbers have been calculated based on the turbulent kinetic energy k and the turbulence dissipation rate ϵ, obtained from the gas phase solution. More specifically, for each axial position one representative value of k and ϵ has been chosen from the center region as it contains most of the droplets. These graphs should therefore be interpreted as being indicative rather than being quantitatively correct.

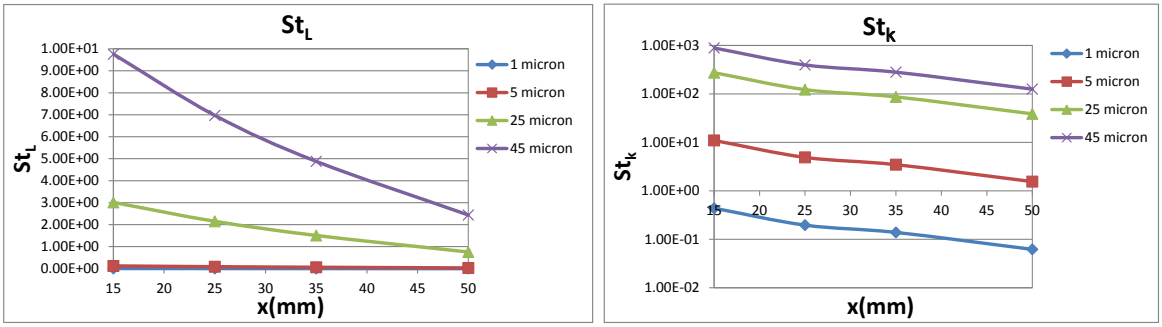

Figure 5.13: The Stokes numbers in the center region of the flow as a function of the axial coordinate: a/ The Stokes number based on the integral timescale St_L (linear scale) b/ The Stokes number based on the Kolmogorov timescale St_k (logarithmic scale).

In general both Stokes numbers decrease with the axial distance to the inlet due to the increase of τ_L and τ_k. As $St_L << 1$ for $D_p = 1\mu m$ and $D_p = 5\mu m$, the droplets of the $0-10\mu m$ class are expected to closely follow the mean gas flow captured by the RANS equations. For the larger droplet diameters $St_L >> 1$, so the larger droplet classes are expected to move more independently of the calculated gas flow. The figure of St_k suggests that in the experiments preferential segregation might occur for the first droplet class $(0-10\mu m)$, but should be negligible for the larger droplets. With this in mind, the droplet flow fields are now discussed. In the pictures below, only the statistically relevant experimental data is shown. The measurements consist of 2 series of measurements: one in the axial-radial plane (RA) and one in the axial-tangential plane (TA). The measurements of the axial properties can differ quite substantially as is seen in the figures below. For the profiles of the calculation only the part with high droplet concentrations, i.e. $0.1n_{max}(x) < n(x) < n_{max}(x)$, are shown as these are

most important for the prediction of the general vapor field.

In figure 5.14, the axial droplet velocity is shown for three droplet classes. At $x = 15mm$, the axial droplet velocities are reasonably predicted, with the largest errors for the intermediate droplet class $(20-30\mu m)$ at more radially outward positions. At $x = 35mm$ the calculation profile of the intermediate droplet class $(20-30\mu m)$ is positioned more radially inward compared to the experimental measurements, suggesting that the radial spread of the droplets is somewhat under-predicted. This is confirmed by the under-prediction of the radial velocity of the intermediate droplet class at that position (figure 5.15) and can be explained by the under-prediction of the radial gas velocities. However, apart from this deviation, the axial velocities are quite well predicted and all the major trends are captured, e.g. the more rapid slowing down between $x = 35mm$ and $x = 75mm$ of the largest droplet class compared to the classes of the smaller droplets. Notice also the larger difference between the two series of measurements further downstream. The radial droplet velocities shown in figure 5.15

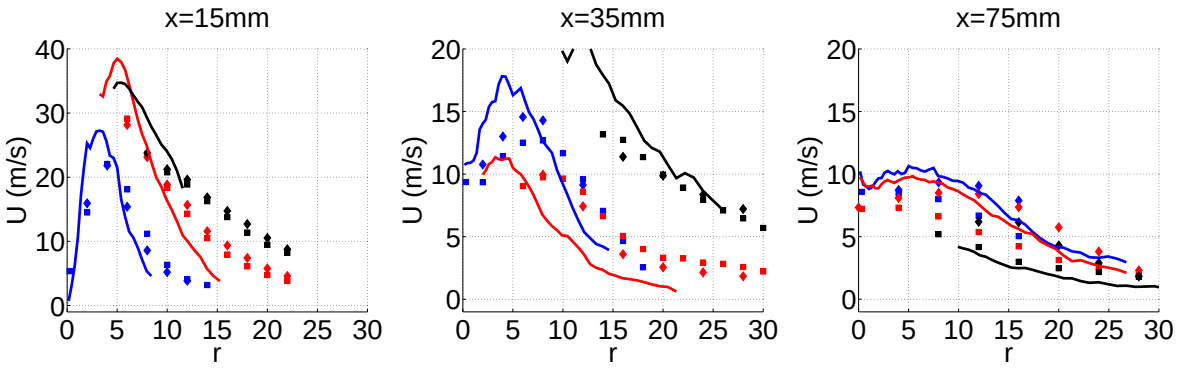

Figure 5.14: Mean axial droplet velocity profiles. blue: $0-10\mu m$, red: $20-30\mu m$, black: $40-50\mu m$. Lines: simulation results. Symbols: experimental data.

are predicted the best for the smallest droplets. This is rather surprising as the radial velocity field of the gas phase was not predicted correctly and the dynamics of smallest droplets are strongly affected by the gas phase. The radial velocity of the larger droplet classes is predicted less satisfactorily but the results are still reasonable and the general evolution of the experimental profiles when moving further downstream is captured by the calculations. It should also be noted that at $x = 35mm$ and $x = 75mm$ the experimental measurements show at the centerline radial velocities different from zero. This was also seen for the radial gas velocities and this either suggests that the case is not perfectly axisymmetric or that there are errors in the measurements. In the axisymmetric calculations the radial velocity at the centerline is obviously zero. In

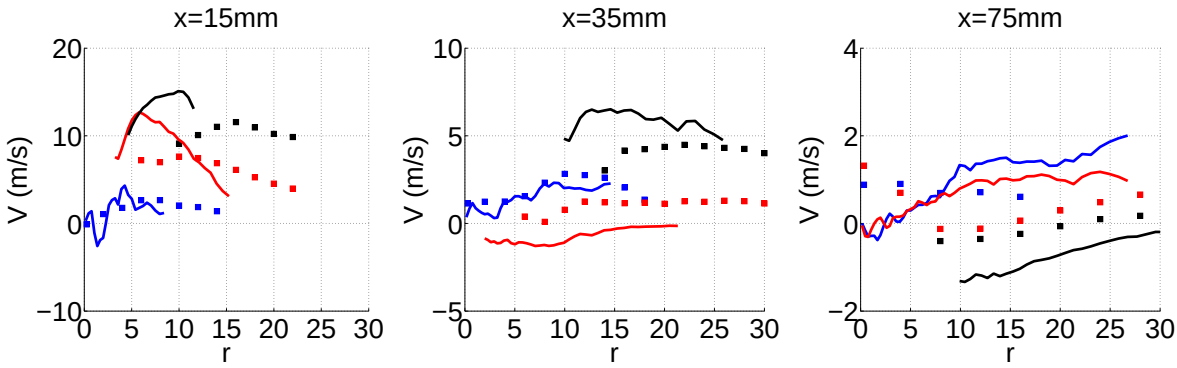

Figure 5.15: Mean radial droplet velocity profiles. blue: $0-10\mu m$, red: $20-30\mu m$, black: $40-50\mu m$. Lines: simulation results. Symbols: experimental data.

figure 5.16, the tangential droplet velocities are shown. Apart from an over-prediction of the peak value for the smallest droplets, due to an over-prediction of the tangential gas velocity, the calculation correctly predicts the tangential flow field for the different droplet classes. The axial droplet velocity fluctuations shown in figure 5.17 are

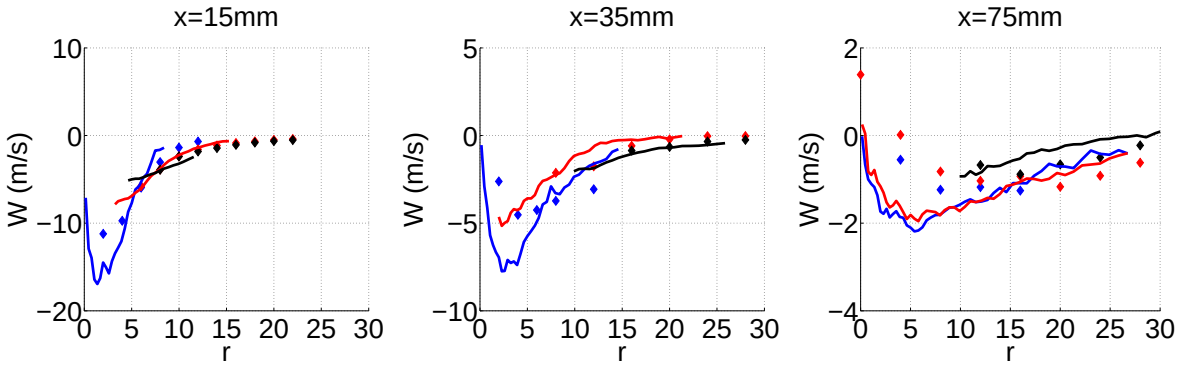

Figure 5.16: Mean tangential droplet velocity profiles. blue: $0-10\mu m$, red: $20-30\mu m$, black: $40-50\mu m$. Lines: simulation results. Symbols: experimental data.

largely over-predicted for all the droplet classes. This over-prediction is the strongest for the smaller droplet classes and this can be explained by the over-prediction of the turbulent stresses in the gas phase. The predictions are better for the largest droplets as these are least affected by the over-predictions of the turbulent stresses in the gas phase. For the radial droplet velocity fluctuations shown in figure 5.18 similar results are observed. For the tangential droplet velocity fluctuations shown in figure 5.19 on the other hand the predictions are better as the tangential turbulent stresses in the gas phase are also better predicted than the axial and radial stresses.

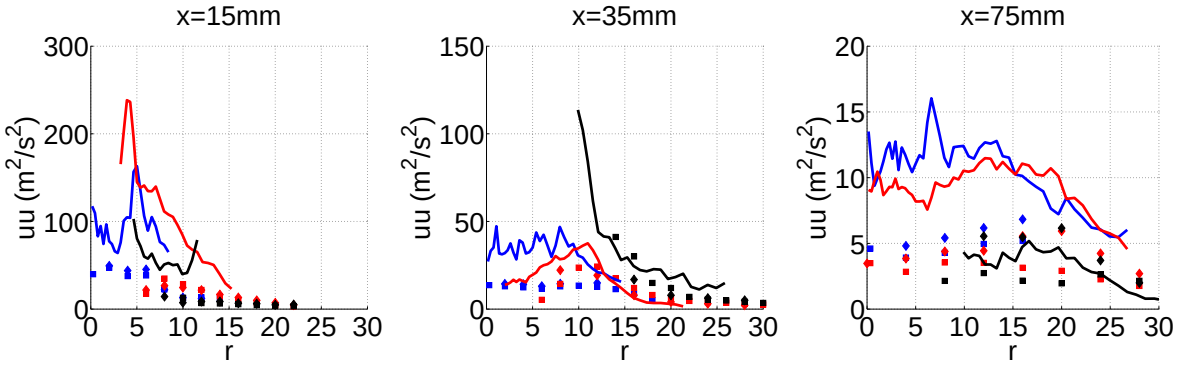

Figure 5.17: Mean axial droplet velocity fluctuations profiles. blue: $0-10\mu m$, red: $20-30\mu m$, black: $40-50\mu m$. Lines: simulation results. Symbols: experimental data.

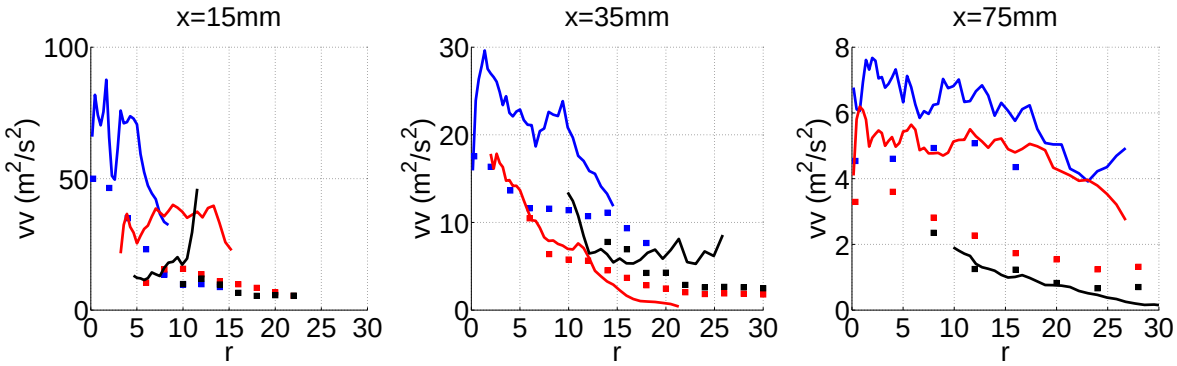

Figure 5.18: Mean radial droplet velocity fluctuations profiles. blue: $0-10\mu m$, red: $20-30\mu m$, black: $40-50\mu m$. Lines: simulation results. Symbols: experimental data.

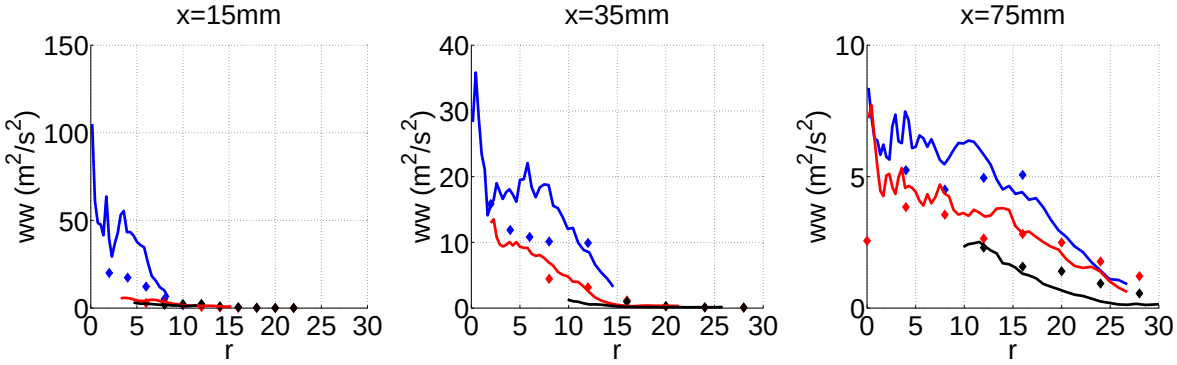

Figure 5.19: Mean tangential droplet velocity fluctuations profiles. blue: $0-10\mu m$, red: $20-30\mu m$, black: $40-50\mu m$. Lines: simulation results. Symbols: experimental data.

Concluding, the mean velocities are quite well captured, with the best results for

the smallest droplet class. This is encouraging for the discussion of the mixing fields in the next section, as the the smallest droplets have the largest contribution to the global evaporation rate due to their larger overall surface for a certain amount of mass. The droplet fluctuations on the other hand are generally over-predicted. This is most likely due to the over-prediction of the gas phase fluctuations. However, the general trends are still captured quite well.

5.3.2 Composition fields

In this section the influence on the mixture fraction field of the vapor distribution model, the seen properties model and the mixing model is discussed. The combination of these three models determines the global evaporation rate.

Influence of vapor distribution modeling

As discussed earlier, two different vapor distribution models have been used in this PhD research: the uniform distribution model and the feed the saturation peak model. The former is the most basic model and is often used in standard RANS calculations with sprays as it does not require any extra modeling compared to the presumed β-PDF model. In this model the mean evaporation rate in a cell is distributed uniformly in mixture fraction space or in other words unconditionally. In the hybrid RANS-PDF framework, this means that the mean evaporation source term is distributed unconditionally over the computational gas particles based on their weight. This model is somewhat nonphysical as computational gas particles which are far from saturation and thus also in physical space far from the droplet surface instantaneously receive vapor. For this specific gas particle the diffusion process of vapor from the droplet surface to a gas particle far away is not accounted for and an over-prediction of the mixing rate can be expected. The 'feed the saturation peak' model on the other hand gives the evaporated vapor to the computational gas particles which are in enthalpy space close to the state at the droplet surface or which are in other words closest to saturation. When looking at the PDF of mixture fraction inside a computational cell this model will result in an extra peak around the mixture fraction corresponding to the saturation composition, hence the name 'feed the saturation peak' model. This model is physically more correct as the gas particles which are close to saturation can also be expected to be representative of the gas close to the droplet surface. The model introduces thus a localness in physical space. The diffusion

of the vapor from these almost saturated gas particles to less saturated gas particles is modeled by the mixing model and the overall mixing rate can be expected to be better predicted. In the present study the EMST mixing model has been used

Table 5.3: Combination of models to test the influence of the vapor distribution model.

Case	Vapor distribution model	Seen composition model
PS	feed saturation peak	closest to saturation
US	uniform	closest to saturation
UM	uniform	cell mean

and three combinations of the vapor distribution model and the seen composition model have been used as can be seen in table 5.3. The reference calculation is the PS-calculation as this is believed to be the physically most correct combinations of models. Comparison with the US-calculation will highlight the effect the vapor distribution model. For completeness the UM-calculation is added as it is more representative of a spray calculation within the standard RANS framework. It should also be noted that the inlet conditions for the droplet distribution have been chosen to obtain the best predictions of the mean mixture fraction for the PS-calculation. The following comparisons will therefore focus more on the difference between the calculations than on the quantitatively correct prediction of the experimental measurements.

Mean mixture fraction and rms mixture fraction In figure 5.20 the mean mixture fraction profiles are shown. At $x = 7.5mm$ all calculations under-predict the mean mixture fraction. This is partly due to the choice of the droplet distribution at the inlet, which has been chosen to give an overall good agreement for the PS calculation. At this position the difference between the calculations is rather small. Further downstream, the influence of the models becomes more important. When comparing the PS and US calculations it is clear that the uniform distribution model leads to higher values of the mean mixture fraction due to a larger global evaporation rate. This is due to the fact that the diffusion process of vapor from the droplet surface to the least saturated gas particles is not accounted for, leading to faster mixing. Therefore the most saturated gas particles will be less saturated in the US-calculation and in combination with the most saturated gas particles seen properties model, the difference in vapor mass fraction $Y_{surf} - Y_{seen}$ and the Spalding mass transfer number B_m will be larger. This eventually results in a larger evaporation rate for

the droplets. For the UM-calculation even larger values of the mean mixture fraction are observed. This can be explained by the fact that the mean vapor mass fraction is smaller than the vapor fraction of gas particles which are close to saturation and thus resulting in an even larger mass transfer number B_m. Overall, the PS calculation seems to have the best predictions as it has similar results to the other calculations at $x = 7.5mm$, but over-predicts $\widetilde{Z}$ less severely at the centerline further downstream. However, it should also be noted that the measurements of the mean mixture fraction should be interpreted with some reserve, as it is not completely clear how correct these measurements are. In the experimental papers an error of 7% on the methanol mole fraction measurements is reported, but these vapor measurements in sprays are definitely not straightforward and the strange shape of the experimental profiles in the center region at $x = 75mm$ and $x = 100mm$, could be nonphysical. In the mixture

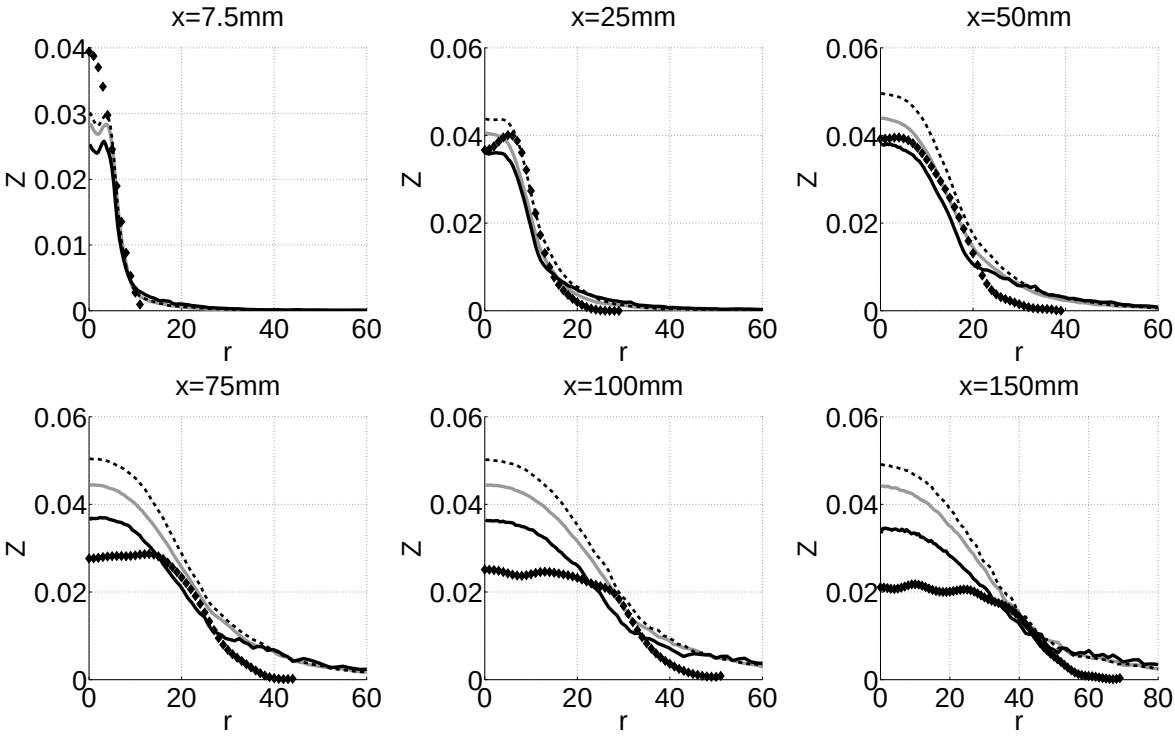

Figure 5.20: Mean mixture fraction profiles. Grey line: US, Dashed black line: UM, Full black line: PS, Symbols: experimental data.

fraction rms profiles shown in figure 5.21 the effect of the vapor distribution model can be clearly observed. The 'feed the saturation peak model' used in the PS calculation predicts substantially larger fluctuations of mixture fraction. This is exactly due to the extra peak in the mixture fraction PDF created by the model. The smaller fluctuations with the uniform distribution model confirm that this model results in

faster mixing and thus a faster decay of the scalar fluctuations. The difference is the largest close to the inlet as there the evaporation rate is the strongest. This can be seen better when looking at the actual PDFs.

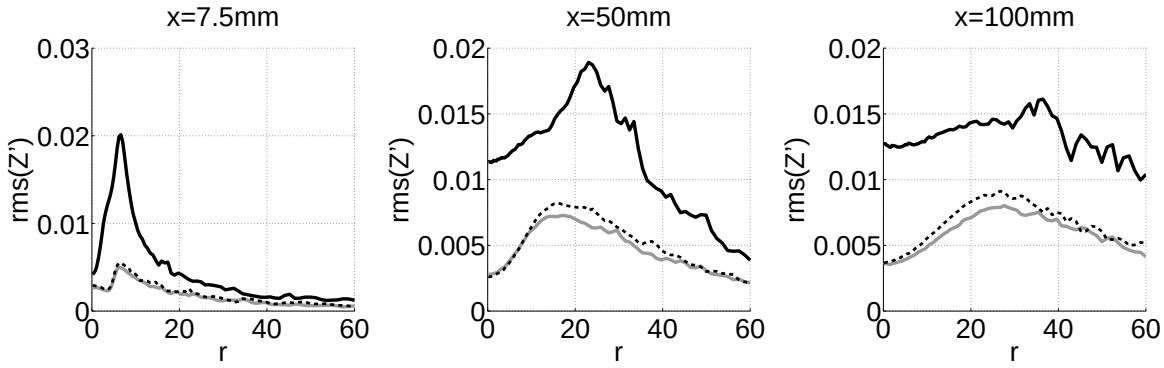

Figure 5.21: Mixture fraction rms profiles. Grey line: US, Dashed black line: UM, Full black line: PS.

Mixture fraction PDF In figure 5.22 the mixture fraction PDFs of the PS-and the US-calculations are shown at $x = 7.5mm$ at several radial locations in the center region. At $r = 0.8$ the two calculations result in similar Z-PDFs, but radially more outward the influence of the vapor distribution model can be clearly seen. For the PS-calculation, the 'feed the saturation peak' model results in a wider PDF with a small hump around $Z = 0.05$, which is most likely a saturation peak caused by the model. The uniform distribution model, on the other hand, results in more narrow Z-PDFs concentrated around the mean value. This is a result of the over-prediction of mixing due to non-local distribution of the vapor and hence resulting in a faster decay of the fluctuations. The β-PDF based on the mean mixture fraction and mixture fraction rms of the calculation, capture the transported PDF from the calculation quite well. Only the saturation peaks are not captured.

Mean Temperature Finally also the temperature profiles are shown in figure 5.23. The PS calculation has the highest temperature profiles as it has the smallest global evaporation rate. Indeed, the temperature profiles resemble the inverse of the mean mixture fraction profiles because evaporation results in an increase of the mixture fraction and a decrease of the gas temperature. In general the temperature drop in the gas phase due to evaporation is small and it could be neglected.

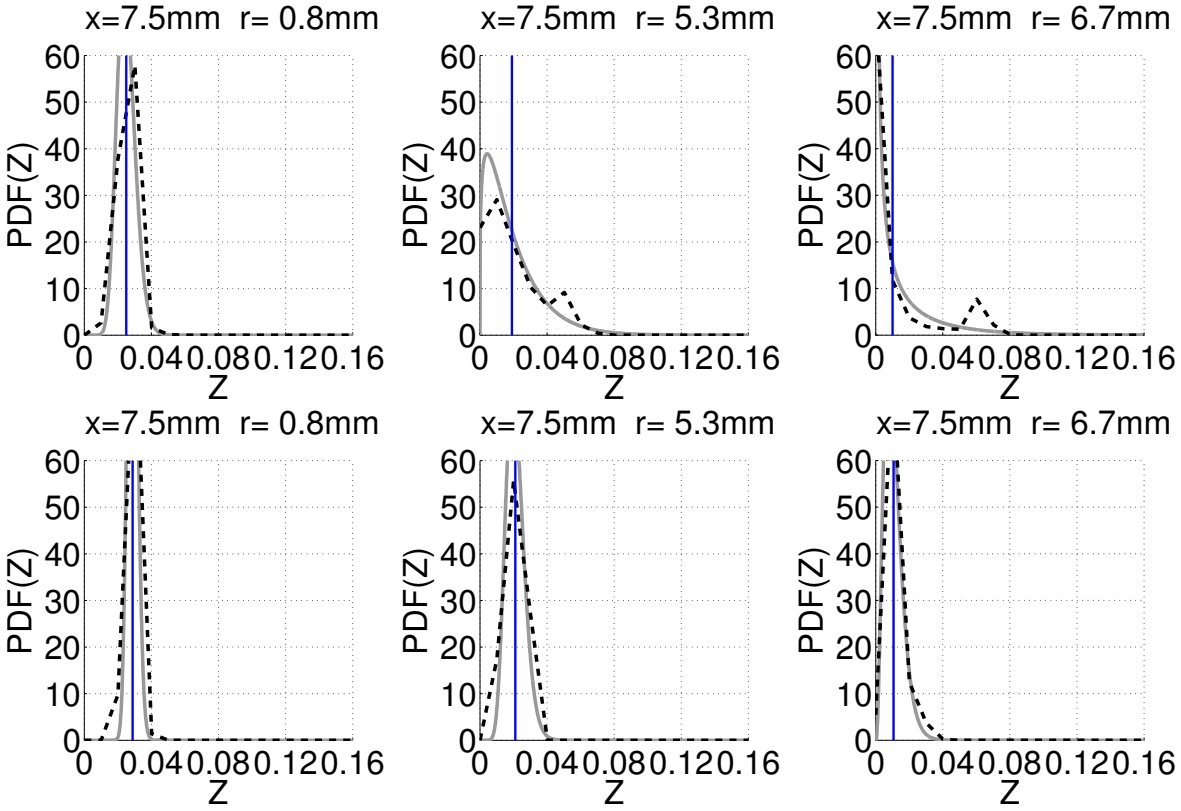

Figure 5.22: Mixture fraction PDF profiles of the PS- (upper row) and US-calculations (lower row) at $x = 7.5mm$ Grey line: β-PDF, Dashed black line: transported PDF, Vertical blue line: mean mixture fraction.

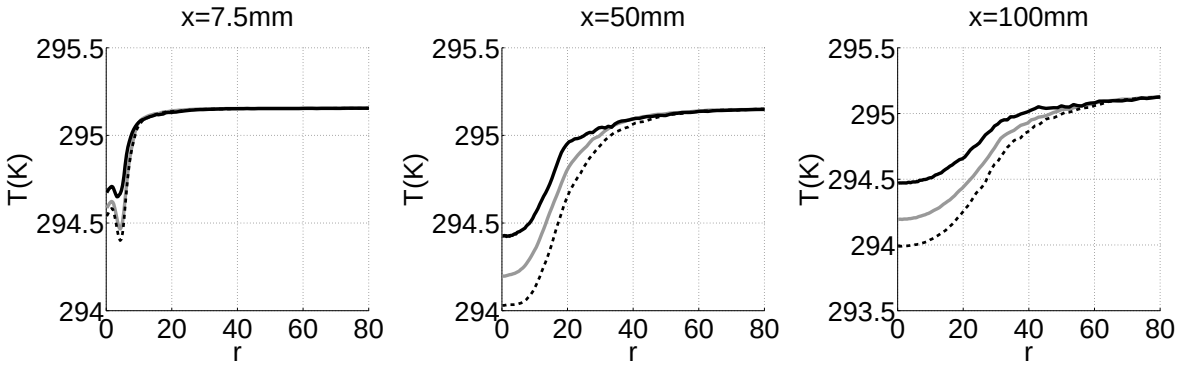

Figure 5.23: Mean mixture fraction profiles. Grey line: US, Dashed black line: UM, Full black line: PS.

Influence of seen composition modeling

Now the influence of the seen composition model is tested by comparing three models in combination with the 'feed the saturation peak' model. The combinations of models

are summarized in table 5.4. The influence of the 'closest to saturation model' and the 'cell mean' model have already been briefly discussed in the previous section. The third model uses the properties of a random gas particle in the cell. It is more an ad hoc model, but it is still interesting to see its influence on the evaporation rate and the mixture fraction field.

Table 5.4: Combination of models to test the influence of the seen composition model

Case	Vapour distribution model	Seen composition model
PS	feed saturation peak	closest to saturation
PM	feed saturation peak	cell mean
PR	feed saturation peak	random gas particle

Mean Mixture fraction and mixture fraction rms In figure 5.24 the mean mixture fraction profiles are shown. At $x = 7.5mm$, again all the calculations underpredict the mean mixture fraction. As explained this is partly due to the choice of the droplet diameter distribution at the inlet. Further downstream the differences become more pronounced. The use of the mean composition for the seen properties results in higher values of the mean mixture fraction. This was also seen in the previous section when both models were used together with the uniform distribution model. As previously explained this is due to the mean methanol mass fraction in a computational cell being smaller than the methanol mass fraction of gas particles that are almost saturated, resulting in a larger mass transfer number B_M and a larger evaporation rate. With the seen composition taken from a random gas particle, the mixture fraction profiles reach even higher values. The difference between the mean seen composition model and the model taking the seen composition of a random gas particle can be explained by the non-linear relationship between the seen composition and the evaporation rate so that $\overline{\dot{m}_p(Y_{seen})} \neq \dot{m}_p(\overline{Y_{seen}})$. The mixture fraction rms profiles shown in figure 5.25 are also affected by the seen composition model. At $x = 7.5mm$, the profiles are very similar, but further downstream surprisingly the calculations with the largest mean mixture fraction have the smallest mixture fraction fluctuations. This is different from what would be observed in a gas phase flow without droplets acting as point sources of fuel vapor. This specific behavior can be explained by studying the mixture fraction PDFs shown in figure 5.26.

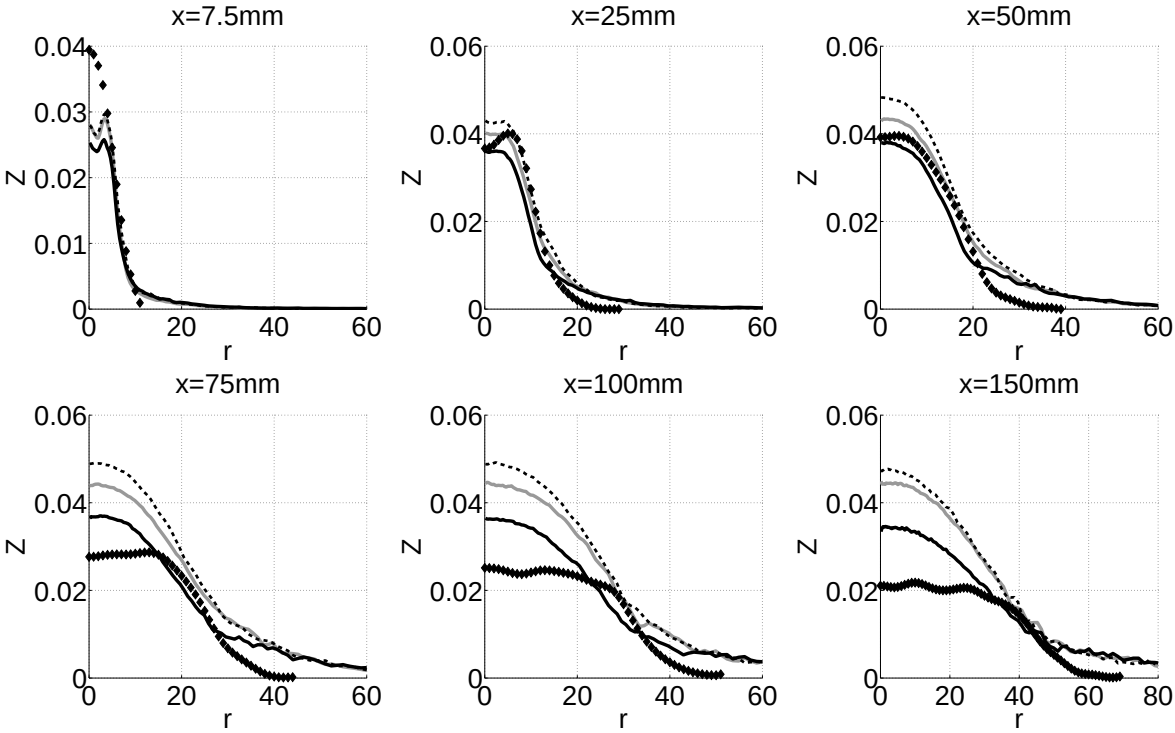

Figure 5.24: Mean mixture fraction profiles. Grey line: PM, Dashed black line: PR, Full black line: PS, Symbols: experimental data.

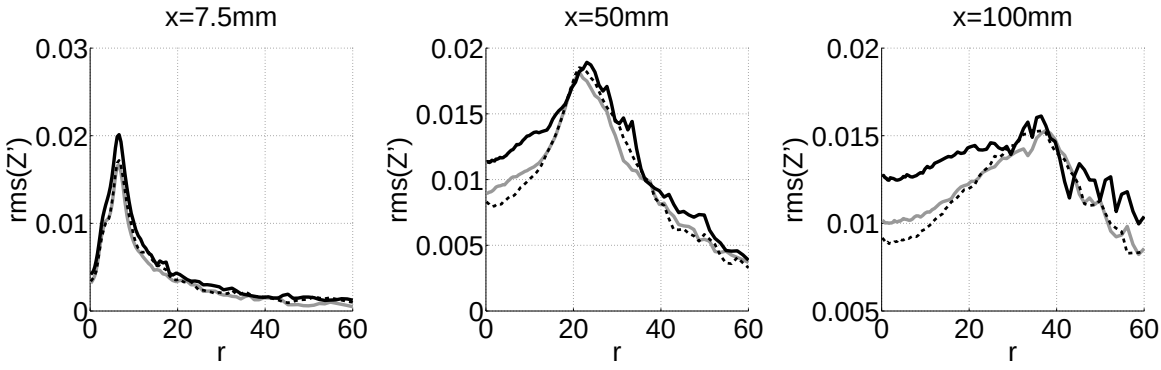

Figure 5.25: Mixture fraction rms profiles. Grey line: PM, Dashed black line: PR, Full black line: PS

Mixture fraction PDF In figure 5.26 the Z-PDFs of the PS- and PM-calculation at $x = 7.5mm$ are shown. Close to the centerline, the PDFs are similar, but more radially outward the PDFs start to differ, due to the larger saturation peak for the PM-calculation. This can be explained by the larger evaporation rate for the PM-calculation due to the less saturated seen composition with the seen mean composition model. The similar PDFs close to the centerline can be explained by the for both

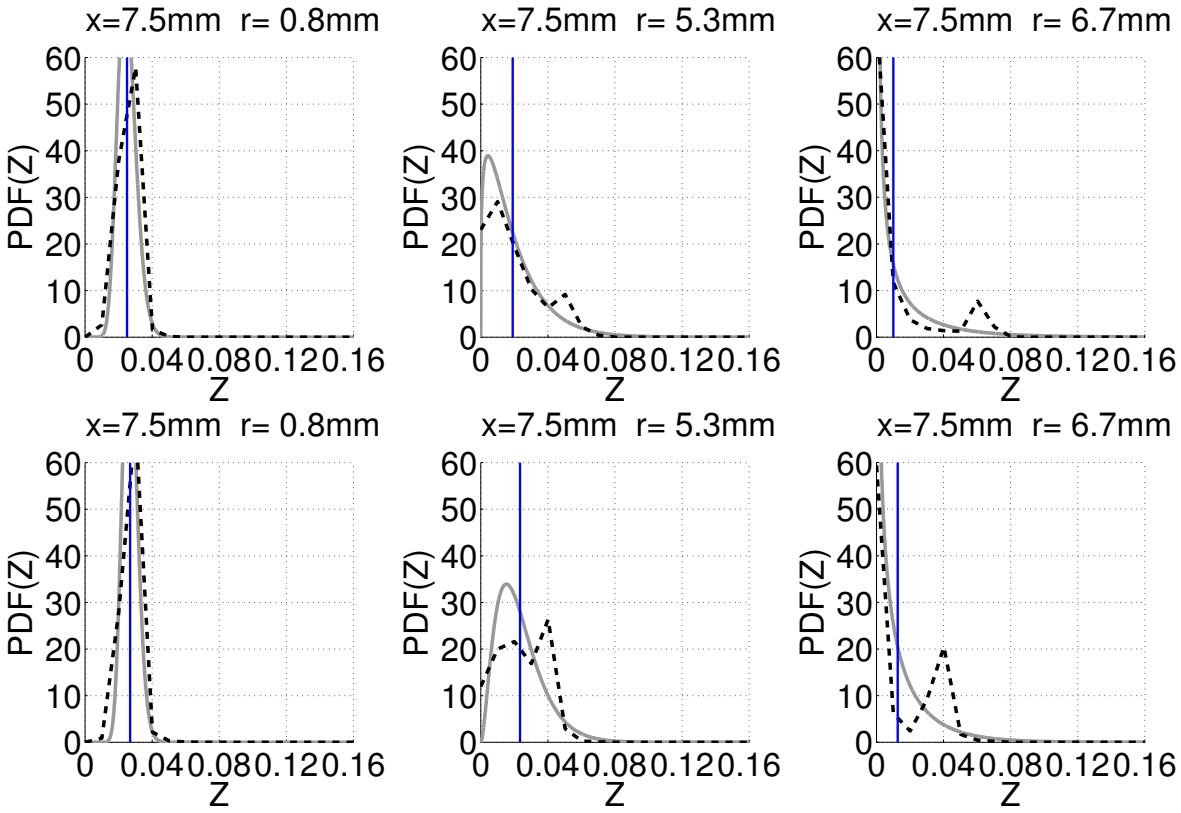

Figure 5.26: Mixture fraction PDF profiles of PS- (upper row) and PM-calculations (lower row) at $x = 7.5mm$. Grey line: β-PDF, Dashed black line: transported PDF, Vertical blue line: mean mixture fraction.

calculations lower evaporation rate at that position. Also note the different position of the saturation peak for the PS- and PM-calculations, with the peaks at smaller mixture fraction for the PM-calculation. This can be explained by the lower droplet surface temperature for the PM-calculation (not shown), due to the higher evaporation rate. The droplet surface temperature is also the saturation temperature and therefore lower values of the droplet surface temperature result in lower values of the vapor mass fraction at saturation and saturation peaks at lower mixture fraction values. Further downstream, at $x = 50mm$ (figure 5.27), the PDFs from the PS-calculation are wider and more asymmetrical than those from the PM-calculation, as was suggested by the mixture fraction rms profiles. A possible explanation for this is that, with the lower evaporation rate in the PS-calculation, fewer gas particles get vapor resulting in a less homogeneous mixture. Also the higher gas temperature for the PS-calculation (figure 5.28) results in higher values of the saturation vapor mass fraction, which leads to even less saturated particles with a higher saturation mass fraction. Apart from

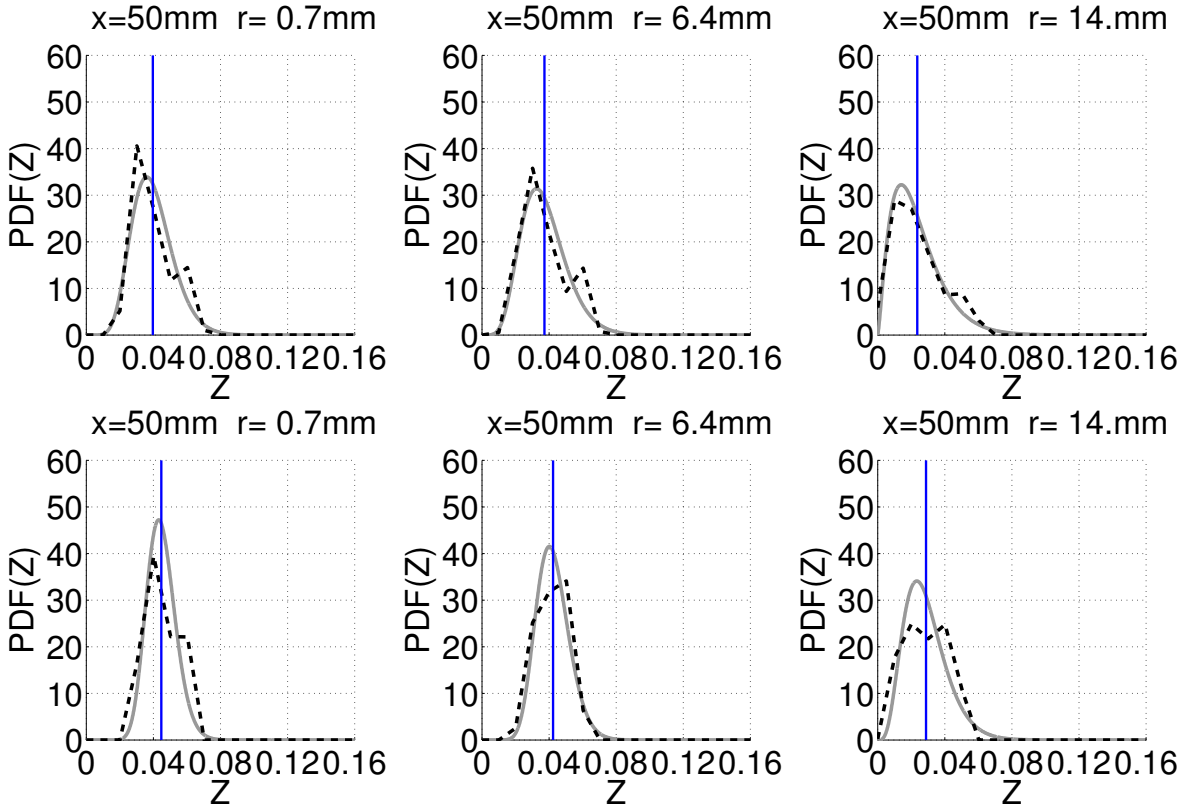

Figure 5.27: Mixture fraction PDF profiles of PS- (upper row) and PM-calculations (lower row) at $x = 50mm$. Grey line: β-PDF, Dashed black line: transported PDF, Vertical blue line: mean mixture fraction.

the saturation peaks, the β-PDF again reasonably captures the transported PDF.

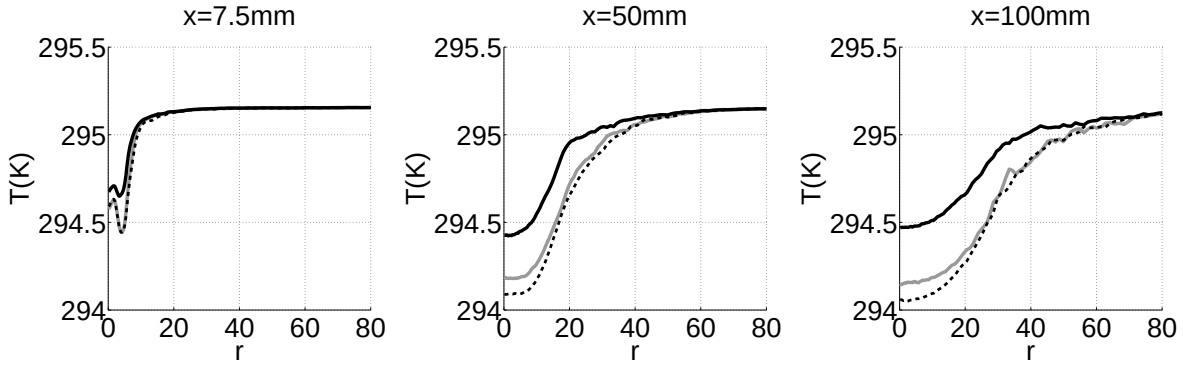

Figure 5.28: Mean mixture fraction profiles. Grey line: PM, Dashed black line: PR, Full black line: PS.

Mean Temperature The mean temperature profiles shown in figure 5.28, again show that higher mixture fraction values, caused by a higher evaporation rate, result in lower gas temperatures.

Influence of the mixing model

Finally the influence of the mixing model is discussed. Within the framework of the 'feed the saturation peak' vapor distribution model, the mixing model models the distribution of the vapor from the most saturated gas particles which receive vapor from the droplet, to the least saturated gas particles. In physical space this can be interpreted as the modeling of the diffusion of the vapor from close to the droplet surface to the environment further away from the droplet. In general the EMST model is preferred as it takes into account the localness of scalar mixing. Nonetheless it is still instructive to do a comparison with the CD model which is non-local. Due to the non-localness it becomes possible for the most saturated gas particles to mix with the least saturated gas particles, resulting in a faster decrease of the vapor mass fraction of the most saturated gas particles. In other words, the peak at saturation is expected to be flattened faster. If the most saturated gas particles are used for the seen properties, this can also result in a larger evaporation rate as the droplets see a smaller vapor mass fraction. Also the influence of the mixing rate is tested by doing an EMST calculation with $C_\phi = 1.5$ instead of the standard value of 2.

Mean Mixture fraction and mixture fraction rms In figure 5.29 the mean mixture profiles are shown. At $x = 7.5mm$, the CD mixing model seems to result in an overall higher mean mixture fraction with a wider profile compared to the calculation with the EMST model. This could be explained by the lower seen vapor mass fraction due to the non-localness of the CD mixing model as has been explained in the previous paragraph. Further downstream, on the other hand, the mean mixture fraction for the CD calculation drops in the center region below that of the EMST calculation. The influence of the mixing constant becomes only visible further downstream. The lower mixing constant, resulting in a slower mixing rate, results in a slightly higher mean mixture fraction in the center region. Also in the figures of the mixture fraction rms (Figure 5.30) the mixing constant influences the results only further downstream. The slower mixing due to the smaller mixing constant results, as expected, in higher mixture fraction fluctuations. The profiles of CD evolve similarly as the mean mixture fraction profiles: close to the inlet the CD model results in higher values than with

the EMST model, while further downstream lower values are predicted with the CD model. Note that this is the opposite behavior of what happened with different seen composition models, where larger mean mixture fraction coincided with less mixture fraction fluctuations. Again the mixture fraction PDFs give more insight into this behavior.

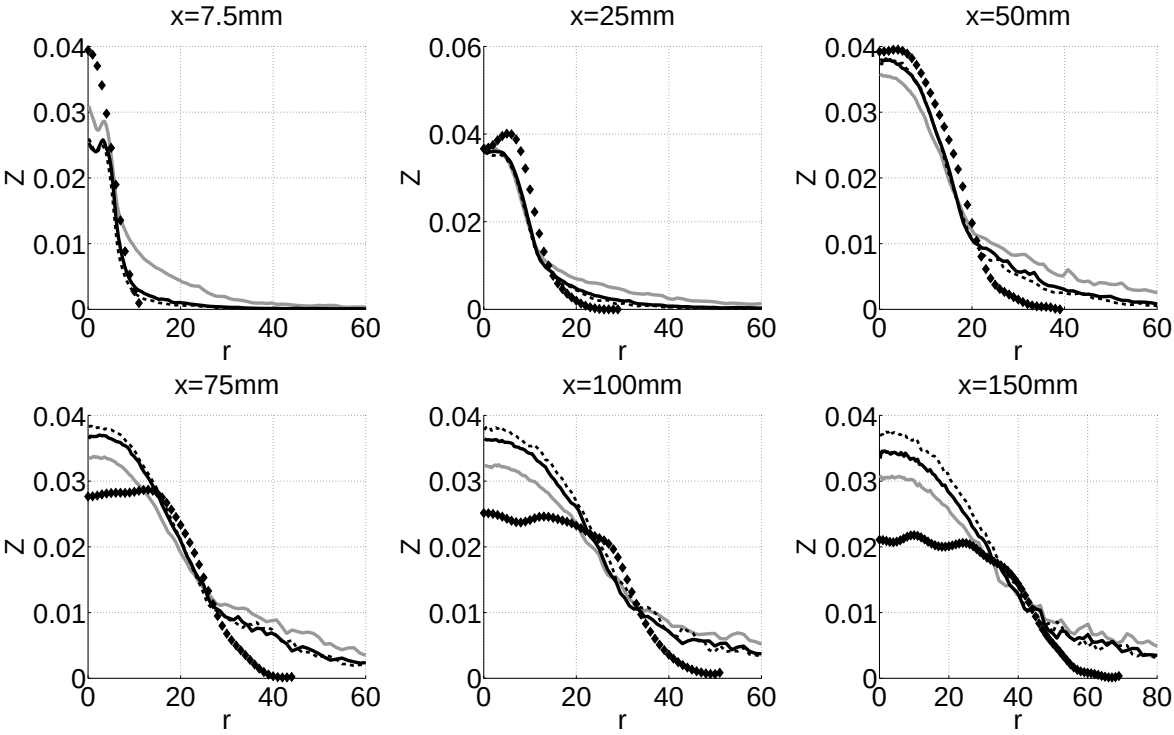

Figure 5.29: Mean mixture fraction profiles. Grey line: CD $C_\phi = 2$, Dashed black line: EMST $C_\phi = 1.5$, Full black line: EMST $C_\phi = 2$, Symbols: experimental data.

Mixture fraction PDF The Z-PDFs in figure 5.31 differ again the most more radially outward. At $r = 14mm$, the PDF of the EMST calculation has no saturation peak, while for the CD calculation there is a peak. This suggests that for the EMST model there is almost no evaporation at this location radially, while for the CD calculation there is. This is confirmed by the higher mean mixture fraction for the CD calculation at this position. Together with the higher mean value, the saturation peak in the CD calculation also explains the higher mixture fraction rms at this position. Again the β-PDF captures the shape of the transported PDF reasonably, with the exception of the saturation peak, which only has a minor influence on the overall distribution.

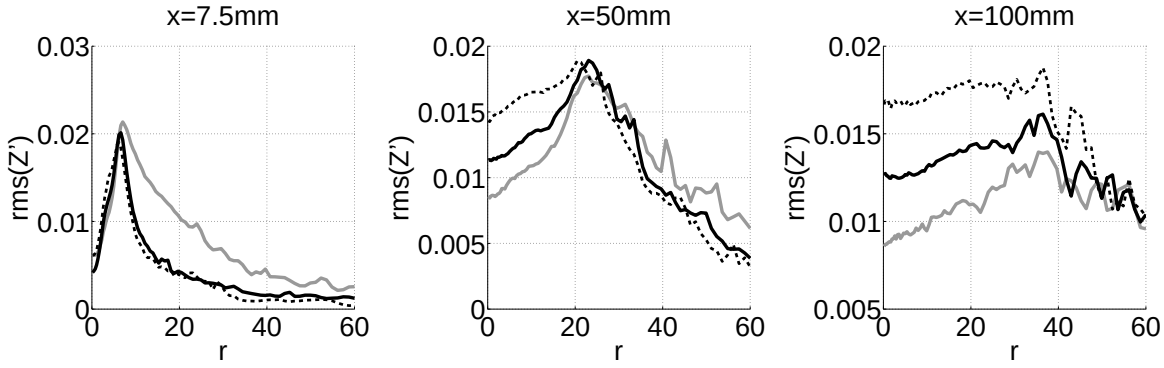

Figure 5.30: Mixture fraction rms profiles. Grey line: CD $C_\phi = 2$, Dashed black line: EMST $C_\phi = 1.5$, Full black line: EMST $C_\phi = 2$, Symbols: experimental data.

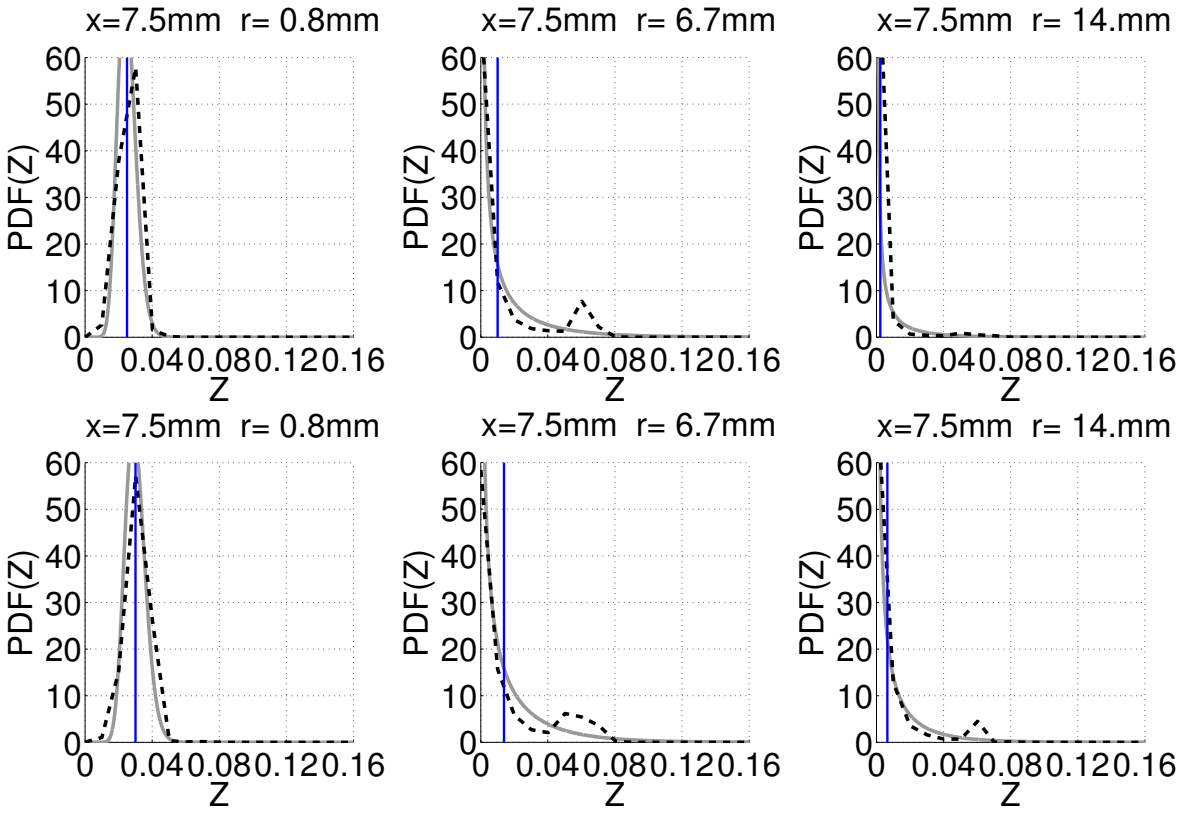

Figure 5.31: Mixture fraction PDF profiles for EMST-(upper row) and CD-calculations (lower row) at $x = 7.5mm$ Grey line: β-PDF, Dashed black line: transported PDF, Vertical blue line: mean mixture fraction.

5.4 Conclusions

The hybrid RANS gas-PDF droplet-PDF framework has been tested for the case of a swirling inert methanol spray. The gas and droplets velocity fields are predicted reasonably and sufficiently well so that the mixture fraction fields can be studied without being affected too much by a strongly deviating droplet distribution. However, for the specific case at hand there is a large uncertainty about the inlet conditions for both the gas phase and the droplets. Therefore it is hard to make a quantitative comparison with the experimental measurements. The focus of this study has thus been more on testing the relative influence of the different models.

The use of the velocity-scalar-PDF for the gas phase provides more information for the modeling of the unresolved flow and scalar field in the immediate vicinity of the droplet surface. In the case of Monte Carlo methods, properties of specific computational gas particles can be used for the modeling of the composition seen by a droplet.

In line with this observation, a new seen composition model, which uses the properties of the gas particle which is in enthalpy space closest to the state of the gas at the droplet surface, is introduced. This model uses the composition vector of one if the most saturated gas particles for the modeling of the seen composition. In physical space this corresponds to taking properties from the immediate surrounding of the droplet surface.

The influence of the vapor distribution model, the seen composition model and the mixing model on the mixing field has been investigated. The combination of the EMST mixing model with the 'feed the saturation peak' model and 'the most saturated' seen properties model is regarded as the most consistent and physically correct modeling framework as the vapor is distributed to the same gas particles as the particles whose composition is 'seen' by the droplets and therefore is used in the calculation of the evaporation rate.

For the vapor distribution model, the 'uniform distribution' model results generally in larger mean mixture fraction values compared to the 'feed the saturation peak' model. This can be explained by the higher evaporation rate due to an inherent over-prediction of mixing in the 'uniform distribution' model, caused by non-local distribution of vapor. This is confirmed by the lower values of the mixture fraction rms.

For the seen composition model, the new model using the properties of the most saturated gas particles, resulted in the lower mean mixture fraction than when the cell mean was used for the seen properties.

The mixing model also influenced the results. More specifically the difference in localness properties between the EMST model and the CD model affected the evolution of the mixture fraction PDF, indirectly influencing the evaporation rate and the mean mixture fraction profile.

Apart from profiles of the mean mixture fraction and the mixture fraction rms, PDF profiles of mixture fraction have been studied to better discern the influence of the different models and to test the β-PDF assumption. The most pronounced effect of the modeling on the PDF shape is the occurrence of a saturation peak at higher mixture fraction values with the 'feed the saturation peak' model. For the limited amount of the PDF profiles studied in this chapter, the β-PDF captures the shape of the transported PDFs reasonably, with the exception of the saturation peak caused by the 'feed the saturation peak' model.

Concluding, many new insights have been gained on the influence of the modeling of scalar mixing on the evaporation rate and the mixture fraction field. The hybrid RANS gas-PDF droplet-PDF framework has been validated sufficiently for the inert spray, so that it can be used in the more complex situation of spray flames.

Chapter 6

Calculations of a swirling methanol spray flame

6.1 Introduction

After the investigation of the inert spray, now a reacting spray with the same inlet conditions is investigated. However, this case is quite different as now droplets might reach their boiling temperature due to the high temperature environment. A stronger influence of the different models is expected as now there is a stronger feedback to the evaporation of the droplets from the temperature field, which itself is a result of the evaporation of the droplets. Again the influence of the vapor distribution and the seen composition properties model is tested. Also the influence of the combustion model is tested by comparing flamelet calculations to REDIM calculations.

6.2 Test case description and modeling framework

6.2.1 Swirling methanol spray flame

The swirling methanol spray flame of McDonell and Samuelsen is studied [9]. This experiment has the same operating parameters as the inert spray studied in the previous chapter. The burner is mounted in a $495mm$ x $495mm$ duct. The air flow in the duct has a velocity of $0.8m/s$. At about $180mm$ from the centerline the zero gradient assumption is valid. A simplex atomizer is used, which is in this case assisted

with swirling atomizing air. The geometry of the atomizer is shown in figure 6.1a. The diameter of the atomizer opening is $4.90mm$ and the burner has a total width of $50.8mm$. The methanol is injected at a mass flow rate of $1.26g/s$. The mass flow rate of the atomizing air is $1.32g/s$. Methanol and air are injected at $18-22°C$. Also

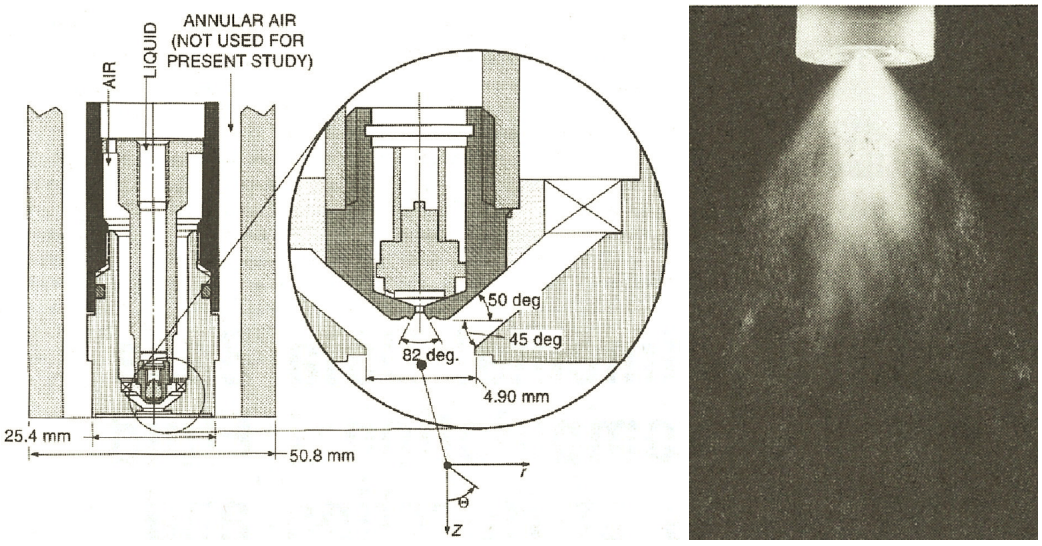

Figure 6.1: a/Atomizer geometry of the McDonell and Samuelsen spray experiments (from [9]) b/Photo of the reacting swirling spray experiment (from [9])

the same properties as for the inert case are measured: gas phase mean velocities and turbulent stresses, methanol vapor mole fraction, droplet mean velocities and turbulent stresses, droplet rates. However, for the reacting case also the temperature of the gas phase is measured. As, due to reaction, now more species than air and methanol vapor are present in the gas phase, the methanol mole fraction from the experiments cannot be recalculated to a mixture fraction as the total composition of the gas phase is not known. However, the methanol mole fraction could be retrieved from the calculations and compared with the measurements. This has not been done in the present study, but might be interesting for future research.

6.2.2 Modeling of the gas phase

The modeling of the gas phase is very similar to what was described in the previous chapter for the inert spray calculations. The largest differences compared to the framework for the inert spray calculations are:

1. the extra independent property, Y_{CO_2}, for the computational gas particles in the REDIM calculations,

2. the inclusion of a combustion model,

3. the disregard of the effect of the droplet heat transfer on the gas phase.

Turbulence modeling

The LRR-IPM turbulence model of [12] is used. In order to deal with turbulence-chemistry interaction, a transported velocity-scalar PDF approach is used and the general Langevin model is consistent with the LRR-IPM model.

Micro-mixing

The EMST mixing model [56] with $C_\phi = 2$ is used. For the flamelet calculations, also the CD mixing has been tested and only a small influence was seen. This can be explained by the fact that in the reacting case the evaporated vapor is consumed by reaction, so that the mixing model might have a less direct influence on the distribution of the vapor mass fraction than in the inert spray calculations. In REDIM calculations, on the other hand, also the shape of the Y_{CO_2}-PDF is affected, and this might affect the flame structure. However, the use of the CD model with REDIM has not been investigated and is suggested for future research.

Heat transfer

The effect on the gas phase of heat transfer with the droplets is not accounted for as this is negligible compared to the production of heat due to reaction. So the calculation of the gas phase is adiabatic. Also the inert spray calculations showed that the influence of evaporation on the gas temperature is rather small.

Turbulence-chemistry interaction in RANS modeling framework

Similar to the inert spray calculations a velocity-composition-PDF is used to capture the turbulence-chemistry interaction. Depending on the combustion model, the composition vector $\boldsymbol{\psi}$ consists of (Z, h) (flamelet) or (Z, YCO_2, h) (REDIM).

Combustion model

Similarly to the swirling methane flame calculations a single steady diffusion flamelet or a REDIM based on methanol will be used as combustion model.

Single steady diffusion flamelet The simplest combustion model used in this study is the single steady diffusion flamelet, which can be seen as a 1D table only parametrized by Z. This flamelet has been calculated in the OPPDIF program [7] with the Chevalier-Warnatz mechanism [146] for methanol for a strain rate of $100s^{-1}$.

Reaction-Diffusion Manifold (REDIM) The methanol REDIM has been constructed in the same manner as was explained in chapter 2 for the methane REDIM. Again Z and Y_{CO_2} are used as independent parameters. Also again pure gaseous fuel and pure air are used as boundary conditions. However the pure gaseous fuel boundary condition does not correctly represent the boundary condition at the droplet surface where the methanol vapour is at saturated conditions. It is not clear yet how this affects the eventual REDIM. It is however not straightforward to take into account as the boundary conditions changes with the surface temperature of the droplet and is thus different for each droplet. The REDIM concept is applied to reduce the Chevalier-Warnatz mechanism [146] (23 species and 94 reactions) for CH_3OH to a 2-dimensional manifold with mass fractions Y_{N_2} and Y_{CO_2} as independent parameters. The mixture fraction is directly related to Y_{N_2} through the following relationship:

$$Z = 1 - \frac{Y_{N_2}}{Y_{N_2,0}}, \tag{6.1}$$

with $Y_{N_2,0}$ the N_2 mass fraction value in the co-flowing air. This definition of mixture fraction does not account for differential diffusion. Equal diffusivities for all species and unity Lewis number are assumed.

The REDIM is stored as a pre-calculated table. Figure 6.2 shows contours of the CO_2 reaction rate as function of mixture fraction and Y_{CO_2}.

6.2.3 Modeling of the droplets

The spray is represented statistically by a droplet PDF. Similar to what is done for the gas PDF, the transport equation of the droplet is solved with a Monte Carlo method.

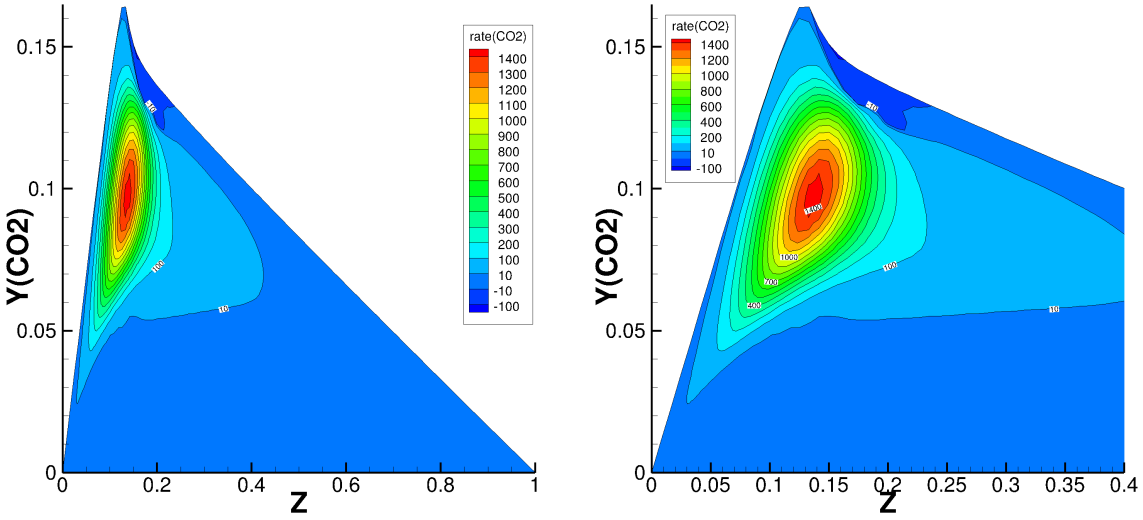

Figure 6.2: Methanol REDIM: Y_{CO_2} production rate ($rCO2$) in $Z - Y_{CO_2}$-space. a/total REDIM b/zoom of the most reactive zone.

For the evaporation model the Abramzon-Sirignano model is used. [80]

Droplet temperature

Similar to what was done in the inert spray calculations both the infinite conductivity and the parabolic temperature profile have been tested and again no effect on the results was seen. This can again be explained by the Biot number. For droplets with a diameter of $10\mu m$ the Biot number is now larger but it is still smaller than 0.2. This means that for the smallest droplets, i.e. $D_p < 10\mu m$, the temperature profile inside the droplets can be assumed to be uniform. As the smallest droplets have by far the largest contribution to the global evaporation rate, the effect of the model for the temperature profile inside the droplet will not affect the global evaporation rate. The largest Biot number, observed for the largest droplets, is now approximately 0.6. However, the contribution of these droplets to the global evaporation rate is marginal. Nonetheless, in the calculations discussed in this chapter the parabolic temperature profile has been used.

Vapor distribution

As was the case for the inert spray calculation, two different models will be used to distribute the evaporated methanol vapor over the computational gas particles: the uniform distribution model and the feed the saturation peak model.

Velocity seen by the droplets

For the spray flame calculations the modified SLM model is used for the velocity seen by the droplets. This is different from the inert spray calculations where a new modified seen GLM model was used.

Composition vector seen by the droplets

The composition vector seen by the droplets is a property of the computational droplet parcels and mainly the seen vapor mass fraction and the seen temperature are important. The same three models for the seen composition vector as in the inert spray calculations will be tested:

1. the interpolated mean cell value ('seen mean properties model')(M) is used,
2. the properties of a randomly chosen gas particle in the same cell are used ('seen random properties model')(R),
3. the properties of the gas particle which is in enthalpy space closest to saturation are used ('seen most saturated properties model')(S).

6.2.4 Hybrid RANS/PDF approach

All calculations are steady axisymmetric and are performed with the same code PDFD [133], which has already been used for reacting spray calculations [75] and which was tested for an inert spray in the previous chapter. In transported PDF calculations, the gas phase equations are solved using a consistent hybrid finite-volume/particle method [133]. Mean velocity $\widetilde{U}$, the mean pressure gradient $\partial\langle p\rangle/\partial x_i$, the mean velocity gradient $\partial\langle U_i\rangle/\partial x_j$ and turbulent dissipation rate ϵ are obtained by a standard finite-volume (FV) method based on a pressure correction algorithm. The transport equation of turbulent dissipation rate (ϵ) solved in the FV method is needed to obtain the turbulent timescale, required in the mixing model. The mean density $\langle\rho\rangle$ in the FV method is obtained from the iteration averaged mean density in the particle method (averaged over 1000 particle time steps). For the evolution of the computational gas particles the fractional step method is used [66]. In every particle time step, the particles first mix and subsequently react. The mixing causes particle motion in 2D composition space of the independent scalars to a new position

(Z^*, $Y^*_{CO_2}$). At this new position the particles react with the reaction rate for CO_2 as obtained from the REDIM table (Figure 6.2). As mixture fraction is conserved during the reactions, the particles move in the 1D Y_{CO_2}-space to the final position in the 2D composition space of the independent scalars (Z^*, $Y^{**}_{CO_2}$). At this final position all the dependent scalars, e.g. temperature, density and species, are retrieved from the REDIM table. A local time-stepping algorithm, developed in the framework of statistically stationary problems [65], is applied. The number of particles per cell is 50. An outer iteration consists of a number of FV iterations and particle time steps. The FV method is iterated until the residuals of all equations are decreasing and the global mean pressure correction is below a specified threshold (with a maximum of 1000 FV iterations per outer iteration). Subsequently 10 coupled gas-PDF droplet-PDF iterations are performed. The general structure of the calculation framework is shown in figure 6.3

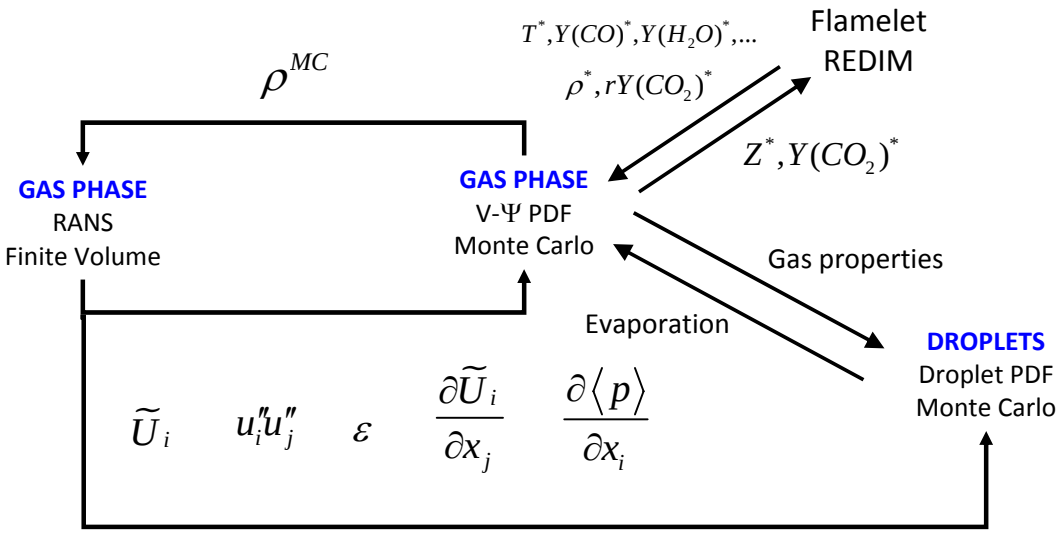

Figure 6.3: General structure of the calculation framework for reacting spray calculations.

6.2.5 Computational domain and boundary conditions

The same computational domain as in the inert spray calculations is used. The 0.15m long computational domain starts at the burner exit. In radial direction, it is 0.15m wide. A non-uniform rectangular grid of 96×128 cells is used.

Also the gas and droplet inlet conditions are almost identical to the inlet condi-

tions used for the inert spray calculations. The only difference is that for the gas coming out of the atomizer, the turbulence dissipation rate $\epsilon = 5.10^5 m^2/s^3$ instead of $10^7 m^2/s^3$, which will result in an over-prediction of the turbulent stresses. However, this adjustment was needed to obtain a better prediction of the temperature field. In this study this is now considered to be the best inlet condition but but there might still be room for improvement. Due the uncertainty of the inlet conditions it will be hard to obtain quantitatively good results. Therefore the focus will be more on the relative influence of the different models. The inlet conditions for the gas phase are summarized in table 6.1.

Table 6.1: Gas boundary conditions of reacting spray calculation.

Inlet	U (m/s)	V (m/s)	W (m/s)	$u_i u_i$	$u_i u_j$	ϵ	T(K)
Jet	58.77	0	-58.77	256	0	5.10^5	295.15
Coflow	0.8	0	0	0.64	0	40	295.15

6.3 Results

6.3.1 Influence of the combustion model: flamelet vs REDIM

In this section the results of the flamelet and the REDIM calculations are compared in the framework of the feed the saturation peak distribution model and the close to saturation seen composition model. First the flow and composition fields of the gas phase are discussed. Subsequently the droplet velocities are studied.

Gas

Flow field In figure 6.4, the mean axial gas velocity profiles are shown. The first general observation is that the profiles are similar close to the inlet, but differ strongly further downstream, which can be explained by the different temperature and density fields resulting from the different combustion models. In general, the REDIM calculations result in the best predictions of the mean axial velocity. Close to the inlet, at $x = 7.5mm$, the width of the profile is predicted correctly, but the peak value is substantially over-predicted. This is most likely due to an over-prediction of the temperature field in the center region. In line with the lower temperature prediction

for the REDIM calculation at that position (figure 6.8), the over-prediction of the axial velocity is smaller for the REDIM calculation. The strong over-prediction of the peak velocity continues further downstream, with consistently better results for the REDIM calculation. Next, the mean tangential velocity profiles, shown in figure 6.5,

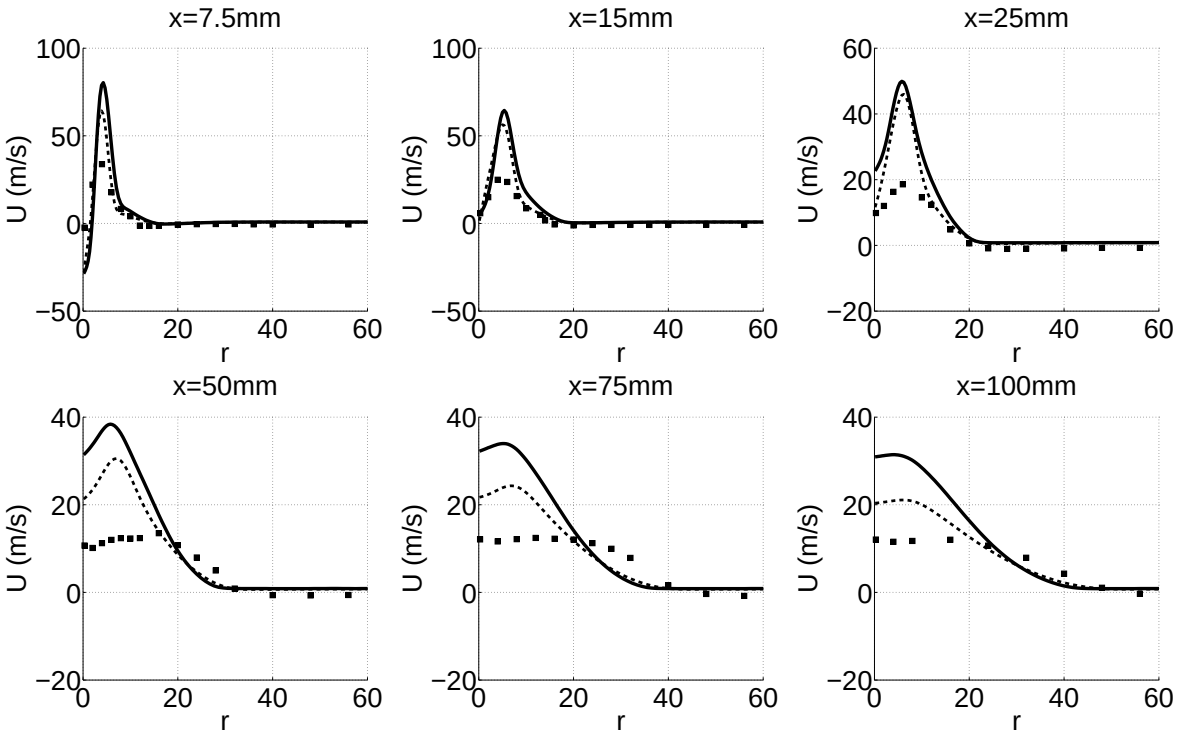

Figure 6.4: Mean axial gas velocity profiles. Dashed black line: REDIM PS, Full black line: Flamelet PS, Symbols: experimental data.

are discussed. Close to the inlet flamelet calculations give the best predictions but from $x = 25mm$ onward the REDIM calculation predicts the decrease of the tangential velocity better. The peak value is consistently over-predicted by both calculations, with the exception of the REDIM calculation at $x = 75mm$. This over-prediction of the peak value is most likely due to the high tangential velocity at the inlet of the atomizer, as also for the inert case the peak values of W were over-predicted. However, this high inlet condition was needed to obtain overall better results. Notice at $x = 7.5mm$ and $15mm$ the non-zero centerline values of W for both calculations. This is due to the combination of a strong gradient $\partial W/\partial y$ and the coarse interpolation in the post-processing. It has been rigorously checked that for all the calculations the tangential velocity at the centerline is zero. In figure 6.6, the mean radial gas velocity profiles are shown. Close to the inlet, at $x = 7.5mm$, both calculations over-predict the peak value of the radial velocity, with the best results for the REDIM calculation.

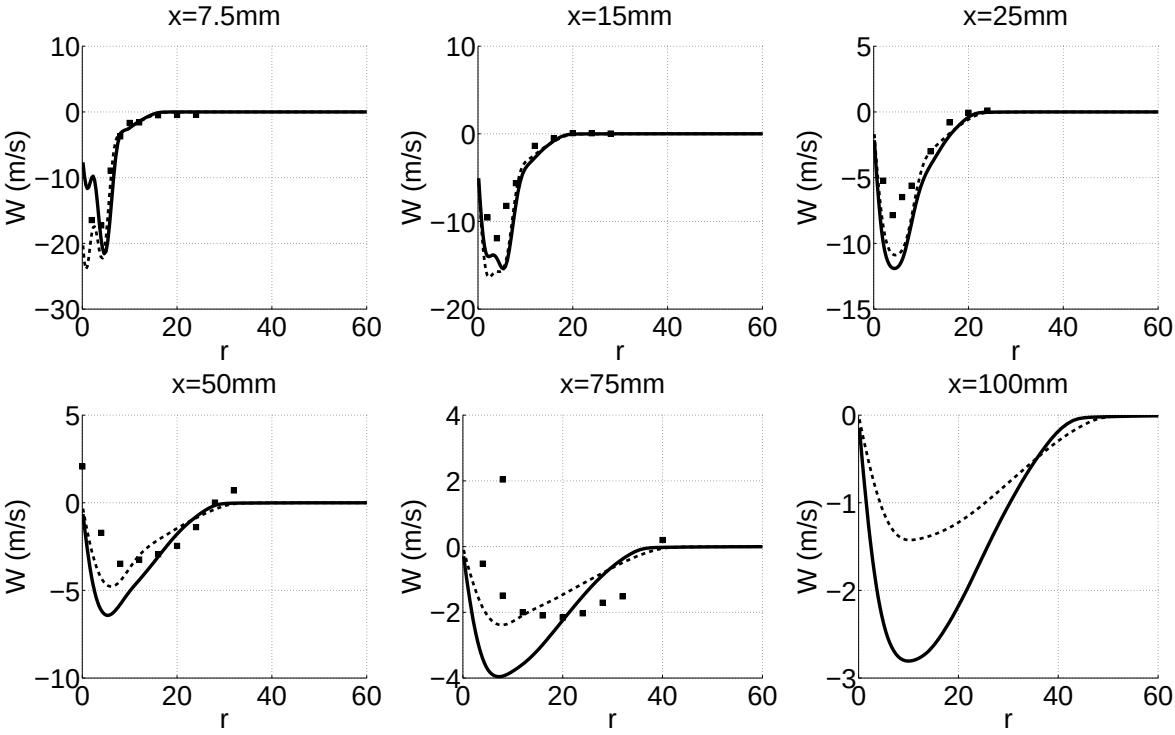

Figure 6.5: Mean tangential gas velocity profiles. Dashed black line: REDIM PS, Full black line: Flamelet PS, Symbols: experimental data.

This is again due to the lower temperature prediction with the REDIM at the location of the radial peak velocity (figure 6.8). Further downstream the deceleration of the radial velocity is smaller in the REDIM calculations, resulting in higher radial velocities than in the flamelet calculations. This is likely due to the lower turbulent stresses in the REDIM calculations. For the $x = 50mm$, $75mm$ and $100mm$, both calculations substantially under-predict the radial velocities. Notice again the non-zero centerline values of the experimental radial velocities at almost all axial positions. This was also observed for the radial velocity measurements in the inert spray case. This is either due to errors in the measurements or due to asymmetry of the experiment. The normal turbulent stresses, shown in figure 6.7, are strongly over-predicted for all positions, due to the strong production of turbulence close to the inlet and the slow dissipation further downstream. The strong production of turbulence can be explained by the strong over-prediction of velocities and the velocity gradients close to the inlet.

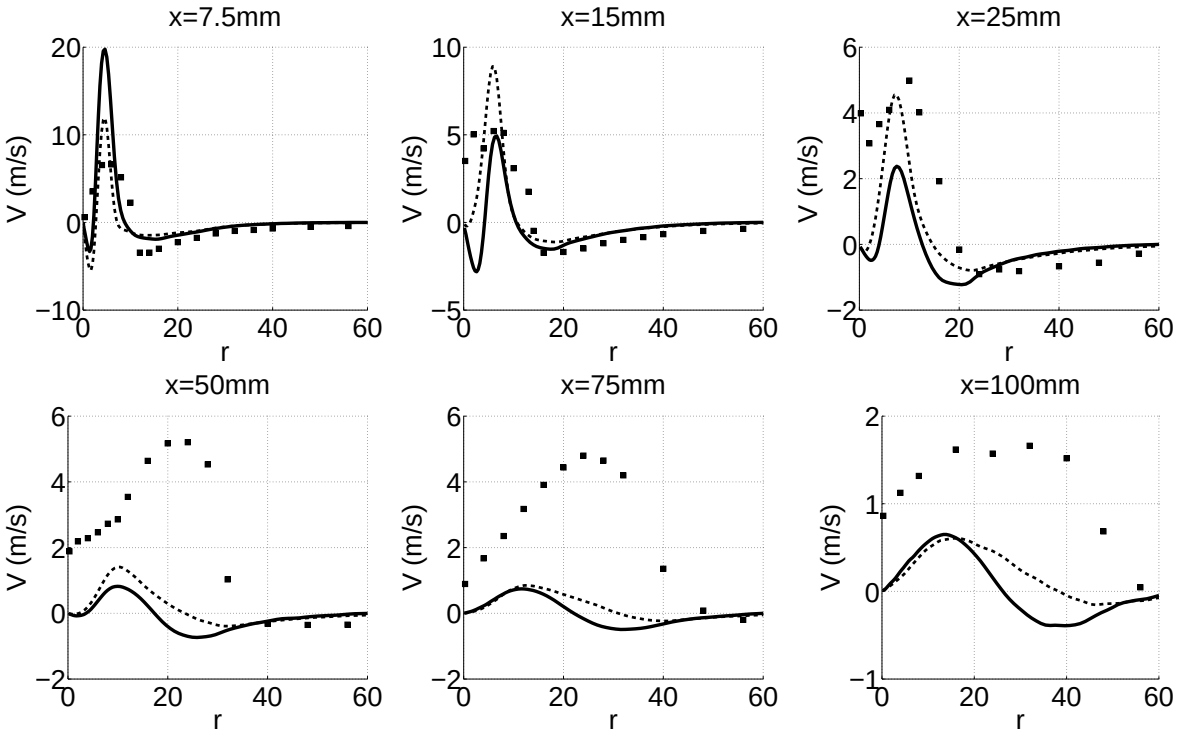

Figure 6.6: Mean radial gas velocity profiles. Grey line: UM, Dashed black line: US, Full black line: PS, Symbols: experimental data.

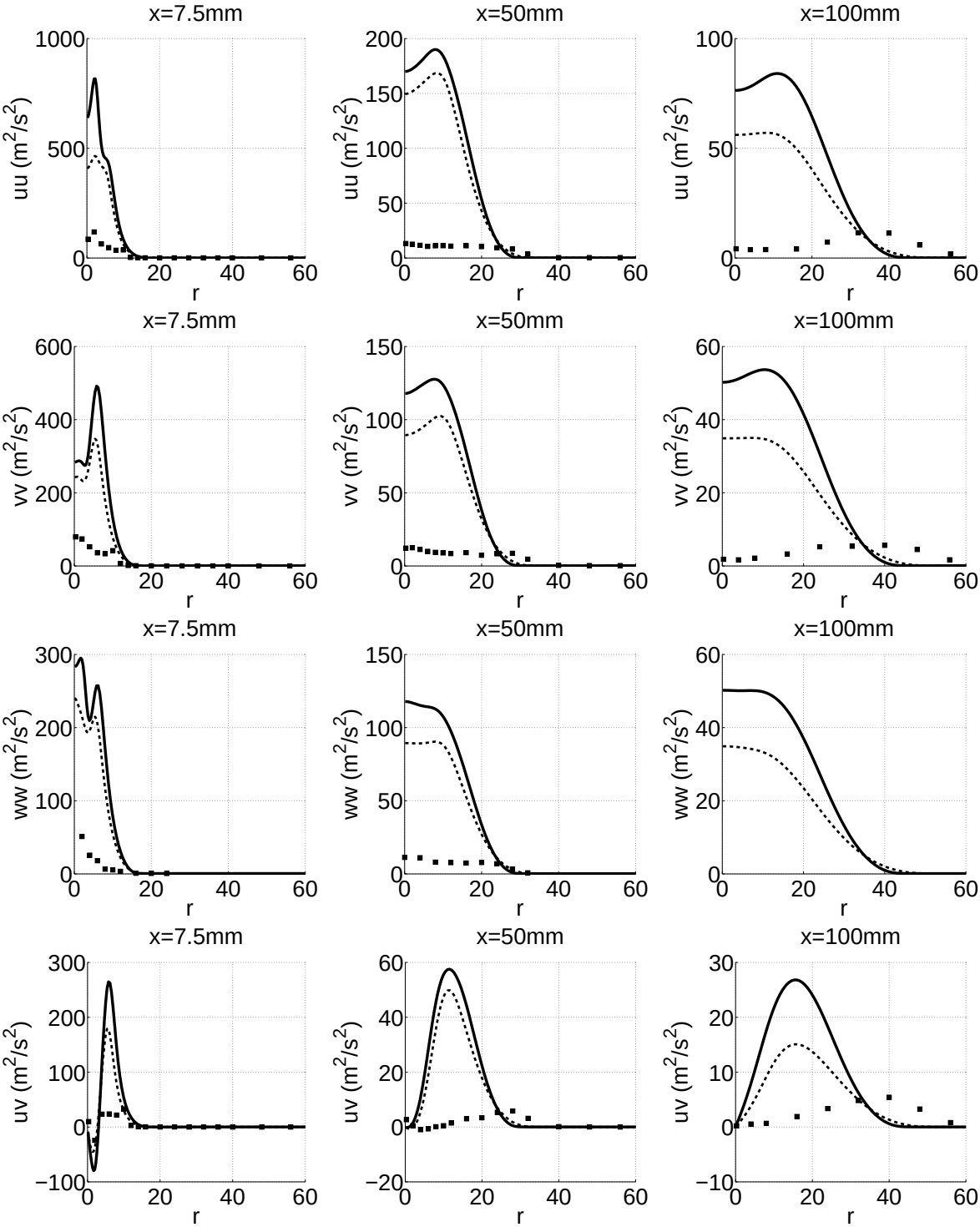

Figure 6.7: Mean gas velocity fluctuation profiles. Dashed black line: REDIM PS, Full black line: Flamelet PS, Symbols: experimental data.

Also the turbulent shear stress $\widetilde{u''v''}$ is largely over-predicted in line with the overall over-prediction of turbulence and the shear stress will itself help in the production of turbulent stresses, through interaction with velocity gradients.

Concluding, all velocities are over-predicted close to the burner inlet. This is likely due to a combination of the uncertainty of the inlet conditions and the over-prediction of the temperature. It might thus help to change the boundary conditions for the gas flow to obtain better results, but on the other hand there is a strong feedback of the temperature field on the flow field, resulting in a strong influence of the combustion model on the flow field predictions. Overall, the best flow field predictions are obtained with the REDIM, but these are not sufficiently good to expect good predictions of the droplet velocities.

Composition fields For the composition fields, the temperature profiles shown in figure 6.8 are first discussed, as the mixture fraction cannot be calculated from the methanol mole fraction measurements. In general, the flamelet calculation seems to result in the best predictions of the temperature. The REDIM calculation, on the other hand, under-predicts the width of the temperature profiles and over-predicts the centerline temperature for $x > 50mm$. In contrast to this is the low centerline temperature for the REDIM calculation at $x = 7.5mm$, which can be explained by finite rate chemistry effects, as can be seen in the temperature scatter plots shown in figure 6.9. For the flamelet calculations a part of the flamelet is retrieved, while for the REDIM calculations at $x = 7.5mm$ there is a substantial amount of scatter in the low temperature region, most likely representing ignition at the flame base. Further downstream, at $x = 25mm$, the amount of scatter has reduced and around $Z = 0.11$ a group of scatters in the shape of a vertical line is observed, which is representing the ignition of gas particles which received vapor from the droplets. Finally, at $x = 50mm$, also the scatter plot of the REDIM calculation resembles a flamelet. A more quantitative comparison can be made with the conditional temperature profiles shown in figure 6.10. At $x = 7.5mm$ the scatters in the low temperature have a substantial effect on the conditional mean, while further downstream the conditional mean resembles the flamelet. In general, the REDIM calculation results in an overall lean flame. In figure 6.11, the mixture fraction profiles are shown. The mixture fraction is a good indicator for the evaporation rate. At $x = 7.5mm$, the mixture fraction profiles are almost identical for both calculations, but further downstream the flamelet calculations predict increasingly higher mixture fractions, while the profiles of the REDIM calculation stay relatively constant. This suggests that in the flamelet calculation, the global evaporation rate is much larger than in the REDIM calculation and this cannot be explained by the rather small differences of the temperature profiles of both

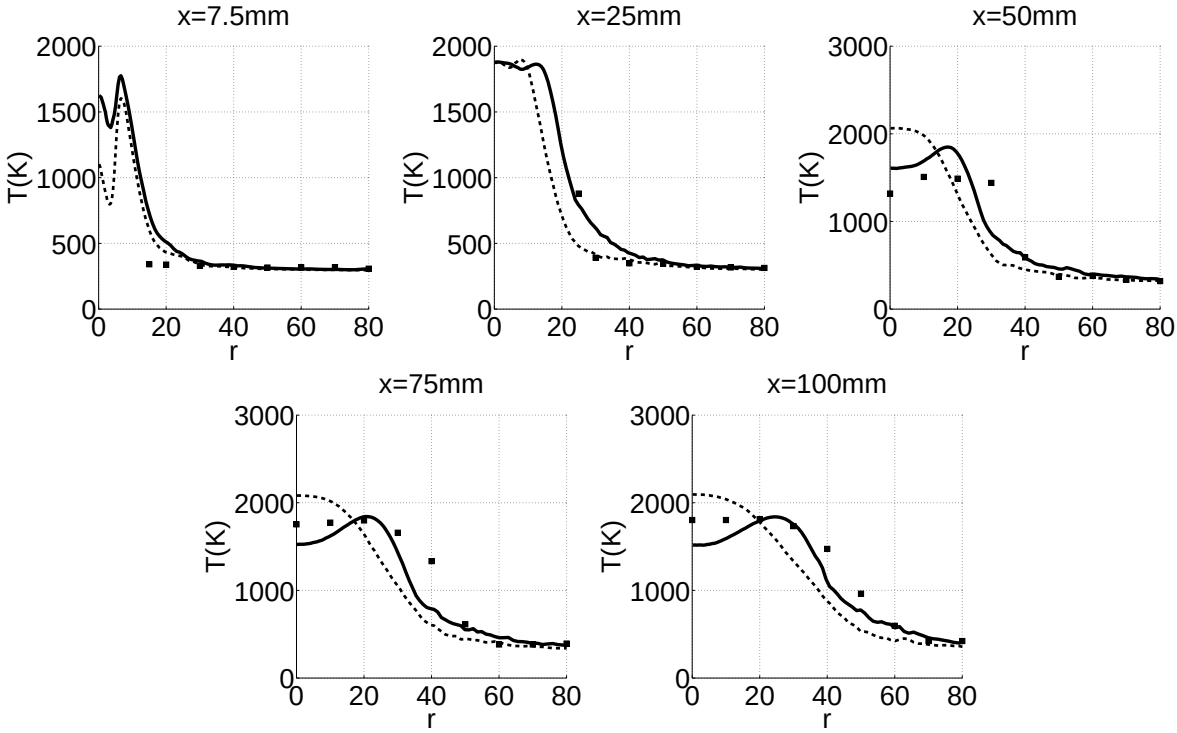

Figure 6.8: Mean mixture fraction profiles. Dashed black line: REDIM PS, Full black line: Flamelet PS, Symbols: experimental data.

calculations. To better understand this behavior, the mean Y_{CH_3OH}-profiles shown in figure 6.12 are studied. At $x = 7.5mm$, the REDIM predicts a high concentration of methanol vapor, while the flamelet calculation predicts no occurrence of methanol vapor. This can be explained by the fact that at this position the flames in both calculations are still lean (figure 6.10 and 6.9). For the flamelet calculation, all methanol vapor is consumed infinitely fast, while the finite rate chemistry effects in the REDIM calculation results a slower consumption of the methanol vapor. Further downstream ($x > 50mm$), the opposite is observed. The flamelet calculations predict occurrence of methanol vapor, while there is no methanol vapor for the REDIM calculations. Based on the methanol mole fraction measurements which have higher values further downstream (not shown), the flamelet calculations seem to better predict the overall structure of the flame. This was already suggested by the temperature profiles. To better understand the flame structures in physical space the Y_{OH}-profiles are studied (figure 6.13). At $x = 7.5mm$, the flame structure is reasonably similar for both calculations, with only a difference in the center region due the finite rate chemistry effects in the REDIM calculation. Further downstream, on the other hand, the flame structures differ strongly. While for the REDIM calculation the reaction takes place in the

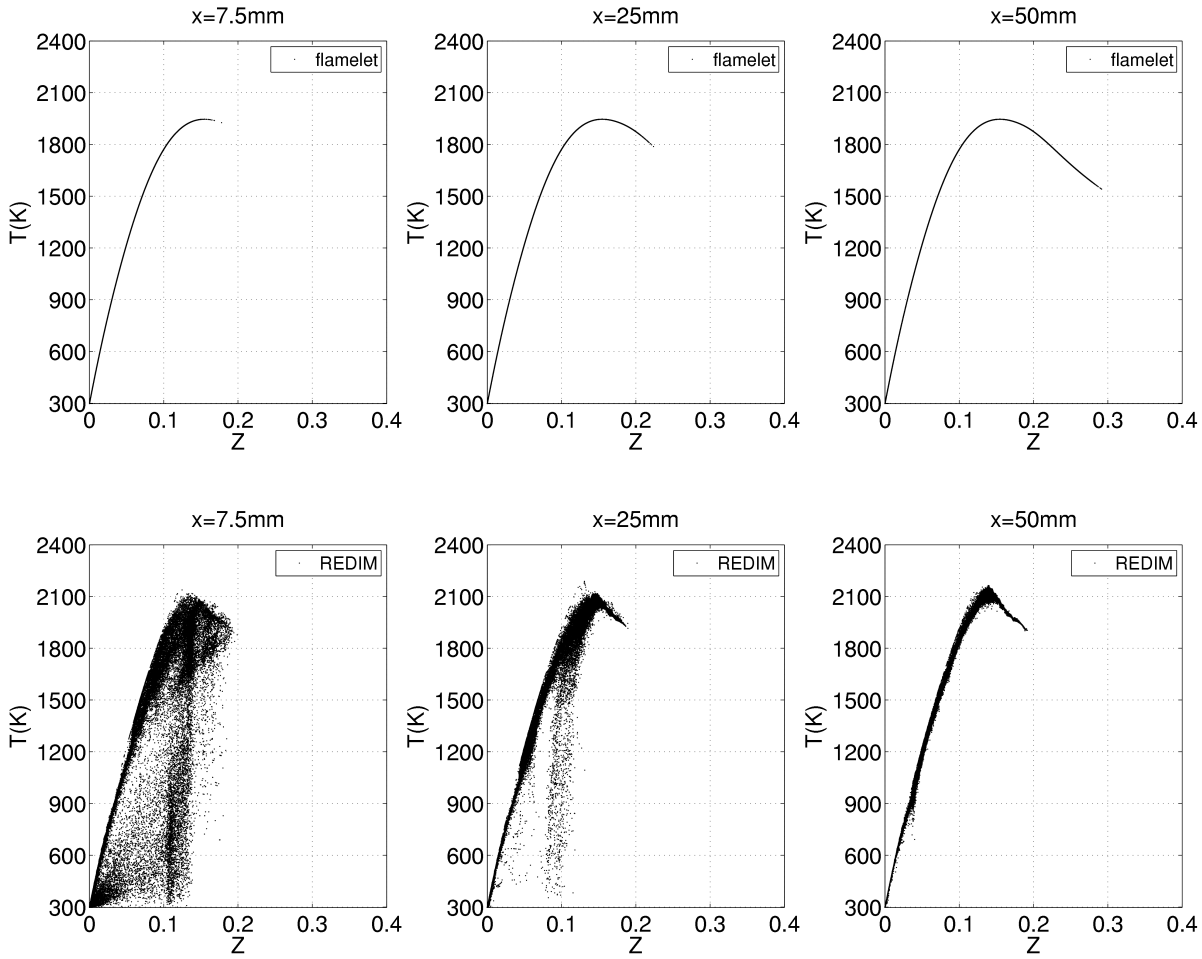

Figure 6.9: Temperature scatter plots of flamelet- (upper row) and REDIM-calculation (lower row) for $0 < r < 70mm$.

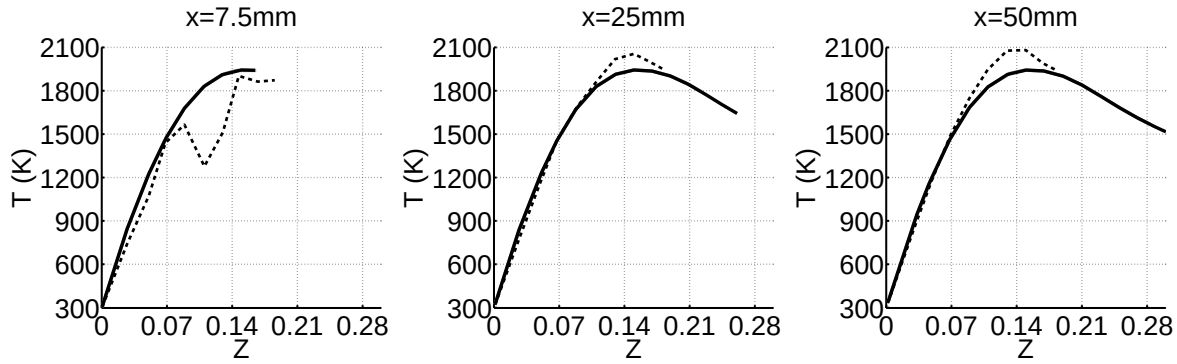

Figure 6.10: Conditional temperature profiles of flamelet (full line) and REDIM calculation (dashed line) for $0 < r < 70mm$.

center region, the flamelet calculation predicts a more radially outwards positioned reaction zone. Together with the low concentration of droplets in the center region

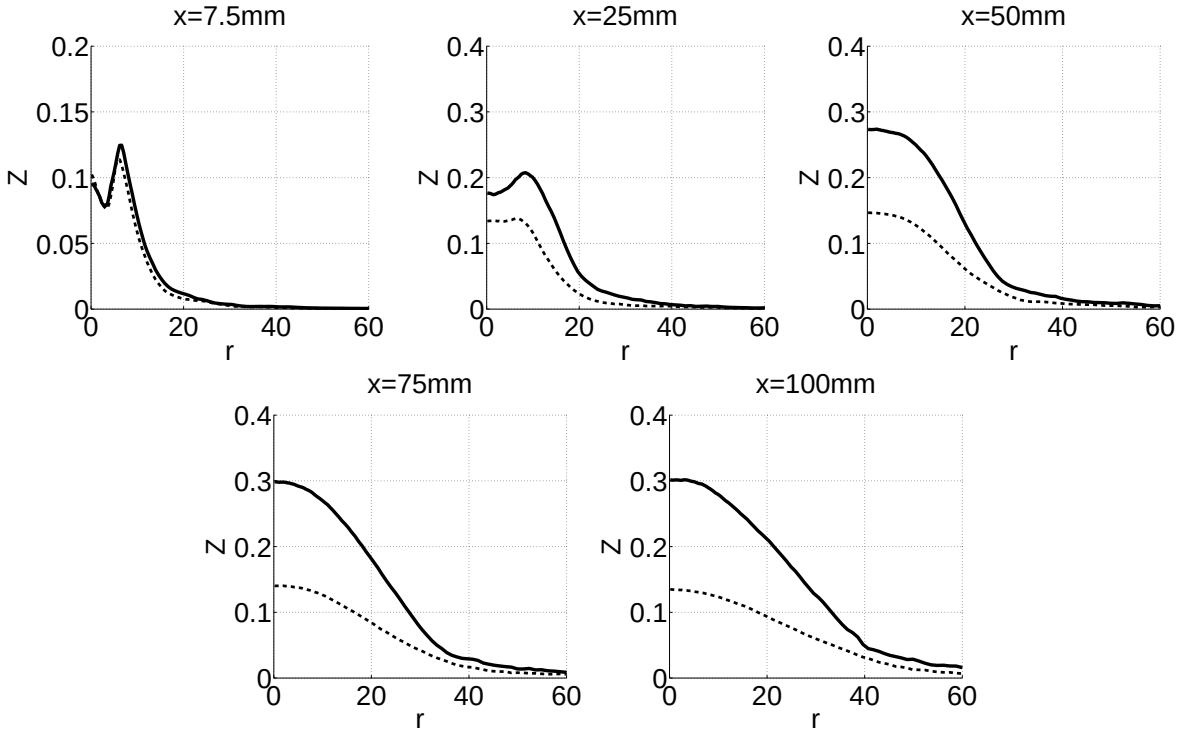

Figure 6.11: Mean mixture fraction profiles. Dashed black line: REDIM PS, Full black line: Flamelet PS.

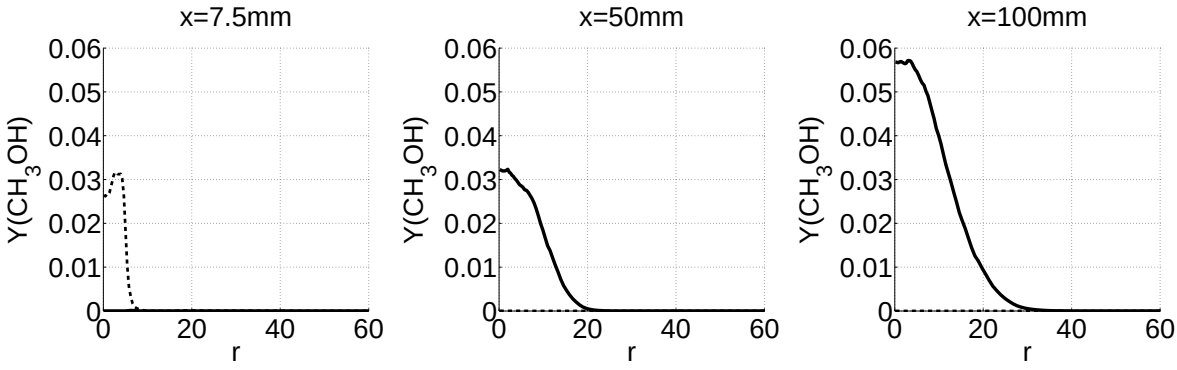

Figure 6.12: Mean methanol mass fraction profiles. Dashed black line: REDIM PS, Full black line: Flamelet PS.

(not shown) this explains the low mixture fraction profiles in combination with no occurrence of methanol vapor in the REDIM calculation. Normally one would expect a strong evaporation due to the lack of methanol vapor, but due to the low concentration of droplets in the center region there is only a small supply of methanol vapor, which is then consumed very quickly by the reaction zone situated in the center region. Concluding, the flamelet and the REDIM result in very different flame structures in

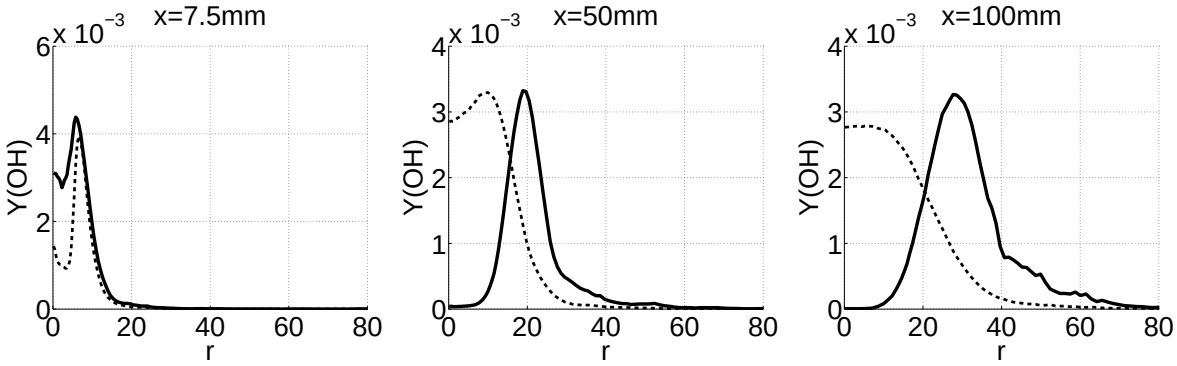

Figure 6.13: Mean OH mass fraction profiles. Dashed black line: REDIM PS, Full black line: Flamelet PS.

physical and composition space. As suggested by the measured temperature and the methanol mole fraction measurements, the flamelet calculation predicts the overall flame structure best. However, it should be noted that there is a large uncertainty about the inlet conditions of the gas and the droplets and this might affect the results.

Droplets

Now the droplet velocities of the flamelet and REDIM calculations are compared. In all figures the calculations are compared with the experiments for 3 different droplet size classes: $0-10\mu m$, $20-30\mu m$ and $40-50\mu m$. For the profiles of the calculation only the part with high droplet concentrations, i.e. $0.1n_{max}(x) < n(x) < n_{max}(x)$, are shown as these are most important for the prediction of the general vapor field. In figure 6.14 the mean axial droplet velocities are shown. In general, both calculations over-predict the axial droplet velocities in the center region, due to the over-prediction of the axial gas velocities in the center region. In the center region, also the relative position of the profiles is incorrect compared to the experiments due to the stronger influence of the gas phase on the smallest droplets. The lower axial gas velocities of the REDIM calculation result in overall lower axial droplet velocities. The mean radial droplet velocity is also predicted poorly as is shown in figure 6.15. At $x = 15mm$ a large over-prediction of the radial droplet velocities is observed for both calculations, with slightly better results for the REDIM calculation. At $x = 35mm$, the best result results are again obtained by the REDIM calculation. At $x = 75mm$, the radial droplet velocities are under-predicted and the relative position of the profiles is incorrect. The tangential droplet velocities shown in figure 6.16 are predicted well by both calculations, with slightly better results for the REDIM calculation

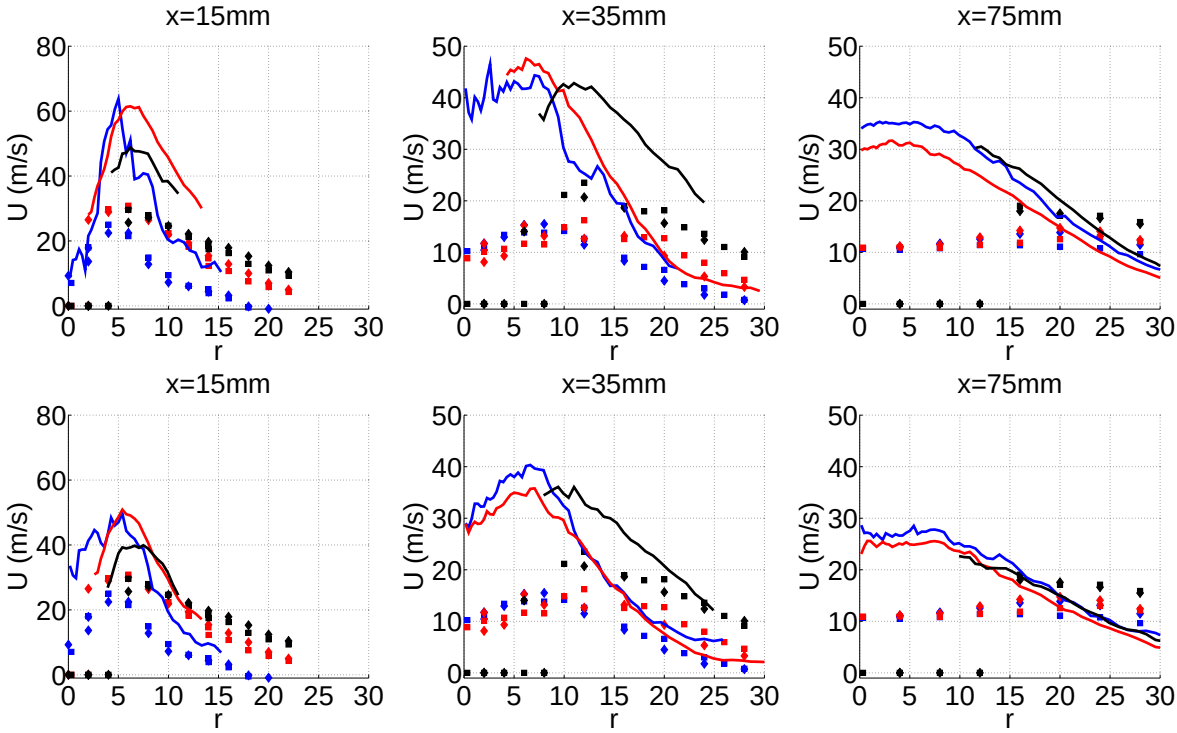

Figure 6.14: Mean axial droplet velocity profiles for the flamelet-(upper row) and REDIM-calculations (lower row). blue: $0-10\mu m$, red: $20-30\mu m$, black: $40-50\mu m$. Lines: simulation results. Symbols: experimental data.

further downstream. In figure 6.17 the profiles for axial normal turbulent stresses are shown. For both calculations the stresses are substantially over-predicted, with the largest over-predictions for the smallest droplets as these are the most affected by the over-prediction of the gas phase turbulence. Also the other normal stresses and the shear stresses are severely over-predicted. Concluding, the droplet velocity fields are not predicted correctly partly due to poor predictions of the gas flow fields and this might affect the droplet distribution and therefore also the mixture fraction field and the flame structure. It is not clear whether this is due to the large uncertainty of the inlet conditions or the inability of the RANS-droplet-PDF framework to capture the dynamics of the droplets. However, good predictions of the droplets velocities were obtained for the inert spray case in the previous chapter, making the latter less plausible.

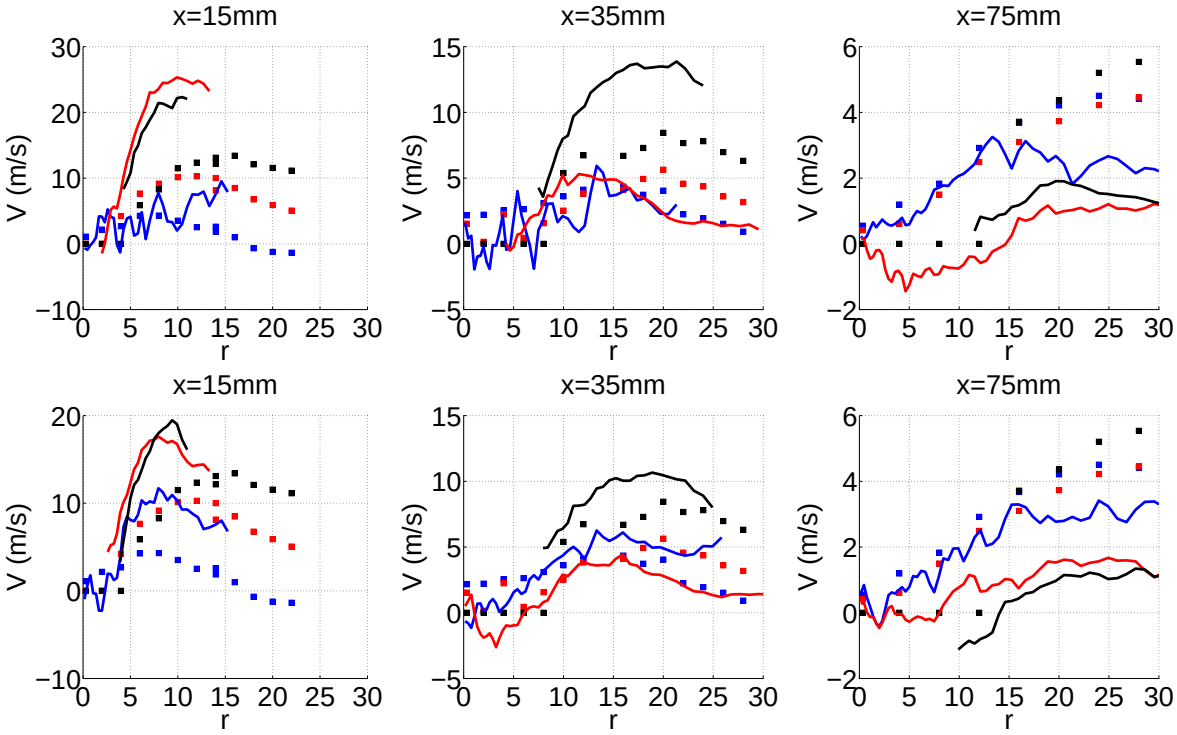

Figure 6.15: Mean radial droplet velocity profiles for the flamelet-(upper row) and REDIM-calculations (lower row). blue: $0-10\mu m$, red: $20-30\mu m$, black: $40-50\mu m$. Lines: simulation results. Symbols: experimental data.

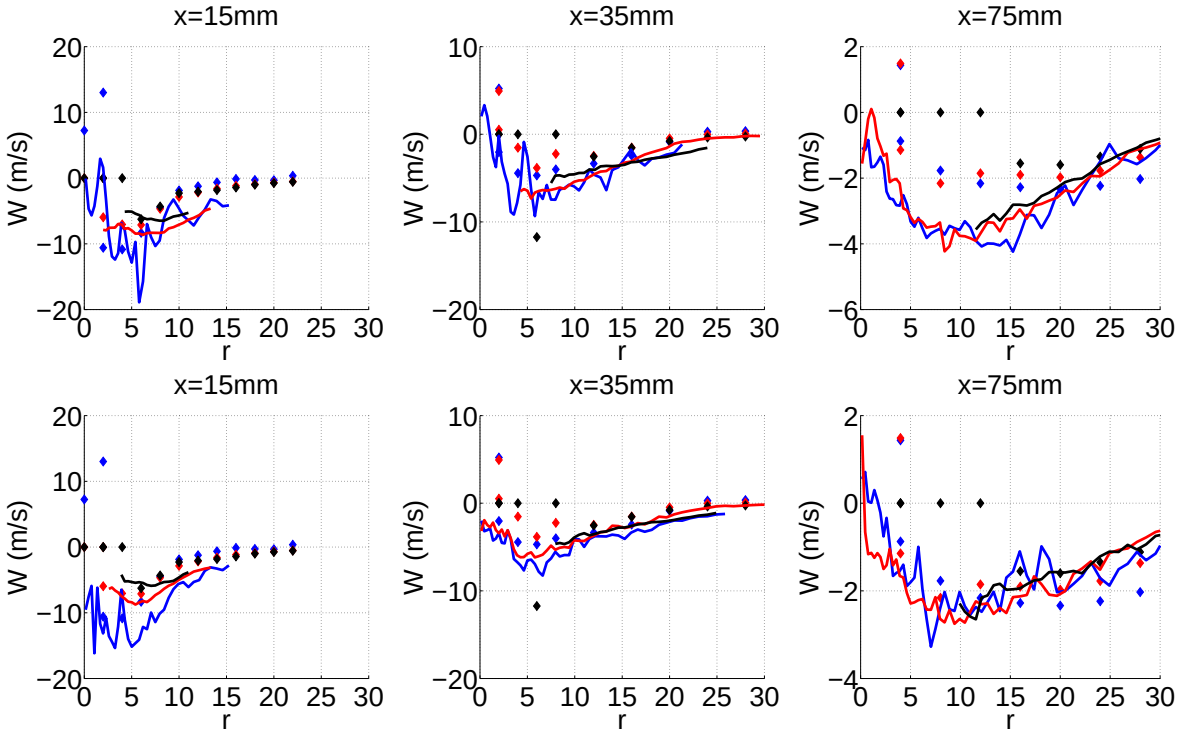

Figure 6.16: Mean tangential droplet velocity profiles for the flamelet- (upper row) and REDIM-calculations (lower row). blue: $0-10\mu m$, red: $20-30\mu m$, black: $40-50\mu m$. Lines: simulation results. Symbols: experimental data.

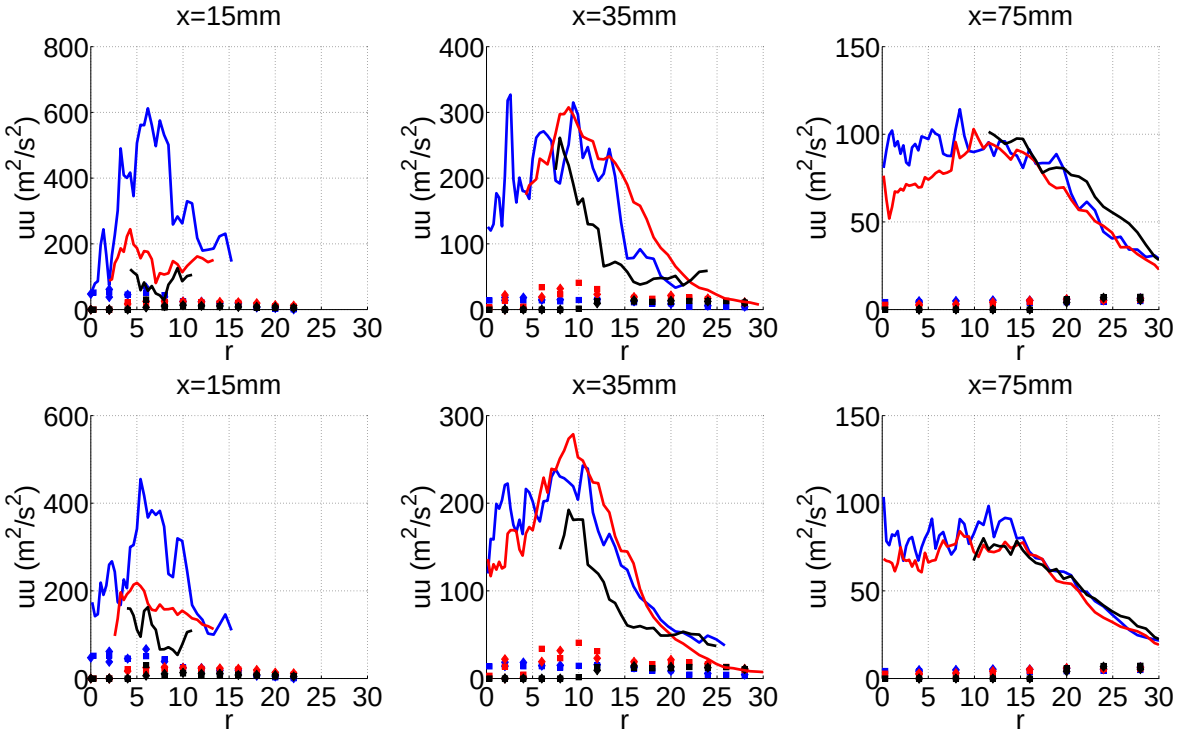

Figure 6.17: Mean axial droplet velocity fluctuation profiles for the flamelet- (upper row) and REDIM-calculations (lower row). blue: $0-10\mu m$, red: $20-30\mu m$, black: $40-50\mu m$. Lines: simulation results. Symbols: experimental data.

6.3.2 Influence of vapor distribution modeling

The influence of the vapor distribution model has been tested in the framework of flamelet calculations and is now discussed. The combinations of models used is summarized in table 6.2.

Table 6.2: Combination of models to test the influence of the vapor distribution model.

Case	Vapor distribution model	Seen composition model
PS	feed saturation peak	closest to saturation
US	uniform	closest to saturation
UM	uniform	cell mean

Mean mixture fraction and mixture fraction rms In figure 6.18 the mean mixture fraction profiles are shown. Close to the inlet, at $x = 7.5mm$, all profiles are similar. Further downstream, the differences become more apparent. In general, the vapor distribution model does not have a large effect on the mean mixture fraction profiles. The seen composition model on the other hand substantially affects the mean mixture fraction predictions, with lower mixture fraction values when the mean properties are used for the seen composition. This will be discussed in more detail in the next section. In figure 6.19 the mixture fraction rms profiles are shown. Similar

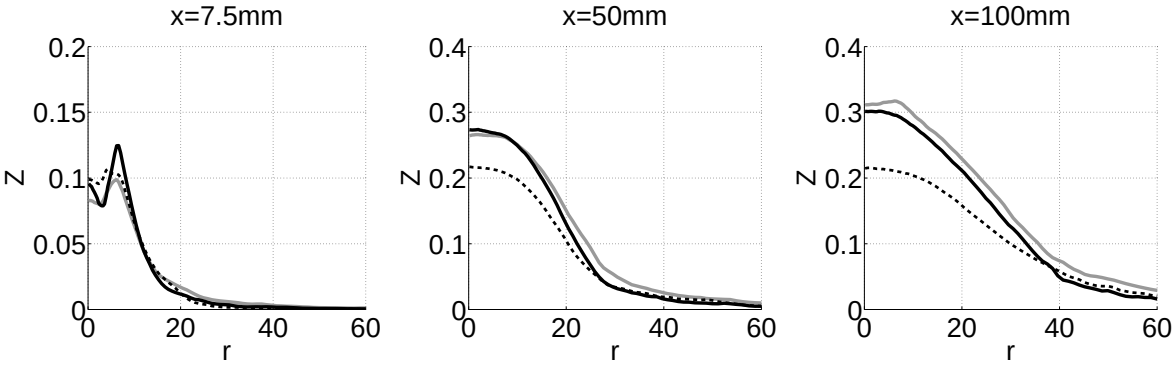

Figure 6.18: Mean mixture fraction profiles. Grey line: US, Dashed black line: UM, Full black line: PS, Symbols: experimental data.

results as for the mean mixture are observed. The vapor distribution model again has a small influence on the results.

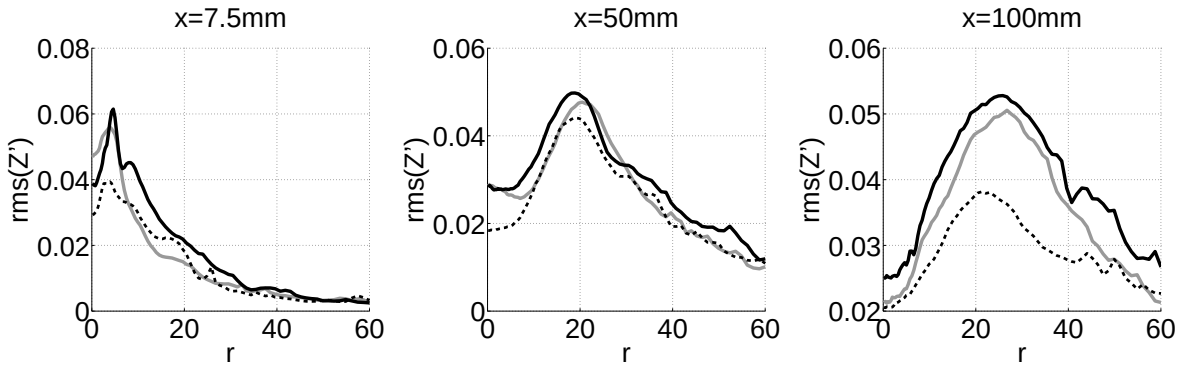

Figure 6.19: Mixture fraction rms profiles. Grey line: US, Dashed black line: UM, Full black line: PS, Symbols: experimental data.

Mixture fraction PDF Even though only a small influence of the vapor distribution model on the mean mixture fraction was observed, the mixture fraction PDFs are studied at the positions with the largest differences in mean mixture fraction. In figure 6.20 the PDFs at $x = 7.5mm$ at different radial positions in the center region are shown for the PS- and the US-calculation. In general, a large influence of the vapor distribution model is observed. This was to be expected as this is a region of strong evaporation resulting in a large 'saturation peaks' in the PS-calculation. The uniform distribution model in the US-calculation brings forth more regularly shaped PDFs due to the inherently faster mixing. Notice also how the β-PDF is not able to represent the transported PDFs of the PS-calculation, while it captures the PDFs of the US-calculation reasonably. In figure 6.21 the PDFs at $x = 50mm$ at different radial positions in a more radially outward region are shown for the PS- and the US-calculation. At $r = 21mm$, the PDF-shapes of both calculations are still similar. However, more radially outward, the influence of evaporation becomes stronger and results in 'saturation peaks' in the PDFs of the PS-calculation. This is not observed for the US-calculation, which again has more regularly shaped PDFs. Again the PDFs of the US-calculation are captured better by the β-PDF, which cannot capture the 'saturation peaks' in the PS-calculation.

Mean temperature The prediction of the temperature is directly connected to the mixture fraction predictions as the conditional temperature is imposed by the flamelet model. The influence of the vapor distribution model on the temperature profiles shown in figure 6.22 is thus rather small (PS vs US) and again the largest differences are seen for different seen composition models (US vs UM).

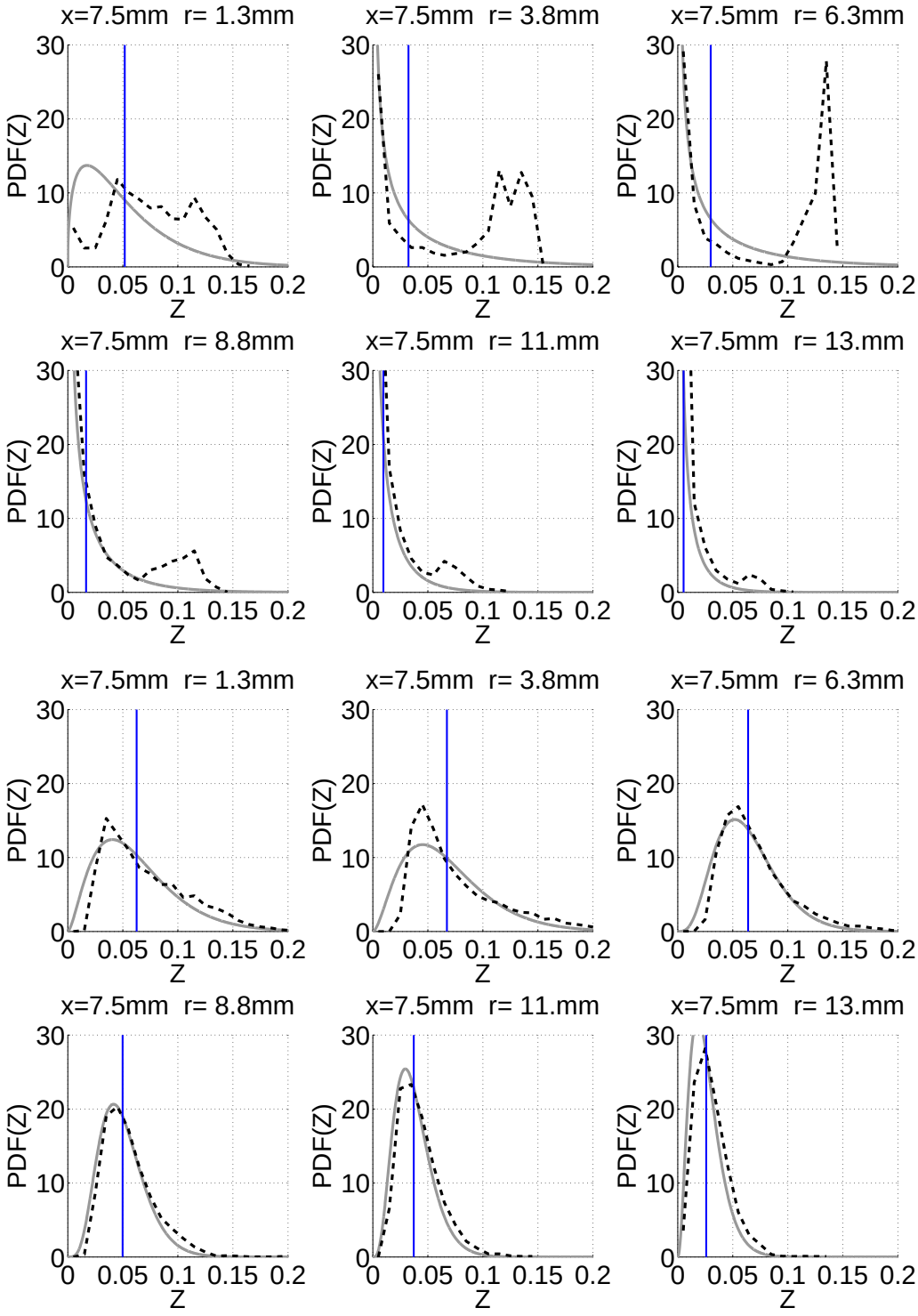

Figure 6.20: Mixture fraction PDF profiles for the PS-(upper rows) and US-calculations (lower rows) at $x = 7.5mm$. Grey line: β-PDF, Dashed black line: transported PDF.

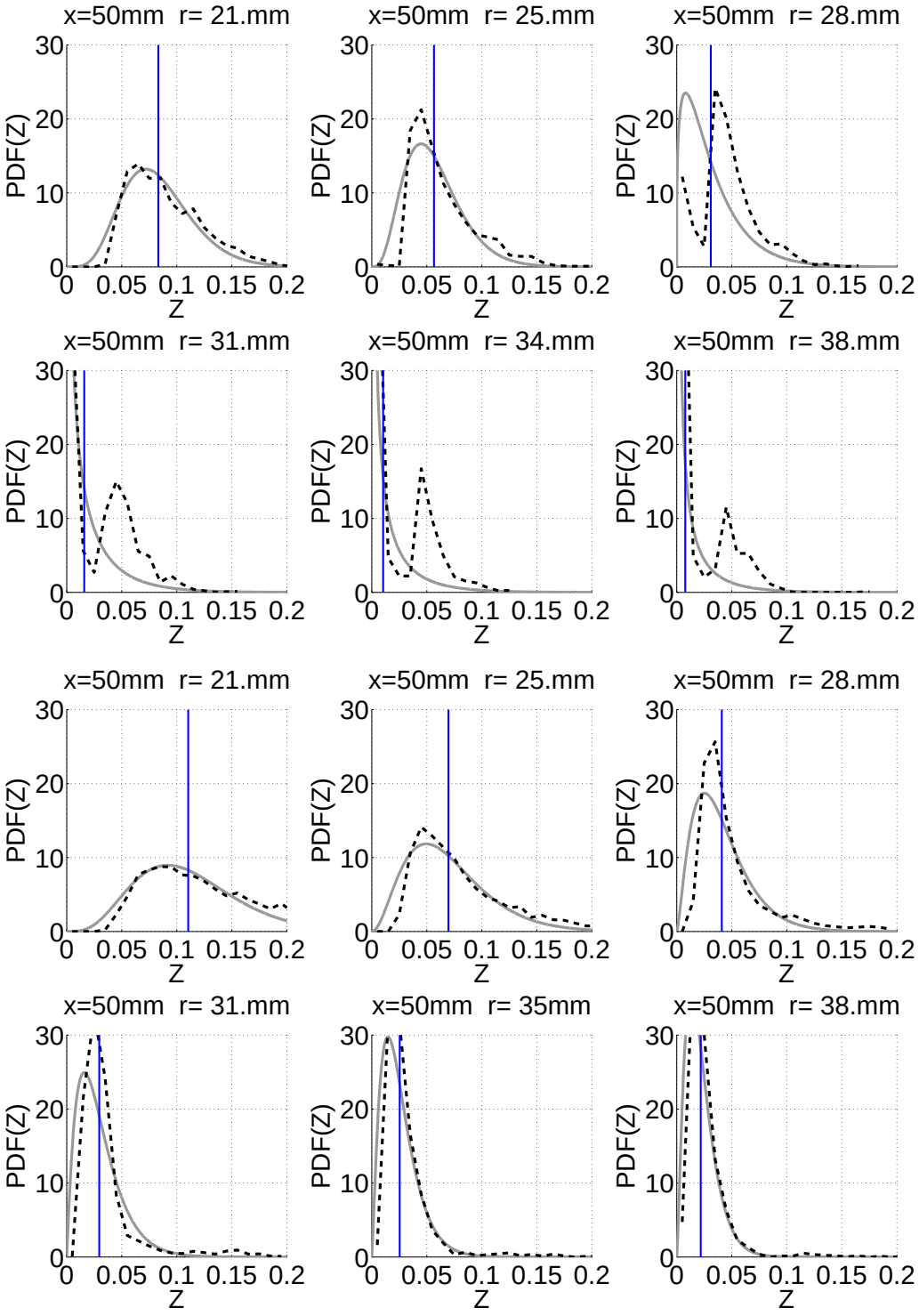

Figure 6.21: Mixture fraction PDF profiles for the PS-(upper rows) and US-calculations (lower rows) at $x = 50mm$. Grey line: β-PDF, Dashed black line: transported PDF.

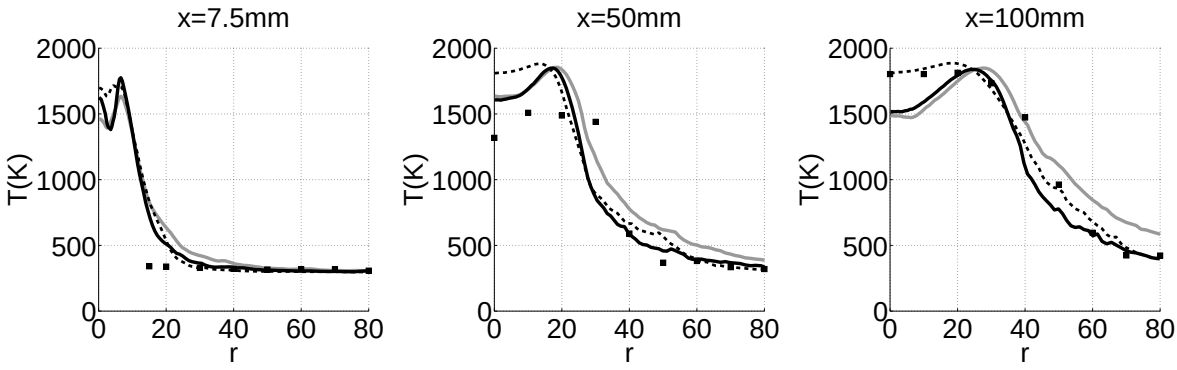

Figure 6.22: Mean temperature profiles. Grey line: US, Dashed black line: UM, Full black line: PS, Symbols: experimental data.

6.3.3 Influence of seen properties modeling

The influence of the seen composition model has been tested in the framework of flamelet calculations with the feed the saturation peak vapor distribution model and is now discussed. The combinations of models used are summarized in table 6.2.

Table 6.3: Combination of models to test the influence of the seen composition model.

Case	Vapour distribution model	Seen composition model
PS	feed saturation peak	closest to saturation
PM	feed saturation peak	cell mean
PR	feed saturation peak	random gas particle

Mean mixture fraction and mixture fraction rms In figure 6.23, the mean mixture profiles are shown. The influence of the seen properties model on the mean mixture fraction is generally more important than the vapor distribution model. The 'seen composition from the most saturated particles' model predicts the highest mixture fraction values, while the seen random composition model, has the lowest mixture fraction profiles. This is the opposite behaviour of what was observed in the inert spray case, where the seen random composition model resulted in the highest mixture fraction profiles. Also the mixture fraction rms profiles shown in figure 6.24 differ strongly. However, based on these mean profiles it is not clear what the reason is for these observed differences. Statistics of the seen composition could help to better understand the mechanism causing the observed differences.

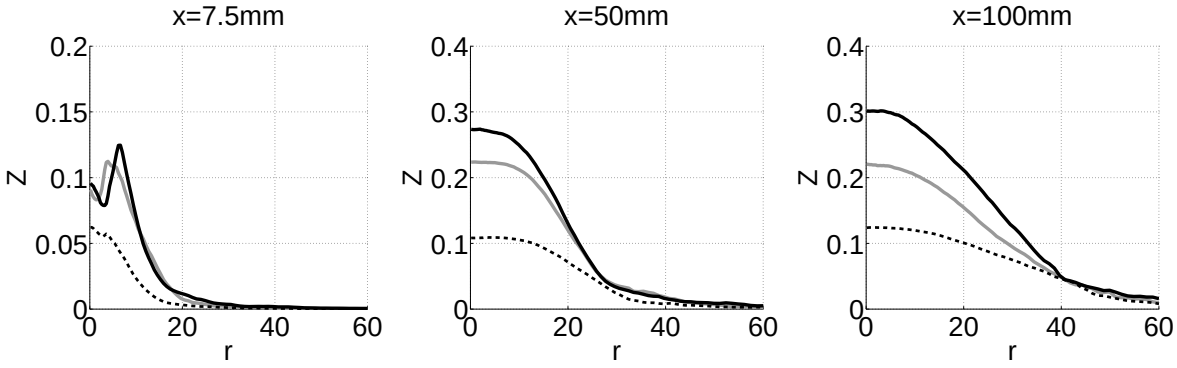

Figure 6.23: Mean mixture fraction profiles. Grey line: PM, Dashed black line: PR, Full black line: PS, Symbols: experimental data.

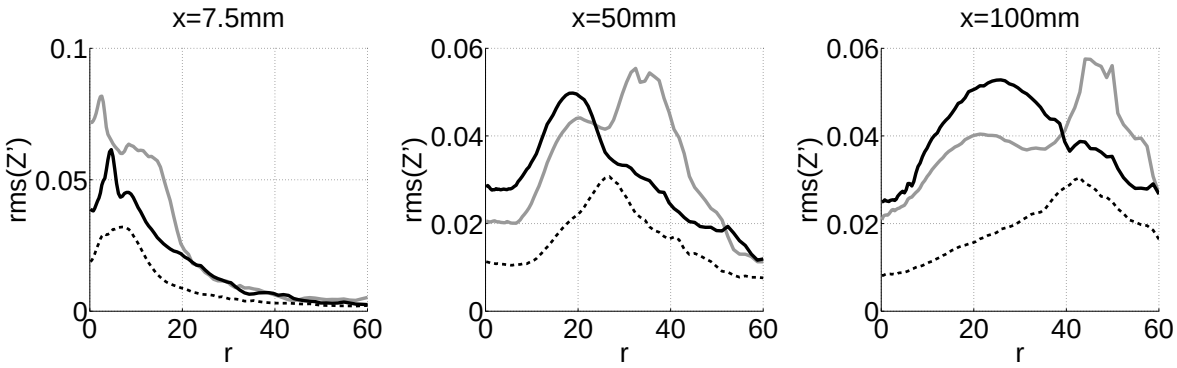

Figure 6.24: Mixture fraction rms profiles. Grey line: PM, Dashed black line: PR, Full black line: PS.

Mean temperature In figure 6.25 the mean temperature profiles are shown. Due to the use of the flamelet model, the conditional mean of the temperature is fixed and the temperature profiles will thus be mainly determined by the mean mixture fraction. The largest difference in the temperature profiles are observed close to the inlet where the seen random composition model (R) predicts substantially lower temperatures compared to the other models. Further downstream the temperature differences become smaller even though the mixture fraction differences are larger.

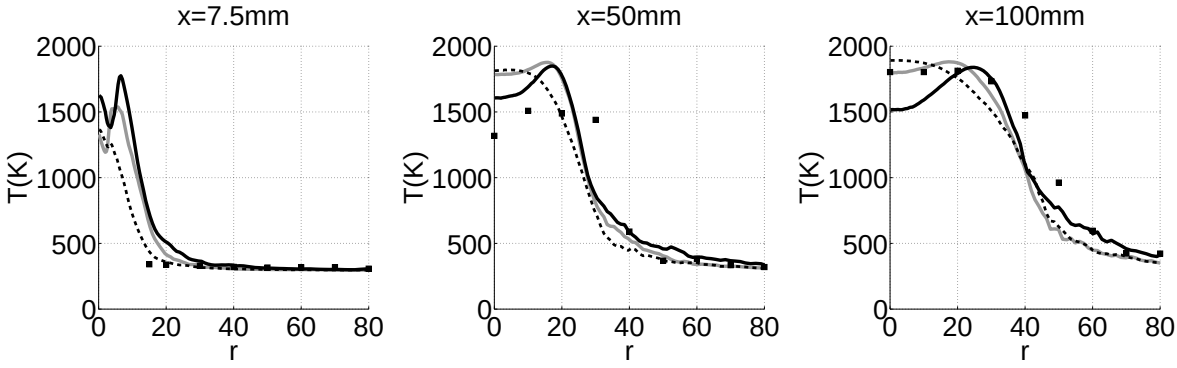

Figure 6.25: Mean temperature profiles. Grey line: PM, Dashed black line: PR, Full black line: PS.

6.4 Conclusions

In this chapter, the hybrid RANS gas-PDF droplet-PDF framework has been tested for the case of a swirling reacting methanol spray.

As combustion model, both a single steady laminar diffusion flamelet and a REDIM have been used. It should be noted that this is the first time that the hybrid RANS gas-PDF droplet-PDF framework gas been combined with a REDIM table.

Due to large uncertainty of the boundary conditions, the gas and droplet velocities are not predicted correctly. Therefore only a qualitative study could be performed, studying the relative influence of the different models. A strong influence of the combustion model on the gas and droplets velocities has been observed, due to the strong influence of the temperature and density on the flow field.

As expected, the predictions of the mixture fraction and the temperature are strongly influenced by the combustion model. In general, the flamelet model resulted in an overall stronger evaporation, seen in the higher mixture fraction values. This can be explained by the fact that in the flamelet calculation the position of the flame resides in more radially outward regions of higher droplet concentration than in the REDIM calculation, where the reaction zone is situated in the less densely populated center region. Thus, both combustion models result in very different flame structures in physical and composition space.

Based on the measurements of temperature and methanol mole fraction, the flamelet calculation results in the best predictions of the overall flame structure for the present inlet conditions. However, as mentioned above, there is a large uncertainty on the inlet conditions for the gas and the droplets and this might have affected the

results. The only conclusion that can be made is thus that the combustion model has a strong influence on the flame structure in physical and composition space.

Finally the influence of the vapor distribution model and the seen composition model have been tested with the flamelet model. The influence of the vapor distribution model on the mean mixture fraction and mean temperature is rather small. The mixture fraction PDFs, on the other hand, are strongly influenced by the vapor distribution model. For the 'feed the saturation peak' model, the PDFs have a high saturation peak in regions of strong evaporation. Therefore a β-PDF cannot capture the resulting complex shape of the transported PDF. The uniform distribution model, on the other hand, results in more regular shapes of the PDF which are captured reasonably well by a β-PDF. The influence of the seen composition model on the mean mixture fraction is stronger. The 'seen composition from the most saturated particles' model (S) results in the highest mixture fraction values, implying the strongest evaporation, while the seen random composition model (R) has the lowest mixture fraction profiles. This is the exact opposite of what was seen in the inert spray calculations, but the reason for this behaviour cannot be determined from the mean profiles. A more detailed study, with e.g analysis of the statistics of the seen composition, is needed to better understand the mechanisms causing the observed differences. The differences observed in the temperature profiles are mainly due to the differences in mixture fraction. This also affects the temperature profiles but the differences are smaller.

For future calculations, it is recommended to try and find better inlet conditions. However, as this is not straightforward, a different reacting spray case with better defined boundary conditions seems to be a better option.

Chapter 7

Conclusions

The objective of this PhD research has been to better understand the behaviour of the hybrid RANS-PDF modeling framework in combination with a reduced chemistry description and its ability to capture finite rate chemistry effects, e.g. local extinction and mixing of incomplete combustion products with a fresh mixture, in complex gas and spray flames.

In chapter 2, the framework for hybrid RANS-PDF calculations of reactive single phase flows has been introduced. Subsequently the framework for hybrid RANS gas-PDF droplet-PDF calculations of inert and reactive sprays has been discussed. In chapter 3, the often made assumptions in presumed PDF modeling have been discussed by analyzing the experimental data of a swirling bluff-body gas flame. The recirculation zone, which causes mixing of incomplete combustion products with the fresh mixture, has been shown to render some of these presumed modeling assumptions invalid. In chapter 4, the focus was on better understanding the interaction between the mixing modeling and the reduced chemistry techniques, i.e. flamelet or REDIM, and how this affects the ability of the hybrid RANS-PDF framework to capture finite rate chemistry effects in the case of gas flames. The hybrid RANS-PDF framework in combination with the REDIM combustion model has been tested in the case of the same swirling bluff-body flame, which was already analyzed in chapter 3. The interaction of the mixing and the combustion model has been investigated through the analysis of the trajectories of the computational gas particles, used to statistically represent the gas-PDF and it has been concluded that the current hybrid RANS-PDF framework is not able to capture local extinction due to the use of a single mixing time scale. In chapter 5, the focus was on the ability of the hybrid RANS gas-

PDF droplet-PDF framework to correctly describe droplet dispersion, evaporation, vapour distribution and scalar mixing in the case of sprays. The hybrid RANS gas-PDF droplet-PDF framework has been tested in the case of a swirling inert methanol spray. The influence of the vapour distribution modeling and the seen composition modeling on the evaporation rate has been investigated in detail and has been shown to be important. Finally, in chapter 6, the focus was on testing the ability of the combination of the hybrid RANS gas-PDF droplet-PDF framework and a reduced chemistry technique, to capture the spray flame structure in physical and composition space. The hybrid RANS gas-PDF droplet-PDF framework has been used in combination with a flamelet or a REDIM to simulate a swirling reactive methanol spray. The influence of the combustion model on the flow and composition fields was shown to be strong. The flamelet calculation resulted in a reasonable prediction of the temperature field but with less satisfactory predictions of the gas and droplet velocities, partially due to the large uncertainty of the inlet conditions.

For the more detailed conclusions, the reader is referred to the end of each chapter.

7.1 Novel aspects

The novelty of this PhD research is found in:

1. An improved REDIM table with the re-enforced upper boundary, as the loss of the upper boundary resulted in numerical fluctuations in composition space.

2. The implementation of the tracer method in the PDFD code.

3. The detailed analysis of the tracer data and the new way to visualize the correlation between physical space and composition space, resulting in new insights into the interaction between the mixing model and the REDIM in the hybrid RANS-PDF framework.

4. The discussion of a new model for the composition seen by the droplets, introducing localness in the seen composition modeling. This model results, in combination with the EMST mixing model and the 'feed the saturation peak' vapour distribution model, in the most consistent and physically most correct modeling of evaporation up to date within the hybrid RANS gas-PDF droplet-PDF framework.

5. Detailed analysis of the seen composition modeling for an inert and a reacting swirling spray.

6. The first application of REDIM in a hybrid RANS gas-PDF droplet-PDF framework.

7.2 Future suggestions

Due to limitations in time and resources many topics were not investigated in this PhD research. Therefore, some suggestions for future research are now made.

- For the construction of the REDIM, it would be interesting to test different assumptions for the gradients in physical space, as was done in [40]. This can be done by prescribing the gradients in physical space in the calculation of the REDIM manifold, instead of taking them from the laminar diffusion flamelet calculations.

- To test the findings of the a priori study it would be interesting to do some presumed PDF calculations with REDIM, to show the influence of the presumed modeling assumptions. On top of this, comparing LES calculations with presumed PDF-modeling with LES calculations with transported FDF-modeling would help to assess the validity of the presumed FDF assumptions in the context of LES.

- In the context of turbulent reactive flow calculations with reduced chemistry tables parametrized by mixture fraction and a progress variable, it would be interesting to account for the different time scales for inert and reactive scalars. This could be done based on the physical gradients of the inert and reactive scalars used to generate the REDIM. This way the mixing time scale for the inert scalars could come from the turbulence model, while the position on the REDIM would determine the ratio of the mixing time scales for the inert and reactive scalars. A similar model was already suggested in [53].

- In the case of the swirling gas flame, it would be very interesting to extend the study of the trajectories of the computational gas particles to calculations with the PSP model, to see how this influences the results and if local extinction is captured. Also a comparison with a RANS-PDF calculation with ISAT using the

detailed mechanism would be interesting, to see the difference with the REDIM calculation.

- In the case of the spray calculation it would be interesting to do a similar study of the vapor distribution and seen composition models in the context of LES and see how the importance of the models is influenced. It is expected that these models remain important as with LES the same point assumption is made and the flow and composition field around the droplets are still unresolved. An LES calculation of the gas flow inside the atomizer would also result in better inlet conditions for the gas flow.

- Similar to the study of the tracers in the swirling gas flame, it would be interesting to store the time evolution of the droplet parcels, to see the effect of the modeling on the droplet size and temperature. Then also the Lagrangian statistics of the composition seen by the droplet parcels could be studied, giving more insight into the modeling.

- It would also be interesting to test the hybrid RANS gas-PDF droplet-PDF framework for a reacting spray case for which the inlet conditions are known more accurately and for which the dilute spray assumption, i.e no break-up, is more valid close to the inlet, so that the study is less corrupted by the uncertainty on the inlet conditions.

- More DNS studies, completely resolving the flow and composition field around one or more droplets, are needed for better modeling of the composition seen by the droplets.

Appendix A

Turbulent Schmidt number

The motivation for the use of a variable turbulent Schmidt number Sc_t stems from an observation of experimental data and calculation results obtained using a constant Sc_t.

In Figure A.1, we observe a plateau above the bluff body for mean mixture fraction (with a value close to $\widetilde{Z} = 0.2$) in the first radial profiles at $x/D = 0.2$. This plateau is missed in our non-linear k-ϵ calculation, where the turbulent flux for mean mixture fraction is modeled using a gradient diffusion model with a constant turbulent Schmidt number with standard value $Sc_t = 0.7$. We could say that we model "too much turbulent diffusion" on the outer edge of the recirculation zone. A first idea would then be to lower the diffusion coefficient by increasing the turbulent Schmidt number. We can see that results obtained with a higher constant value $Sc_t = 1.5$ are indeed improved close to the bluff body, allowing to capture the plateau. However, we observe that further downstream, mean mixture fraction is overestimated on the center-line.

By looking at experimental results for mean mixture fraction in Figure A.1 and for mean axial velocity in Figure A.2, we can see that the steep gradients for mean mixture fraction (the edges of the plateau) coincide with the edges of the first recirculation zone. This observation is the basis for an ad hoc adjustment of the turbulent Schmidt number. The idea is to propose a variable Sc_t that will get the standard constant value $Sc_t = 0.7$ except in the zones corresponding to the edges of the first recirculation zone where it will locally get a higher value.

A way to characterize the edge of the recirculation zone is to look for the high values of the gradient of mean axial velocity $\widetilde{U}$ in the radial direction $\partial\widetilde{U}/\partial r$, or to look for the high values of the shear stress $\widetilde{u''v''}$ directly related to the velocity

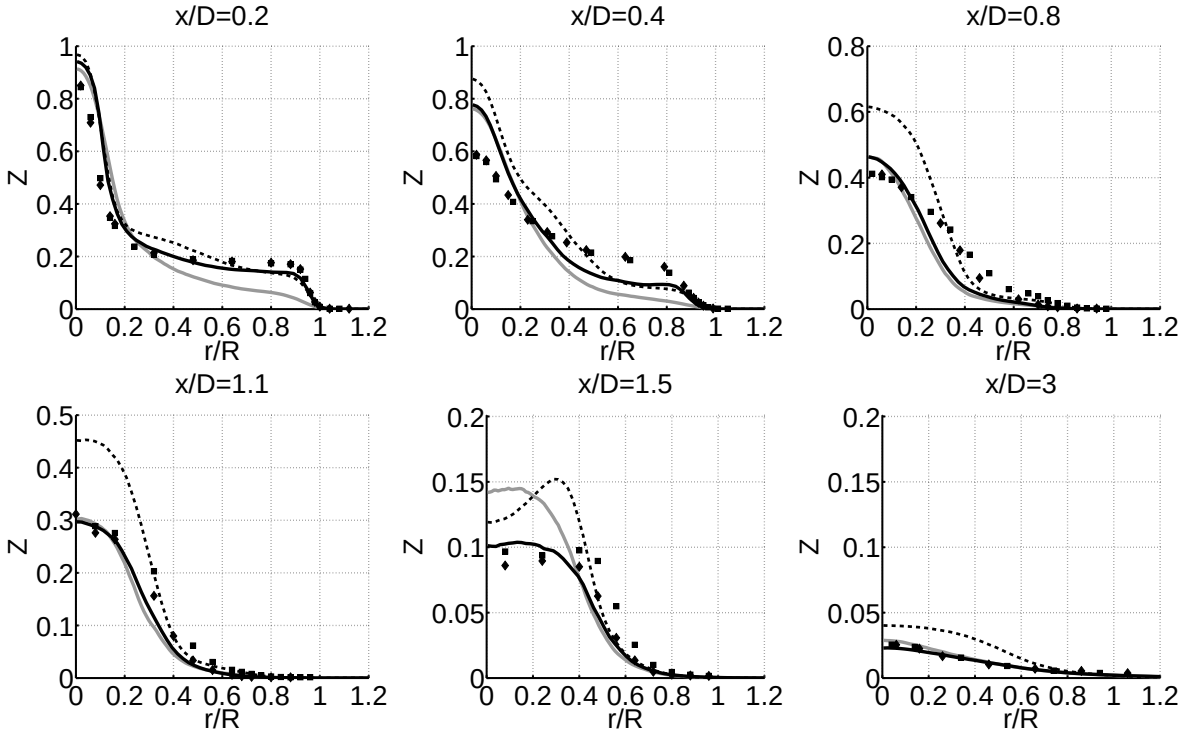

Figure A.1: Mean mixture fraction profiles from REDIM-EMST transported PDF calculations. Full black line: variable Sc_t. Dashed line: $Sc_t = 1.5$. Grey line: $Sc_t = 0.7$. Symbols: experimental data.

gradients in the algebraic model used here:

$$-\langle\rho\rangle\widetilde{u''v''} = \mu_t \left(\frac{\partial \widetilde{U}}{\partial r} + \frac{\partial \widetilde{V}}{\partial x} \right) \tag{A.1}$$

The ad hoc adjustment proposed is based on the following factor:

$$\begin{aligned} \lambda &= -2\frac{\widetilde{u''v''}}{\sqrt{\widetilde{u''u''}.\widetilde{v''v''}}} \qquad \text{if} \quad \widetilde{u''v''} < \widetilde{u''v''}^{(-)}_{\text{thres}} \quad \text{or} \quad \widetilde{u''v''} > \widetilde{u''v''}^{(+)}_{\text{thres}} \\ \lambda &= 0 \quad \text{otherwise,} \end{aligned} \tag{A.2}$$

where $\lambda > 0$ corresponds to the outer edge of the recirculation zone (where $\widetilde{u''v''} < 0$), and $\lambda < 0$ corresponds to the inner edge. We used the threshold values $\widetilde{u''v''}^{(-)}_{\text{thres}} = -10$ and $\widetilde{u''v''}^{(+)}_{\text{thres}} = 20$ in order to localize the outer and inner edges respectively.

We moreover restrict ourselves in physical space to the zone above the bluff-body

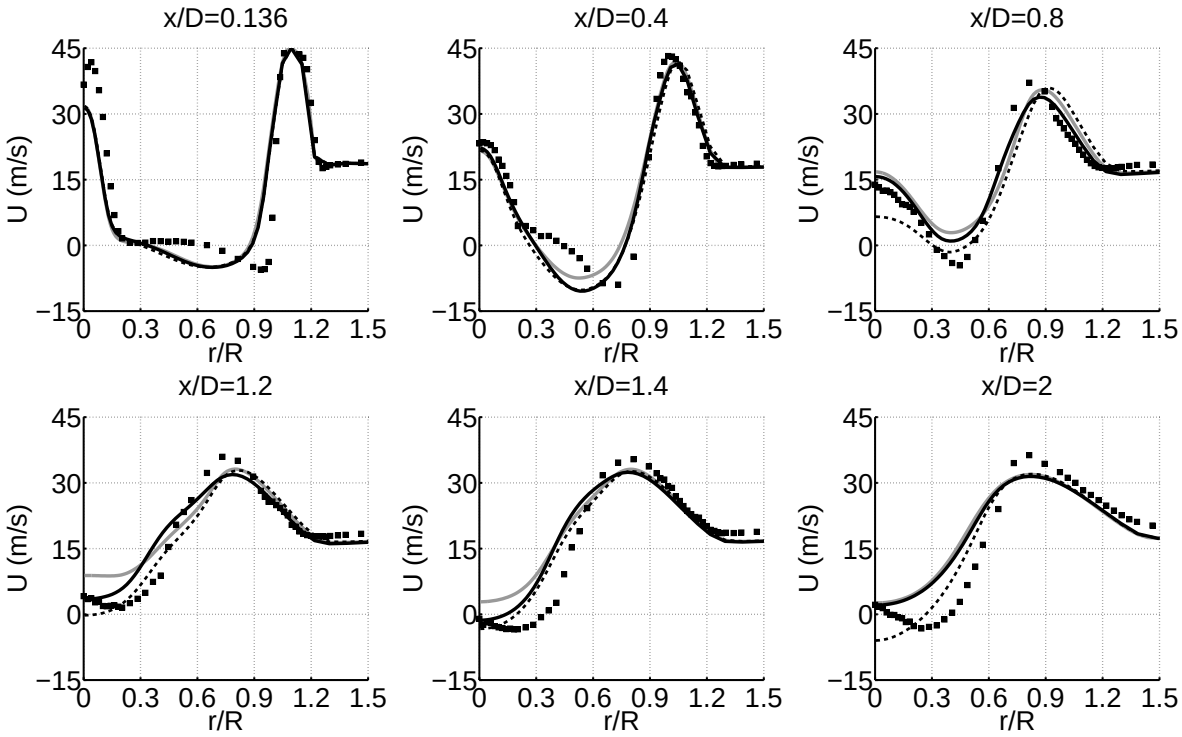

Figure A.2: Mean Axial Velocity profiles from REDIM-EMST transported PDF calculations. Full black line: variable Sc_t. Dashed line: $Sc_t = 1.5$. Grey line: $Sc_t = 0.7$. Symbols: experimental data.

(with maximum axial coordinate $X_{\rm lim}$ and maximum radial coordinate $R_{\rm lim}$) and introduce a smooth transition to zero in axial direction (between $X_{\rm lim}/2$ and $X_{\rm lim}$):

$$\begin{aligned} \lambda^* &= \lambda . \frac{1}{2}\left\{1+\sin\left[\pi\left(\frac{x}{X_{\rm lim}/2}-\frac{1}{2}\right)\right]\right\} \qquad \text{if} \quad x < X_{\rm lim}, \quad r < R_{\rm lim} \\ \lambda^* &= 0 \quad \text{otherwise,} \end{aligned} \tag{A.3}$$

with $X_{\rm lim} = 0.05$ and $R_{\rm lim} = 0.03$.

We finally decide by how much the turbulent Schmidt number should locally be multiplied:

$$Sc_t = 0.7\,(1+\lambda^{**})\,, \tag{A.4}$$

where

$$\begin{aligned} \lambda^{**} &= \lambda^{(\text{inner})}\text{MIN}(1,-\lambda^{*}) \qquad \text{if} \quad \lambda^{*}<0 \\ \lambda^{**} &= \lambda^{(\text{outer})}\text{MIN}(1,\lambda^{*}) \qquad \text{if} \quad \lambda^{*}>0, \end{aligned} \tag{A.5}$$

with $\lambda^{(\text{inner})}=1$ and $\lambda^{(\text{outer})}=3$, such that Sc_t is at most multiplied by 2 on the inner edge and by 4 on the outer edge of the first recirculation zone.

Figure A.3 shows how the adjustment only affects a restricted zone of the computational domain (at the outer and inner edges of the first recirculation zone), while $Sc_t=0.7$ almost everywhere.

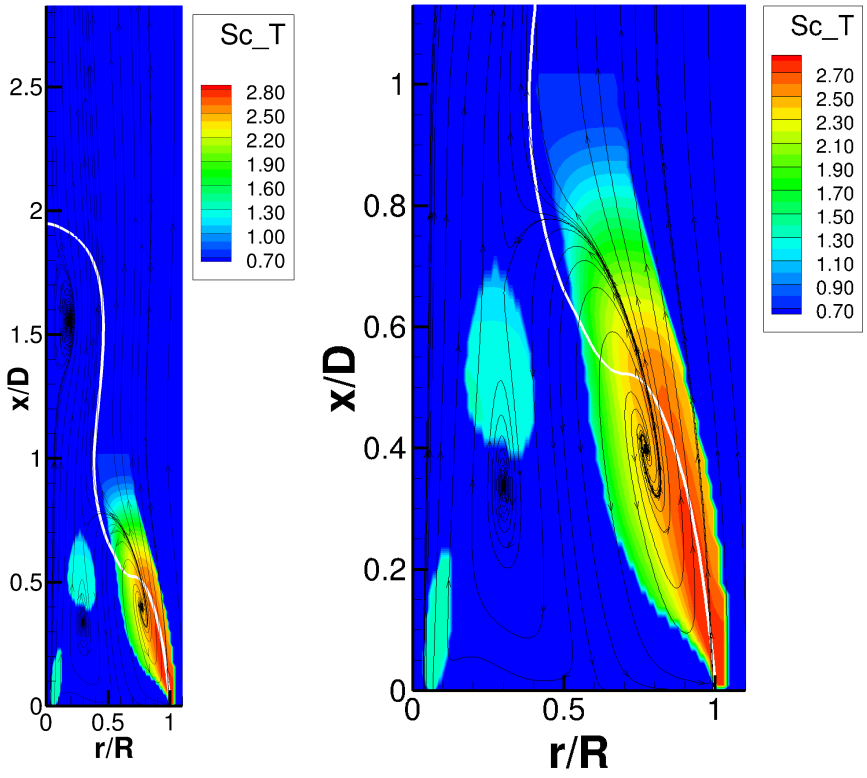

Figure A.3: Contours of Sc_t with streamlines: entire computational domain (left) and zoom on the first recirculation zone (right).

Bibliography

[1] L. Bernstein, P. Bosch, O. Canziani, Z. Chen, O. Christ, R. Davidson, W. Hare, D. Huq, S. Karoly, V. Kattsov, Z. Kundzewicz, J. Liu, U. Lohmann, M. Manning, T. Matsuno, B. Menne, B. Metz, N. Mirza, M.and Nicholls, L. Nurse, R. Pachauri, J. Palutikof, M; Parry, D. Qin, N. Ravindranath, A. Reisinger, J. Ren, K. Riahi, C. Rosenzweig, M. Rusticucci, S. Schneider, Y. Sokona, S. Solomon, P. Stott, R. Stouffer, T. Sugiyama, R. Swart, D. Tirpak, C. Vogel, and G. Yohe. *IPCC 4th Assesment Report: Climate Change 2007*. IPCC, 2007.

[2] G. Monbiot. *Heat: How to stop the planet from burning*. South End Press, 2007.

[3] J. Warnatz, U. Maas, and R.W. Dibble. *Combustion physical and chemical fundamentals, modeling and simulation, experiments, pollutant formation*. Springer, 2006.

[4] D. Veynante and L. Vervisch. Turbulent combustion modeling. *Progress in Energy and Combustion Science*, 28(3):193–266, 2002.

[5] M. Ihme and H. Pitsch. Prediction of extinction and reignition in nonpremixed turbulent flames using a flamelet/progress variable model 1. A. priori study and presumed PDF closure. *Combustion and Flame*, 155(1-2):70–89, October 2008.

[6] http://www.aeromech.usyd.edu.au/thermofluids/swirl_files/burner-plan.pdf, 2002.

[7] A.E. Lutz, R.J. Kee, J.F. Grcar, and F.M. Rupley. OPPDIF: a Fortran program for computing opposed-flow diffusion flames, 1996. Report No.SAND96-8243, Sandia National Laboratories.

[8] M. Ihme and H. Pitsch. Prediction of extinction and reignition in nonpremixed turbulent flames using a flamelet/progress variable model 1. A. priori study and presumed PDF closure. *Combustion and Flame*, 155(1-2):70–89, October 2008.

[9] V.G. McDonell and G.S. Samuelsen. An Experimental Database for the Computational Fluid-Dynamics of Reacting and Nonreacting Methanol Sprays. *Journal of Fluids Engineering - Transactions of the ASME*, 117(1):145–153, March 1995.

[10] S. B. Pope. *Turbulent Flows*. Cambridge University Press, 2000.

[11] B. Merci and E Dick. Heat transfer predictions with a cubic k-epsilon model for axisymmetric turbulent jets impinging onto a flat plate. *International Journal of Heat and Mass Transfer*, 46(3):469–480, January 2003.

[12] B.E. Launder, G.J. Reece, and W. Rodi. Progress in Development of a Reynolds-stress Turbulence Closure. *Journal of Fluid Mechanics*, 68(April15):537–566, 1975.

[13] N. Peters. *Turbulent Combustion*. Camebridge University Press, 2000.

[14] D.B. Spalding. Concentration Fluctuations in a Round Turbulent Free Jet. *Chemical Engineering Science*, 26(1):95–&, 1971.

[15] U Piomelli. Large-eddy simulation: achievements and challenges. *Progress in Aerospace Sciences*, 35(4):335–362, May 1999.

[16] H Pitsch. Large-eddy simulation of turbulent combustion. *Annual Review of Fluid Mechanics*, 38:453–482, 2006.

[17] J Smagorinsky. General ciriculation experiments with the primitive equations. *Monthly Weather Review*, 91:99–164, 1963.

[18] R.B. Fox. *Computational Models for Turbulent Reacting Flows*. Cambridge University Press, 2003.

[19] J. Baldyga and R Pohorecki. Turbulent micro-mixing in cehmical reactors: a review. *The Chemical Engineering Journal*, 58:183–195, 1995.

[20] E Villermaux and C Innocenti. On the geometry of turbulent mixing. *Journal of Fluid Mechanics*, 393:123–147, August 25 1999.

[21] Z Warhaft. Passive scalars in turbulent flows. *Annual Review of Fluid Mechanics*, 32:203–240, 2000.

[22] PE Dimotakis. Turbulent mixing. *Annual Review of Fluid Mechanics*, 37:329–356, 2005.

[23] AY Klimenko and RW Bilger. Conditional moment closure for turbulent combustion. *Progress in Energy and Combustion Science*, 25(6):595–687, 1999.

[24] N. Peters. Laminar flamelet concepts in turbulent combustion. *Proc. Combust. Inst.*, 21(1):1231–1250, 1986.

[25] H. Pitsch, C.M. Cha, and S. Fedotov. Flamelet modelling of non-premixed turbulent combustion with local extinction and re-ignition. *Combustion Theory and Modelling*, 7(2):317–332, June 2003.

[26] J.A. van Oijen and L.P.H. de Goey. Modelling of premixed laminar flames using flamelet-generated manifolds. *Combustion Science and Technology*, 161:113–137, 2000.

[27] O. Gicquel, N. Darabiha, and D. Thevenin. Laminar premixed hydrogen/air counterflow flame simulations using flame prolongation of ILDM with differential diffusion. *Proceedings of the Combustion Institute*, 28(Part 2):1901–1908, 2000. 28th International Symposium on Combustion, Univ Edinburgh, Edinburgh, Scotland, July 30-August 04, 2000.

[28] U. Maas and S.B. Pope. Simplifying Chemical-Kinetics - Intrinsic Low-Dimensional Manifolds in Composition Space. *Combustion and Flame*, 88(3-4):239–264, March 1992.

[29] U. Maas. Efficient calculation of intrinsic low-dimensional manifolds for the simplification of chemical kinetics. *Computing and Visualization in Science*, pages 69–81.

[30] R. Bender, T. Blasenbrey, and U. Maas. Coupling of detailed and ILDM-reduced chemistry with turbulent mixing. *Proceedings of the Combustion Institute*, 28(Part 1):101–106, 2000. 28th International Symposium on Combustion, Univ Edinburgh, Edinburgh, Scotland, July 30-August 04, 2000.

[31] Z. Ren and S.B. Pope. Transport-chemistry coupling in the reduced description of reactive flows. *Combustion Theory and Modelling*, 11(5):715–739, 2007.

[32] C.D. Pierce. *Progress-variable approach for large eddy simulation of turbulent combustion*. PhD thesis, Stanford University, 2001.

[33] C.D. Pierce and P. Moin. Progress-variable approach for large-eddy simulation of non-premixed turbulent combustion. *Journal of Fluid Mechanics*, 504:73–97, April 10 2004.

[34] B. Fiorina, R. Baron, O. Gicquel, D. Thevenin, S Carpentier, and N Darabiha. Modelling non-adiabatic partially premixed flames using flame-prolongation of ILDM. *Combustion Theory and Modelling*, 7(3):449–470, September 2003.

[35] B. Fiorina, O. Gicquel, L. Vervisch, S. Carpentier, and N. Darabiha. Approximating the chemical structure of partially premixed and diffusion counterflow flames using FPI flamelet tabulation. *Combustion and Flame*, 140(3):147–160, February 2005.

[36] A.W. Vreman, B.A. Albrecht, J.A. van Oijen, L. P.H. de Goey, and R.J.M. Bastiaans. Premixed and nonpremixed generated manifolds in large-eddy simulation of Sandia flame D and F. *Combustion and Flame*, 153(3):394–416, May 2008.

[37] M. Ihme and Y.C. See. Prediction of autoignition in a lifted methane/air flame using an unsteady flamelet/progress variable model. *Combustion and Flame*, 157(10):1850–1862, October 2010.

[38] J.-B. M, O. Colin, C. Angelberger, and D. Veynante. Using the tabulated diffusion flamelet model ADF-PCM to simulate a lifted methane-air jet flame. *Combustion and Flame*, 156(7):1318–1331, July 2009.

[39] V. Bykov and U. Maas. The extension of the ILDM concept to reaction-diffusion manifolds. *Combustion Theory and Modelling*, 11(6):839–862, December 2007.

[40] P-D Nguyen, L. Vervisch, V Subramanian, and Pascale Domingo. Multidimensional flamelet-generated manifolds for partially premixed combustion. *Combustion and Flame*, 157(1):43–61, January 2010.

[41] S.B. Pope. Computationally efficient implementation of combustion chemistry using in situ adaptive tabulation. *Combustion Theory and Modelling*, 1(1):41–63, March 1997.

[42] F. Contino, H. Jeanmart, T. Lucchini, and G. D'Errico. Coupling of in situ adaptive tabulation and dynamic adaptive chemistry: An effective method for

solving combustion in engine simulations. *Proceedings of the Combustion Institute*, 33(Part 2):3057–3064, 2011.

[43] Private discussion with Prof. U. Maas.

[44] J.P. Minier and E. Peirano. The pdf approach to turbulent polydispersed two-phase flows. *Physics Reports - Review Section of Physics Letters*, 352(1-3):1–214, October 2001.

[45] D.C. Haworth. Progress in probability density function methods for turbulent reacting flows. *Progress in Energy and Combustion Science*, 36(2):168–259, April 2010.

[46] B. Naud. *PFD modeling of turbulent sprays and flames using a particle stochastic approach*. PhD thesis, TU Delft, 2003.

[47] R.R. Cao, H. Wang, and S.B. Pope. The effect of mixing models in PDF calculations of piloted jet flames. *Proceedings of the Combustion Institute*, 31(Part 1):1543–1550, 2007.

[48] R.P. Lindstedt, H.C. Ozarovsky, R.S. Barlow, and A.N. Karpetis. Progression of localized extinction in high Reynolds number turbulent jet flames. *Proceedings of the Combustion Institute*, 31(Part 1):1551–1558, 2007.

[49] T.S. Kuan, R.P. Lindstedt, and E.M. Vaos. Higher moment based modeling of turbulence enhanced explosion kernels in confined fuel-air mixtures. In *Advances in confined detonations and pulse detonation engines*, pages 17–40, 2003. Torus Press.

[50] A. Mura, V. Robin, and M. Champion. Modeling of scalar dissipation in partially premixed turbulent flames. *Combustion and Flame*, 149(1-2):217–224, April 2007.

[51] M. Stoellinger and S Heinz. Evaluation of scalar mixing and time scale models in PDF simulations of a turbulent premixed flame. *Combustion and Flame*, 157(9):1671–1685, September 2010.

[52] E.R. Hawkes, R. Sankaran, J.C. Sutherland, and J.H. Chen. Scalar mixing in direct numerical simulations of temporally evolving plane jet flames with skeletal CO/H-2 kinetics. *Proceedings of the Combustion Institute*, 31(Part 1):1633–1640, 2007.

[53] C.M. Cha and P. Trouillet. A model for the mixing time scale of a turbulent reacting scalar. *Physics of Fluids*, 15(6):1375–1380, June 2003.

[54] C. Dopazo and E.E. O'Brien. An approach to the autoignition of a turbulent mixture. *Acta Astronautica*, 1:1239–1266, 1974.

[55] J. Janicka, W. Kolbe, and W. Kollmann. Closure of the Transport-equation for the Probability Density-Function of Turbulent Scalar Fields. *Journal of Non-Equilibrium Thermodynamics*, 4(1):47–66, 1979.

[56] S. Subramaniam and S.B. Pope. A mixing model for turbulent reactive flows based on Euclidean minimum spanning trees. *Combustion and Flame*, 115(4):487–514, December 1998.

[57] Z.Y. Ren and S.B. Pope. An investigation of the performance of turbulent mixing models. *Combustion and Flame*, 136(1-2):208–216, January 2004.

[58] D.W. Meyer and P. Jenny. An improved mixing model providing joint statistics of scalar and scalar dissipation. *Combustion and Flame*, 155(3):490–508, November 2008.

[59] D.W. Meyer and P. Jenny. Micromixing models for turbulent flows. *Journal of Computational Physics*, 228(4):1275–1293, March 1 2009.

[60] D.W. Meyer and P. Jenny. A mixing model providing joint statistics of scalar and scalar dissipation rate. *Proceedings of the Combustion Institute*, 32:1613–1620, 2009.

[61] M. Hegetschweiler, B.T. Zoller, and P. Jenny. Reactive parametrized scalar profiles (R-PSP) mixing model for partially premixed combustion. *Combustion and Flame*, 159(2):734–747, February 2012.

[62] J Xu and SB Pope. Assessment of numerical accuracy of PDF Monte Carlo methods for turbulent reacting flows. *Journal of Computational Physics*, 152(1):192–230, June 10 1999.

[63] Private discussion with B. Naud.

[64] P Jenny, SB Pope, M Muradoglu, and DA Caughey. A hybrid algorithm for the joint PDF equation of turbulent reactive flows. *Journal of Computational Physics*, 166(2):218–252, January 20 2001.

[65] M. Muradoglu and S.B. Pope. Local time-stepping algorithm for solving probability density function turbulence model equations. *AIAA Journal*, 40(9):1755–1763, September 2002.

[66] S.B. Pope. PDF Methods for Turbulent Reactive Flows. *Progress in Energy and Combustion Science*, 11(2):119–192, 1985.

[67] B Yang and SB Pope. An investigation of the accuracy of manifold methods and splitting schemes in the computational implementation of combustion chemistry. *Combustion and Flame*, 112(1-2):16–32, January 1998.

[68] M. Sommerfeld, B. van Wachem, and R. Oliemans. *Best practice guidelines for computational fluid dynamics of dispersed multiphase flows*. Swedish Industrial Association for Multiphase Flows (SIAMUF), 2008.

[69] DL Marchisio and RO Fox. Solution of population balance equations using the direct quadrature method of moments. *Journal of Aerosol Science*, 36(1):43–73, January 2005.

[70] A Vié, M Sanjosé, S Jay, C. Angelberger, B. Cuenot, and M. Massot. Evaluation of a Multifluid Mesoscopic Eulerian Formalism on the Large Eddy Simulation of an aeronautical type configuration. In *7th International Conference on Multiphase Flow - ICMF 2010 Proceedings*, 2010.

[71] P Fevrier, O Simonin, and KD Squires. Partitioning of particle velocities in gas-solid turbulent flows into a continuous field and a spatially uncorrelated random distribution: theoretical formalism and numerical study. *Journal of Fluid Mechanics*, 533:1–46, June 25 2005.

[72] S. de Chaisemartin, L. Freret, D. Kah, F. Laurent, R. O. Fox, J. Reveillon, and M. Massot. Eulerian models for turbulent spray combustion with polydispersity and droplet crossing. *Comptes Rendus Mechanique*, 337(6-7):438–448, June-July 2009. 2nd INCA Workshop, CORIA, Rouen, France, October 23-24, 2008.

[73] D. Kah, F. Laurent, L. Freret, S. de Chaisemartin, R. O. Fox, J. Reveillon, and M. Massot. Eulerian Quadrature-Based Moment Models for Dilute Polydisperse Evaporating Sprays. *Flow Turbulence and Combustion*, 85(3-4, SI):649–676, December 2010.

[74] B. Naud. Particle dispersion modelling based on the Generalized Langevin Model for the seen velocity. In *Turbulence, Heat and Mass Transfer 7*, 2012.

[75] N. Beishuizen. *PFD modeling and particle-turbulence interaction of turbulent spray flames*. PhD thesis, TU Delft, 2008.

[76] Beishuizen N.A. and Roekaerts D. Reynolds stress and PDF modelling of two-way coupling and vaporisation interaction in a turbulent spray flame. In *Experiments and Numerical Simulations of Diluted Spray Turbulent Combustion*, 2011.

[77] RS Miller, K Harstad, and J Bellan. Evaluation of equilibrium and non-equilibrium evaporation models for many-droplet gas-liquid flow simulations. *International Journal of Multiphase Flow*, 24(6):1025–1055, September 1998.

[78] J Bellan and K Harstad. Analysis of the convective evaporation of nondilute clusters of drops. *International Journal of Heat and Mass Transfer*, 30(1):125–136, January 1987.

[79] R. Kurose, A. Fujita, and S. Komori. Effect of relative humidity on heat transfer across the surface of an evaporating water droplet in air flow. *Journal of Fluid Mechanics*, 624:57–67, April 10 2009.

[80] B. Abramzon and W.A. Sirignano. Droplet Vaporization Model for Spray Combustion Calculations. *International Journal of Heat and Mass Transfer*, 32(9):1605–1618, September 1989.

[81] Yuen M.C. and L.W. Chen. Drag of Evaporating Liquid Droplets. *Combustion Science and Technology*, 14(4-6):147–154, 1976.

[82] X.Q. Chen and J.C.F. Pereira. Computation of turbulent evaporating sprays with well-specified measurements: A. sensitivity study on droplet properties. *International Journal of Heat and Mass Transfer*, 39(3):441–454, February 1996.

[83] M.R.G. Zoby, S. Navarro-Martinez, A. Kronenburg, and A.J. Marquis. Evaporation rates of droplet arrays in turbulent reacting flows. *Proceedings of the Combustion Institute*, 33(Part 2):2117–2125, 2011.

[84] H.-W. Ge and E. Gutheil. Probability density function (PDF) simulation of turbulent spray flows. *Atomization and Sprays*, 16(5):531–542, 2006.

[85] H.-W. Ge and E. Gutheil. Simulation of a turbulent spray flame using coupled PDF gas phase and spray flamelet modeling. *Combustion and Flame*, 153(1-2):173–185, April 2008.

[86] L. C. Selle and J. Bellan. Evaluation of assumed-PDF methods in two-phase flows using direct numerical simulation. *Proceedings of the Combustion Institute*, 31(Part 2):2273–2281, 2007.

[87] J. Reveillon and F.-X. Demoulin. Effects of the preferential segregation of droplets on. evaporation and turbulent mixing. *Journal of Fluid Mechanics*, 583:273–302, July 25 2007.

[88] B. Duret, G. Luret, J. Reveillon, T. Menard, A. Berlemont, and F. X. Demoulin. DNS analysis of turbulent mixing in two-phase flows. *International Journal of Multiphase Flow*, 40:93–105, April 2012.

[89] P. Durand, M. Gorokhovski, and R. Borghi. An application of the probability density function model to diesel engine combustion. *Combustion Science and Technology*, 144(1-6):47–78, 1999.

[90] F.X. Demoulin and R. Borghi. Assumed PDF modeling of turbulent spray combustion. *Combustion Science and Technology*, 158:249+, 2000. 17th International Colloquium on the Dynamics of Explosions and Reactive Systems, Heidelberg, Germany, July 25-30, 1999.

[91] V. Massebeuf, B. Bedat, J. Helie, R. Lauvergne, O. Simonin, and T. Poinsot. Direct numerical simulation of evaporating droplets in turbulent flows for prediction of mixture fraction fluctuations: application to combustion simulations. *Journal of the Energy Institute*, 79(4):212–216, December 2006. 4th International Conference on Computational Heat and Mass Transfer (ICCHMT 2005), Paris, France, May 17-20, 2005.

[92] R. W. Bilger. A mixture fraction framework for the theory and modeling of droplets and sprays. *Combustion and Flame*, 158(2):191–202, February 2011.

[93] H.H. Chiu and T.M. Liu. Group Combustion of Liquid Droplets. *Combustion Science and Technology*, 17(3-4):127–142, 1977.

[94] J. Reveillon and L. Vervisch. Analysis of weakly turbulent dilute-spray flames and spray combustion regimes. *Journal of Fluid Mechanics*, 537:317–347, August 25 2005.

[95] Y. Baba and R. Kurose. Analysis and flamelet modelling for spray combustion. *Journal of Fluid Mechanics*, 612:45–79, October 10 2008.

[96] J.-B. M, O. Colin, and D. Veynante. Modeling ignition and chemical structure of partially premixed turbulent flames using tabulated chemistry. *Combustion and Flame*, 152(1-2):80–99, January 2008.

[97] P. Domingo, L. Vervisch, and K. Bray. Partially premixed flamelets in LES of nonpremixed turbulent combustion. *Combustion Theory and Modelling*, 6(4):529–551, December 2002.

[98] M. Ihme, C.M. Cha, and H. Pitsch. Prediction of local extinction and re-ignition effects in non-premixed turbulent combustion using a flamelet/progress variable approach. *Proceedings of the Combustion Institute*, 30(Part 1):793–800, 2005. 30th International Symposium on Combustion, Univ Illinois Chicago, Chicago, IL, July 25-30, 2004.

[99] L. Vervisch, R. Hauguel, P. Domingo, and M. Rullaud. Three facets of turbulent combustion modelling: DNS of premixed V-flame, LES of lifted nonpremixed flame and RANS of jet-flame. *Journal of Turbulence*, 5, January 30 2004.

[100] P.A.M. Kalt, Y.M. Al-Abdeli, A.R. Masri, and R.S. Barlow. Swirling turbulent non-premixed flames of methane: Flow field and compositional structure. *Proceedings of the Combustion Institute*, 29(Part 2):1913–1919, 2002. 29th International Combustion Symposium, Hokkaido Univ, Sapporo, Japan, July 21-26, 2002.

[101] Y.M. Al-Abdeli and A.R. Masri. Recirculation and flowfield regimes of unconfined non-reacting swirling flows. *Experimental Thermal and Fluid Science*, 27(5):655–665, May 2003. 14th Australasian Fluid Mechanics Conference, Adelaide Univ, Adelaide, Australia, December 09-14, 2001.

[102] A.R. Masri, P.A.M. Kalt, and R.S. Barlow. The compositional structure of swirl-stabilised turbulent nonpremixed flames. *Combustion and Flame*, 137(1-2):1–37, April 2004.

[103] Y.A. Al-Abdeli, A.R. Masri, G.R. Marquez, and S.H. Starner. Time-varying behaviour of turbulent swirling nonpremixed flames. *Combustion and Flame*, 146(1-2):200–214, July 2006.

[104] A.R. Masri, P.A.M. Kalt, Y.M. Al-Abdeli, and R.S. Barlow. Turbulence-chemistry interactions in non-premixed swirling flames. *Combustion Theory and Modelling*, 11(5):653–673, 2007.

[105] http://sydney.edu.au/engineering/aeromech/thermofluids/swirl.htm.

[106] J. Floyd, A.M. Kempf, A. Kronenburg, and R.H. Ram. A simple model for the filtered density function for passive scalar combustion LES. *Combustion Theory and Modelling*, 13(4):559–588, 2009.

[107] M. Ihme and H. Pitsch. Prediction of extinction and reignition in nonpremixed turbulent flames using a flamelet/progress variable model 2. Application in LES of Sandia flames D. and E. *Combustion and Flame*, 155(1-2):90–107, October 2008.

[108] T. Landenfeld, A. Sadiki, and J. Janicka. A turbulence-chemistry interaction model based on a multivariate presumed beta-PDF method for turbulent flames. *Flow Turbulence and Combustion*, 68(2):111–135, 2002.

[109] H. Lehtiniemi, F. Maus, M. Balthasar, and I. Magnusson. Modeling diesel spray ignition using detailed chemistry with a progress variable approach. *Combustion Science and Technology*, 178(10-11):1977–1997, October-November 2006. 20th International Colloquium on the Dynamics of Exposions and Reactie Systems, Montreal, CANADA, July 31-August 05, 2005.

[110] R.S. Barlow. Web site for the International Workshop on Measurement and Computation of Turbulent Non-premixed Flames (TNF), http://www.ca.sandia.gov/TNF/, 1996.

[111] A.R. Masri, R.W. Dibble, and R.S. Barlow. The structure of turbulent non-premixed flames revealed by Raman-Rayleigh-LIF measurements. *Progress in Energy and Combustion Science*, 22(4):307–362, 1996.

[112] R.S. Barlow and J.H. Frank. Effects of turbulence on species mass fractions in methane/air jet flames. In Burgess, A.R. and Dryer, F.L., editor, *27th Symposium (International) on Combustion*, pages 1087–1095, 1998. 27th International Symposium on Combustion, Univ Colorado, Boulder, CO, August 02-07, 1998.

[113] R. Cabra, T. Myhrvold, J.Y. Chen, R.W. Dibble, A.N. Karpetis, and R.S. Barlow. Simultaneous laser Raman-Rayleigh-Lif measurements and numerical

modeling results of a lifted turbulent H-2/N-2 jet flame in a vitiated coflow. *Proceedings of the Combustion Institute*, 29(Part 2):1881–1888, 2002. 29th International Combustion Symposium, Hokkaido Univ, Sapporo, Japan, July 21-26, 2002.

[114] R. Cabra, J.Y. Chen, R.W. Dibble, A.N. Karpetis, and R.S. Barlow. Lifted methane-air jet flames in a vitiated coflow. *Combustion and Flame*, 143(4):491–506, December 2005.

[115] K. Bray, P. Domingo, and L. Vervisch. Role of the progress variable in models for partially premixed turbulent combustion. *Combustion and Flame*, 141(4):431–437, June 2005.

[116] R. De Meester, B. Naud, U. Maas, and B. Merci. Transported scalar PDF calculations of a swirling bluff-body flame ('SM1') with a reaction diffusion manifold. *Combustion and Flame*, 159(7):2415–2429, July 2012.

[117] C. Olbricht, F. Hahn, A. Ketelheun, and J. Janicka. Strategies for presumed PDF modeling for LES with premixed flamelet-generated manifolds. *Journal of Turbulence*, 11(38):1–18, 2010.

[118] A. Yoshida, T. Igarashi, and Y. Kotani. Extinction of turbulent diffusion flames by Kolmogorov microscale turbulence. *Combustion and Flame*, 109(4):669–681, June 1997.

[119] S.K. Omar, D. Geyer, A. Dreizler, and J. Janicka. Investigation of flame structures in turbulent partially premixed counter-flow flames using planar laser-induced fluorescence. *Progress in Computational Fluid Dynamics*, 4(3-5):241–249, 2004. Workshop on Trends in Numerical and Physical Modelling for Turbulent Processes in Gas Trubine Combustors, Tech Univ Darmstadt, Darmstadt, Germany, November 14-15, 2002.

[120] F. Takahashi and V.R. Katta. Unsteady extinction mechanisms of diffusion flames. In Burgess, A.R. and Dryer, FL, editor, *26th Symposium (International) on Combustion*, pages 1151–1160, 1996. 26th International Symposium on Combustion, Naples, Italy, July 28-August 02, 1996.

[121] S. Mitarai, J.J. Riley, and G. Kosaly. A Lagrangian study of scalar diffusion in isotropic turbulence with chemical reaction. *Physics of Fluids*, 15(12):3856–3866, December 2003.

[122] P. Sripakagorn, S. Mitarai, G. Kosaly, and H. Pitsch. Extinction and reignition in a diffusion flame: a direct numerical simulation study. *Journal of Fluid Mechanics*, 518:231–259, November 10 2004.

[123] M. Ihme and H. Pitsch. Prediction of extinction and reignition in nonpremixed turbulent flames using a flamelet/progress variable model 2. Application in LES of Sandia flames D. and E. *Combustion and Flame*, 155(1-2):90–107, October 2008.

[124] P.A.M. Kalt, Y.M. Al-Abdeli, A.R. Masri, and R.S. Barlow. Swirling turbulent non-premixed flames of methane: Flow field and compositional structure. *Proceedings of the Combustion Institute*, 29(Part 2):1913–1919, 2002. 29th International Combustion Symposium, Hokkaido Univ, Sapporo, Japan, July 21-26, 2002.

[125] A.R. Masri, S.B. Pope, and B.B. Dally. Probability density function computations of a strongly swirling nonpremixed flame stabilized on a new burner. *Proceedings of the Combustion Institute*, 28(Part 1):123–131, 2000. 28th International Symposium on Combustion, Univ Edinburgh, Edinburgh, Scotland, July 30-August 04, 2000.

[126] S. James, J. Zhu, and M.S. Anand. Large eddy simulations of turbulent flames using the filtered density function model. *Proceedings of the Combustion Institute*, 31(Part 2):1737–1745, 2007.

[127] A. Kempf, W. Malalasekera, K.K.J. Ranga-Dinesh, and O. Stein. Large Eddy Simulations of Swirling Non-premixed Flames With Flamelet Models: A. Comparison of Numerical Methods. *Flow Turbulence and Combustion*, 81(4):523–561, December 2008.

[128] W. Malalasekera, K.K.J. Ranga-Dinesh, S.S. Ibrahim, and A. R. Masri. LES of recirculation and vortex breakdown in swirling flames. *Combustion Science and Technology*, 180(5):809–832, 2008. 5th Mediterranean Combustion Symposium, Monastir, Tunisia, September 09-13, 2007.

[129] O. Stein and A. Kempf. LES of the Sydney swirl flame series: A study of vortex breakdown in isothermal and reacting flows. *Proceedings of the Combustion Institute*, 31(Part 2):1755–1763, 2007.

[130] H. El-Asrag and S. Menon. Large eddy simulation of bluff-body stabilized swirling non-premixed flames. *Proceedings of the Combustion Institute*, 31(Part 2):1747–1754, 2007.

[131] B. Merci, B. Naud, D. Roekaerts, and U. Maas. Joint Scalar versus Joint Velocity-Scalar PDF Simulations of Bluff-Body Stabilized Flames with REDIM. *Flow Turbulence and Combustion*, 82(2):185–209, March 2009.

[132] D. Roekaerts, B. Merci, B. Naud, and U. Maas. Elimination of Fast Modes in the Coupled Process of Chemistry and Diffusion in Turbulent Nonpremixed Flames: An Application of the REDIM Approach. *International Journal for Multiscale Computational Engineering*, 7(6):487–508, 2009. Delft-Center-for-Computational-Science-and-Engineering Symposium, Delft, Netherlands, September 19, 2008.

[133] B. Naud, C. Jimenez, and D. Roekaerts. A consistent hybrid PDF method: implementation details and application to the simulation of a bluff-body stabilised flame. *Progress in Computational Fluid Dynamics*, 6(1-3):146–157, 2006.

[134] G.X. Li, B. Naud, and D. Roekaerts. Numerical investigation of a bluff-body stabilised nonpremixed flame with differential Reynolds-stress models. *Flow Turbulence and Combustion*, 70(1-4):211–240, 2003.

[135] H. Wang and S.B. Pope. Lagrangian investigation of local extinction, re-ignition and auto-ignition in turbulent flames. *Combustion, Theory and Modelling*, pages 857–82.

[136] L. Lu and S. B. Pope. An improved algorithm for in situ adaptive tabulation. *Journal of Computational Physics*, 228(2):361–386, February 1 2009.

[137] D.A. Goussis and U. Maas. *Turbulent Combustion Modeling: Advance, New Trends and Perspectives, Fluid Mechanics and Its Applications*, volume 95, pages 193–220. Springer-Verlag, 2011.

[138] H. Pitsch and W. Steiner. Large-eddy simulation of a turbulent piloted methane/air diffusion flame (Sandia flame D). *Physics of Fluids*, 12(10):2541–2554, October 2000.

[139] K. Koenig, V. Bykov, and U. Maas. Investigation of the Dynamical Response of Methane/Air Counterflow Flames to Inflow Mixture Composition and Flow

Field Perturbations. *Flow Turbulence and Combustion*, 83(1):105–129, July 2009.

[140] R. De Meester, B. Naud, and B. Merci. Hybrid RANS/PDF Calculations of a Swirling Bluff-Body Flame('SM1'): Influence of the Mixing Model. In *Proceedings of the 7th Mediterranean Combustion Symposium,*, pages TC–21, 2011. Chia Laguna, Cagliari, Sardinia, Italy, September 11-15, 2011.

[141] K. Liu, S.B. Pope, and D.A. Caughey. Calculations of bluff-body stabilized flames using a joint probability density function model with detailed chemistry. *Combustion and Flame*, 141(1-2):89–117, April 2005.

[142] M. Ihme, C. Schmitt, and H. Pitsch. Optimal artificial neural networks and tabulation methods for chemistry representation in LES of a bluff-body swirl-stabilized flame. *Proceedings of the Combustion Institute*, 32:1527–1535, 2009.

[143] B. Merci, D. Roekaerts, B. Naud, and S.B. Pope. Comparative study of micromixing models in transported scalar PDF simulations of turbulent non-premixed bluff body flames. *Combustion and Flame*, 146(1-2):109–130, July 2006.

[144] K. Gkagkas, R.P. Lindstedt, and T.S. Kuan. Transported PDF Modelling of a High Velocity Bluff-Body Stabilised Flame (HM2) Using Detailed Chemistry. *Flow Turbulence and Combustion*, 82(4):493–509, June 2009. 2nd ECCOMAS Thematic Conference on Meshles Methods, Porto, Portugal, July 09-11, 2007.

[145] M. Adachi, V.G. McDonell, and G.S. Samuelsen. Nonintrusice Measurement of Gaseous Species in Reacting and Nonreacting Sprays. *Combustion Science and Technology*, 75(4-6):179–194, 1991.

[146] C. Chevalier, J. Warnatz, and H. Melenk. Automatic Generation of Reaction-Mechanisms for the Description of the Oxidation of Higher Hydrocarbons. *Berichte der Bunsen-Gesellschaft-Physical Chemistry Chemical Physics*, 94(11):1362–1367, November 1990. 89th General Assembly of the Deutsche Bunsen-Gesellschaft fur Physikalische Chemie: Chemical Elemental Reactions, Tubingen, Federal Republic Germany, May 24-26, 1990.